Structure, electronic structure and dynamic in layered transition metal oxides for Na-ion batteries

Yohan Biecher

To cite this version:

Yohan Biecher. Structure, electronic structure and dynamic in layered transition metal oxides for Na-ion batteries. Material chemistry. Université de Bordeaux, 2019. English. NNT : 2019BORD0307 . tel-03475586

HAL Id: tel-03475586
https://theses.hal.science/tel-03475586

Submitted on 11 Dec 2021

THÈSE PRÉSENTÉE

A L'UNIVERSITE DE BORDEAUX

POUR L'OBTENTION DU GRADE DE

DOCTEUR

par

Yohan BIECHER

ÉCOLE DOCTORALE DES SCIENCES CHIMIQUES

SPÉCIALITÉ : physico-chimie de la matière condensée

Structure, electronic structure and dynamics in layered transition metal oxides for Na-ion batteries

Soutenu le 10 décembre 2019

Membres du jury :

M. MAGLIONE, Mario	Directeur de Recherche, ICMCB	Président
M. DUPRE, Nicolas	Chargé de Recherche, IMN	Rapporteur
Mme LAURENCIN, Danielle	Chargée de Recherche, ICGM	Rapporteure
M. BERTHELOT, Romain	Chargé de Recherche, ICGM	Examinateur
Mme GOWARD, Gillian	Professeure, McMaster University	Examinatrice
M. DELMAS, Claude	Directeur de Recherche Emérite, ICMCB	Co-encadrant
Mme CARLIER-LARREGARAY, Dany	Professeure, Université de Bordeaux, ICMCB	Directrice de thèse

Remerciements

Dans un premier temps, je voudrais remercier tout particulièrement mon encadrante de thèse, Dany CARLIER pour sa bienveillance et la confiance qu'elle m'a accordé pour mener ce projet. Je tiens également à remercier mes co-encadrants, Claude DELMAS pour son et Gillian GOWARD pour son accueil au sein de son équipe pendant deux mois.

Je tiens également à remercier Mario MAGLIONE en sa qualité de directeur du laboratoire mais aussi en sa qualité de président de mon jury de thèse.

Je tiens aussi à exprimer ma gratitude envers tous les membres de mon jury, d'avoir accepté d'en faire partie : Danielle LAURENCIN et Nicolas DUPRE en tant que rapporteurs et Romain BERTHELOT en tant qu'examinateur.

Je souhaite également remercier le Fonds France-Canada pour la Recherche (FFCR) pour avoir financé ces travaux.

Durant ces trois années, j'ai été amené à collaborer avec plusieurs personnes que je souhaite également remercier : Laurence CROGUENNEC responsable du groupe II pour sa gentillesse et les valeurs qu'elle véhicule au sein du groupe, Mathieu DUTTINE pour toute son aide aux spectromètres RMN, Axelle GRELARD et Estelle MORVAN (service RMN de l'IECB), Eric LEBRAUD et Stanislav PECHEV (service DRX), Francois Fauth (Synchrotron d'ALBA), Benoit MORTEMARD DE BOISSE, Stéphane TOULIN, Didier CAMPAGNE, Abder SALHI. Je suis également reconnaissant envers Cathy DENAGE pour tout ce qu'elle apporte au groupe et au laboratoire ainsi qu'à Sabine GOMA et Philippe DAGAULT pour leur aide mais aussi leur bonne humeur.

La suite de mes remerciements s'adresse à tous les permanents du groupe II avec qui j'ai pu avoir de nombreux échanges enrichissants : Marie GUIGNARD, Liliane GUERLOU-DEMOURGUES, Jacob OLCHOWKA, Emmanuel PETIT (« ça mérite une choco ! »), Jérôme KALISKY, Brigitte PECQUENARD, Frédéric LE CRAS, François WEILL et Philippe VINATIER.

Je suis également reconnaissant envers l'Université de Bordeaux et l'EDSC de m'avoir donné l'opportunité d'enseigner pendant deux années ainsi qu'à tous les représentant-doctorant de l'école doctorale avec qui j'ai eu la chance d'organiser trois journées de l'école doctorale pendant cette thèse. Je remercie aussi « mes » stagiaires avec qui j'ai eu la chance de travailler : Antoine, Mehdi et Alexis. Faire partie de l'Association des Doctorant Chimistes (ADoC) a aussi été un privilège et une joie et j'en remercie Damien, Cindy, Fiona, Maël, Kenneth et Camille.

Je suis également reconnaissant envers mes amis externes au laboratoire : Julien, Adrien, Marie-Anne, Manon, Clémence, Patrick, Léopold, Pauline, Clément, Maxence, Grégoire, Alex et Thibault qui ont toujours su m'offrir des week-end afin de décompresser.

Je voudrais aussi remercier tous mes anciens coéquipiers du dimanche matin de l'US Talence : Chris (x2), Nikko, Pascal, Jacques, Abdel, Cédric (x2), Igor, Seb, Fab', César, Yann et Greg ainsi qu'à l'équipe du CAES du lundi midi : Eric, Olive, Thomas, Tom, JC et bien d'autres.

J'ai également une pensée pour les membres du groupe de Gillian Goward au Canada pour leur accueil et leur aide : Dave, Danielle, Chelsey, Blosom, Kris, Chris et Sergey.

Enfin un travail de trois ans de thèse est aussi une œuvre collective et faire partie de ce groupe a été une véritable aubaine et un bonheur énorme. Ainsi je souhaite remercier tous les membres non-permanents du groupe II : Tiftif, Marie « Chasseuse de Pokémon », Quentin « Comment est votre blanquette ? », Annie-Kim « Canadab », JB « coach », Long « les synthèses fonctionnent mieux à Bordeaux », Adrien « la bière c'est de l'eau », Ronando, Fatima « Wallah », Gwen, Vola, Valentin « très tchatcheur », Vadim, Léah, Edgar, Sunkyu, Damieng, Elodie, Cedric, Paula, Vincent, Thibault, Céline, Alex, Alberto, Ségolène, Louisiane, Tahya, Laura, Florian, Max, Charlotte « va laver ton four », Mathias et Aurélien « Skyrock ». J'ai aussi une pensée pour les doctorants d'autres groupes : Maël, Béatrice et Fan pour ne citer qu'eux.

Pour finir, ma plus grande pensée est envers ma famille pour leur soutien et notamment sur la fin de ma thèse.

Merci encore à tous !

Table of contents

Table of contents

General Introduction

The lamellar oxides, A_xMO_2 (A = alkali ions, M = transition metal ions) are phases largely studied in solid-state chemistry. They can be described as an alternation of MO_2 slabs formed by CoO_6 octahedra and interslab spaces in which x A^+ ions are intercalated. Depending of the slabs packing, the alkali ions can intercalate in sites with different possible geometries. For instance, on **Figure GI-1**, the A^+ ions are represented in octahedral sites. In order to describe easily the lamellar oxides, Delmas *et al.*[1] proposed a specific nomenclature in 1980. This nomenclature is composed of letter(s) which correspond to the intercalation site geometry for the alkali ions and one number corresponding to the number of A_x interslab spaces necessary to describe the hexagonal unit cell. If the cell undergoes a distortion (monoclinic or orthorhombic), then a **'** symbol is used in the structure name.

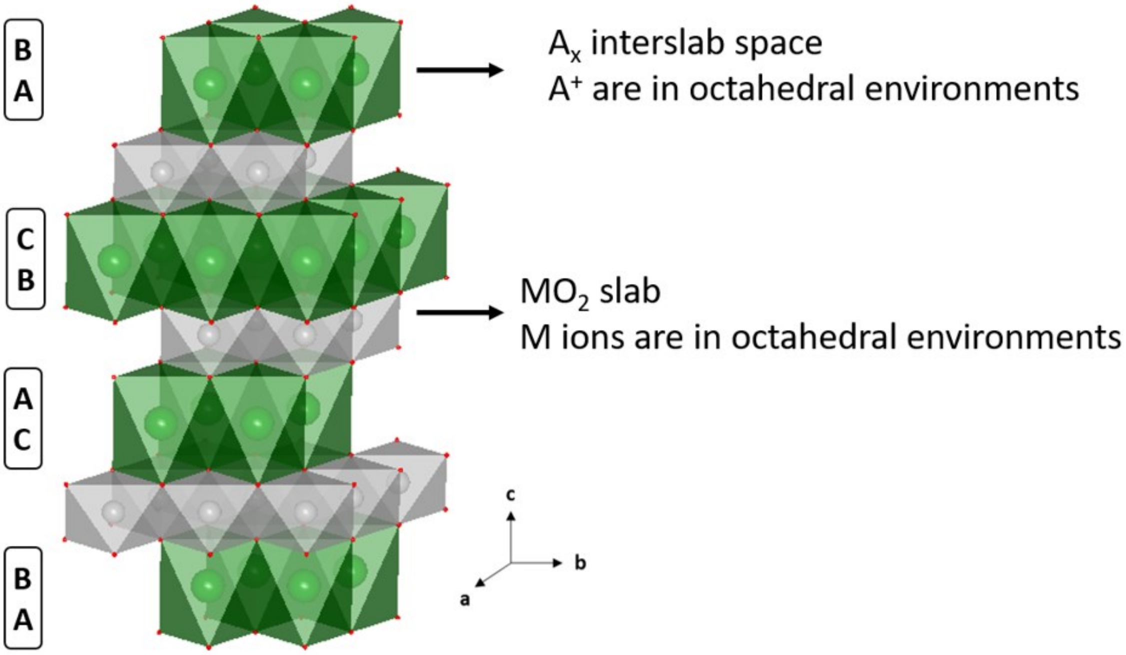

***Figure GI-1**: Representation of the A_xMO_2 structure. The M ions are in grey, the A ions are in green and the O ions are in red. The A, B and C letters corresponds to the oxygen positions in order to have a compact stacking.*

Generally, for the $LiMO_2$ phases, the Li^+ ions are intercalated in octahedral sites and it is necessary to include three interslab spaces in the structure to describe the unit cell of the materials leading to an O3 structure. For instance, the O3-$LiCoO_2$ phase is well-known because of its high electrochemical performances as positive electrode material for Li-ion batteries. It was commercialized by SONY in 1991 for mobile applications. On this system, Li deficient phases can be only prepared by chemical or electrochemical deintercalation. Several other stacking sequences can be thus observed as O1[2].

If Li^+ ions are replaced by Na^+ ions, the variety of layered Na_xMO_2 phases that can be synthetized is much larger. The larger Na^+ ions size (0.99 Å) compared to Li^+ (0.59 Å)[3] can be localized either in octahedral or in prismatic sites with two or three interslab spaces in their unit cell (usually O2, P2 and P3 structures) depending on the synthesis conditions like the nature of the transition metal ions, the synthesis temperature or the initial Na^+/M ratio used for the synthesis[4–6]. **Figure GI-2** proposes an overview of the different polytypes that can be synthetized for Na_xCoO_2 depending of the temperature and initial Na^+/Co ratio and highlights the rich phases diagram of the Na_xCoO_2 systems.

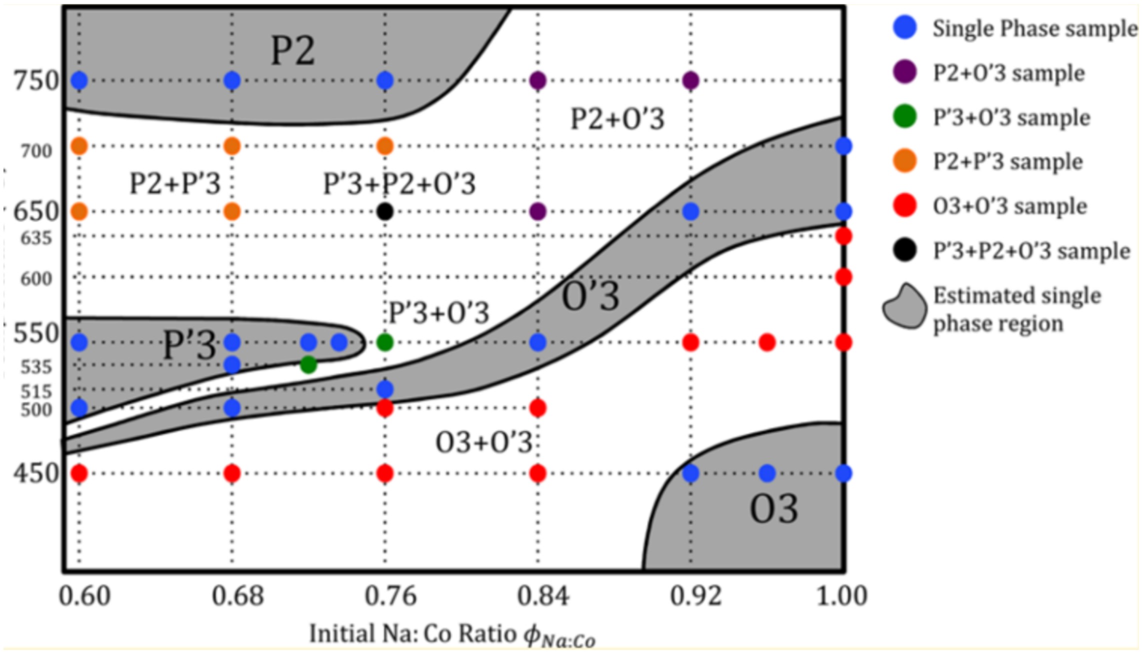

***Figure GI-2**: Phases diagram of Na_xCoO_2. The grey zones represent the single phase synthesis zones while the white zones are the multiple phases synthesis zones. Extracted from [7]*

Many Na_xMO_2 systems are (re)investigated as positive electrode material for Na-ion batteries because of a drastic decrease of the Li resources amount involving a large increase of the Li materials precursors price compared to the Na precursors like Na_2CO_3[8,9]. The interest for P2-Na_xMO_2 and especially, the P2-Na_xCoO_2 system was reactivated with reports concerning the $Na_{0.5}CoO_2$ phase in 1997[10,11] and later the hydrated Na_xCoO_2 phases, showing interesting thermoelectric power and superconductivity performances[12,13]. Lee *et al.*[14,15] also showed an enhancement of the thermopower for $x > 0.75$ in P2-Na_xCoO_2. In 2004, Huang *et al.*[16] showed that the ordered phase $Na_{1/2}CoO_2$ exhibits a metal-insulator transition at 53 K, increasing the interest about this system and its peculiar phases.

K_xCoO_2 proposed, also interesting physical properties and especially magnetic and electronic properties for different x values ($x = 0.67$, $x = 0.5$[17] and $x = 0.36$[18]). $K_{0.36}CoO_2$ has a semi-conductor behavior while $K_{0.5}CoO_2$ and $K_{0.67}CoO_2$ have a metallic behavior. K_xMO_2 systems were investigated as positive electrode material for K-ion batteries as an alternative to the Na and Li-ion batteries. Komaba and coworkers[19] proposed the first investigation of K_xCoO_2 as positive electrode material with two different polytypes, P2 and P3 after the first report of the phases synthesis in 1975[17]. Note that other lamellar oxides were tested for K-ion batteries as $K_xFe_{0.5}Mn_{0.5}O_2$[20], K_xMnO_2[21,22], $K_xMn_{0.9}Mg_{0.1}O_2$[23] or K_xCrO_2[24]. Moreover, many studies focused on other phases as polyanionic or Prussian blue compounds which present, also, interesting electrochemical performances[25].

In this manuscript, we propose to study the average structure of different layered systems used as battery positive electrode materials by *ex-situ* and *in-situ* X-Ray Diffraction (XRD) but also the local structure and electronic structure by solid state Magic Angle Spinning Nuclear Magnetic Resonance (MAS NMR). MAS NMR was already performed successfully in the solid state chemistry field for the investigation of many local and electronic structures and especially in the group, for NVPF[26], phosphate[27] or tavorite[28] structures for example. MAS NMR is a powerful technique which can be used in the battery domain[29,30]. In fact, NMR allows the investigation of different parts of a battery as the electrodes, the electrolyte, the interfaces or the SEI[31–38]. Moreover, NMR is an interesting technique to get information about the mechanisms occurring during an electrochemical cycling[39,40].

In this work, two original layered oxides are, firstly, reported in the chapters II and III, respectively, OP4-(Li, Na)CoO_2 and O4-$LiCoO_2$. The OP4 phase was reported for the first time by Balsys and Davis in 1994[41] and can be described as an 1:1 alternation of Na and Li interslab spaces intercalated between the CoO_2 slabs along the c axis while the O4-$LiCoO_2$ phase proposed an 1:1 alternation of O3 and O2-type Li interslab spaces. Both phases were already investigated in the group during Romain Berthelot PhD[42–44]. He mainly studied their average structures by XRD, the influence of the temperature on their structures and their electrochemical properties. In this work, we correlated together, thanks to NMR acquisitions, the average, the local and the electronic structures of both phases. A specific attention was also given to the understanding of the chemical formula of both materials and to the ionic mobility of the Li^+ ions in both structures with 2D MAS NMR acquisitions. I investigated the dynamics of the Li^+ ions in both phases in McMaster University (Hamilton, Canada) under the supervision of Gillian Goward during two one-month visits in 2017 and 2018.

Then, we focused our study on layered oxides for Na-ion batteries, P2-$Na_xCo_yMn_{1-y}O_2$ ($y = 2/3$, 1/2, 1/3 and 1) and O3-Na_xRuO_3 which propose interesting electrochemical properties[45,46]. A new formulation of electrolytes allows to reach, reversibly, higher voltages than previously. Therefore, a new part of the P2-Na_xCoO_2 phases diagram can be reached for low Na^+ contents, in fact, Berthelot *et al.*[47] studied this system by *in-situ* XRD but limited his investigations to $x > 1/2$. In the chapter IV, we report the electrochemical properties of the P2-$Na_xCo_yMn_{1-y}O_2$ ($y = 2/3$, 1/2, 1/3 and 1) systems in two voltage ranges. Moreover, we propose the investigation of the structural evolution of these systems during the Na^+ deintercalation by *in-situ* XRD.

The chapter V focuses on the P2-Na_xCoO_2 and P2-$Na_xCo_{2/3}Mn_{1/3}O_2$ systems. Different phases were synthetized at specific voltages by an electrochemical technique and analyzed by *ex-situ* XRD and ^{23}Na MAS NMR in order to understand the mechanisms involved by the Na^+ deintercalation.

Finally, the chapter VI proposes the investigation of the local structure evolution of the O3-Na_xRuO_3 system by *ex-situ* ^{23}Na MAS NMR in collaboration with Benoît Mortemard de Boisse (from Pr. Yamada group in Tokyo). Previous studies[46,48] reported an extra capacity due to the participation of the oxygen ions in the redox process. The different phases were synthetized in Japan with the same technique than in the chapter V and only the ^{23}Na MAS NMR results are proposed in this chapter.

Chapter I: Generalities

1. The lamellar oxides

1.1 O3-$NaFeO_2$ structure

In 1933, Goldzstaub[49] described the lamellar oxides A_xMO_2 (A = alkali ion(s), M = transition metal ion(s)) as a stacking derived from the structure of α-$NaFeO_2$[50] or O3-$NaFeO_2$[1]. O3-$NaFeO_2$ derived from the NaCl lattice, as shown on **Figure I-1a**, by switching the chloride ions by oxygen ions and filling the cationic sites by iron and sodium ions. A deformation along the [1 1 1] direction (**Figure I-1b**) due to the Na^+ (1.02 Å) and Fe^{3+} (0.645 Å)[3] ions dimension difference occurs and leads to a rhombohedral lattice. A hexagonal description, as shown in general introduction, is also possible in the $R\bar{3}m$ (number 166) space group by considering the [1 1 1] direction as the c axis. The hexagonal description allows to represent the cell as a stacking of FeO_2 and NaO_2 slabs with a 1:1 alternation in the case of O3-$NaFeO_2$ (**Figure GI-1**). The atomic positions are reported by Takeda *et al.*[50] as Na (3a, 0, 0, 0), Fe (3b, 0, 0, 1/2) and O (6c, 0, 0, Z_O).

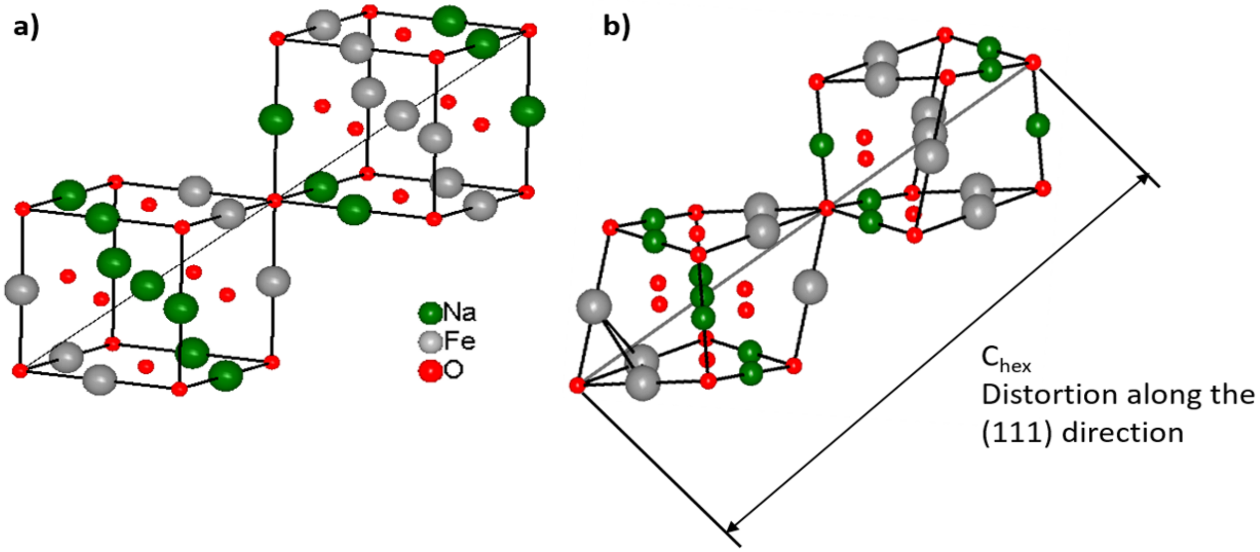

***Figure I-1**: a) Representation of O3-$NaFeO_2$ structure in NaCl rock salt type structure. The dashed line in the cell represents the (111) direction b) Representation of O3-$NaFeO_2$ structure considering the distortion along the (111) direction[50].*

The hexagonal and rhombohedral representations of the O3-$NaFeO_2$ are shown in **Figure I-2** and the equations to switch from one cell to another are the following:

$$a_{hex} = 2a_{rh} * \sin\left({}^{\alpha}/_{2}\right)$$

$$b_{hex} = a_{hex}$$

$$c_{hex} = a_{rh} * \sqrt{3 + 6 * \cos(\alpha)}$$

It is important to note the existence of a third representation which is also possible in a monoclinic cell (**Figure I-2**). The monoclinic cell is involved by a distortion of the MO_6 octahedra. The following equations allow to switch from a hexagonal to a monoclinic representation.

$$a_{mon} = a_{hex} * \sqrt{3}$$

$$b_{mon} = a_{hex}$$

$$c_{mon} = \frac{\sqrt{c_{hex}^2 + 3a_{hex}^2}}{3}$$

$$\beta_{mon} = {}^{\pi}/_{2} + \arctan\left(\frac{a_{hex} * \sqrt{3}}{c_{hex}}\right)$$

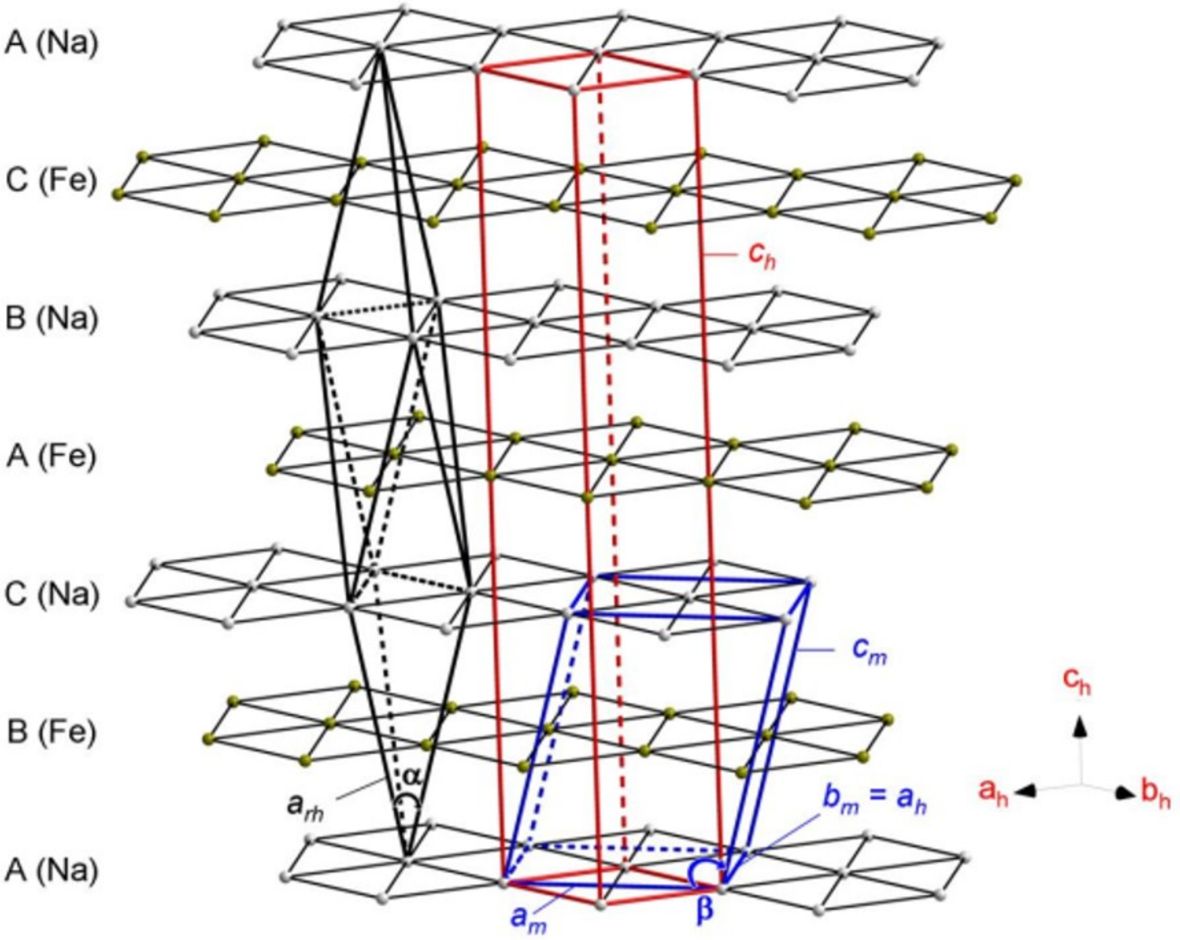

***Figure I-2**: Representation of the hexagonal, monoclinic and rhombohedral cells from the O3 structure. The equations introduced before allow to switch from one cell to another.*

1.2 The different polytypes and their intercalation sites

The other lamellar oxide polytypes can be obtained by considering elemental symmetry operations on the O3 structure as translations or rotations. By considering these operations, changes in the intercalation sites and in the oxygen ions positions lead to the P2, P3 or O2 structures (**Figure I-3**). P sites correspond to prismatic interstitial sites for the alkali ions intercalation. In this report, materials with prismatic and octahedral sites are reported that's why a short overlook of every stacking is necessary. Note that other intercalation sites are reported in the literature like tetrahedral (T)[51] or linear (D for Dumbbell)[52]. **Figure I-3** depicts a representation of the O3, P2 and P3 structures and shows the geometry of the intercalation sites in each case.

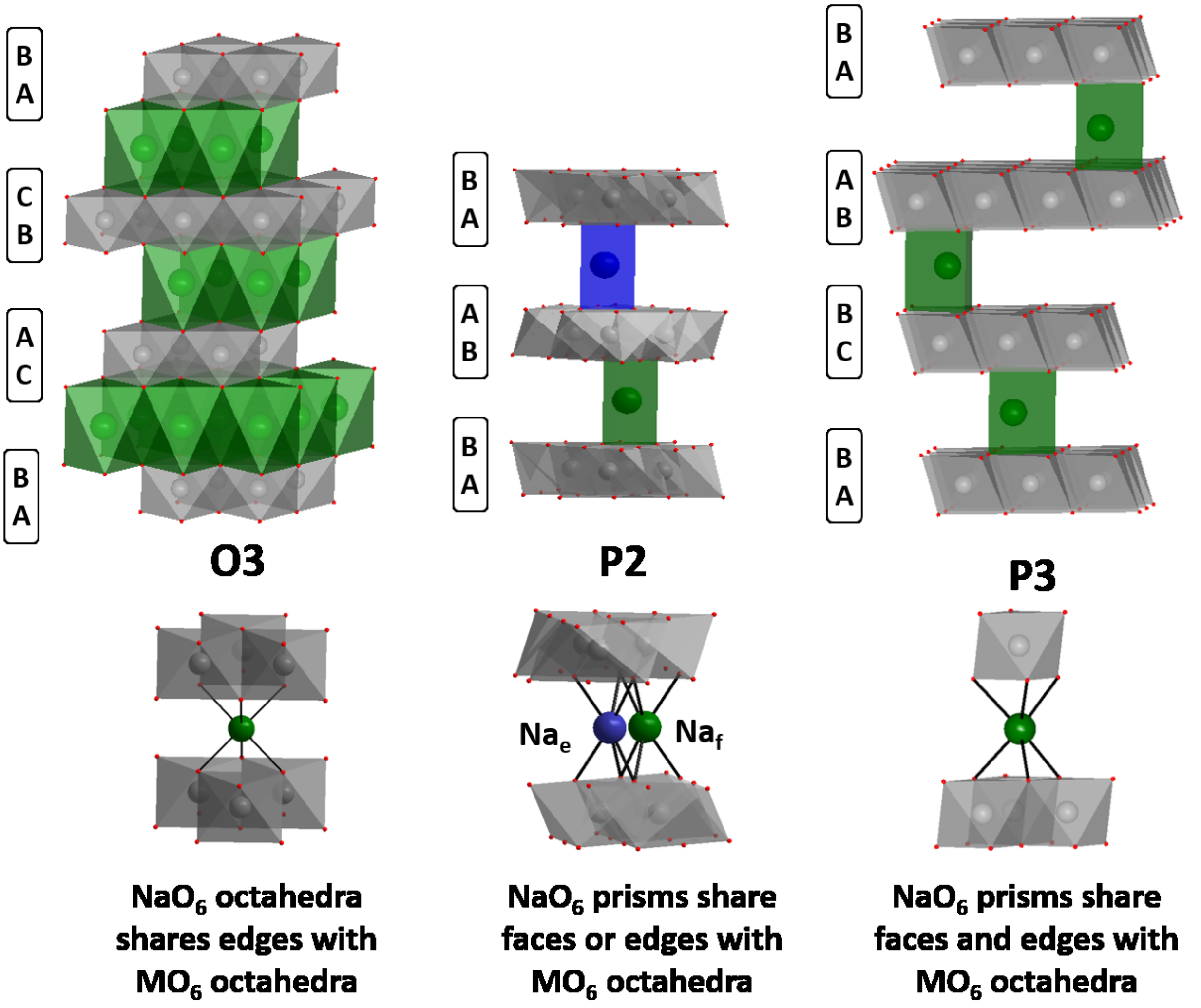

***Figure I-3**: Representation of the O3, P2 and P3 structures and representation of the corresponding Na$^+$ intercalation sites*

- In the O3 structure, the A$^+$ ions share only the edges with the surrounding MO$_6$ octahedra. The O3 structures are obtained for A$^+$/M ratio close to one. Note that lamellar oxides O3-LiMO$_2$ can be synthetized only for M = Cr, Co, Ni or V while the panel of 3d transition metals is larger concerning the synthesis of O3-NaMO$_2$ (for instance O3-NaCoO$_2$[53]).

- In the P3 structure, the A$^+$ ions share simultaneously edges and faces with the surrounding MO$_6$. They are usually synthetized at moderate temperature (≈500°C) and for low A$^+$/M ratio (≈0.6)[1].

- In the P2 structure, the prismatic sites can either share edges (site labelled A_e) or faces (site labelled A_f) with the surrounding MO_6. As the electrostatic repulsions are more intense between the A^+ in A_f sites and the M ions, the A_e sites are favored for the A^+ intercalation involving amount of A^+ ions in A_e twice bigger than in A_f.

Finally, for the structures with prismatic sites, filling the whole interslab spaces with Na^+ ions is impossible due to the too large Na^+ ions size compared to the distance between the neighbor sites. This point isn't true for lithium in octahedral sites and explained why the Li interslab spaces are totally full after thermal treatment. Moreover, each structure can be described by a specific space group and specific atomic positions. These data are summarized in **Table I.1**.

Structure	**Space Group**	**Atomic positions**			
		A		**M**	**O**
		A_e	**A_f**		
O3	$R\bar{3}m$ (#166)	3b (0, 0, 1/2)		3a (0, 0, 0)	6c (0 0 z) $z \approx 0.27$
P3	$R\bar{3}m$ (#166)	6c (0, 0, z) $z \approx 0.84$		3a (0, 0, 0)	6c (0 0 z) $z \approx 0.4$
P2	$P6_3/mmc$ (#194)	2b (2/3, 1/3, 1/4)	2d (0, 0, 1/4)	2a (0, 0, 0)	4f (1/3, 2/3, z) $z \approx 0.09$

***Table I-1** : Usual space groups and atomic positions for the O3, P3 and P2 structures.*

1.3 Co electronic structure in lamellar oxides

1.3.1 Octahedral symmetry

Figure I-4 depicts the representation of the 3d orbitals of the M transition metal ions in an octahedral environment. In the lamellar oxides, the metal transition ions are surrounded by six O ions. The crystal field theory shows that the interaction between the 3d orbitals and the electrostatic potential due to the oxygen ions negatively charged leads to a breaking of degeneracies of the d_{z^2} and $d_{x^2-y^2}$ orbitals. They are, therefore, located at a higher energy level than the free M ion. The three orbitals d_{xy}, d_{yz} and d_{xy} which point between the O ligands are stabilized due to a lower energy level compared to the free Co ion. These three orbitals are called t_{2g}. The e_g orbitals represent the two remaining orbitals, $d_{x^2-y^2}$ and d_{z^2}.

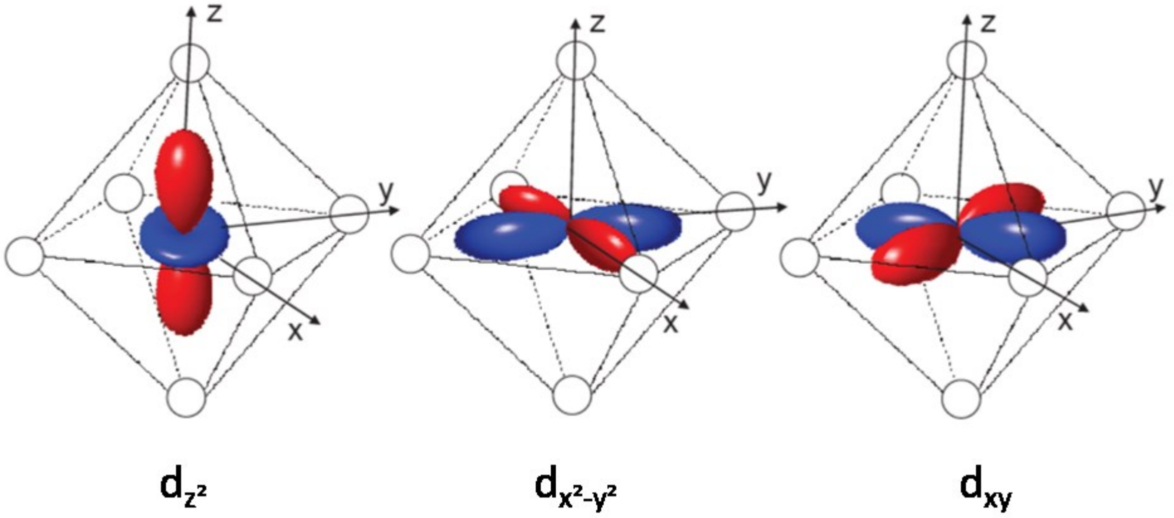

***Figure I-4** : Representation of the 3d orbitals in an octahedral environment. The d_{z^2} and $d_{x^2-y^2}$ orbitals point to the ligands while the d_{xy} orbitals point between the O ligands. d_{xy} and d_{xz} are not represented but are symmetrically equivalent to d_{xy}*

In the octahedral sites (O_h symmetry), only the t_{2g} orbitals are occupied in the case of the Co ions due to the low spin configuration of Co^{3+} and Co^{4+} (**Figure I-5**).

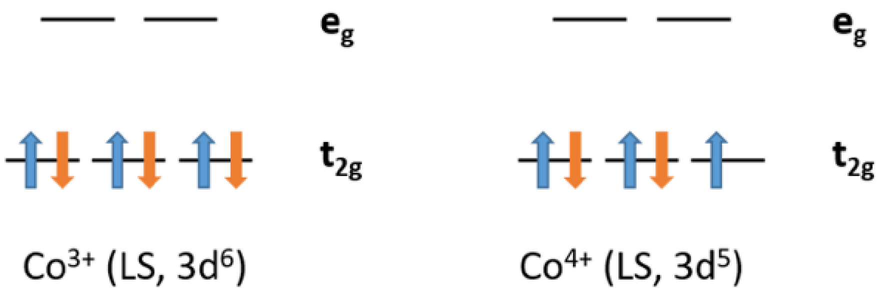

Figure I-5 : (a) Electronic configurations of the Co ions in O_h symmetry

1.3.2 Trigonal distortion of the octahedra

A θ_{O_h} angle is defined between the z axis and an axis along the Co-O direction. In regular octahedra, $\theta_{O_h} \sim 54.74°$. In layered oxides, the CoO_6 octahedra are usually distorted by a compression along the z axis as represented in **Figure I-6b**. It leads to a trigonal distortion in the D_{3d} symmetry. Consequently, the θ angle becomes larger than θ_{O_h}. The distortion is associated with a breaking of degeneracies of the t_{2g} orbitals into one a_{1g} orbital and two e_g' orbitals (**Figure I-6a**). However, there is a large debate concerning the stabilized orbital(s) between a_{1g} and e_g'. In fact, the band structures[54,55], *ab-initio* calculations[13] or angle-resolved photoemission spectroscopy (ARPES) experimental measurements[56] suggest that the orbitals e_g' are stabilized at a lower energy than a_{1g} while LDA calculations[57] found the opposite result. Landron and Lepetit[58] showed that the controversy was due to an incorrect treatment of the correlation integrals within the 3d shell. They proposed as model to consider the two cobalt sites Co(1) and Co(2) in $Na_{0.5}CoO_2$. For both cobalt sites, the a_{1g} orbitals are much energetically higher than the e_g' orbitals. The model proposes also close but different energy levels for both eg' orbitals (**Figure I-7**).

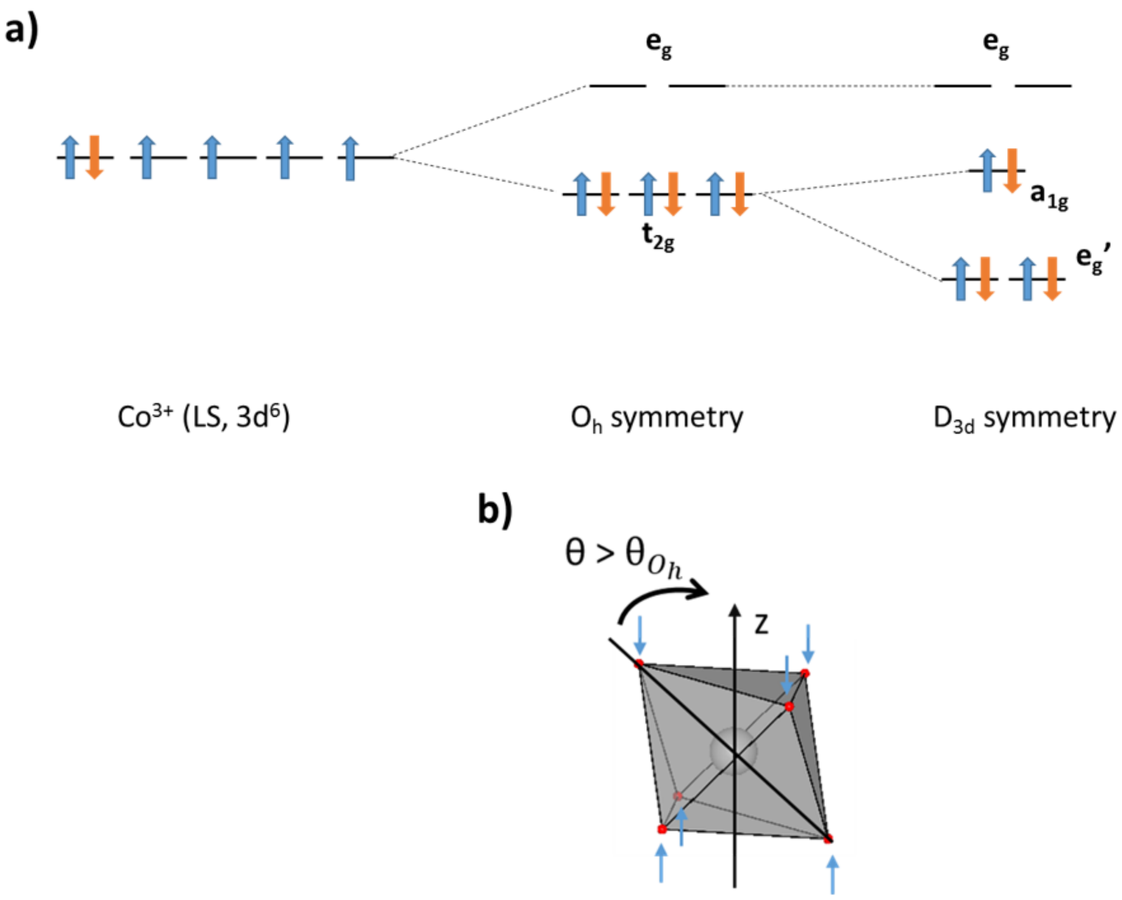

Figure I-6 *: (a) Electronic configurations in O_h and D_{3d} symmetry for Co^{3+} ions. (b) Representation of the compression due to the D_{3d} symmetry occurring on CoO_6 octahedra.*

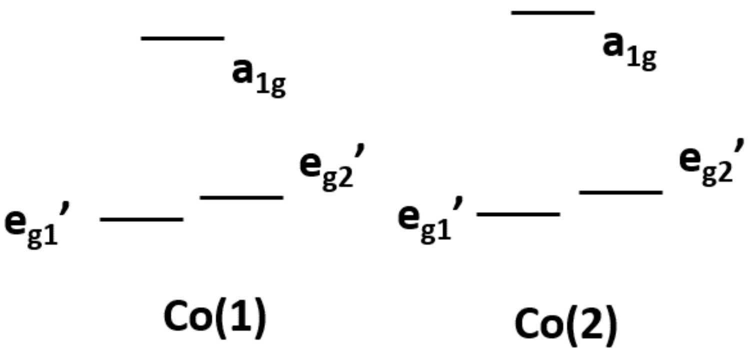

Figure I-7 *: Representation of Co t_{2g} orbital after trigonal distortion for $Na_{1/2}CoO_2$. Landron et al.*[58] *model considers two Co sites with different energy gaps between the levels.*

The **Figure I-8** represents the band structure of P2-Na_xCoO_2 after the t_{2g} orbitals degeneracy with the D_{3d} trigonal distortion. An overlap is observed between the narrow a_{1g} band and the broad e_g' at the Fermi level, providing "heavy" and "light" charge carriers. This point suggests that delocalized and localized electrons contribute to the electronic structure for Na_xCoO_2.

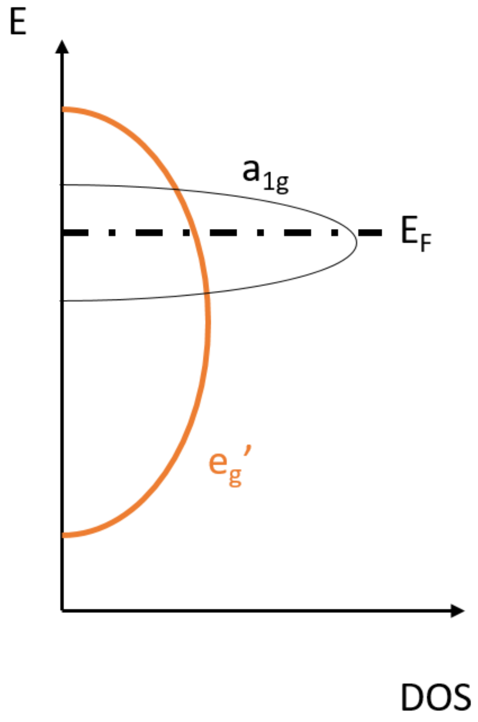

***Figure I-8** : Schematic representation of the band structure of P2-Na_xCoO_2 after the splitting of the t_{2g} orbitals with the D_{3d} distortion.*

2. Na-ion and Na batteries

2.1 Principles

The Na and Na-ion batteries are technologies composed of a positive electrode, a negative electrode and an electrolyte (**Figure I-9a**). During this report, the terms negative and positive electrode are favored instead of cathode and anode in order to avoid any misunderstanding as the cathode and anode side changes depending if the battery is charging or discharging. The electrolyte separates both electrodes and is usually a sodium salt dissolved in an organic or aqueous solvent. The electrolyte ensures the ionic conductivity from one electrode to the other. It is important to distinguish the difference between a Na battery and a Na-ion battery, in fact, both terms differ by the nature of the material used as negative electrode. For the Na batteries, the negative electrode is sodium metal (Na(s)). The Na-ion batteries term is used for the batteries with an Na^+ intercalation material as negative electrode. These materials involve no reduction or oxidation of the Na^+ ions but only, as their name indicates, an intercalation. In this work, we only made Na-batteries.

During the charge of a Na battery, a current is applied imposing the electrons flux from the positive to the negative electrode through the external circuit. In order to balance the charge neutrality of the positive electrode material, Na^+ ions are removed from the interslab spaces into the electrolyte and reach the negative electrode where they are reduced. Moreover, the extraction of the electrons from the positive electrode involved an oxidation of the metal transition ions. The following equations summarize the phenomena happening during the charge.

$$Na_xMO_2 \rightarrow Na_{x-x'}MO_2 + x'Na^+ + x'e^- \ (positive\ electrode)$$

$$x'Na^+ + x'e^- \rightarrow x'Na(s) \ (negative\ electrode)$$

During the discharge (no applied current), the phenomena are reversed involving a reduction of the transition metal ions in the positive electrode material and an intercalation of the Na^+ ions inside the Na interslab spaces (**Figure I-9c**).

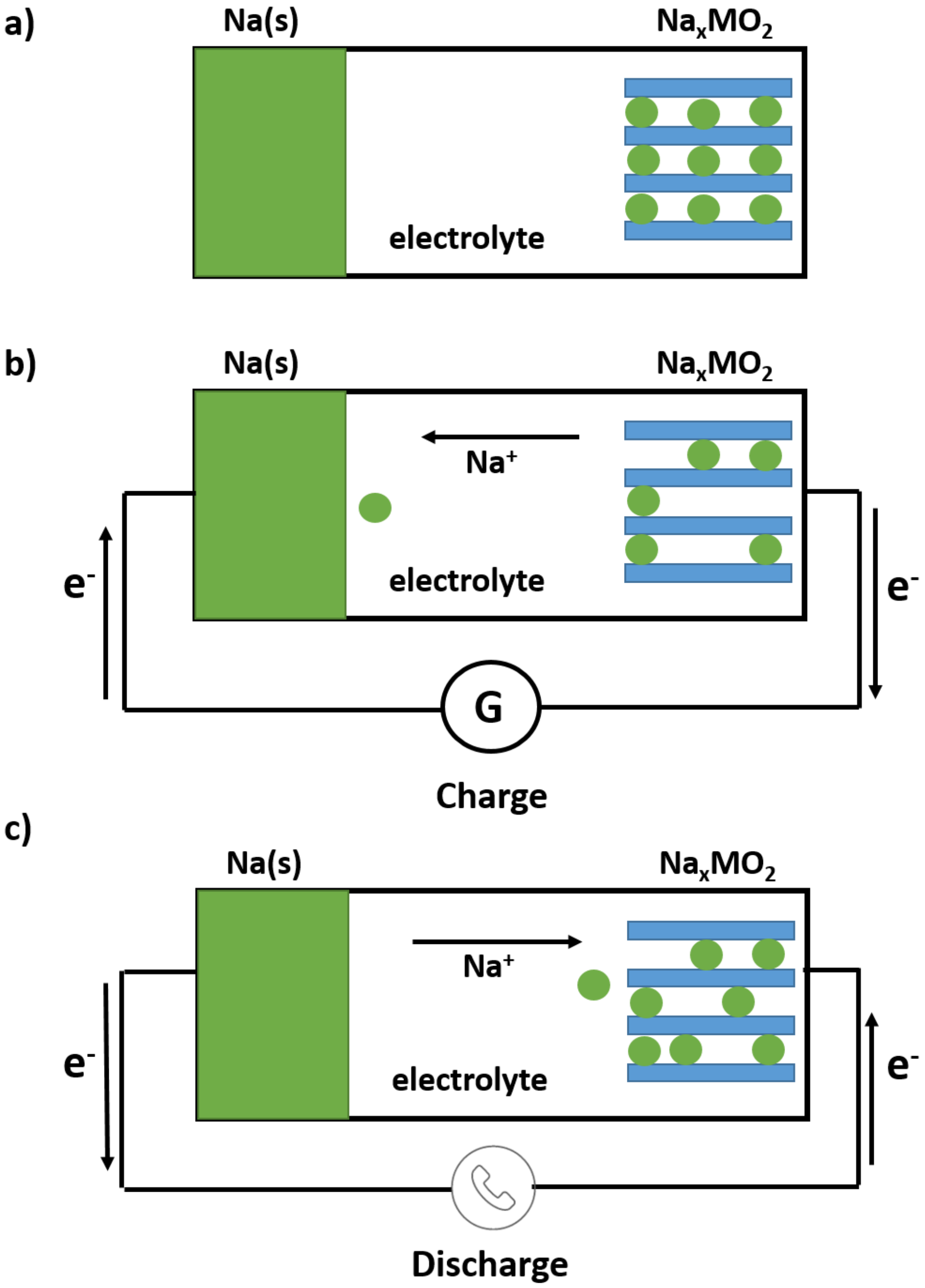

***Figure I-9** : (a) Initial state of the Na battery with Na_xMO_2 as positive electrode material. Metal sodium is used as negative electrode and the electrolyte is liquid. Representation of a Na battery during (b) the charge with the Na^+ deintercalation from Na_xMO_2 and (c) the discharge with the intercalation of Na^+ in Na_xMO_2. The Na^+ ions are represented by the green circle.*

2.2 Electrochemical curves

Two electrochemical experiments were, mainly, performed in this work in order to characterize the studied materials, one of them is the galvanostatic measurement. The voltage evolution is monitored as a function of time or the sodium content (x) in a selected voltage window (**Figure I-10)** while a fixed current is applied. The galvanostatic curves give many information about potential structural changes during the electrochemical cycling. Three behaviors can be discerned on the E = f(x or t) curve depending of the slope inclination.

slo

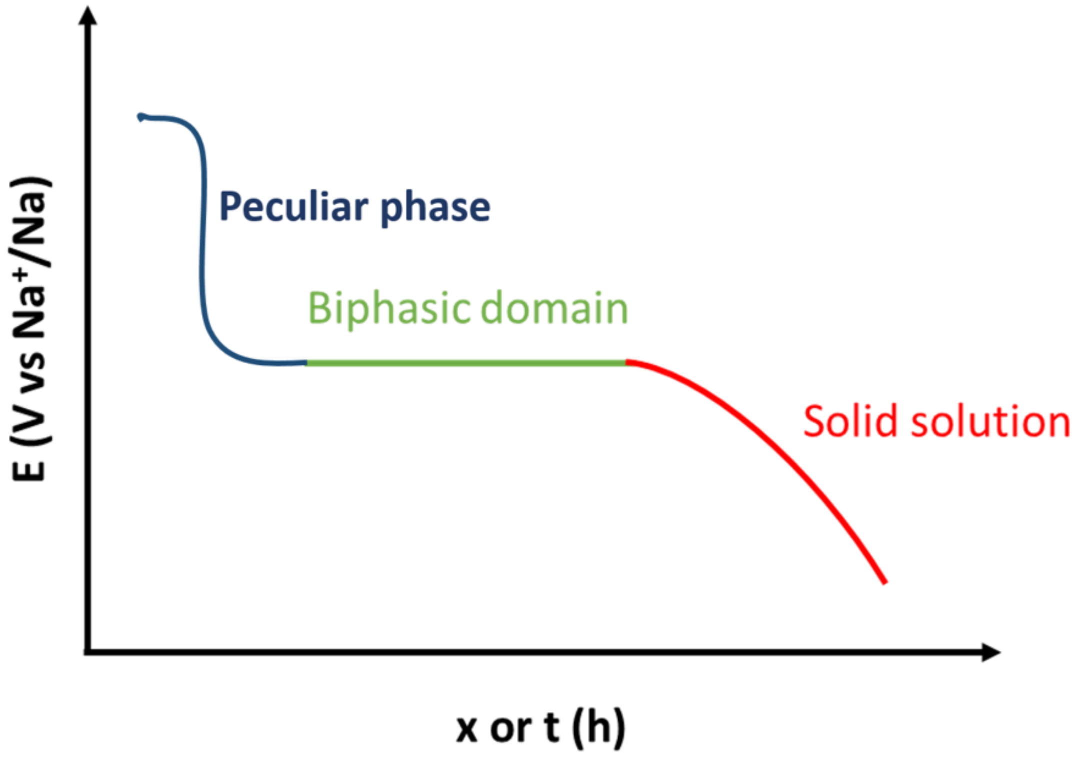

***Figure I-10** : Representation of the different slopes that can be observed on a galvanostatic cycling.*

Peculiar phase. This behavior is characterized by an abrupt voltage jump (in charge) or drop (in discharge) on the galvanostatic curve. It highlights the presence of a single phase obtained for a specific Na^+ content with a Na^+/vacancy ordering in the interslab spaces. Usually, the Na^+/vacancy ordering involves the appearance of a supercell and therefore superstructures peaks on the XRD patterns.

Biphasic domain. Two phases are in equilibrium involving a voltage plateau. Along the plateau, only the proportion of both phases in equilibrium is changing.

Solid Solution. The E = f(x or t) curves evolve smoothly and it means that the structure remains the same while only the Na^+ content is modified during the cycling.

The other technique reported in this work is the potentiostatic experiment which consists of applying a constant voltage and to monitor the current evolution as a function of time or x. The combination of both techniques was useful in order to synthetize phases at selected voltage on the different studied systems and will be discuss later in this chapter.

2.3 Electrochemical properties

In order to characterize the electrochemical performances of the different materials, it is necessary to introduce different variables.

2.3.1 Sodium content (x) and capacity (Q)

These variables are the most used in this report and are directly correlated one to each other. x corresponds to the concentration of Na^+ ions in the Na_xMO_2 materials at a specific moment. x is dimensionless. Q represents the electrical charge that the battery can store or deliver. Q is expressed in A.h and can be expressed as follows:

$$Q = I * t = \frac{F * \Delta x * m}{M * 3600}$$

Q: capacity (A.h)

I: applied current (A)

t: duration of (dis)charge (h)

F: Faraday constant ($C.mol^{-1}$)

Δx: number of (de)intercalated sodium at a specific time

m: weight of active material (g)

M: molecular weight of active material at t = 0 ($g.mol^{-1}$)

For Na_xMO_2 materials, Δx is included between 0 and 1.

2.3.2 Specific capacity (Q_m)

Usually the capacities values correspond to the discharge one and are expressed per weight of active material in order to be comparable to other systems. This value is labelled Q_m and called specific capacity. It is expressed in $A.h.g^{-1}$.

2.3.3 Charge and discharge voltages

In order to realize electrochemical cycling and especially for the galvanostatic measurements, two voltages have to be introduced. The cutoff voltage represents the maximal voltage value imposed during a charge while the discharge voltage is the minimal voltage value imposed during a discharge. In this report, the voltage values are reported against the Na^+/Na redox couple because our reference electrode was the negative electrode, Na(s).

2.3.4 Cycling rate

The rate is directly correlated to the applied current for a galvanostatic measurement. It corresponds to the time (t) that needs the system to reach the maximal charge/discharge capacity for $\Delta x = 1$.

$$I = {}^{Q_m}/_{t}$$

This rate is labeled C/t. For example, C/20 means that 20 h are necessary to (de)intercalate 1 mol of Na^+ ions.

2.4 Preparation for the galvanostatic measurements

2.4.1 Positive electrode preparation for galvanostatic cycling

In this report, the positive electrodes were a mixture of the studied material, black carbon (a mixture of graphite and soot) and polytetrafluoroethylene (PTFE) for the galvanostatic cycling in an 88:10:2 wt ratio. All the powders were ground together in an Ar-filled glovebox. The black carbon is used in order to improve the electric conductivity of the electrode while PTFE allows to maintain all the compounds together and therefore, to obtain electrodes easier to handle. After the mixing, a paste is obtained and a circular electrode with 10 mm diameters was cut with a mass included between 20 and 50 mg.

2.4.2 Coin Cell assembly

In this work, the galvanostatic measurements were performed in sealed coin cells assembled in a Ar-filled glovebox in order to avoid either the reaction of the metal sodium with water or the oxidation of the solid sodium with the air. **Figure I-11** shows the stacking realized in a coin cell: the positive electrode is directly in contact with the positive current collector and separated from the negative electrode (metal sodium) by three glass fiber separators. The metal sodium negative electrode is flattened in the glovebox before being cut to obtain a 12 mm diameter electrode. The solid sodium is finally deposited on a stainless steel support and put directly in contact with the separators soaked of electrolyte. A stainless steel spring is put between the negative electrode and the negative current collector to converse a constant pressure during the sealing and a good electrical contact during the cycling. Finally, a joint allows to prevent the contacts between both current collectors and therefore to avoid short circuits. The joint also ensures the airtightness of the coin cell after sealing in the glovebox with a press.

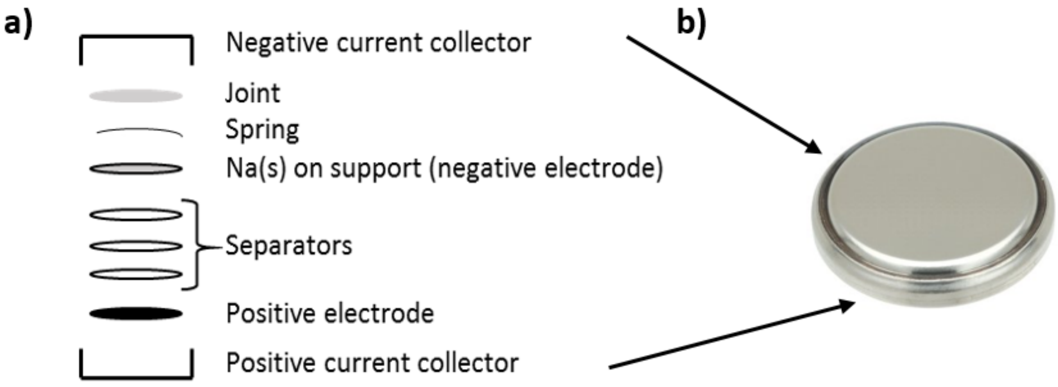

Figure I-11 *: (a) Representation of the stacking used to assemble of the battery in a coin cell (b) Sealed coin cell after assembly*

After sealing, the coin cell can be removed from the glovebox and be connected to a galvanostat. The ECLAB software was used to set up all the electrochemical measurements and to monitor the evolution of the current as a function of time or x.

2.5 Synthesis by electrochemical (de)intercalation

In this report, some phases were synthetized by electrochemical (de)intercalation. This technique needs two steps: (1) a galvanostatic (dis)charge to the targeted voltage at a selected C/t rate. (2) a potentiostatic step. Once the targeted voltage is reached by the battery, the voltage is maintained while the current is relaxing until a negligible value (**Figure I-12**). A negligible current value means that the battery can be disconnect without any risk of a structural evolution. This technique will be used to synthetize the samples studied in the chapter V for *ex-situ* characterization techniques. More information about the experimental set-up of the cell will be discussed at that time.

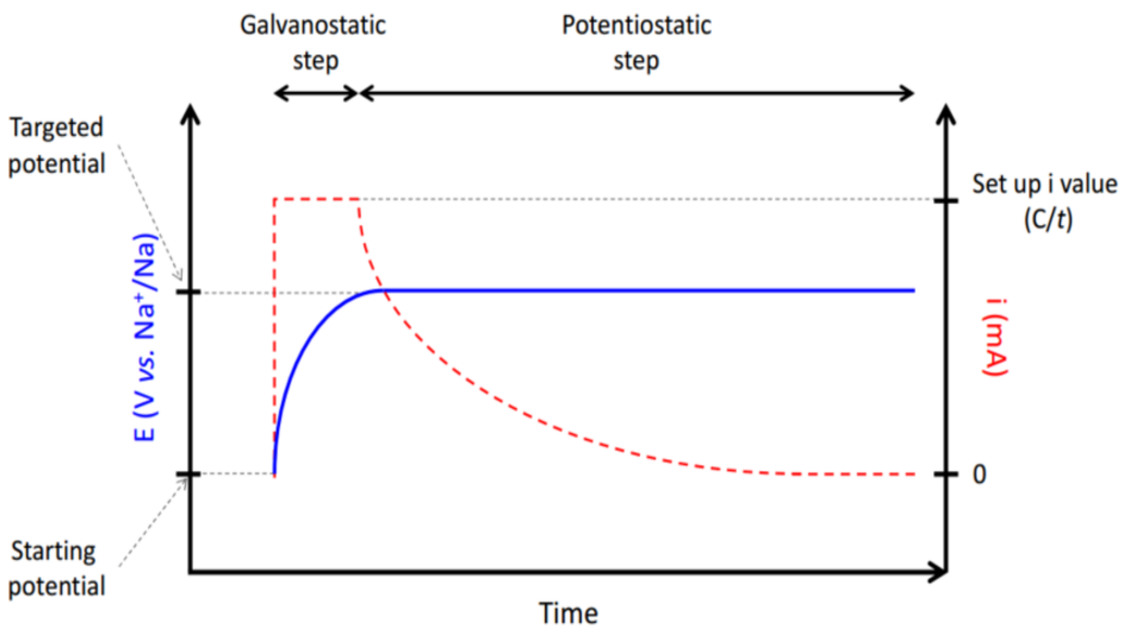

Figure I-12 *: Evolution of the voltage and the current as a function of time during the two steps necessary to synthetize a phase by electrochemical (de)intercalation.*

3. Characterization techniques

3.1 X-Ray Diffraction (XRD)

XRD was used as a structural characterization technique to determine for example, the lattice parameters of the synthetized powders, the space group or the atomic positions, in fact, XRD gives information about the average structure of an analyzed sample. In this work, as the studied materials were air-sensitive, the samples were packed in airtight systems for the XRD characterization.

3.1.1 Ex-situ XRD

Many diffractometers are available at ICMCB and have their own advantages and drawbacks. In this manuscript, the XRD patterns were mainly collected on two of them using two different techniques of samples packing.

- PANalytical X'Pert Pro uses Co K$\alpha_{1,2}$ radiations. The air-sensitive samples have to be placed in an airtight sample holder for the analyses on this diffractometer. The none air-sensitive samples can also be analyzed easily with this diffractometer.

- PANalytical X'Pert^3 Powder uses Cu K$\alpha_{1,2}$ radiations. The air-sensitive samples have to sealed in an airtight capillary for the analyses on this diffractometer.

3.1.1.1 Airtight sample holder (Co K$\alpha_{1,2}$ radiations)

Before the acquisitions, the powders were ground and placed in an airtight sample holder with an Al base. A polyimide (Kapton) window which is transparent to the X-Rays was used to let the beam pass as shown on **Figure I-13**. This technique allows to get acquisitions with a good quality. In fact, a fluorescence of the Na_xMO_2 (M with Co) phases is observed when using Cu K$\alpha_{1,2}$ radiations and leads to lower quality XRD patterns. The limitation of this technique is the necessity to fill completely the sample holder to avoid the presence of aluminum diffraction peaks on the XRD patterns. Therefore, a relatively high amount of powder was necessary. The acquisitions could be carried from 6° to 150° in the 2θ range. Le Bail and Rietveld refinements[59] allowed to determine information about the average structure of the analyzed powders. The refinements were performed on the software FullProf[60].

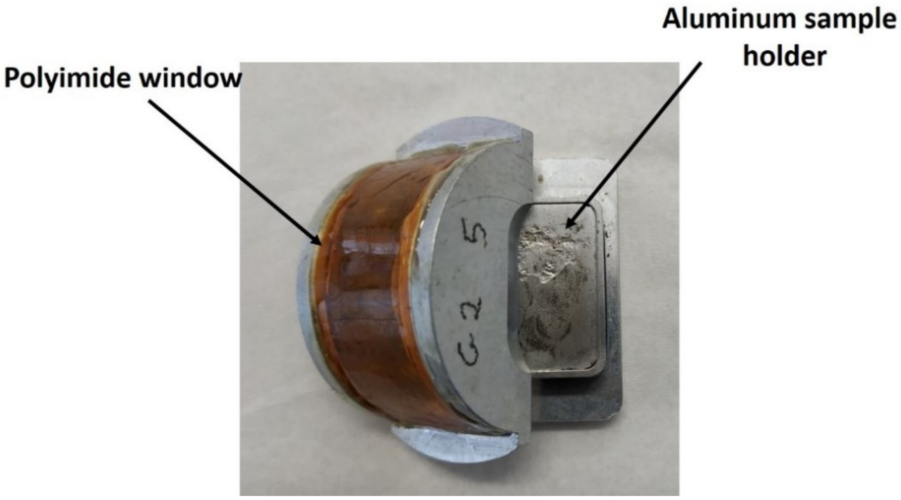

Figure I-13: Pictures of the airtight sample holder used for XRD acquisitions

3.1.1.2 Airtight glass capillaries (Cu K$\alpha_{1,2}$ radiations)

The samples were ground for a long time before the packing because the capillaries have a small diameter of 0.3 mm for the acquisitions at ICMCB. The powder was, then, loaded in the capillary inside the glovebox and sealed with a flame to ensure the airtightness outside the glovebox. In this report, only glass capillaries were used. The advantage of this technique is the use of a low amount of powder but only Cu K$\alpha_{1,2}$ radiations were available on the corresponding diffractometer.

3.1.2 In-situ XRD (Synchrotron radiations)

Some samples were analyzed using Synchrotron radiations. For the Synchrotron XRD characterization, the filling and sealing techniques of the capillaries were the same than for the laboratory acquisitions but with 0.5 mm diameter capillaries. The acquisitions were performed on the BL04-MSPD beamline of the ALBA synchrotron facilities (Cerdanyola del Vallès, Spain) in collaboration with Francois Fauth. The data were collected for 2θ from 2° to 73° with a wavelength of $\lambda = 0.8261$ Å.

Moreover, XRD acquisitions *in-situ i.e.* during the charge and the discharge of the battery were also performed. We used a specific home-made coin cell in order to let the beam pass through the electrochemical cell without any air contamination.

In-situ XRD allows to monitor the materials structural evolution during the Na^+ (de)intercalation in order to have an insight of the structural changes occurring during the charge and the discharge.

In order to let the beam pass through the coin cells, 3 mm diameters holes had been drilled at ICMCB in both current collectors and in the support where the metal sodium negative electrode was deposed. Moreover, to ensure the airtightness of the cell, a 7 mm diameter polyimide had been stuck on both current collector holes (**Figure I-14b**). Moreover, to improve the sticking, the Kapton film and the current collectors faces had been abraded. Finally, a 10 mm diameter thin aluminum foil had been inserted between the positive electrode and the positive current collector to improve the conductivity between both. The next steps of the assembly were the same than for the usual coin cell.

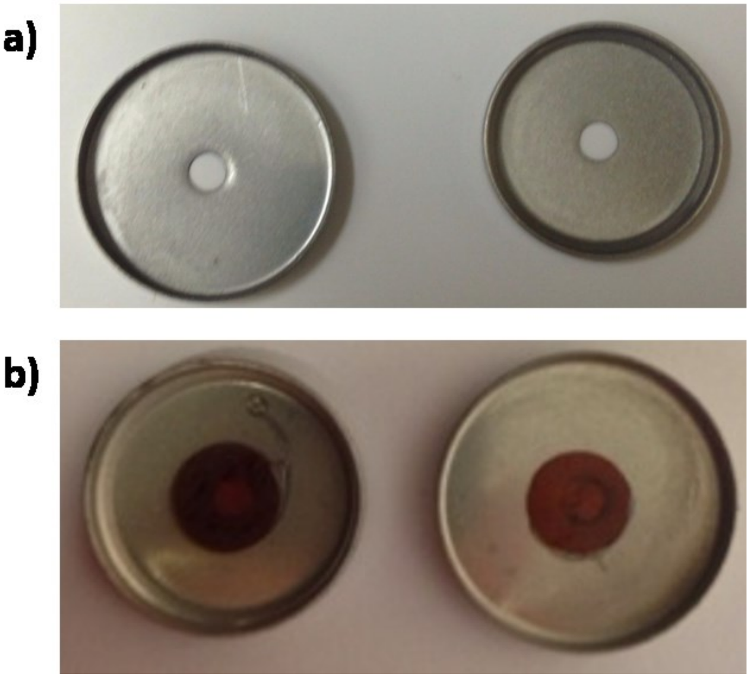

***Figure I-14** : (a) Coin cell drilled with 3 mm diameter holes on both current collectors. (b) Current collector holes covered with a polyimide 7 mm diameter film.*

Some tests had been realized before assembling on the drilled coin cells in order to see if the electrolyte reacts or not with the glue. The electrolyte had been poured in the current collectors and after one day, no leakage had been observed between the polyimide film and the current collectors.

In ALBA, four coin cells were plugged to a galvanostat/potentiostat at the same time. The data were collected from 2° to 45° while the batteries were cycled. Some additional peaks on the patterns are due to the different elements like the graphite in the black carbon, the PTFE, the aluminum or the sodium foil.

3.2 Nuclear Magnetic Resonance (NMR)

3.2.1 Generalities

3.2.1.1 Zeeman effect

Each atom is characterized by a specific quantum number, I (also called nuclear spin quantum number). I value depends of the nucleons number A and the Z number parity. If A and Z are both even, I is null. If A is odd, I is half integer and if A is even and Z odd, I is a whole number. The NMR measurements are only possible on non-null I value atoms.

If I is different from zero, I is associated to a spin magnetic moment without any preferential orientation without a magnetic field. But by applying a magnetic field $\overrightarrow{B_0}$, the spin magnetic moment can be aligned either in the parallel or in the anti-parallel direction to $\overrightarrow{B_0}$. Two energy levels are, then, created by the magnetic field (**Figure I-15**). This breaking of degeneracies of the m = +1/2 and m = -1/2 levels is called Zeeman effect. The energy gap between the two energy levels varies linearly with the magnetic field magnitude.

$$\Delta E = \gamma \hbar B_0 = g_n \beta_n B_0$$

g_n : Landé g-factor

β_n : nuclear magneton

γ: magnetogyric ratio

$\hbar$: Planck constant

For I > 1/2, the Zeeman effect, can't describe the system alone as different interactions have to be considered. These interactions involve modifications in the energy levels or new nuclear transitions.

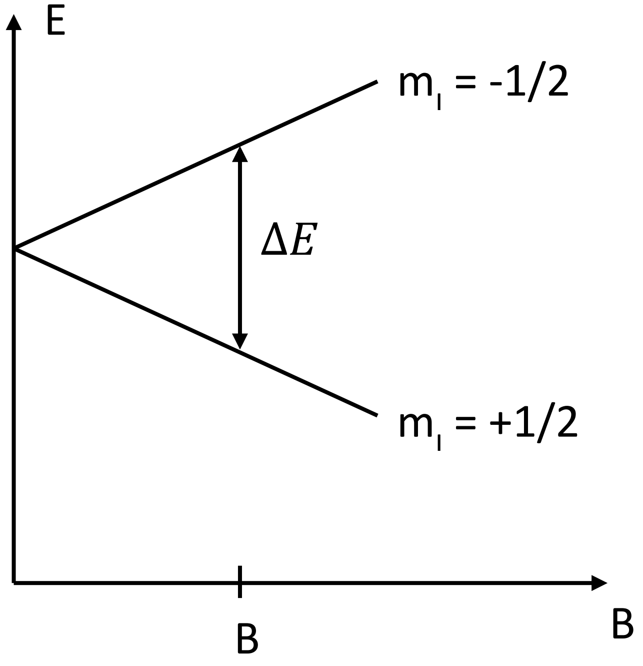

Figure I-15 *: Zeeman effect with the splitting in two magnetic levels when a magnetic field is applied for I = ½ and γ> 0*

3.2.1.2 Principles of the NMR single pulse

The samples are placed under a $\overrightarrow{B_0}$ magnetic field which induces the Zeeman effect described previously. The spin excess in the $\overrightarrow{B_0}$ direction involves the appearance of a macroscopic nuclear magnetization $\vec{M}$ also aligned with the magnetic field. In order to provide the adequate energy quantum $\omega_0 = \gamma B_0$ necessary to the transition between the Zeeman levels, an additional $\overrightarrow{B_1}$ magnetic field is used. This additional magnetic field oscillates in a plane perpendicular to $\overrightarrow{B_0}$ and at the ω_0 frequency. Consequently, the population of both spins (up and down) tends thus to become similar. When the magnetic field $\overrightarrow{B_1}$ is cut off, the system recovers its equilibrium state.

By applying $\overrightarrow{B_1}$, the magnetization is removed from its equilibrium position (along $\overrightarrow{B_0}$) with an angle $\alpha = \gamma B_1 \tau$ where τ is the time during which $\overrightarrow{B_1}$ is applied. Due to the angular momentum theorem, the magnetization have a precession movement around the $\overrightarrow{B_0}$ axis. This precession frequency is called Larmor frequency and is equal to ω_0. For a magnetization brought in the plane perpendicular to $\overrightarrow{B_0}$, a maximal electric signal at ω_0 frequency is detected by the same coil that generates $\overrightarrow{B_1}$ magnetic field (**Figure I-16)**.

After the perturbation, the measured signal decreases due to two relaxation mechanisms:

- The T2-type relaxation which expresses the defocusing of the magnetizations induced by the different interactions on the individual spins in the (x',y') plane.
- The T1-type relaxation which expresses the recovery of $\overrightarrow{\mathrm{M}}$ along $\overrightarrow{B_0}$.

In solid state NMR, T1 >> T2 and the temporal evolution of magnetization measured in the (x',y') plane is called Free Induction Delay (FID). A Fourier transformation of the FID monitored in the (x',y',z') plane gives the NMR spectrum in Hz or ppm. An NMR acquisition corresponds at the repetition of this experiment in order to increase the quality (signal/noise ratio) of the NMR spectrum. A D_0 time is added between each experiment in order to allow the system to come back to equilibrium ($D_0 \approx 5 * T1$).

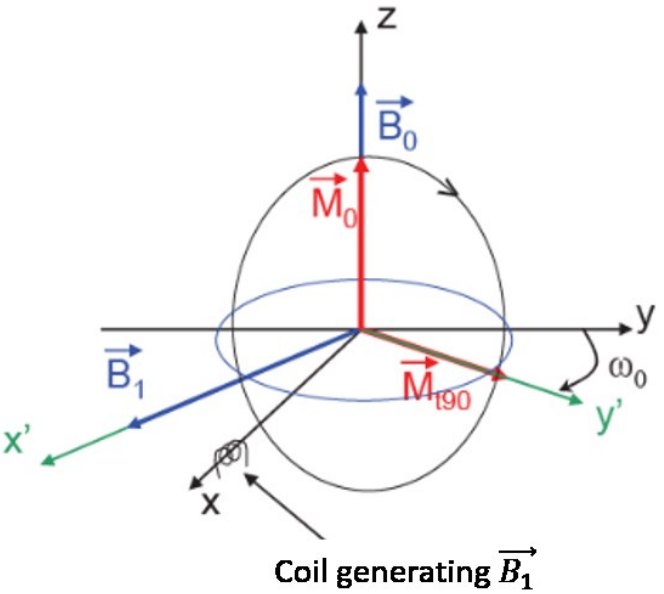

Figure I-16 : Representation of a NMR experiment. At equilibrium, $\overrightarrow{M_0}$ *is parallel to* $\overrightarrow{B_0}$*.* $\overrightarrow{B_1}$ *perturbation leads to the magnetization flip in the (x,y) plane. (0, x', y', z' (=z)) is the new system considering the rotation of the magnetization around* $\overrightarrow{B_0}$*.*

3.2.1.3 Magic Angle Spinning

Magic Angle Spinning (MAS) is used in order to enhance the resolution of the solid state NMR spectra, in fact, the fast rotation at 54.74° with the external field vector (**Figure I-17**) leads to a partial averaging of many anisotropic interactions (dipolar coupling, chemical shift anisotropy and first order quadrupolar interactions). If the spinning is fast enough, a single signal is observed on the NMR spectra. If it is not the case, “signals” called spinning side bands are observed on the spectra. The isotropic signal and the spinning side bands are separated, in frequency, by a multiple of the spinning frequency.

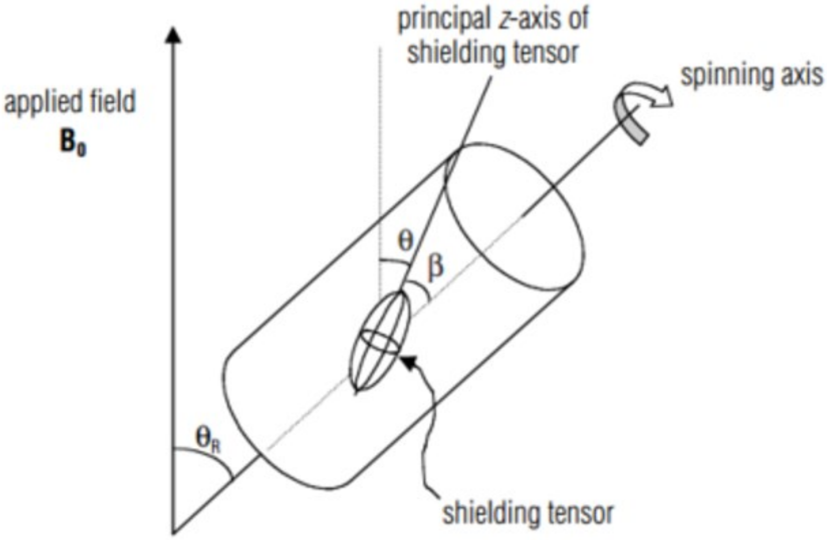

Figure I-17 *: Representation of the rotors in the NMR probe at the Magic Angle for MAS experiments. The picture is extracted from* [61].

Experimentally, the samples are packed in a rotor and are placed at the θ_R magic angle formed with $\overrightarrow{B_0}$ at fast spinning. Different NMR spectrometers with different magnets are commercialized and, therefore, different magnetic fields can be used for the acquisitions. By using the MAS, the spinning side bands become closer when the magnetic field increases. In this work, measurements of five different spectrometers are reported with different magnetic fields: 2.35 T, 7.05 T, 11.75 T, (spectrometers available in Bordeaux with a spinning frequency of 30 kHz), 4.7 T and 7.05 T (available in McMaster, University with a spinning frequency of 60 kHz).

3.2.2 Hyperfine interaction

NMR is sensitive to the presence of single electrons in the probed nucleus environment. The hyperfine coupling between a single electron and the probed nucleus involves a NMR shift and a signal broadening. The Hamiltonian of the hyperfine interaction H_{SI} between single electrons can be written as follows:

$$H_{SI} = A^i \hat{I}.\hat{S} + \hat{I}.\widetilde{A_{d\imath p}}.\hat{S}$$

A^i: Fermi contact coupling constant

$\hat{I}$: spin operator

$\hat{S}$: spin operator

$\widetilde{A_{d\imath p}}$: dipolar tensor

Regarding, the Hamiltonian formula, the hyperfine interactions have two contributions: The Fermi contact interaction and the dipolar interaction.

3.2.2.1 Fermi contact interaction

This interaction is due to the presence of single electrons spin density transferred from the transition metal ion (M) orbital to the s orbital of the alkali ion via the 2p orbital of the oxygen ion leading to M-O-A bond pathway .The Fermi contact involves, generally, important NMR shifts called Fermi contact shifts and is observed for paramagnetic compounds. The NMR shift signal due to Fermi contact can be expressed as follows[62]:

$$\delta^i_{iso} = \frac{A^i}{\hbar}\frac{\chi_M(T)}{\mu_0 \gamma^i g_e \mu_B}$$

χ_M: magnetic molar susceptibility

μ_0: magnetic constant

μ_B: Bohr magneton

A^i is the only parameter able to change the shift sign to negative or positive values. This constant depends of the electronic spin density on the *i* nucleus called $\rho^i(0)$.

$$A^i = \frac{\mu_0}{3S}\gamma^i g_e \mu_B \hbar \rho^i(0)$$

S: spin quantum number

$\rho^i(0) = \sum_j(\left|\psi_j \uparrow (0)\right|^2 - \left|\psi_j \downarrow (0)\right|^2)$ with $\left|\psi_j \uparrow (0)\right|^2$ the probability of presence of positive polarized spin and $\left|\psi_j \downarrow (0)\right|^2$ the probability of presence of a negative polarized spin.

By combining both expressions, one obtained an easier expression considering only magnetic susceptibility and the spin density at the probed nucleus:

$$\delta^i_{Fermi} = \frac{1}{3SN_A}\rho^i(0)\chi_M(T)$$

If the nucleus environment is composed of many paramagnetic transition metal ions, the Fermi contact shifts are cumulative, each contribution is added in order to get the total shift. Moreover, the Fermi contact is also temperature dependent as shown by $\chi_M(T)$ in the previous equations. Schematically, the Fermi contact represents the amount of electronic spin transferred from a metal transition ion to the probed nucleus through bonds (**Figure I-18** in the case of ^{23}Na MAS NMR and a 90° interaction). Note also that the sign and magnitude of the individual shift strongly depend of the geometry of the material, the covalency of the bond pathway, the occupation of the t_{2g} and e_g orbitals occupation and the magnetic state of the material.

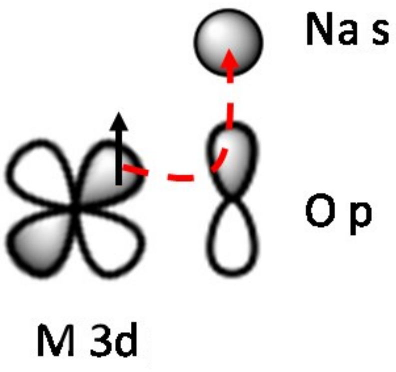

Figure I-18: *Representation of the Fermi contact shift for a 90° interaction between a half-filled* t_{2g} *orbital of a M ion and a Na nucleus via an 2p orbital of the oxygen ion.*

3.2.2.2 Dipolar interaction

Dipolar interaction is an interaction between the electronic spin and the probed nuclear spin trough the space and have a $1/r^3$ dependence. Thus, the dipolar interaction strongly depends of the distance between the single electrons and the probed nucleus. As explained previously, this interaction (as every dipolar interaction) is partially removed by the MAS due to an anisotropic nature contribution. However, the isotropic contribution is called dipolar shift or "pseudocontact".

Usually, the Fermi contact shift contribution is stronger than the pseudo-contact. For instance, in the oxides NMR[63,64], the pseudo-contact shift can be neglected compared to the Fermi contact. It is also the case for the lamellar oxides with transition metal ions in their structure. If the spinning (at Magic Angle) is not fast enough, an anisotropic contribution of the hyperfine interaction is in charge of the signal broadening and have consequences on the isotropic signal position. Thus, it is necessary to spin the rotors at the maximum rate that the rotor size allows.

3.2.3 Knight shift

The Knight shift is observed for metallic phases and is due to the electronic spin density on the probed nucleus. However, contrary to the Fermi contact, the electronic density depends of the participation of the electrons in the “s” orbitals contribution at the Fermi level of the probed nucleus labelled $\langle|\psi_{r=0}|^2\rangle$.

$$K = \frac{8\pi}{3}\langle|\psi_{r=0}|^2\rangle\chi_s^e$$

χ_s^e: Pauli susceptibility of conduction bands electrons at Fermi level

$\langle|\psi_{r=0}|^2\rangle$ is the contribution of “s” orbitals at Fermi level of probed nucleus

This electron-nucleus interaction leads to strong positive shifts. In rare cases, Knight shift can involve a negative NMR shift. Moreover, for ideal metallic phases, no shift evolution is expected with temperature.

3.2.4 Quadrupole Coupling

The quadrupolar coupling magnitude depends on the interaction between an electric field gradient (EFG) and on the nuclear electric quadrupole moment at the probed nucleus (Q). The Hamiltonian for the first order can be written as follows:

$$H_Q = \frac{eQ}{2I(I-1)}\mathbf{I}\cdot\boldsymbol{V}\cdot\mathbf{I}$$

e: electron charge

$\mathbf{I}$: nuclear spin vector

V: EFG tensor

Q: nuclear quadrupole moment

The EFG increases with the anisotropy of the charge distribution of the crystal environment (**Figure I-19**). MAS allows to remove completely or partially, the first and second order isotropic signal broadening effects. However, a part of the second order term of H_Q can't be removed by MAS and broadens the central transition signal. This second-order term involves a small additional contribution to the total shift which varies inversely to B_0^2, with B_0 the strength of the magnetic field. Consequently, high magnetic fields reduce the magnitude of this contribution and therefore, the broadening of the spectral line due to the quadrupolar interaction. The signals can be fitted using the DMFit software[65] in order to determine the different quadrupolar parameters.

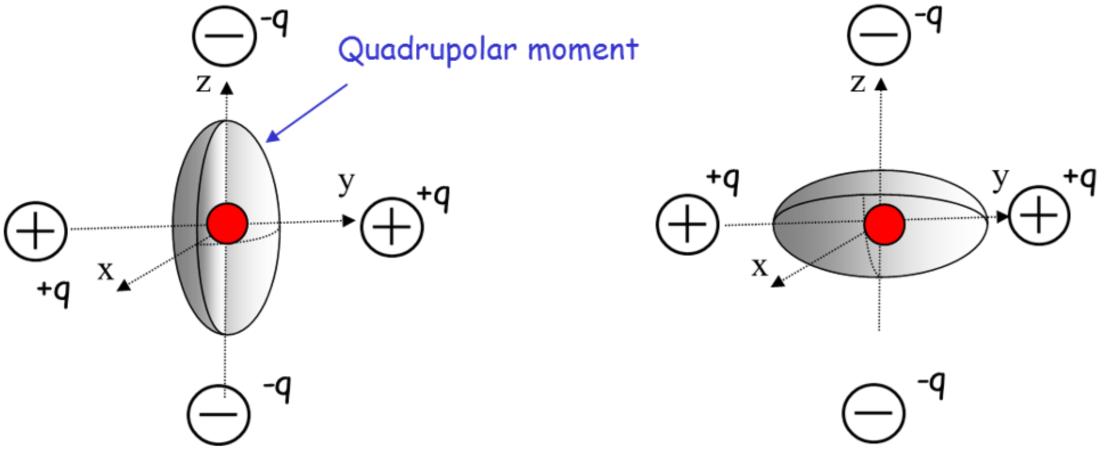

***Figure I-19** : Repartition of the quadrupolar moments created for I > 1/2 spin*

Nucleus	I	Quadrupolar moment Q (fm²)	Natural abundancy (%)	Larmor frequency at 7.05 T (MHz)
^{6}Li	1	-0.083	7.6	44.17
^{7}Li	3/2	-4.01	92.4	116.6
^{23}Na	3/2	10.40	100	79.39

***Table I-2:** NMR properties of ^{6}Li, ^{7}Li and ^{23}Na nuclei.*

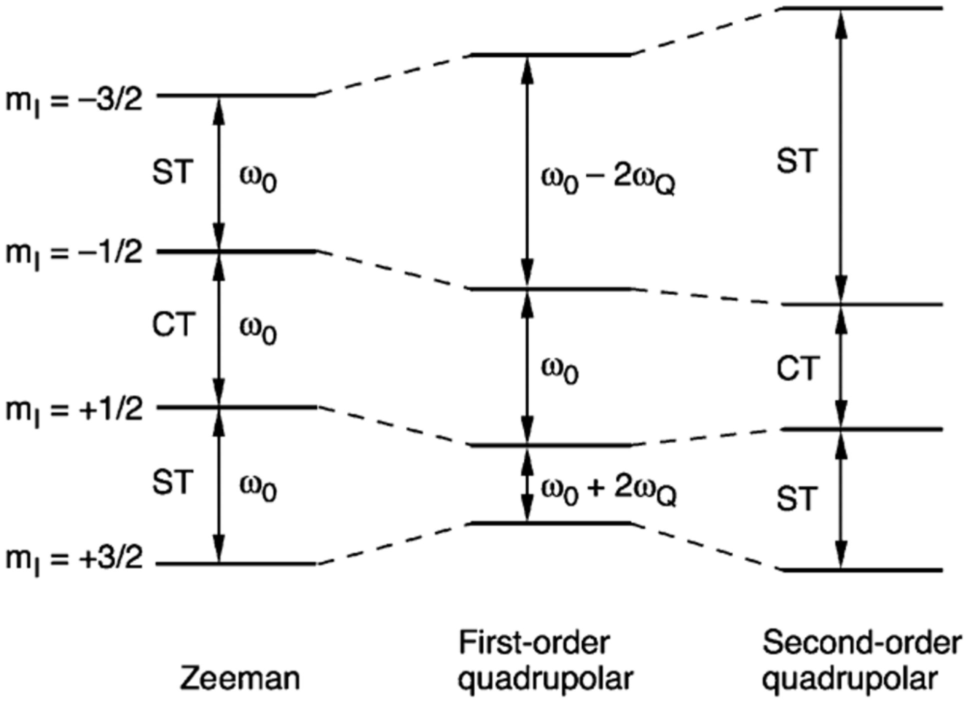

Figure I-20: *Energy level diagram for the I = 3/2 nuclei after application of a magnetic field. Extracted from* [66]*.*

Table I-2 shows the that ^{6}Li,^{7}Li and ^{23}Na are quadrupolar nuclei because I > 1/2. The large quadrupole moment Q of the ^{23}Na nucleus compared to the two Li isotopes suggests that the quadrupolar interactions can't be neglected for ^{23}Na MAS NMR and that the first and second order quadrupolar terms have to be taken into account to interpret the ^{23}Na MAS NMR spectra. As the ^{6}Li and ^{7}Li quadrupolar moments are low compared to the hyperfine interactions, the quadrupolar contribution can be neglected for these nuclei. **Figure I-20** represents the influence of the first and second orders quadrupolar terms on the ^{23}Na energy level. The first order term doesn't affect the central transition for ^{23}Na. However, the second order quadrupolar interaction affects all the energetic transitions. Note that in many cases, the broadening of the satellite transitions (ST) is so important that only the central transition can be observed on the different spectra.

3.2.5 1D NMR pulse sequences

Many parameters can be modified in an NMR pulse sequence. For 1D NMR, two pulse sequences had been mainly used during this work, simple pulse and Hahn Echo.

3.2.5.1 Simple pulse sequence

This experiment is the most basic one in NMR and is similar to the description made previously (**section 3.2.1.2**). The $\overrightarrow{B_1}$ pulse duration allows the magnetization to move from its equilibrium position. For the simple pulse experiments, it is not mandatory to flip the magnetization in the (x,y) plane because only the projection in the plane is measured. However by flipping the magnetization in the (x,y) plane, higher magnitudes are measured. A time out is also added between the pulse end and the beginning of the measurement due to the double use of the coil which generates the B_1 magnetic field and receives the signal. This double use involves perturbations at the beginning of the FID. The time out prevents from recording the first points of an already short FID (**Figure I-21**). Two consequences are that the broad signals can’t be correctly observed and the use of a first order phasing of the NMR spectrum which involves a baselines distortion in sin(x)/x. The impulsion times ans times out are around few µs for while the recycle delays are around 1 s for paramagnetic compounds and around 10 s for diamagnetic compounds.

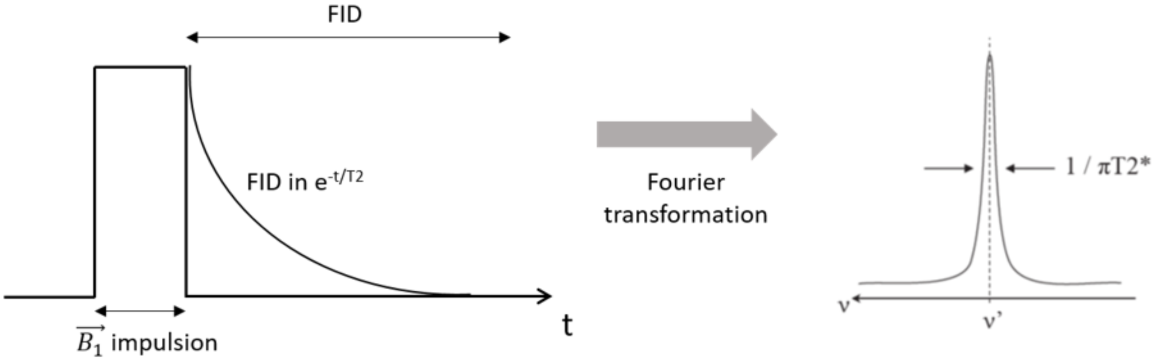

***Figure I-21** : Recording of the FID and Fourier transformation for a simple pulse sequence*

3.2.5.2 Hahn Echo sequence

In solid state NMR, a Hahn Echo is performed in order to avoid the drawback involved by the used of the time out in the simple pulse sequence. For the Hahn Echo sequences, two pulses are successively performed (**Figure I-22**). The first one is a pulse at 90° and the second pulse at 180°. Both pulses are separated by a τ time. An additional time also equal to τ is performed after the second pulse in order to allow the focalization of all the individual magnetizations. For this sequence, it is mandatory to flip the magnetization in the (x,y) plane. As the FID recording begins after the second τ time (at the top of echo), no time out is needed before starting the measurements and therefore the baseline needn't a 1st order correction allowing to obtain a flat baseline.

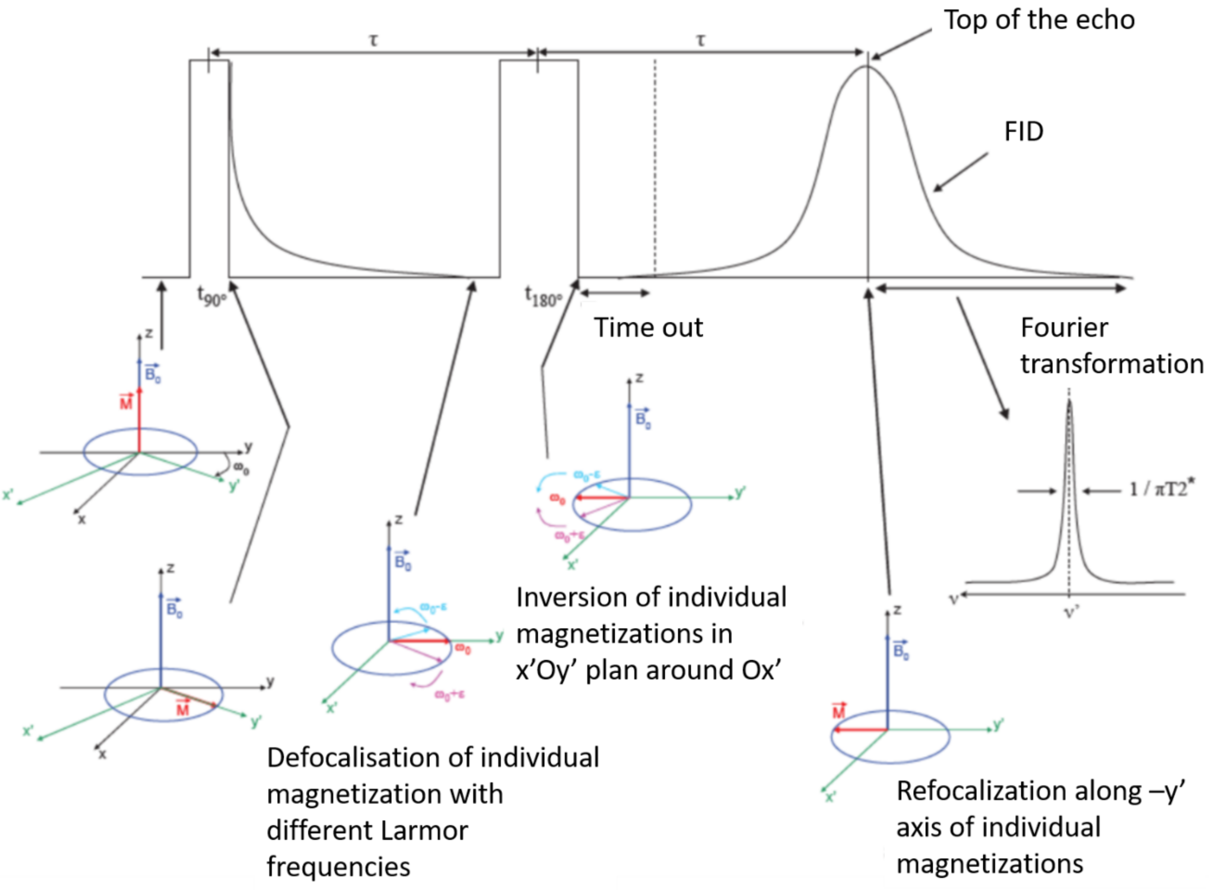

Figure I-22 : *Hahn Echo sequence*

3.2.6 NMR for dynamics

The 2D NMR experiments have been developed in order to have information about the ionic dynamics in different phases. By performing dynamics NMR experiments in temperature, it is possible to experimentally probe the intermolecular potential in order to determine the dynamics rates[67]. The dynamics NMR is based on the fact that the nuclear spin interactions depend of the molecular orientation within the applied magnetic field. In fact, the change of orientation is correlated with a change in some interaction strengths. 2D methods allow to study very slow dynamics by introducing a mixing time, τ_m during which the molecular reorientation can occur. Two periods in two different dimensions should also be considered: t_1 and t_2. During the t_1 period, the strength of a particular nuclear spin interaction is monitored while during the t_2, the new strength after the reorientation of the interaction is monitored. In order to obtain the 2D NMR spectrum, the interaction strengths during t_1 and t_2 are correlated. Finally, this experiment is repeated with different mixing times. In the 2D NMR experiments through this report, mixing times allow a chemical exchange between the different sites observed with 1D MAS NMR.

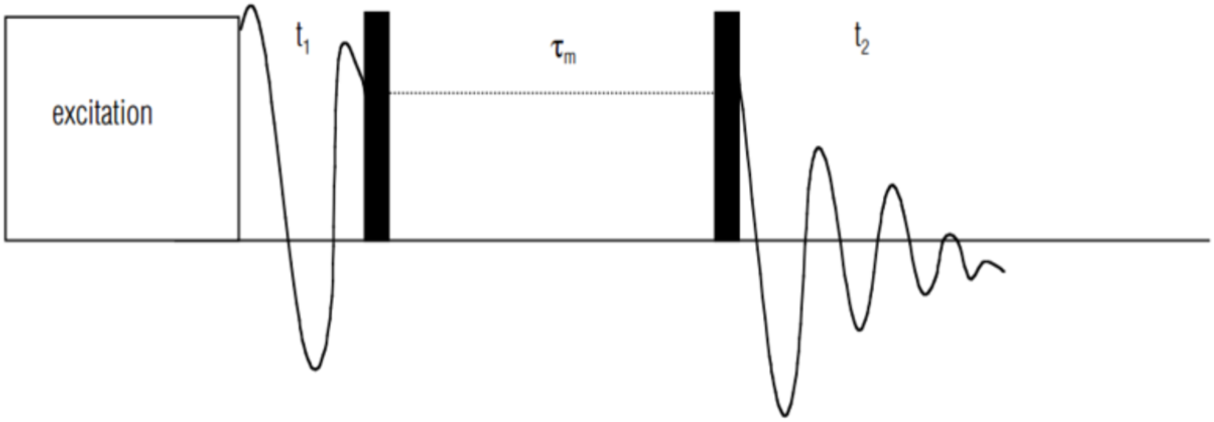

***Figure I-23**: Basic form of a 2D exchange experiment. Both pulses are 90°. Excitation label corresponds to the first pulse to transverse magnetization in (x,y) plane. Second pulse allows to restore the magnetization along $\overrightarrow{B_0}$ direction. Third pulse reconverts the magnetization in (x,y) plane. Extracted from [61].*

Experimentally, an initial 90° pulse is used to create a transverse magnetization allowing to evolve during the t_1 period (**Figure I-23**). The magnetization is then stored along the $\overrightarrow{B_0}$ magnetic field direction during the mixing time thanks to a second pulse. Finally, the magnetization is flipped into the (x,y) plane by a third 90° pulse. The FID is registered during the t_2 period. A Fourier transform is then applied to obtain the 2D RMN spectrum for many acquisitions with different mixing times. If sites exchanges occur, the offset frequency after mixing time labelled ω_2 is different from the initial offset frequency before the mixing time labelled ω_1. If $\omega_1 = \omega_2$ (no exchange during mixing times), the spectral intensity appears only along the diagonal of the spectrum. If there is an exchange, the spectral intensity appears along the diagonal but also off the diagonal. These intensities off the diagonal will be called cross-peaks troughout this manuscript. An example is shown on **Figure I-24.**

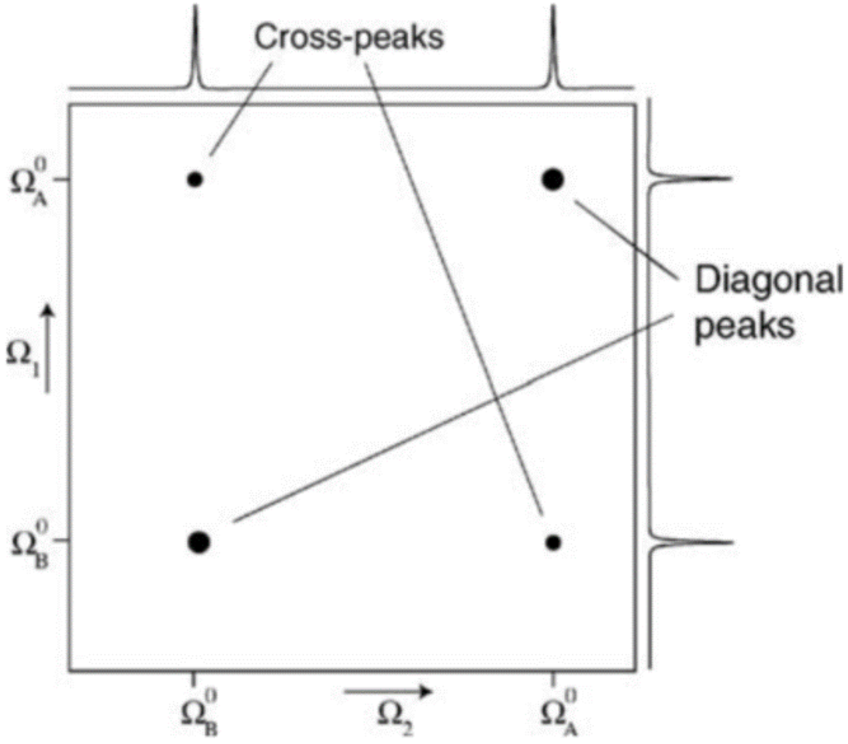

Figure I-24 : *Schematic representation of a 2D EXSY spectrum. Ω represents the peaks frequency. Extracted from* [61].

The limitation of this technique concerns the time scales because one supposes that there are no molecular dynamics or chemical exchange during t_1 and t_2 and that all the dynamics/exchanges occur during the mixing times. That's why it is necessary that $\tau_m >> t_1, t_2$. For the solid state NMR, these experiments have to be performed with the MAS which allows to monitor only the chemical exchanges. In our case, MAS NMR suggested the presence of several sites in 1D NMR and allowed us to study potential correlations between the different sites.

3.3 DFT calculations

3.1.1 Principle

Hohenberg and Kohn are at the origin of DFT calculations by proving that the total energy of a gas of electrons in attendance of a extern potential $V_{ext}(\vec{r})$ can be expressed as :

$$E(\rho) = \int V_{ext}(\vec{r})\rho(\vec{r})d\vec{r} + F(\rho)$$

$F(\rho)$ depends of the electronic density independent from V_{ext}. Using the Born-Oppenheimer approximation and the Hamiltonian for m electrons in the field of N nuclei, the energy functional can be expresses as :

$$E(\rho) = \int V_{ext}(\vec{r})\rho(\vec{r})d\vec{r} + T(\rho) + \frac{1}{2}\int \frac{\rho(\vec{r})\rho(\vec{r}')}{|r-r'|}d\vec{r}d\vec{r}' + E_{sc}(\rho)$$

$$= E_{Ne}(\rho) + T(\rho) + E_{ee}(\rho) + E_{sc}(\rho)$$

$E_{Ne}(\rho)$ is an electron-nuclear Coulomb term

$T(\rho)$ is the kinetic energy of a system of electrons at density n(r)

$E_{ee}(\rho)$ is an electron-electron Coulomb term

$E_{sc}(\rho)$ is the exchange-correlation energy

3.2.2 In the case of colbatates

The first principles calculations were performed within the Density Functional Theory (DFT) framework. In a previous study of the group, they showed that PAW-PBE potentials as implemented in the Vienna ab initio Simulation Package (VASP) code[68] can be used to compute theoretically the Fermi contact shifts in paramagnetic materials[69]. A plane wave energy cut-off of 600 eV and a k-mesh dense enough to reach a convergence were used. All the calculations were done with a ferromagnetic ordering which is considered appropriate for the Fermi contact shift, as described in reference [70]. In the Generalized Gradient Approximation (GGA), the inherent selfinteraction error has detrimental effect on localized transition-metal d (or rare earth f) orbitals. Although, the addition of a Hubbard U correction can produce theoretical average potentials or Fermi contact shifts in better agreement with experiments[71], this method is not used in this study it has been shown to yield some unphysical results for layered cobalt oxide systems: phase stability inversion between O1 and O3 in CoO_2 and incorrect phase diagram for the P2-Na_xCoO_2 system[72]. On the contrary, GGA has been successfully used to describe the phase diagram of the Li_xCoO_2 system[73]. The difficulty to properly model layered cobalt oxides probably comes from the dual character of the electronic properties: some electrons are fully delocalized leading to metallic conduction in plane[74] and some are localized leading to a Curie-Weiss type paramagnetism[75].

3.3.3 NMR shift calculation

The following equation is used to calculate the spin density, and uses the hyperfine coupling constant (A_{FC}) determined by VASP in addition to the total number of unpaired electrons in the unit cell and gyromagnetic ratio of the nucleus to which spin density is being transferred to determine the total amount of spin density at each Na nucleus.

$$\rho(0) = \frac{A_{FC} 3S}{\mu_0 \hbar \gamma_I g_e \mu_B}$$

where μ_0 is the permeability of free space, $\hbar$ is the reduced Planck constant, γ_I is the gyromagnetic ratio of the NMR observed nucleus, g_e is the electron g-factor, and μ_B is the Bohr magneton. The expected paramagnetic contribution to the NMR shift can then be determined by taking into account the spin density at the nucleus ($\rho(0)$) and the magnetic susceptibility of the material (χ_M) according to:

$$\delta_{iso,FC} = \frac{1}{3S} \rho(0) \chi_M$$

Part A:

Study of the average structure, electronic structure and dynamics of the Li^+ ions in OP4-$(Li,Na)CoO_2$ and O4-$LiCoO_2$

Chapter II: New insights on OP4-(Li,Na)CoO_2 structure, electronic structure and dynamics

1. Introduction

In this chapter, we were interested in a unique (Li/Na) mixed lamellar oxide with stacking of edge-shared CoO_6 octahedra layers forming CoO_2 slabs with an alternative occupation of the interslab spaces by Na^+ and Li^+ (**Figure II-1)** and first reported in 1994 by Balsys and Davis[41]. This material was synthetized from the O3-$LiCoO_2$ and P2-$Na_{0.7}CoO_2$ precursors in a 1:1 molar ratio, therefore the $Li_{0.5}Na_{0.35}CoO_2$ ideal formula was, firstly, expected. However, the presence of $LiCoO_2$ as impurity called the theoretical formula into question and a $Li_{0.43}Na_{0.36}CoO_{1.96}$ phase composition was deduced from a Rietveld refinement on neutron diffraction data. The alkali ions keep the intercalation site symmetry of the used precursors: O3-$LiCoO_2$ and P2-$Na_{0.7}CoO_2$, *i.e.* octahedral and trigonal prismatic for the lithium and sodium ions respectively thus forming an OP4 stacking[76]. Na^+ ions can, therefore, occupy either the Na_e or the Na_f sites[77] (**Figure I-3**).

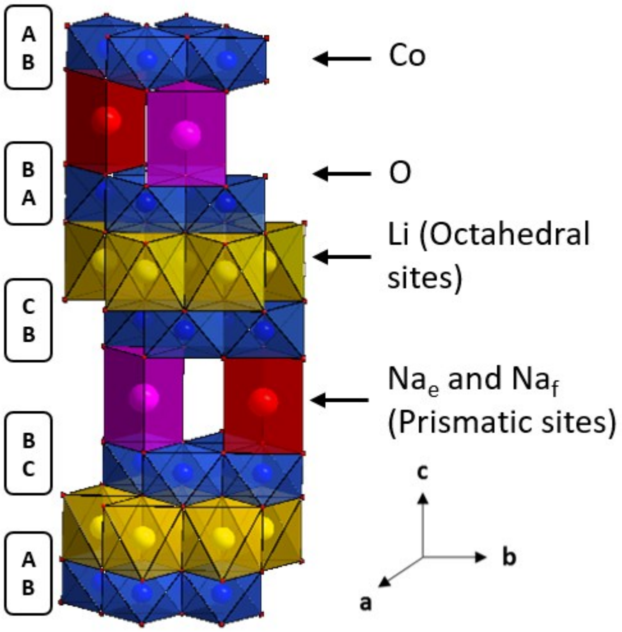

Figure II-1 *: Perspective representation of OP4-(Li/Na)CoO_2. Na^+ ions occupy prismatic sites which can either share faces (Na_f, in red) or edges (Na_e, in purple) with the surrounding CoO_6 octahedra (in blue). The Li^+ ions occupy octahedral sites (in yellow). The oxygen ions positions are labelled with the letters A, B and C.*

By using O3-$LiCoO_2$ and P2-$Na_{0.7}CoO_2$ as precursors for their synthesis, Balsys and Davis indicated the difficulty to obtain a pure phase. Additional publications proposed the synthesis of this phase without any consensus concerning the best precursors or thermal treatment to obtain the purest phase[44,78–83]. **Table II-1** summarizes the chemical compositions and cell parameters reported in the literature for the OP4 phases.

Ref	Chemical formula	Space group	a_{hex} (Å)	c_{hex} (Å)	Precursors
41	$Li_{0.43}Na_{0.36}CoO_{1.96}$	$P6_3mc$	2.839(4)	20.36(3)	P2-$Na_{0.7}CoO_2$ + O3-$LiCoO_2$
78	$Li_{0.48}Na_{0.35}CoO_2$	$P6_3/mmc$	2.824	20.293	Na_2CO_3 + Li_2CO_3 + Co_3O_4
79	$Li_{0.41}Na_{0.31}CoO_2$	$P6_3mc$	2.8266(3)	20.265(2)	Na_2CO_3 + Li_2CO_3 + Co_3O_4
80	$Li_{0.42}Na_{0.36}CoO_2$	$P6_3mc$	2.839(4)	20.36(3)	Na_2CO_3 + Li_2CO_3 + Co_3O_4
44	$Li_{0.42}Na_{0.37}CoO_2$	$P6_3/mmc$	2.8301(2)	20.286(2)	P2-$Na_{0.7}CoO_2$ + O3-$LiCoO_2$
81	$Li_{0.48}Na_{0.35}CoO_2$	$P6_3mc$	2.821(3)	20.163(2)	P2-$Na_{0.7}CoO_2$ + O3-$LiCoO_2$
82	$Li_{0.42}Na_{0.36}CoO_2$	$P6_3mc$	2.831	20.26	P2-$Na_{0.7}CoO_2$ + O3-$LiCoO_2$
83	$Li_{0.37}Na_{0.31}CoO_2$	$P6_3/mmc$	2.8208(2)	20.277(1)	Na_2CO_3 + Li_2CO_3 + Co_3O_4

***Table II-1** : Comparison of the crystallographic data and precursors used for the syntheses of the different OP4 phases reported in the literature.*

All the proposed chemical formulas are slightly different from the ideal $Li_{0.5}Na_{0.35}CoO_2$ one, but the presence of traces of O3-$LiCoO_2$ and P2-$Na_{0.7}CoO_2$ may alter the composition that was determined by Inductively Coupled Plasma (ICP) measurements. An air quench is also used in some publications whereas others used a slow cooling. Berthelot *et al.*[44], for the first time, studied the formation of the OP4-(Li,Na)CoO_2 phase by *in-situ* variable temperature XRD: the phase is formed at around 855°C but decomposes into O3-$LiCoO_2$ and P2-$Na_{0.7}CoO_2$ if slowly cooled. The lattice parameters are relatively close in each publication, although different space groups are used: $P6_3mc$ or $P6_3/mmc$ that only differ by one symmetry operation. In this manuscript, the $P6_3/mmc$ space group was used in fact, the two positions of the oxygen ions (labelled O_{Li} and O_{Na} on **Figure II-1**) can be adjusted in order to refine the eventual slight dissymmetry of the Co ions in their octahedra. Moreover, a structure labelled OPP9-(Li,Na,Na)CoO_2 was evidenced (**Figure II-3**) as competitor of OP4-(Li,Na)CoO_2 formation by varying the ratios between the O3-$LiCoO_2$ and P2-$Na_{0.7}CoO_2$ precursors[44].

In this chapter, since the layered OP4 phase is really original in solid state chemistry and might exhibit peculiar properties, especially because of a different occupation ratio of the alkaline layers, we decided to reinvestigate further its structure in order to have a better insight of the correlation between its chemical formula and its structure. We will investigate the local structure, the electronic structure and the dynamics of the Li^+ ions by NMR as a local probe. Note that the ionic mobility in the positive electrode materials was already probed in the literature by different technique as exchange spectroscopy[84–86], Variable Temperature[85] or rotational-echo double resonance[87]. Selective inversion is also a technique, detailed in this chapter, to study the ionic mobility[67].

2. Synthesis, average structure characterization and physical properties

While by reproducing the synthesis many times with slightly different alkaline initial compositions, a real pure OP4 phase could not be, easily, synthetized. Among all the prepared samples, we selected for the discussion in this chapter, three of them, representative of all the resulting powders. The samples are labelled A, B, and C in this chapter.

2.1 Synthesis route

In the literature, the syntheses were performed using either alkaline carbonates and cobalt oxide Co_3O_4, or O3-$LiCoO_2$ and P2-$Na_{\sim 0.7}CoO_2$ as precursors. As less impurities were observed by XRD in the first case, we report only syntheses carried on using Li_2CO_3 (Sigma-Aldrich, 99.9%, dried at 350°C), Na_2CO_3 (Sigma Aldrich, 99.9%, dried at 200°C) and Co_3O_4 (home-made from cobalt nitrate, heat treated under air at 450°C). Those precursors were initially mixed and ground together in a Ar-filled glovebox targeting slightly different chemical compositions around $Li_{0.42}Na_{0.38}CoO_2$ in order to compensate possible alkaline ion loss by evaporation[44]. The initial alkali compositions are summarized in **Table II-2.**

	Initial alkaline content for $Li_xNa_yCoO_2$	
	x	**y**
Sample C	0.42	0.40
Sample B	0.42	0.41
Sample A	0.44	0.38

Table II-2: *Initial alkaline compositions of the three samples A, B and C*

The powders were then pressed into pellets under a controlled argon atmosphere and were heated in a furnace under air at 870 °C for 48 h with a 2°C/min heating rate. After the heat treatment, all the pellets were rapidly quenched to room temperature and entered in the Ar-filled glovebox. The expected reaction for the $Li_{0.42}Na_{0.38}CoO_2$ synthesis in stoichiometric proportions is:

$$0.21\, Li_2CO_3 + 0.19\, Na_2CO_3 + \frac{1}{3}\, Co_3O_4 \rightarrow\, Li_{0.42}Na_{0.38}CoO_2 + y\, CO_2$$

All the OP4 phases were then stored and prepared for characterization in a glovebox in order to avoid any air contamination.

Typical SEM images of the sample A can be found in **Figure II-2**. One can distinguish the layered structure of the OP4 phase. It is also possible to observe the hexagonal shape of the crystals. The bigger particles measure almost 200 µm while the smaller particles are 3 µm long. Nanometric particles can also be observed on the particles which either can be trace of Co_3O_4 or the result of a reaction to air.

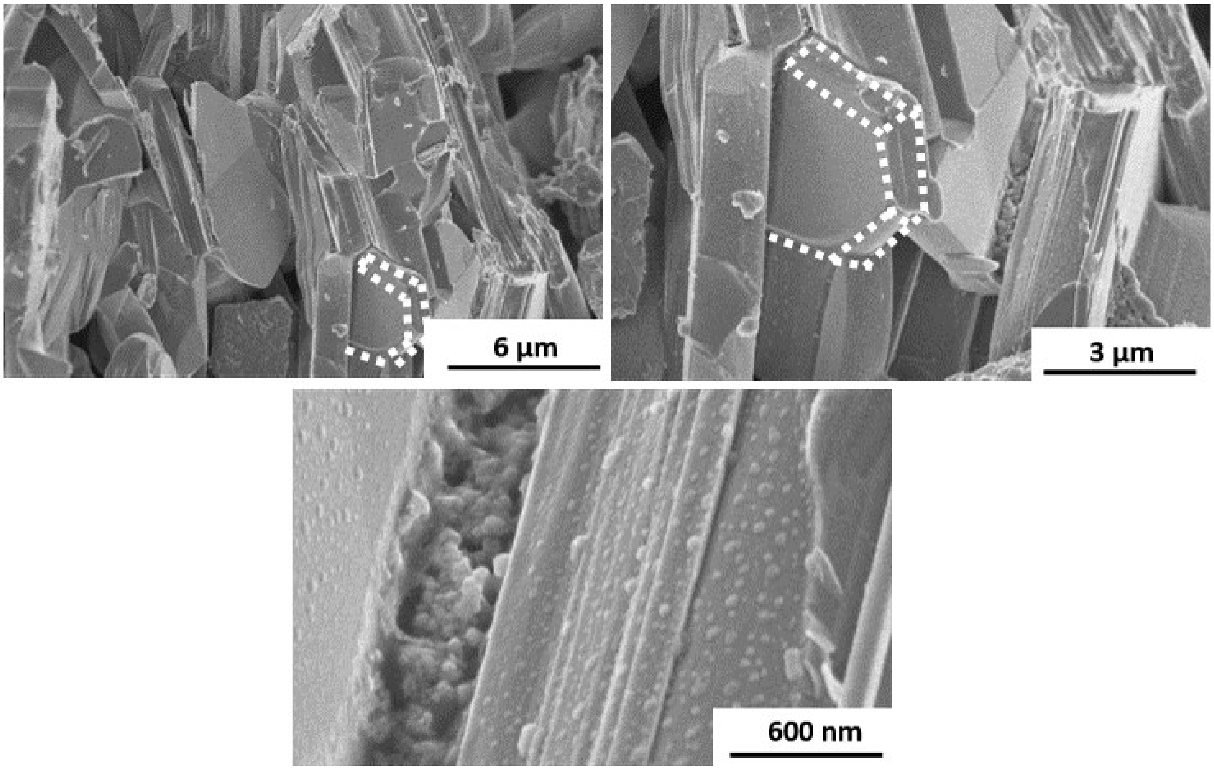

Figure II-2 *: SEM pictures of the sample A at different magnifications. Dashed lines represent the hexagonal shape of a OP4 crystal.*

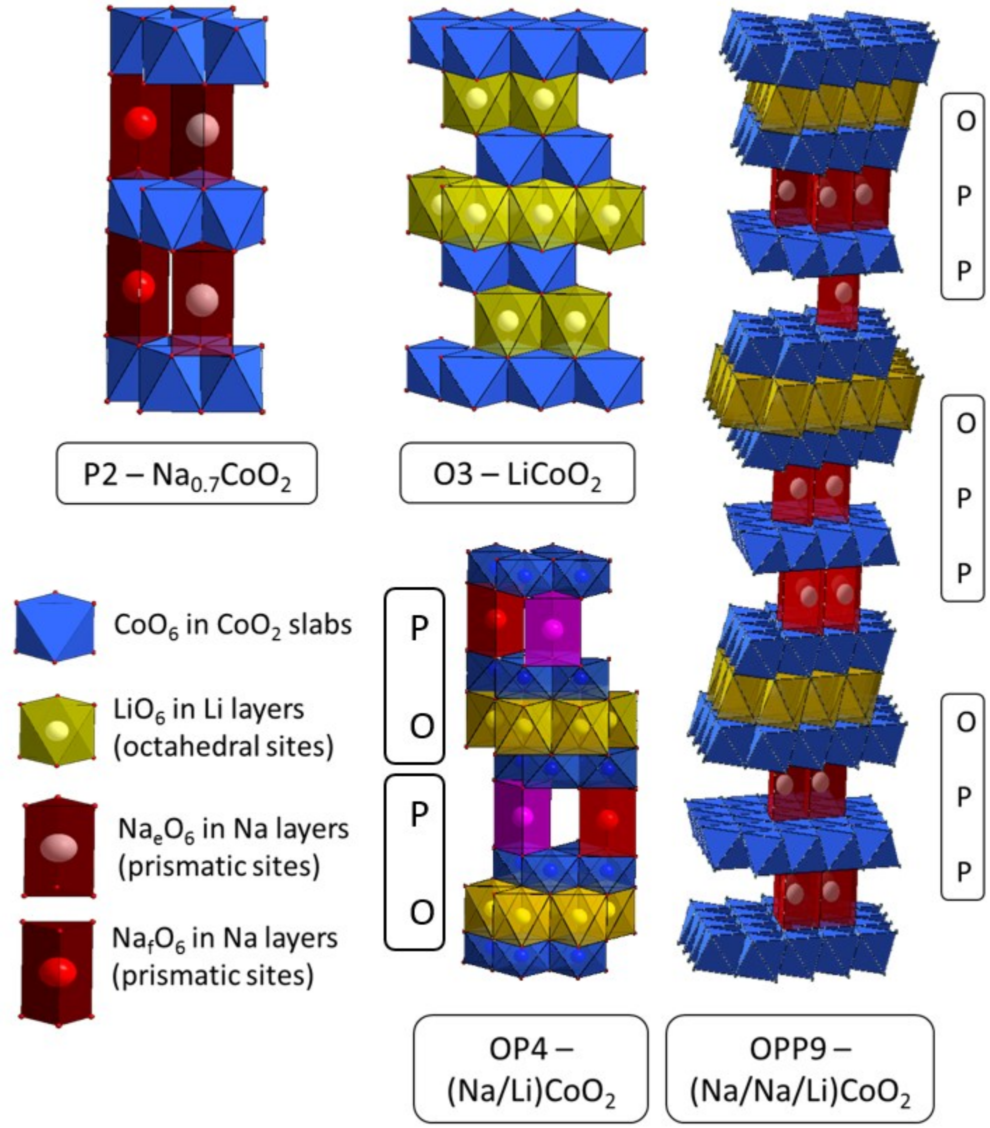

Figure II-3 *: Representation of the different structures introduced in this chapter.*

2.2 Structural characterization

Angular resolution synchrotron X-Ray powder diffraction (SXRPD) experiments were performed on the BL04-MSPD beamline of the ALBA synchrotron (Cerdanyola del Vallès, Spain) for the sample A only. The data were collected in a 2° to 73° 2θ range at a wavelength of λ = 0.8261 Å. The laboratory XRD characterization of the samples B and C was performed on a PANalytical X'Pert Pro with a X'Celerator detector and equipped with Co $K_{\alpha_{1,2}}$ radiations ($\lambda(K_{\alpha_1})$ = 1.789 Å and $\lambda(K_{\alpha_2})$ = 1.793 Å). The measurements were performed between 10° and 80°. Note that as needed high quality XRD patterns to observe the presence of impurities, we used the Co radiations diffractometer. However, the low amount of powder synthesized prevented us from completely filling the XRD sample holder that's why aluminum peaks are present on the XRD patterns of the sample B and C (**Figure II-4**).

As all the XRD patterns were not recorded at the same wavelength, **Figure II-4** shows the patterns of the three samples as a function of d spacing in Å. The insert represents a zoom, in the 4.5 – 5.75 Å range, on the most intense diffraction line, (004) at d = 5.1 Å. The XRD patterns of the three samples exhibit, in addition to the diffraction lines expected for the OP4 phase, one or two peaks corresponding to phases as impurities. The sample A XRD pattern shows traces of O3-$LiCoO_2$ as better seen on the zoom by the presence of its (003) diffraction line at 4.7 Å. The sample B XRD pattern evidences traces of P2-$Na_{\sim 0.7}CoO_2$ and OPP9-(Li,Na,Na)CoO_2 phases as better seen on the zoom by the presence of the (002) peak of P2 at 5.4 Å and (009) peak of OPP9 at 5.2 Å. The sample C exhibits only traces of the OPP9 phase as an impurity on its pattern.

Thus, our quenching procedure was fast enough to avoid the OP4 phase decomposition in O3-$LiCoO_2$ and P2-$Na_{\sim 0.7}CoO_2$ as observed previously[44]. The XRD patterns of all the phases were first refined using the Le Bail method to extract the cell parameters which are summarized in **Table II-3**. The refined lattice parameters of the OP4 phase, $a_{hex.}$ ~ 2.824(2) Å and $c_{hex.}$ ~ 20.28(1) Å, are in good agreement with the value ranges reported in the literature (**Table II-1**). The calculated cell parameters of the O3-$LiCoO_2$, P2-$Na_{\sim 0.7}CoO_2$ and OPP9-(Li,Na,Na)CoO_2 impurities phases are also in agreement with the literature[44,74,77]. The structural Rietveld refinement using the SXRD data of the sample A will be discussed after the NMR characterization of the local OP4 structure which provided new structural information concerning the filling of the different slabs.

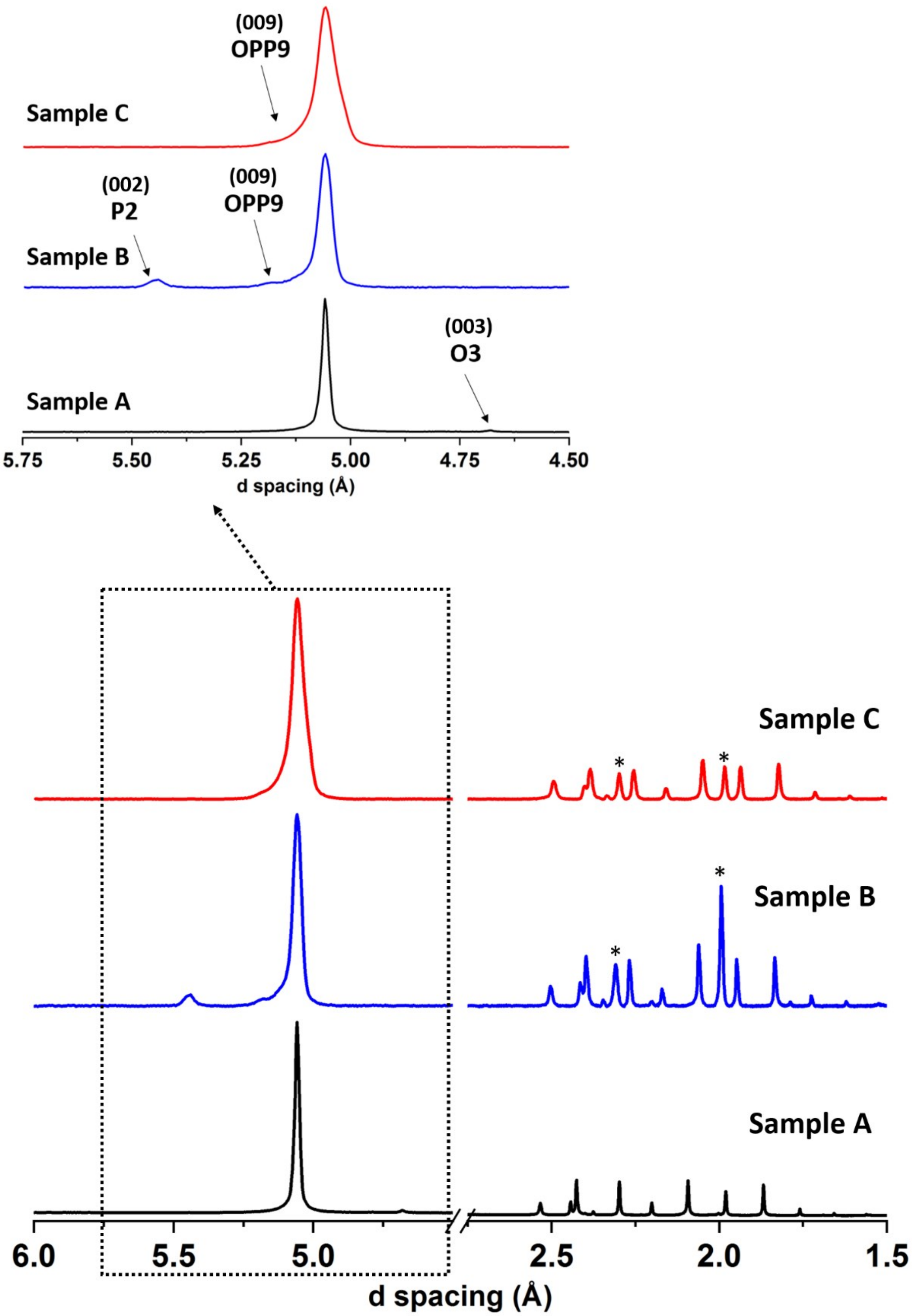

Figure II-4 *: Experimental XRD patterns of the samples A, B and C plotted as a function of d spacing. Insert: Zoom in the 5.75 Å- 4.50 Å region in order to focus on the impurities peaks. * are the Al peaks due to the sample holder used for the XRD acquisition.*

		Sample A	Sample B	Sample C
OP4 ($P6_3/mmc$)	a_{hex}	2.826(1) Å	2.826(3) Å	2.822(1) Å
	c_{hex}	20.29(3) Å	20.28(3) Å	20.28(2) Å
O3 ($R\bar{3}c$)	a_{hex}	2.81(2) Å	-	-
	c_{hex}	14.08(8) Å		
P2 ($P6_3/mmc$)	a_{hex}	-	2.838(3) Å	-
	c_{hex}		10.92(1) Å	
OPP9 ($R\bar{3}m$)	a_{hex}	-	2.835(3) Å	2.837(2) Å
	c_{hex}		46.7(2) Å	46.1(2) Å

***Table II-3**: Refined lattice parameters of the different phases reported in the samples A, B and C*

3. Physical properties

3.1 Electronic conductivity

In **Figure II-5**, the electrical conductivity of a sample synthetized during R. Berthelot PhD is plotted as a function of temperature in the 6 K – 300 K range. The electronic conductivity was measured using a standard four probe technique. Note that no sintering of the pellet could be done due to the fast quench required to avoid the decomposition of the OP4 phase. The evolution of the conductivity denotes a semi-conductive behavior probably due to inter particles boundaries resistivity. Ren *et al.*[78] reported similar data as well as Seebeck coefficient measurements that showed that the OP4 phase should exhibit a metallic conductivity in the (a, b) plane relatively similar to the P2-Na_xCoO_2[88,89] and O3-Li_xCoO_2[74] phases.

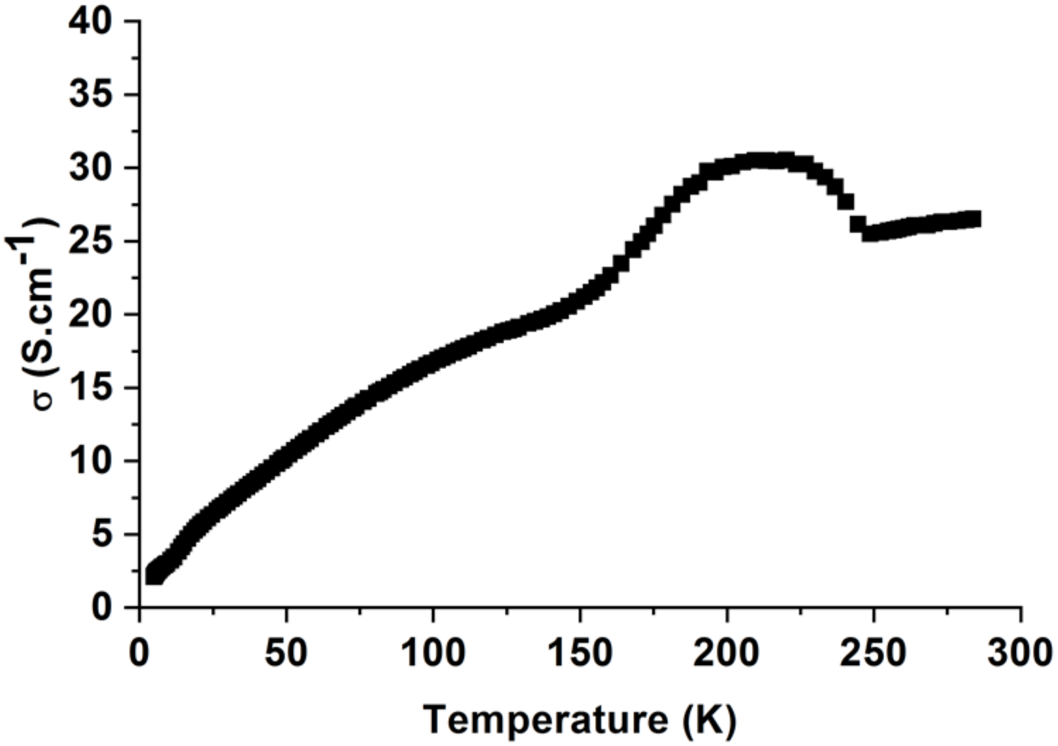

***Figure II-5**: Electrical conductivity of an OP4 phase as a function of temperature (from 6K to 300 K).*

3.2 Magnetic measurements

Figure II-6 displays the evolution of the magnetic susceptibility of the sample A as a function of temperature from 7 K to 300 K with a constant magnetic field of 1 T. The measurements were performed on a Super Quantum Interference Device (SQUID) magnetometer MPMS5 The sample A was cooled without any application of a magnetic field (ZFC). The fit of the experimental data was realized taking into account a paramagnetic contribution χ_0, following a Curie-Weiss law:

$$\chi(T) = \frac{\boldsymbol{C}}{\boldsymbol{T-\theta}} + \chi_0 \quad \text{eq(II-1)}$$

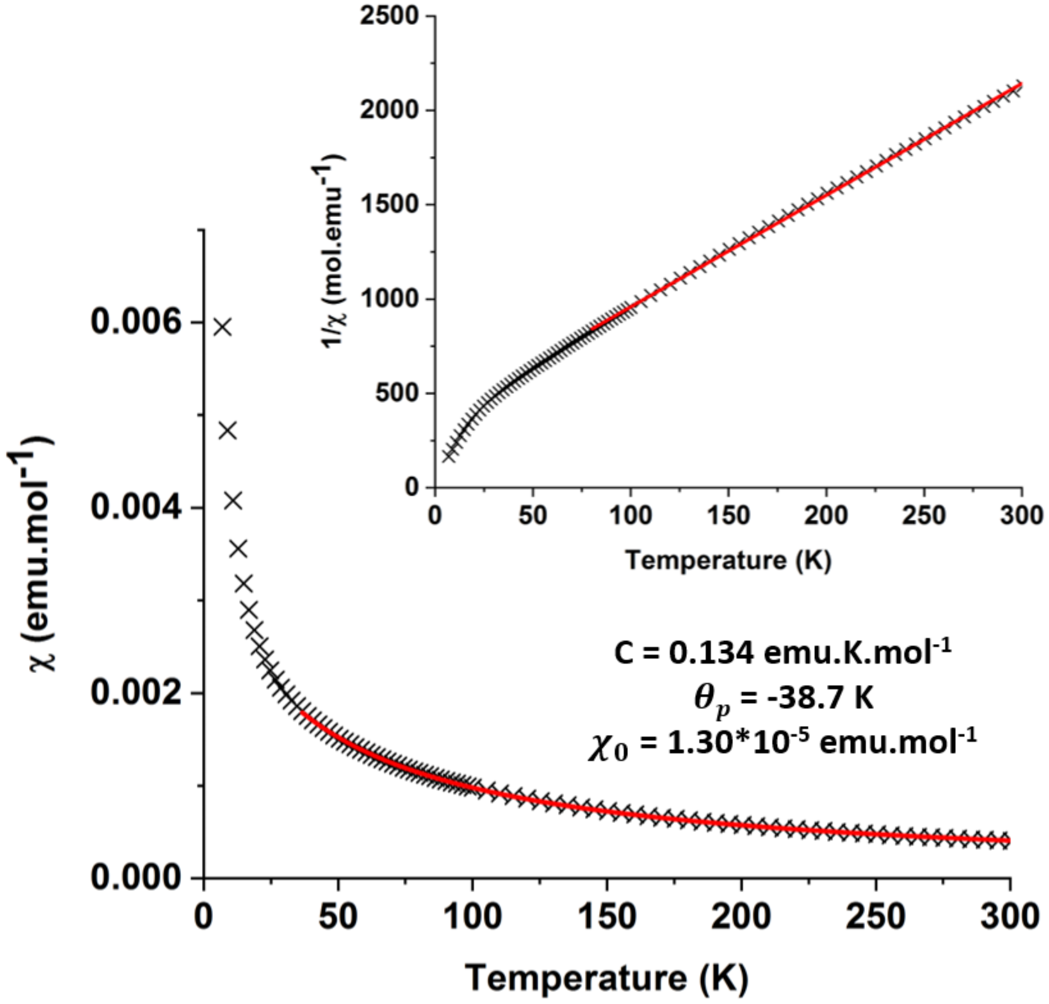

Figure II-6: *Magnetic susceptibility and inverse magnetic susceptibility (in the insert) of the sample A as a function of temperature (6 K to 300 K) realized under a 1T magnetic field.*

The fitted corresponding values are C = 0.134 emu.K.mol^{-1}, θ_p = -38.7 K and χ_0 = 1.30*10^{-5} emu.mol^{-1}. The C value is relatively high compared to the theoretical one (C_{th} = 0.05 emu.K.mol^{-1}) by considering the $Li_{0.42}Na_{0.38}CoO_2$ formula with 0.2 LS-Co^{IV} and 0.8 LS-Co^{III}. This difference indicates that the material doesn't completely follow a Curie-Weiss law and a part of the susceptibility can be due to delocalized electrons. This point will be discussed again regarding the variable temperature ^{7}Li MAS NMR spectra.

4. Local structure, electronic structure and dynamics studied by ^{7}Li MAS NMR

4.1 1D NMR

^{7}Li MAS NMR spectra were acquired using a 7.05 T magnet spectrometer at 116.6 MHz and a 2.35 T magnet at 38.9 MHz using a standard Bruker 2.5 MAS probe and a 30 kHz spinning frequency. Recycle delay of 5 s was long enough to avoid T_1 saturation effects and all the shifts are referred to a 1M LiCl (aq) solution. A Hahn echo sequence was applied on both spectrometers to confirm the number of signals and the origin of the lineshape (**Figure II-7**). While higher magnetic fields are useful for reducing the magnitude of the nuclear dipolar couplings and quadrupolar coupling, the resulting increase in the electron-nuclear dipolar coupling broadening results in rather similar line resolution. However, since the same 30 kHz spinning frequency is used in both experiments, the spectrum recorded at 2.35 T exhibits less spinning side bands and therefore more intensities in the isotropic positions. The advantage is clearly seen for the negatively shifted signal that exhibits a wider spinning side bands distribution that the others. Moreover, at low field (2.35 T) we can clearly observe the weak signal at -203 ppm that is located under a spinning side band with the 7.05 T magnet.

The 1D ^{7}Li MAS NMR spectra of the three samples are shown in **Figure II-8** under a 2.35 magnetic field and a 30 kHz spinning frequency. The three samples exhibit 5 signals located after fitting at 32, 18 ppm, 0, -84 and -203 ppm and respectively labelled 1 to 5 (**Figure II-9**). The presence of many signals suggests a repartition of different Co ions environments in the layers. The signal 3 can be assigned to Li^+ ions in diamagnetic LS-Co^{3+} (t_{2g}^6) environments similar to the one in O3-$LiCoO_2$[90,91], whereas all the other signals are clearly due to the Fermi contact interaction observed for Li^+ in octahedral environments surrounded by paramagnetic ions. After fitting the signals of the spectra (**Figure II-9**) including the spinning side bands, the resulting signal intensities were extracted and summarized in **Table II-4**. The signal 5 was not considered because of its very low intensity. The intensity values obtained for the signal 2 are similar for all the samples and are therefore not affected by the nature of the impurities in the samples. Contrary to the signal 2, the signal 3 (0 ppm) intensity is slightly larger for the sample A in agreement with the presence of O3-$LiCoO_2$ as impurity.

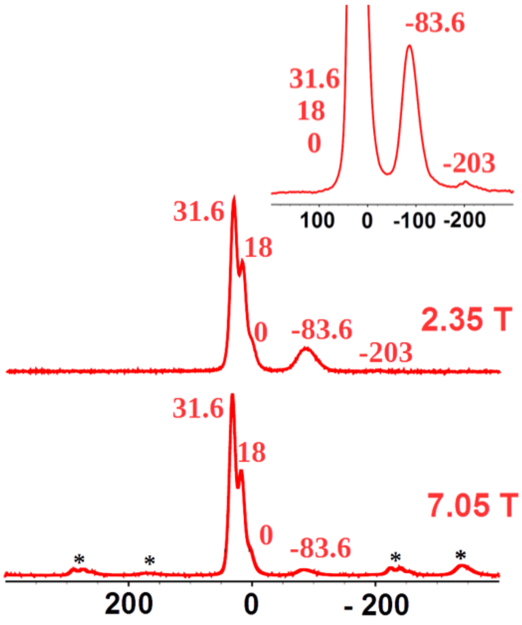

Figure II-7 *: Comparison of the ^{7}Li MAS NMR spectra recorded on the sample C at two different magnetic fields (2.35 and 7.05 T) using the same spinning frequency (30 kHz) with a Hahn Echo sequence. Insert: Zoom in order to highlight the presence of the signal at -203 ppm.*

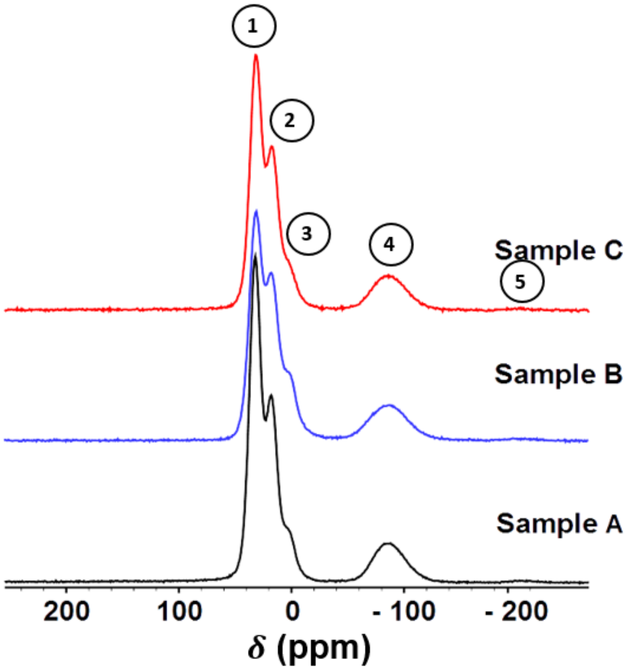

Figure II-8 *: Experimental ^{7}Li MAS NMR spectra of the samples A, B and C (2.35 T magnet, spinning frequency = 30 kHz, Hahn echo sequence).*

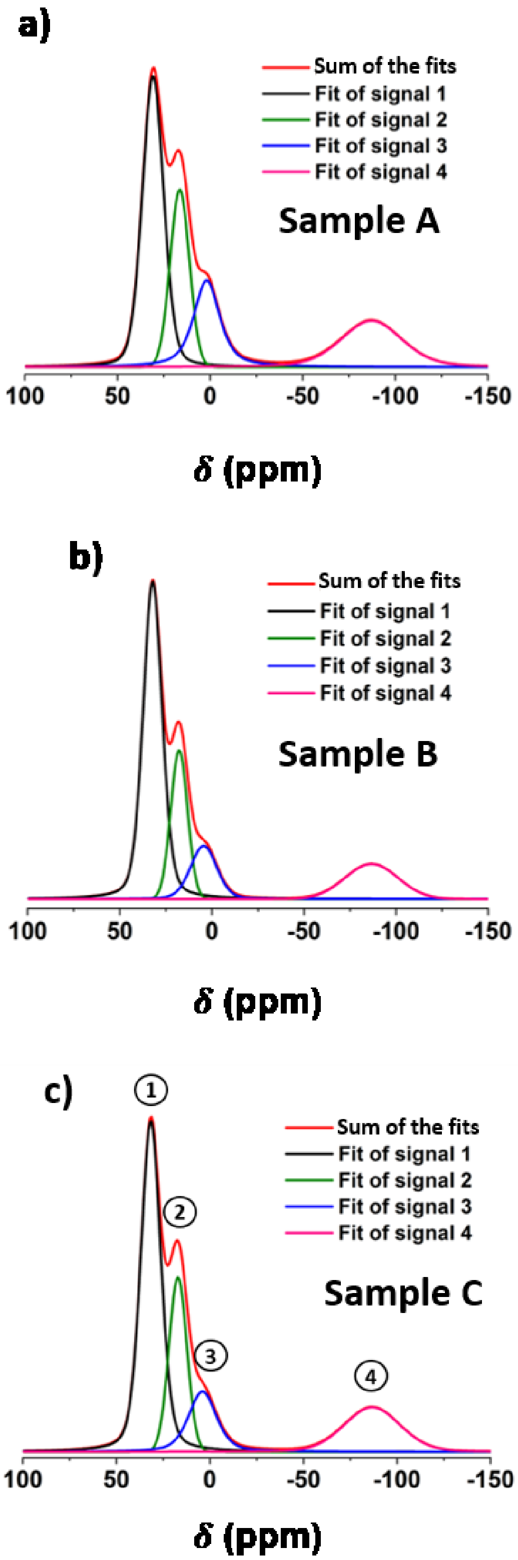

Figure II-9 *: Fits of the signals 1, 2, 3 and 4 compared to the experimental spectra (in red) recorded on samples (a) A (b) B (c) C.*

	Signal 1 (31.6 ppm)	**Signal 2 (18 ppm)**	**Signal 3 (0 ppm)**	**Signal 4 (-83.6 ppm)**
Sample C	47%	19%	12%	22%
Sample B	52%	18%	11%	19%
Sample A	41%	19%	18%	22%

***Table II-4** : Repartition of the fitted areas of each Li^+ signal for the three studied samples. The signal 5 was neglected because of its low intensity.*

4.2 DFT calculations

4.2.1 Description of the considered cell

A model compound was considered with the $Li_{1/2}Na_{1/3}CoO_2$ stoichiometry, considering full Li interslab spaces as in O3-$LiCoO_2$ and the a Na^+/vacancy ordering as reported by Platova *et al.*[92] for P2-$Na_{2/3}CoO_2$ (**Figure II-10**). The used supercell formula is $Li_{24}Na_{16}Co_{48}O_{96}$. A quasi-Newton algorithm was used for the ionic relaxations. To obtain accurate final energies, all the relaxations were followed by a final static calculation with the linear tetrahedron method. For the magnetic susceptibility we used $\chi = C/(T - \theta_p)$, with C and θ_p determined from the linear fit of the inverse of the magnetic susceptibility (1/ χ) versus temperature using the modified Curie-Weiss law (**Figure II-6**). Calculations were also realized by considering the theoretical Curie constant value C_{th}.

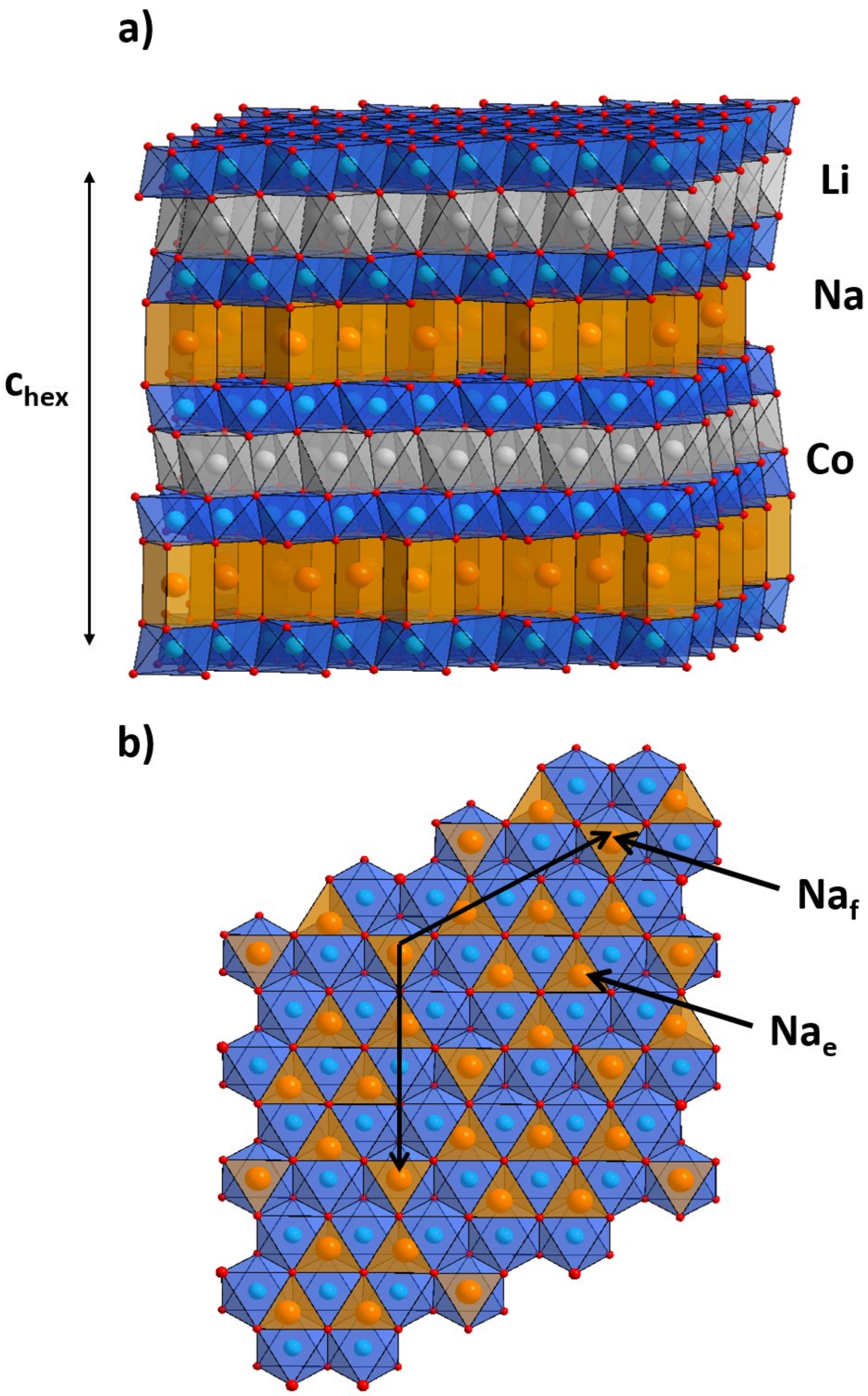

***Figure II-10** : a) Representation of the hypothetical cell $Li_{1/2}Na_{1/3}CoO_2$ used as model for DFT calculations. This model considers full Li layers and 67% filled Na layers. b) Highlighting of the Na^+/vacancy ordering in the Na interslab spaces.*

5.2.2 Results

Even if the stoichiometry is slightly different from the real one and eventhough in our Generalized Gradient Approximation (GGA) approach, all the cobalt ions are partially oxidized, the calculations showed that considering a specific Na ordering tends to partially localize the charges. The global spin calculated in the cell is in agreement with the expected value for 1/6 LS-Co^{4+} (t_{2g}^{5}) and 5/6 LS-Co^{3+} (t_{2g}^{6}) (**Figure II-11**).

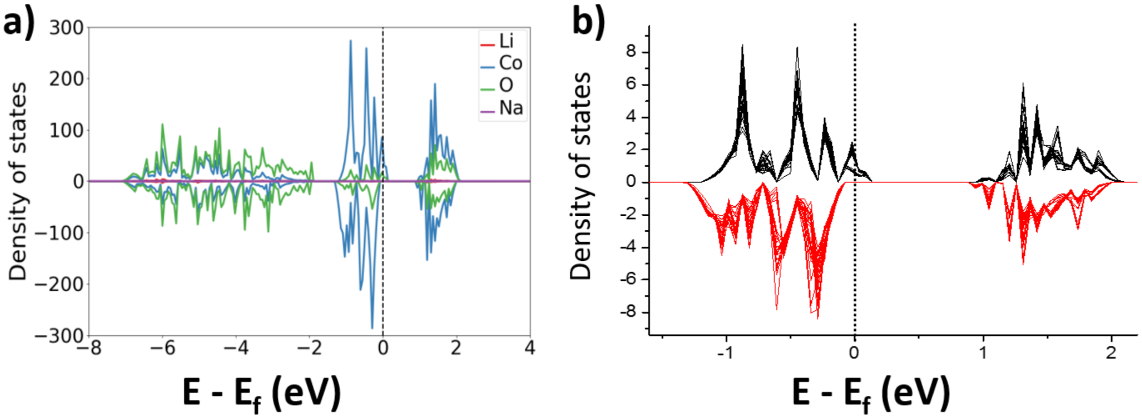

Figure II-11: *(a) Calculated spin DOS of the model presented in* ***Figure II-10****. (a) total. (b) partial on the Co 3d orbitals.*

As expected from the larger C value experimentally calculated, the resulting shifts magnitude is larger than by using the theoretical C_{th}. Whatever the method used, the experimental data cannot be properly simulated **(Figure II-12**).

This emphasizes the difficulty to model the electronic structure for layer cobalt oxides as discuss in chapter I. In our modelling, the t_{2g} orbitals degeneracy is lifted because of the CoO_6 distortion along the c axis leading to the a_{1g} and e_g' orbitals[58]. Note that the 3D spin density map clearly shows that the a_{1g} orbital resulting from a recombination of the t_{2g} orbitals as discussed in chapter I (**section 1.3.2**), is mainly carrying the spins (**Figure II-13**).

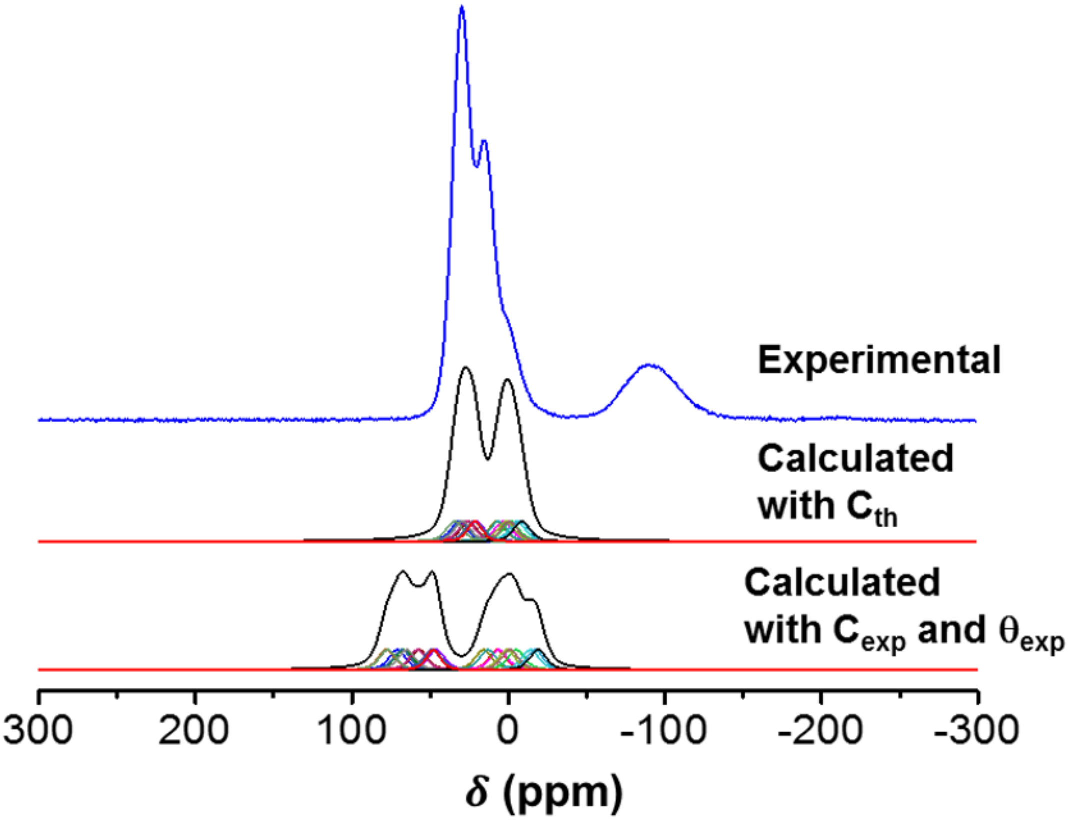

Figure II-12 *: Comparison between the experimental* ^{7}*Li MAS NMR spectrum of the OP4 phase and the calculated spectra considering the theoretical Curie constant and the experimental one.*

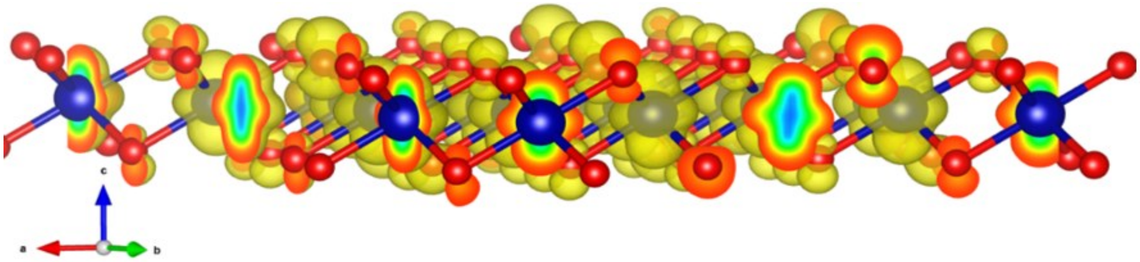

Figure II-13 *: Calculated 3D spin density map plotted using a* 10^{-3} e^{-}/A^{2} *isosurface value.* a_{1g} *orbital is mainly carrying the spins. The yellow color represents the positive spin density.*

In reality, the local electronic structure should be more complex and one expect some localized and some delocalized electrons in the t_{2g} orbital of the Co ions. The delocalized electrons would lead to a Knight type contribution to the shift whereas the localized one would involve a Fermi contact type contribution. Nevertheless, the e_g' orbitals involving the t_{2g} ones that overlap through the middle of the CoO_6 common edge of the octahedra should be responsible for the delocalized behavior in the (a, b) plane while the electrons in the a_{1g} oriented along the c axis should be mostly responsible of the localized character. The schematic band structures for the transition metal ions in O_h symmetry and D_{3d} symmetry when the octahedra are distorted along the c axis, are shown on **Figure II-14** and highlights the presence of localized and delocalized electrons in case of the D_{3d} symmetry. The Fermi contact shift calculations indicate that considering a specific Na ordering in the sodium layer, tends to partially localize the charges on the Co ions and lead to slightly different Li environments and several Li calculated shifts. Therefore, no complete signals assignment could be proposed from this study.

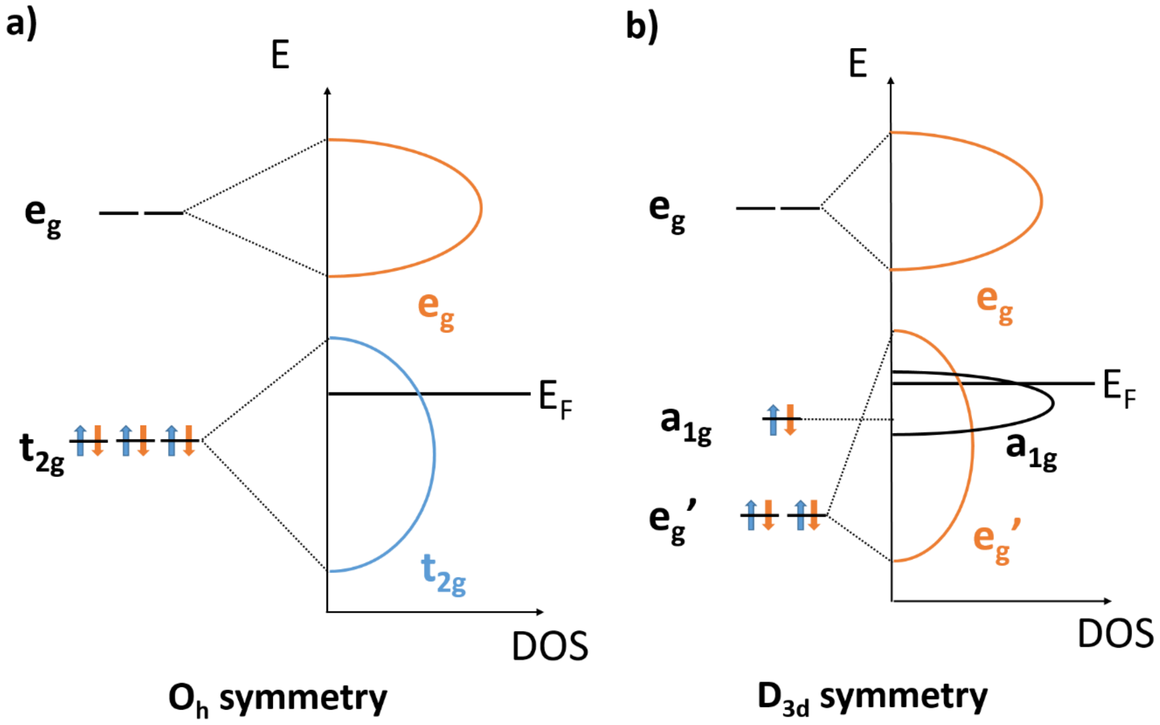

***Figure II-14**: Band structure of the Co^{3+} ions in the case of Na_xCoO_2 (a) before and (b) after the octahedra distortion.*

4.3 Variable temperature (VT)

VT-MAS NMR experiments were performed at a 13 kHz spinning frequency in a 265 K ≤ T ≤ 450 K temperature on the 7.05 T magnet equipped of a 4 mm WVT MAS probe (**Figure II-15**). Hahn echo sequences were used. Note that at 450 K, one can also distinguish a new component labelled 3'. A coalescence phenomenon seems to occur when T increases indicating a slow chemical exchange between the Li sites. The signals narrowing when T increases is also due to a low increase of the mobility. The mobility of the Li^+ ions will be investigated by NMR later in the next section of this chapter. Nevertheless, the variation of the signals position reveals the complexity of the origin of the shifts. Indeed, for Fermi contact shifted signals observed in paramagnetic compounds, the shifts are following the same trend versus T as does the magnetic susceptibility, *i.e* a $\frac{C}{T-\theta}$ for a Curie-Weiss law and should tend to 0 ppm for T $\rightarrow +\infty$.

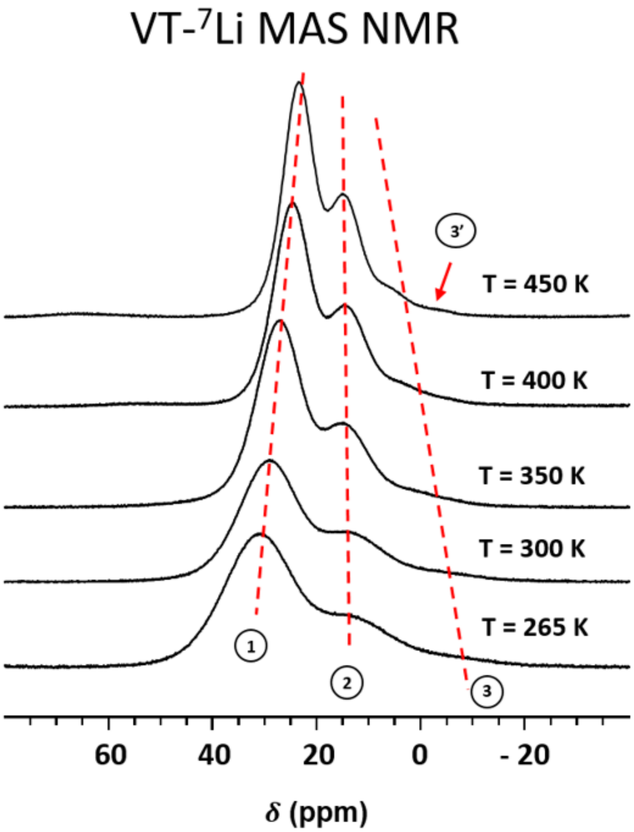

***Figure II-15** : Experimental ^{7}Li MAS NMR spectra recorded on a 7.05 T magnet at different temperatures in the 265 K – 450 K. The NMR sequences were Hahn echoes and the spinning frequency was 13 kHz.*

For the OP4 phase, the signals shifts do not follow such law; especially the position of signal 2 remains almost temperature independent. Higher resolution experiments performed at 30 kHz were also done in narrower temperature range showing also the temperature independency of signal 2 (**Figure II-16**).

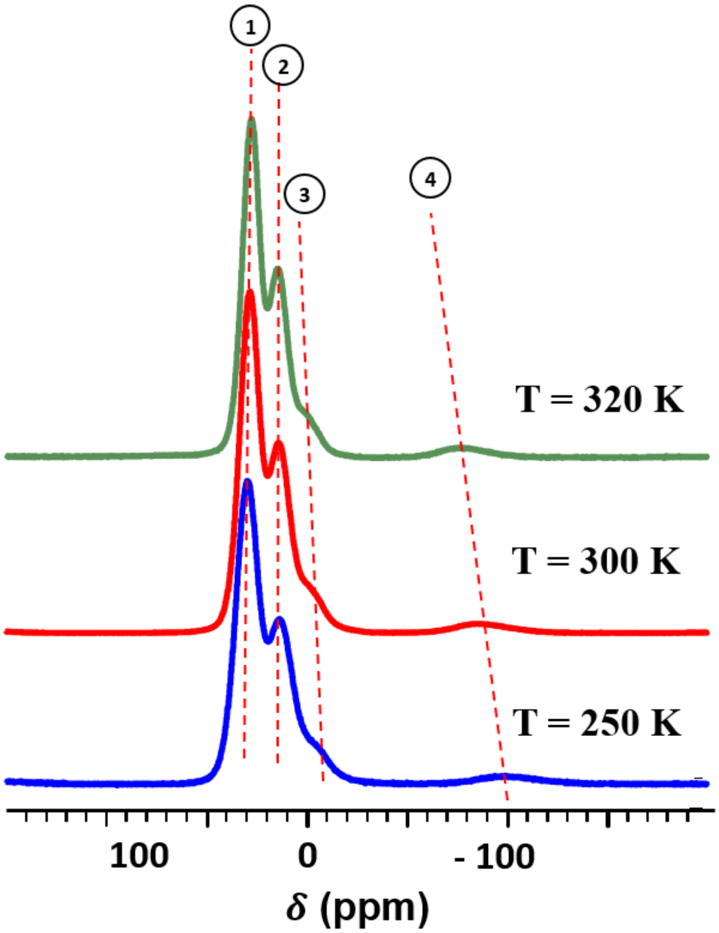

Figure II-16: *Experimental ^{7}Li MAS NMR spectra recorded on a 7.05 T magnetic field with a spinning frequency of 30 kHz for T = 250 K, 300 K and 320 K.*

The evolution of the shifts position as a function of temperature is plotted on **Figure II-17**. Our VT-MAS NMR results are further confirming the dual character of the OP4 phase that exhibits delocalized electrons and localized ones. Indeed, the temperature evolution of the ^{7}Li MAS NMR shifts can be interpreted considering that the shifts are due to two interactions: the Fermi contact interaction (for localized electrons), that is temperature dependent, and the Knight interaction (for delocalized electrons) that is temperature independent. The total shift for a *i* nucleus can be expressed by:

$$\delta^{i}_{tot}(T) = \delta^{i}_{Fermi}(T) + \delta^{i}_{Knight} \qquad \text{eq.(II-2)}$$

$$\delta^{i}_{Fermi}(T) = \frac{1}{3SN_A}\rho^{i}(0) * \frac{C}{T-\boldsymbol{\theta}} \qquad \text{eq.(II-3)}$$

$$\delta_{Knight} = \frac{8\pi}{3}\langle|\psi_{r=0}|^2\rangle\chi^{e}_{S} \qquad \text{eq.(II-4)}$$

By fitting the evolution of the signals position versus T (**Figure II-17**), the ^{7}Li MAS NMR shifts tend to a rather similar Knight shift contribution for all the signals to ~ 16 ppm for T → +∞ (**Table II-5**). This position is clearly out of range of the chemical shift for ^{7}Li in diamagnetic environment and can be indeed attributed the Knight shift component. The Fermi contact coupling constant incorporated in a constant labelled B (B = $\frac{C}{3SN_A}\rho^{i}(0)$), is found to be either positive of negative depending on the signals. A positive contribution is excepted for a 90° LS-Co^{IV}-O-Li interaction (delocalization mechanism) while a negative shift is expected for a 180° LS-Co^{IV}-O-Li interaction similarly to the case of Li(Co$^{III}_{1-y}$Cr$^{III}_{y}$)O$_2$ phases[70,93].

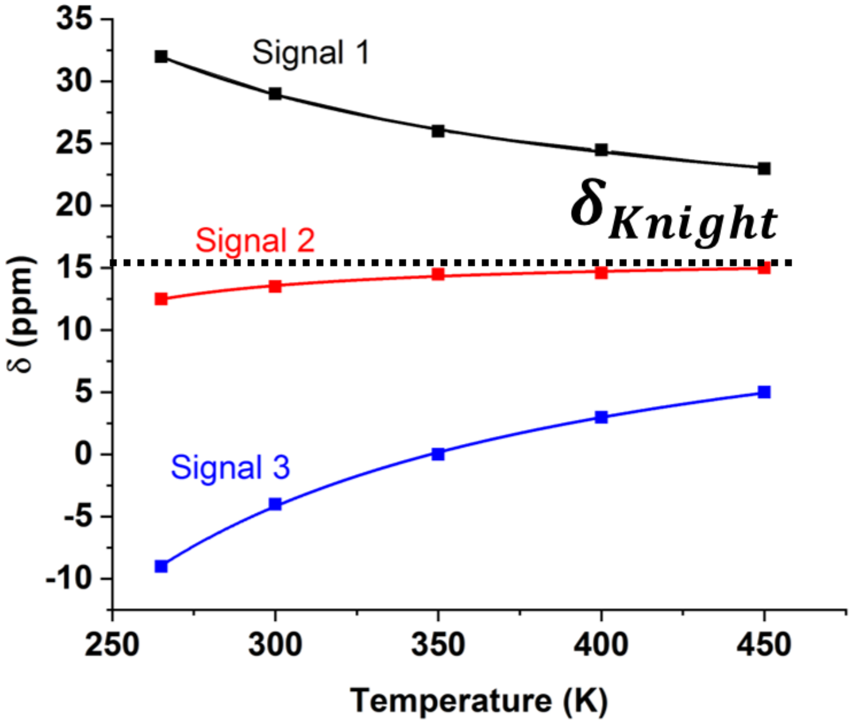

***Figure II-17**: Fitted lines of the NMR shifts evolution of the signals 1, 2 and 3 as a function of temperature.*

	Signal 1 (31.6 ppm)	**Signal 2 (18 ppm)**	**Signal 3 (0 ppm)**
B (ppm.K)	2400 ± 500	-270 ± 150	-3700 ± 500
θ_p (K)	115 ± 20	200 ± 30	120 ± 15
δ_{Knight} (ppm)	16 ± 1	16 ± 1	16 ± 1

***Table II-5:** Calculated values for B, θ_p and δ_{Knight} after the fitting of the curves showed on **Figure II-17**.*

4.4 Dynamics of the Li$^+$ ions in the interslab spaces

Selective inversion is a technique used to investigate the dynamics of Li$^+$ ions in the OP4 material in order to investigate a possible deficit of Li$^+$ inside the Li layers. This technique introduces a mixing time which allows a chemical exchange between the different Li sites by hopping. In order to apply a coherent mixing times range, the longitudinal relaxation time T1 of each Li signal have to be determined. For that, the inversion recovery technique was processed at different temperatures.

4.4.1 T1 measurements

Figure II-18 represents the pulse sequence of the inversion-recovery technique.

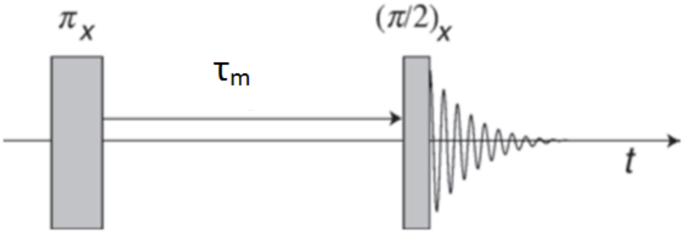

***Figure II-18** : Pulse sequence of the inversion recovery. Extracted from reference* [61]

This technique consists of applying two pulses separated by a τ_m delays. The pulse sequence is repeated many times with different τ_m delays. The first pulse allows to invert the population distribution while the τ_m delays allows the relaxation of the populations. Finally, the second pulse allows to convert the population difference into coherences.

In order to determine the T1 value, the evolution of the signals intensity as a function of τ_m delays is plotted using the formula as follows:

$$I(t) = I_0 + A * \exp(-{}^{t}/_{T1}) \qquad \text{eq(II-5)}$$

Where I_0 and A are constant values.

The TopSpin software allows measuring the intensity of each signal and calculating for each T1 value. The full recovery of the magnetization has to be reached for the longest mixing times that's why a criterion for a good inversion recovery acquisition is to have $\tau_m \sim 5{*}T1$. The ^{7}Li MAS NMR inversion-recovery was performed on a probe for 1.3 mm-diameter zirconia rotors (spinning frequency = 65 kHz) with a 7.05 T magnet at McMaster University, Canada. The measurements were performed on the sample B with different mixing times depending of the temperature (**Table II-6**). For each measurement, 16 mixing times were applied.

RT	310 K	320 K / 340 K
50 ns	50 ns	50 ns
1 ms	10 ms	10 ms
5 ms	50 ms	50 ms
10 ms	100 ms	100 ms
15 ms	150 ms	150 ms
25 ms	200 ms	200 ms
50 ms	250 ms	250 ms
75 ms	300 ms	300 ms
100 ms	350 ms	350 ms
200 ms	400 ms	400 ms
300 ms	500 ms	500 ms
400 ms	750 ms	750 ms
500 ms	1 s	1 s
1 s	5 s	4 s
5 s	10 s	5 s
10 s	15 s	6 s

Table II-6 : *τ_m delays used at the different temperatures for ^{7}Li MAS NMR inversion recovery*

Only the intensities as a function of τ_m delays at RT are plotted in this manuscript (**Figure II-19**). Similar plots were obtained at 310 K, 320 K and 340 K. The fitted T1 values are reported in **Table II-7** for each temperature and signal. The signal 4 shows a low modification of its intensity with the increasing τ_m delays that's why it is not plotted in this manuscript. Moreover, the signal 5 is located under a spinning side band at this magnetic field.

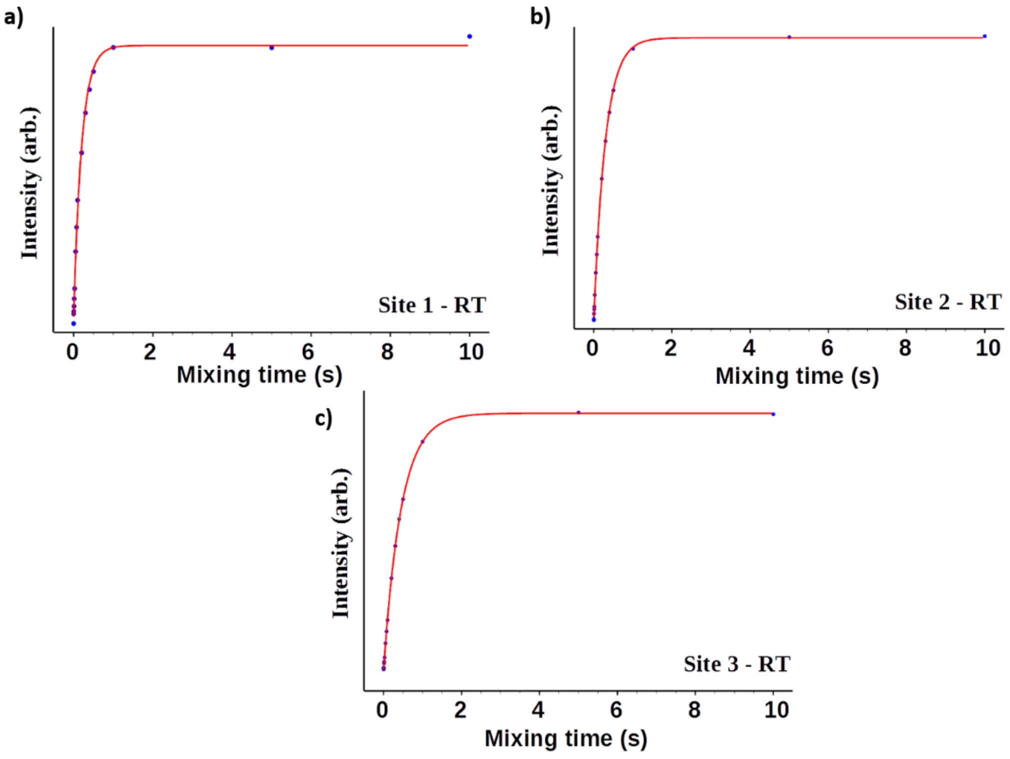

Figure II-19 : *Evolution of the signals intensities for each signal as a function of τ_m delays*

	RT	310 K	320 K	340 K
Signal 1	461 ms	457 ms	464 ms	471 ms
Signal 2	296 ms	304 ms	315 ms	315 ms
Signal 3	222 ms	193 ms	215 ms	225 ms

Table II-7 *: T1 relaxation times determined after the fit of the curve showed in* ***Figure II-19*** *for the different temperatures and for the signal 1, 2 and 3.*

The T1 values are almost constant whatever the considering temperature for each site. Moreover, the small differences between some values are probably due to the low resolution between the different signals on the NMR spectra. Therefore, it is difficult to the define the range of each signal and to process a proper integration.

4.4.2 Selective Inversion

Selective inversion consists of a succession of two pulses separated by the mixing time, 180°- τ_{mix}-90°. The 180° pulse is a soft power Gaussian shaped pulse with a longer length than the usual pulses[67] (**Figure II-20**). A range of mixing times is also used to allow different chemical exchange times.

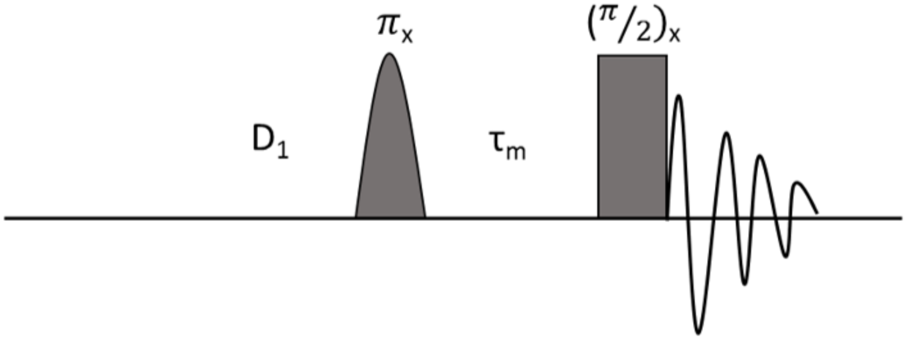

Figure II-20 *: Selective Inversion pulse sequence*

The advantage of this technique is the fact that many data points are collected, compared to other 2D NMR techniques, and therefore, it allows to model efficiently the relaxation of the magnetization back to equilibrium. Selective inversion is also a good technique in order to calculate the rate constants of different signals if an ionic mobility is observed[67]. By processing at different temperatures, the activation energies can be determined. This technique proposes to initially invert selectively one Li signal using the Gaussian shaped soft pulse. The mixing time allows then the magnetization to return to equilibrium. During the different mixing times (and the T1 relaxation), chemical exchanges between the inverted and the non-inverted Li signals are possible if the Li^+ ions are able to hop from one site to another. The consequence on the NMR spectra is a buildup of the magnetization due to the chemical exchanges and the T1 relaxation for the inverted signal. For the non-inverted signals, an attenuation of their intensities characterizes an ionic mobility in the structure due to the chemical exchange with the inverted signal. If no attenuation is observed, that means that no chemical exchange occurs during the probed timescale.

Only the sample B was analyzed with this technique. For the selective inversion ^{7}Li MAS NMR experiments, a probe for 1.3 mm-diameter zirconia rotors (spinning frequency = 65 kHz) was used. The 180° pulse was a soft power Gaussian shaped pulse (40 dB) with a length of 900 µs in order to invert the selected signal. The measurements were performed at RT, 310 K, 320 K and 340 K on the three signals 1, 2 and 3. The signal 5 was neglected again because of its low magnitude and the signal 4 was not really affected by the change of mixing time. The mixing time list was the following: 0.05 µs, 10 ms, 50 ms, 100 ms, 200 ms, 250 ms, 300 ms, 350 ms, 400 ms, 500 ms, 750 ms, 1 s, 4 s and 6 s (16 values).

The **Figure II-21** shows the ^{7}Li MAS NMR spectra resulting from the selective inversion acquisition and with increasing mixing times recorded on the sample B at 340 K. The signal 2 shows a slight modification of its peak intensity with the mixing time evolution. That could be due to a weak chemical exchange between the two sites but it is more likely that the weak separation between the probed signal and the signal 2 is in charge of the attenuation of the signal 2. Therefore, no correlation between the different sites can be clearly evidenced by MAS NMR which allows to conclude on the absence of dynamics concerning the Li^+ ions in the Li interslab spaces. The consequence is the presence of full or almost full Li layers in the OP4-(Li/Na)CoO_2 phase. By probing the other signals, no dynamics involving hopping rates higher than the frequency gap between signals (typically ~1500 Hz) is observed. This result is the same whatever the temperature in the RT – 330 K range.

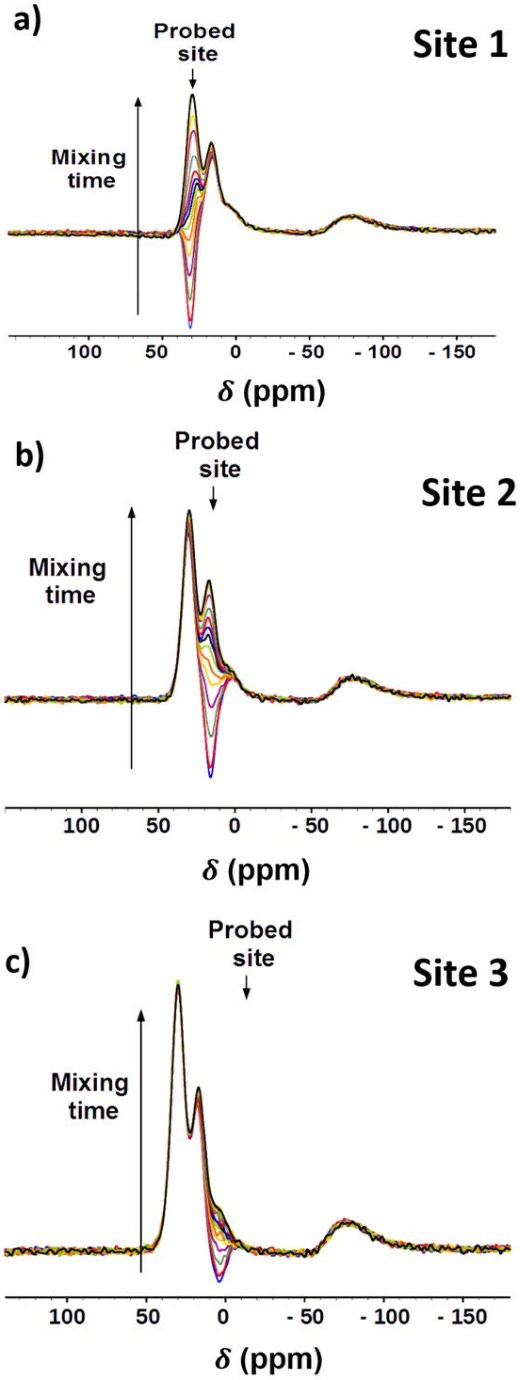

Figure II-21 : *Experimental ^{7}Li MAS NMR spectra of the sample B performed with the selective inversion technique at 340 K with mixing times from 0.05 ms to 6 s. The acquisitions were realized on a 7.05 T magnet with a spinning frequency of 65 kHz. (a) The signal 1 was selectively inverted. (b) The signal 2 was selectively inverted. (c) The signal 3 was selectively inverted.*

5. Na$^+$ ions in Li interslab spaces

As NMR shows full Li interslab spaces and stacking fault simulations discredit the hypothesis of plenty of successive Na layers in the material[43] in order to explain the chemical formula of the OP4 phase, it becomes difficult to explain the difference between the expected ($Li_{0.5}Na_{0.35}CoO_2$) and the experimental ($Li_{0.42}Na_{0.38}CoO_2$) chemical formula for the OP4 pure phase. Another idea to explain the gap between the formulas is to consider Na$^+$ ions intercalated in the Li layers after the thermal treatment. ^{23}Na MAS NMR was performed in order to confirm this hypothesis.

5.1 1D NMR

5.1.1 Magnetic field comparison

^{23}Na MAS NMR was performed on a Bruker Avance spectrometer at 79.4 MHz (7.05 T magnet) and 132.3 MHz (11.75 T magnet). As ^{23}Na is a strong quadrupolar nucleus with $I = 3/2$, a short pulse length of 1 µs corresponding to a $\pi/8$ pulse determined using an aqueous 1 M NaCl solution was employed. In these conditions, the main signal observed is due to the $-½ \rightarrow +½$ central transition. The spectral width was set to 1 MHz, and the recycle time $D_0 = 0.5$ s, is long enough to avoid T_1 saturation effects. Using a 7.05 T magnetic field increases, a second order quadrupolar broadening of the signal at 203 ppm is observed and preventing the resolution of the different signals. Nevertheless, under a 11.75 T magnetic field a second order quadrupolar lineshape is still observed for all the lines but allow the resolution of the Na signal in the structure.

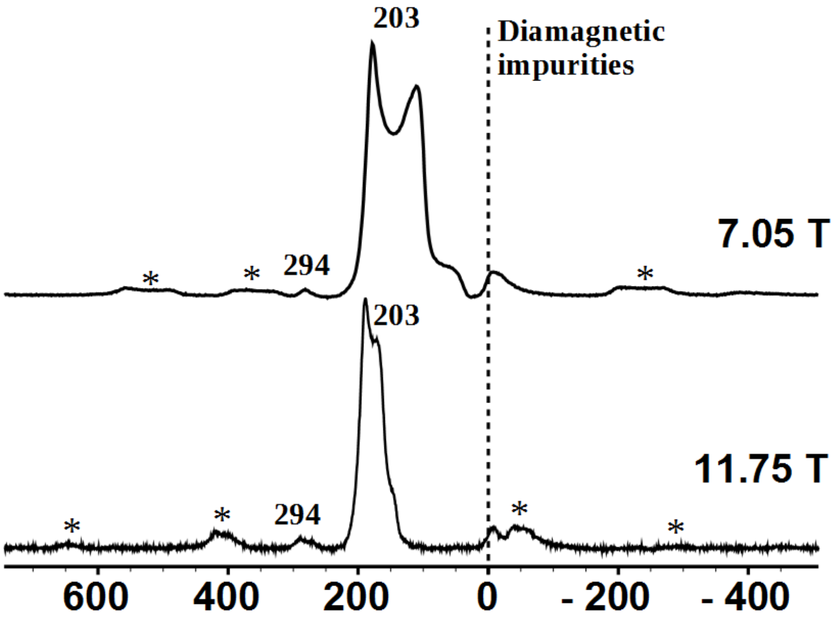

Figure II-22: *Comparison of the ^{23}Na MAS NMR spectra recorded of the sample A for two different magnetic fields (7.05 T and 11.75 T). The spinning frequency was 30 kHz and the sequence was a single pulse.*

5.1.2 Comparison of the samples

Figure II-23a shows the ^{23}Na MAS NMR spectra recorded on the three (Li,Na)CoO_2 compounds under a 11.75 T magnetic field. **Figure II-23b** shows the presence of two signals which can be further fitted using a 2nd quadrupolar lineshape (**Figure II-23b and Table II-8**). Here, the fitted parameters are the signals positions, intensities but also the quadrupolar-coupling constant and the asymmetry of the electric field gradient tensor.

In the sample A spectrum, only two signals are observed around 300 and 200 ppm and are assigned to the central transition of two different Na environments. As the XRD pattern of sample A (**Figure II-4**) doesn't exhibit any Na impurity, we can assign the signals 1 and 2 to environments in the OP4 structure. The samples B and C exhibit the same both signals, but also one additional located around 360-380 ppm. Their positions are in good agreement with the NMR shift of $Na_{\sim 0.7}CoO_2$[94] and can be assigned to Na^+ in environments similar to the P2 phase (P2 and OPP9 impurities). **Table II-8** shows that the major signal is the one labelled 2 on **Figure II-23b.** This signal corresponds to the average signal for the Na^+ ions in the Na_e and Na_f sites in the Na interslab spaces. Therefore, we can confirm that the presence of Na^+ ions in the Li layers are at the origin of this signal 1. The Co-O-Na distance in that case should be shorter, making the hyperfine interaction larger[44]. The presence of Na^+ ions in Li layers will be discussed again with the Rietveld refinement performed on SXRD data.

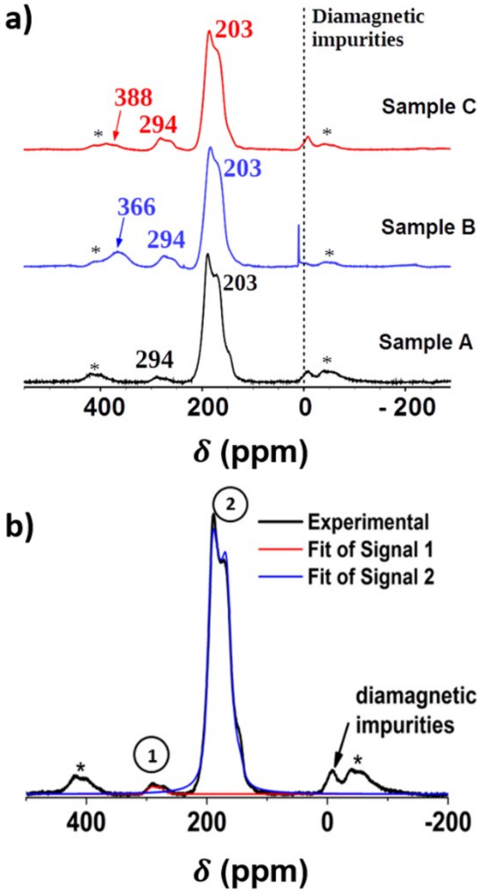

***Figure II-23** : (a) Experimental ^{23}Na MAS NMR spectrum of the three studied samples with performed on a 11.75 T magnet at a spinning frequency of 30 kHz. (b) Fits of the signals 1 and 2 recorded by NMR on sample A compared to the experimental spectrum. * represents the spinning side bands*

	Signal 1 (294 ppm)	Signal 2 (203 ppm)
Sample C	8	92
Sample B	7	93
Sample A	2	98

***Table II-8:** Repartition of the areas of the two signals highlighted on the ^{23}Na MAS NMR spectra for Na^+ ions for the three studied samples. The signals around 370 ppm on the samples B and C spectra are not considered because they are due to Na impurities.*

5.1.3 ^{23}Na Mas NMR Variable Temperature measurements (VT)

^{23}Na MAS NMR VT was also performed with a spinning frequency of 13 kHz for temperatures between 265 and 450 K (**Figure II-24).** Note that using a 13 kHz spinning frequency and a 7.05 T magnetic field, the resolution was not sufficient to follow the change for the signal 1. The temperature increase results in a sharpening of the signal 2 that exhibits at 450 K a well-defined 2nd order line shape as would exhibit a ^{23}Na nucleus in a unique site with an axial symmetry of the electric field gradient (EFG). This signal modification can be interpreted by i) an increase of the Na^+ ions dynamics in the interslab spaces that is not fully achieved at room temperature compared to the NMR timescale and ii) a decrease of the dipolar part of the nuclear –electron spin coupling as also observed for the P2-Na_xCoO_2[94]. A decrease of the shift values is also observed for the increasing temperature as expected for paramagnetic shifts. However, in the case of ^{23}Na MAS NMR, contrary to ^{7}Li, one cannot neglect the quadrupolar shift contribution to the total shift in addition to the Fermi contact and the Knight shifts. The analysis of the isotropic shift position versus the temperature is therefore more complex than for ^{7}Li.

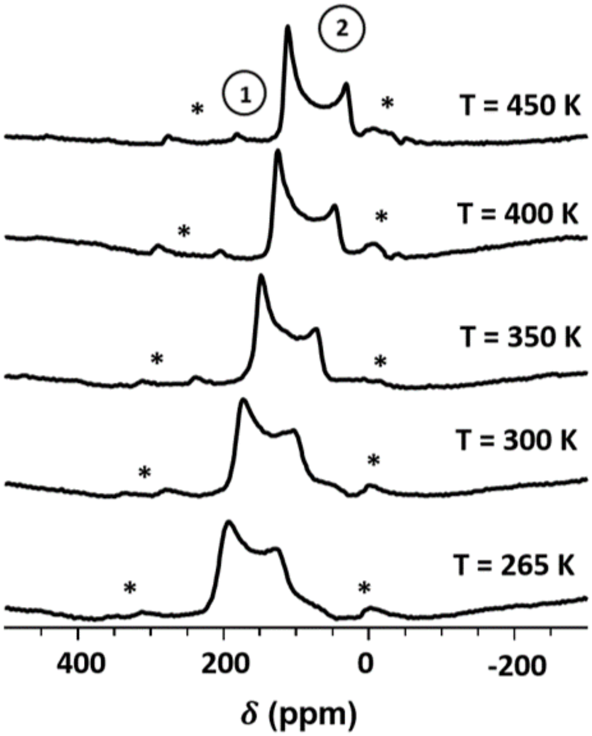

Figure II-24 : VT-^{23}Na MAS NMR recorded on a 7.05 T magnet at a spinning frequency of 13 kHz in the 265 K < T < 450K range. * are the spinning side bands.

5.2 Determination of the composition by Rietveld refinement

High angular resolution synchrotron powder X-ray diffraction (SXRD) experiments were performed on the BL04-MSPD beamline of the ALBA Synchrotron (Cerdanyola del Vallès, Spain) for only the sample A where the targeted composition was $Li_{0.44}Na_{0.38}CoO_2$ (**Table II-2**). Our ^{23}Na MAS NMR study indicates that some Na^+ ions might be located in the Li layer in the OP4 phase. Such a possibility was therefore further considered in the structural model used for the Rietveld refinement of the structure of the sample A using the SXRD data. A good agreement between the calculated pattern and the experimental one could be thus achieved (**Figure II-25)**. The resulting fitted parameters are given in **Table II-9.** Note that the refinement allows to determine that the sample A is composed of 3 % of $LiCoO_2$ and 97 % of OP4 phase. A slight peak asymmetry confirms the presence of a low amount of stacking faults in the structure. For the refinement, we fixed the Co and O sites to be fully occupied. The occupancy of Li sites was also fixed at 0.42 by considering that 97 % of the refined powder is composed of the OP4 phase. The B_{iso} values of the alkali ions were also fixed. Therefore, only the z position of the oxygen ions, the B_{iso} values of the Co and O ions and the occupancy of the Na sites were refined considering the possibility of having Na^+ ions in the Li layers. As a results, we found 0.10(1) Na^+ in addition to the 0.84 Li^+ ions in the O-type interslab spaces involving a global occupation of ~ 95 % in agreement with the absence of observed lithium mobility by selective inversion. The P-type interslab spaces have more vacancies, since they are filled at 64(1) % by Na^+ ions, in agreement with the mobility of Na^+ ions observed by 1D MAS NMR. The resulting chemical formula is OP4-$Li_{0.42}Na_{0.37}CoO_2$ in good agreement with the literature (**Table II-1**) but can be more specifically written as OP4-$[Li_{0.42}Na_{0.05}]Na_{0.32}CoO_2$. The calculated distances are shown in **Figure II-26**. The Co-O_{Li}-Na distance for the Na^+ ions in the O-type interslab spaces is shorter than the Co-O_{Na}-Na distance for Na^+ ions in the P-type interslab spaces, leading to a stronger hyperfine interaction and thus confirming the signal 1 assignment.

	Space group : $P6_3/mmc$					
	$a_{hex.}$ = 2.826(1) Å			$c_{hex.}$ = 20.298(3) Å		
Atom	**Site**	**x**	**y**	**z**	**B (Å²)**	**Occ.**
Co	4f	2/3	1/3	0.3836(2)	0.64(1)	1
Na_f	2d	2/3	1/3	0.25	1.2	0.21(1)
Na_e	2c	1/3	2/3	0.25	1.2	0.43(1)
Li	2a	0	0	0.5	0.9	0.84
Na (Li layer)	2a	0	0	0.5	0.9	0.10(1)
O_{Na}	4e	0	0	0.3363(7)	0.79(1)	1
O_{Li}	4f	1/3	2/3	0.4248(7)	0.42(1)	1
	Rp = 14.1 % Rwp = 15 %			U = 0.0109(5) V = -0.0066(5) W = 0.0005(5) X = 0.10(1) Y = 0.0091(2)		

Table II-9: *Calculated parameters, atomic positions and atomic occupancies obtained for the refined SXRD data performed on the sample A (SXRD pattern on **Figure II-25**) with the $P6_3/mmc$ space group. O_{Na} represent the O ions between a Na layers and Co layers while O_{Li} are the O ions between a Li layers and a Co layers.*

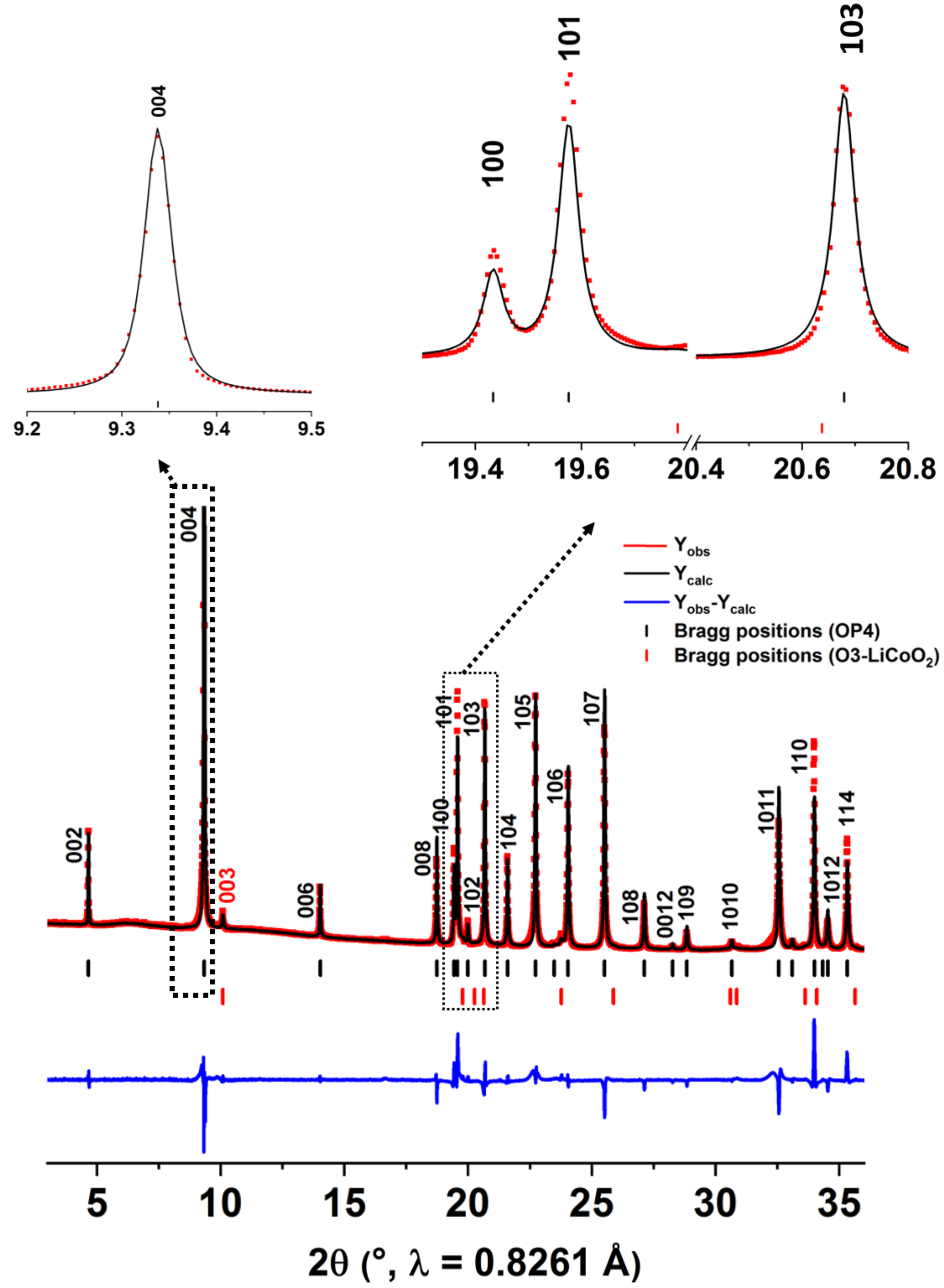

Figure II-25: *Synchrotron XRD pattern as a function of 2θ position of the sample A with λ = 0.8261 Å. Red bars and black bars correspond, respectively, to the Bragg positions of O3-LiCoO$_2$ and OP4-(Li/Na)CoO$_2$. Red points correspond to experimental XRD pattern while black line is the calculated one obtained by Rietveld refinement. The blue line is the difference between the experimental and the calculated lines.*

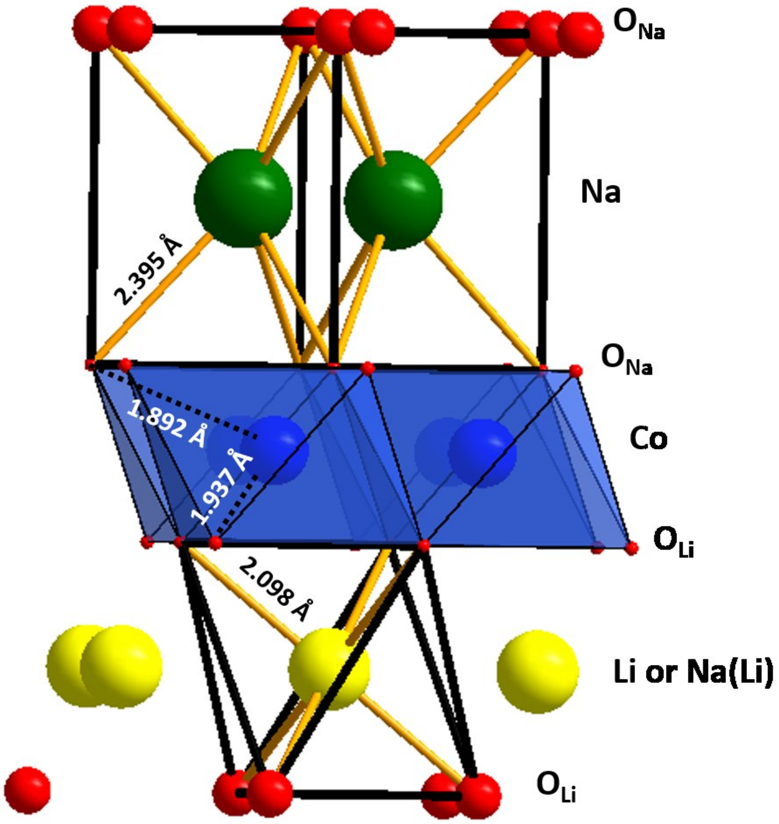

***Figure II-26**: Bonds distances calculated after Rietveld refinement of OP4 phase.*

6. Conclusion

The objective of this chapter was to reinvestigate the complex structure of the OP4-$(Li,Na)CoO_2$ phase in order to understand some unclear points and especially the gap between the theoretical, $Li_{0.5}Na_{0.35}CoO_2$ chemical formula and the experimental one, $Li_{\sim 0.4}Na_{\sim 0.4}CoO_2$ obtained in many papers. The presence of a low amount of stacking faults can’t explain the important gap between both chemical formulas and suggests that its origin concerns more a deficit of Li^+ ions than an excess of Na^+ ions in the structure. In this aim, three samples with controlled amount of impurities were synthetized in order to investigate their average structure by XRD and their local and electronic structure by ^7Li and ^{23}Na MAS NMR. The three samples showed five different environments for the Li^+ ions but DFT calculations were not able to assign properly each signal because of the dual behavior of the OP4 phase with the presence of localized and delocalized electrons. Selective inversion technique was performed and highlighted the absence of Li^+ ions mobility allowing to confirm that the Li interslab spaces are almost full.

Finally, ^{23}Na MAS NMR highlighted the presence of two environments for the Na^+ ions in the OP4 structure: (1) a major signal for Na^+ in prismatic sites in the Na interslab spaces (2) a minor signal for Na^+ in octahedral sites in the Li interslab spaces. The presence of Na^+ ions allows to fill almost the whole Li interslab spaces explaining why there is no mobility of the Li^+ ions in the structure. A Rietveld refinement on SXRD data allowed, finally, to determine the OP4-$[Li_{0.42}Na_{0.05}]Na_{0.32}CoO_2$ chemical formula for the pure OP4 phase.

Chapter III: Structural and dynamics investigation of O4-$LiCoO_2$

1. The different $LiCoO_2$ polytypes

Among the different polytypes of $LiCoO_2$, O3-$LiCoO_2$ is the most famous one because it can be easily synthetized by a solid-sate route and exhibits good electrochemical performances firstly investigated by Goodenough and coworkers[95].

The O2 polymorph was reported for the first time by Delmas *et al*. in 1981[96]. They synthetized the phase by a Na^+/Li^+ ion-exchange from the P2-$Na_{0.7}CoO_2$ phase. During the exchange, one CoO_2 over two slides to generate octahedral sites in the interslab spaces[97,98] **(Figure III-1**). The O2-$LiCoO_2$ polytype is characterized by LiO_6 octahedra sharing edges with three adjacent CoO_6 octahedra of one CoO_2 slab and an adjacent face with a CoO_6 octahedra of the opposite CoO_2 slab. The oxygen stacking is AB-CB and the phase crystallizes in the *P6₃mc* space group. The thickness of one CoO_2 and one LiO_2 slabs is slightly higher than for O3-$LiCoO_2$ because the Li^+-Co^{3+} repulsions are stronger in the O2 stacking due to the sharing of one face (in O3 structure, LiO_6 octahedra only share edges with the surrounding CoO_6). Delmas *et al.*[96] showed that the O2 stacking is metastable, in fact, the structure reorganizes itself irreversibly into the O3 structure when heated. The O2 structure was also studied by ^{7}Li MAS NMR where only a diamagnetic signal is observed[99]. This point confirms that the interslab spaces are fully occupied by Li^+ ions after the exchange and only surrounded by diamagnetic Co^{3+} in a similar case than O3-$LiCoO_2$[90,91].

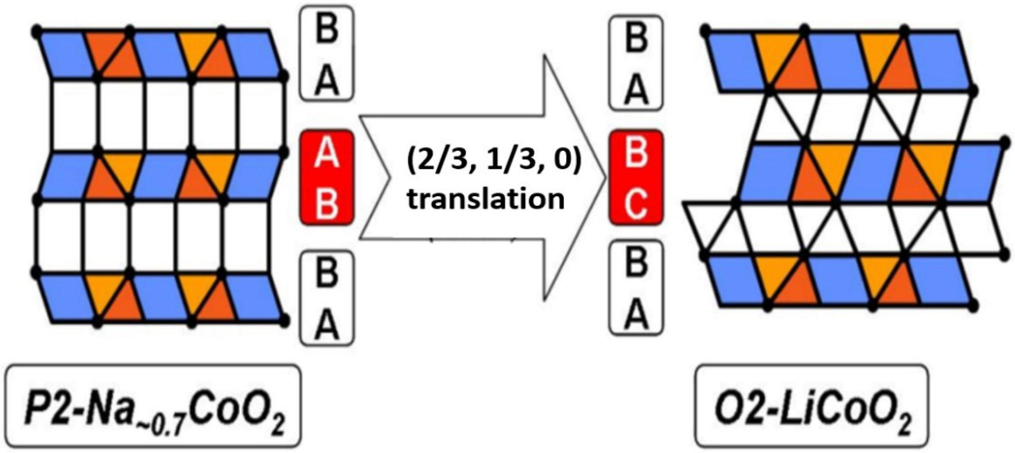

Figure III-1 *: Representation of the CoO_2 gliding to generate octahedra sites and form the O2 polytype. From* [43]

Concerning the O4 polytype, few publications report the synthesis of the O4-$LiCoO_2$ material[42,83,100]. As the OP4-(Li/Na)CoO_2 phase proposes a good alternation of P2-type and O3-type layers, we expected, therefore, that a Na^+/Li^+ ion-exchange leads to an O4-$LiCoO_2$ with an perfect alternation of O3-type and O2-type layers by considering only glidings of the P2 layers to O2 layers with the (2/3, 1/3, 0) translation, as shown on **Figure III-2**.

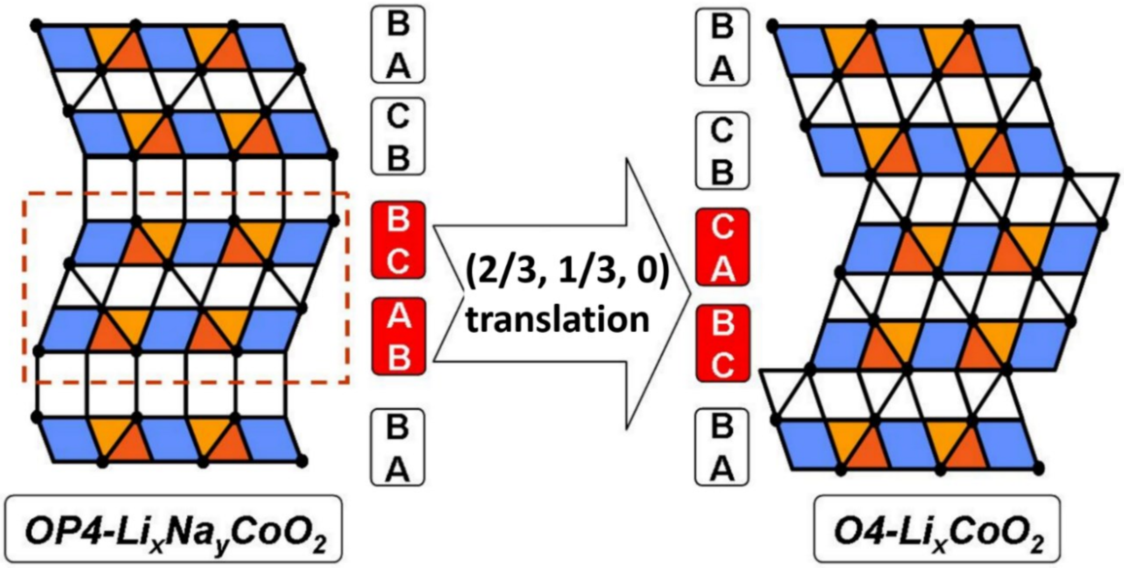

Figure III-2: *Representation of one layer gliding allowing the formation of the O4 phase from the OP4 one. From* [43]

Two ion-exchange techniques are reported in the literature:

(1) Komaba *et al.*[100] proposed an ion-exchange in an aqueous solution of LiOH and LiCl as described previously by Paulsen *et al.* for the O2-$LiCoO_2$ synthesis[101]. The OP4 powder is directly inserted in a Li^+ ion solution under agitation and heated under reflux. At the end of the reflux, the powder is washed for many hours with distilled water and dried.

(2) Berthelot *et al.*[42] proposed an ion-exchange with melted salts $LiNO_3$ in excess and KNO_3. The mixture is heated at 150 °C and washed many times to remove potential traces of

nitrate. This way of synthesis was similar to this used previously by Delmas *et al.*[96] to stabilize the O2-$LiCoO_2$ structure from P2-$Na_{0.7}CoO_2$.

The ideal O4 stacking is composed of a 1:1 alternation of O2-type and O3-type slabs (**Figure III-3)**. The structure crystallizes in the *P6₃mc* space group with lattice parameters $a_{hex.}$ ~ 2.8 Å and $c_{hex.}$ ~ 18.8 Å, two positions for the Co ions, two positions for the Li^+ ions and four positions for the O ions[42,83,100]. Note that in a previous study in the group, simulations showed that the formation of stacking faults during the ion-exchange involves the broadening of the (00l) and (hk0) peaks on the XRD patterns.

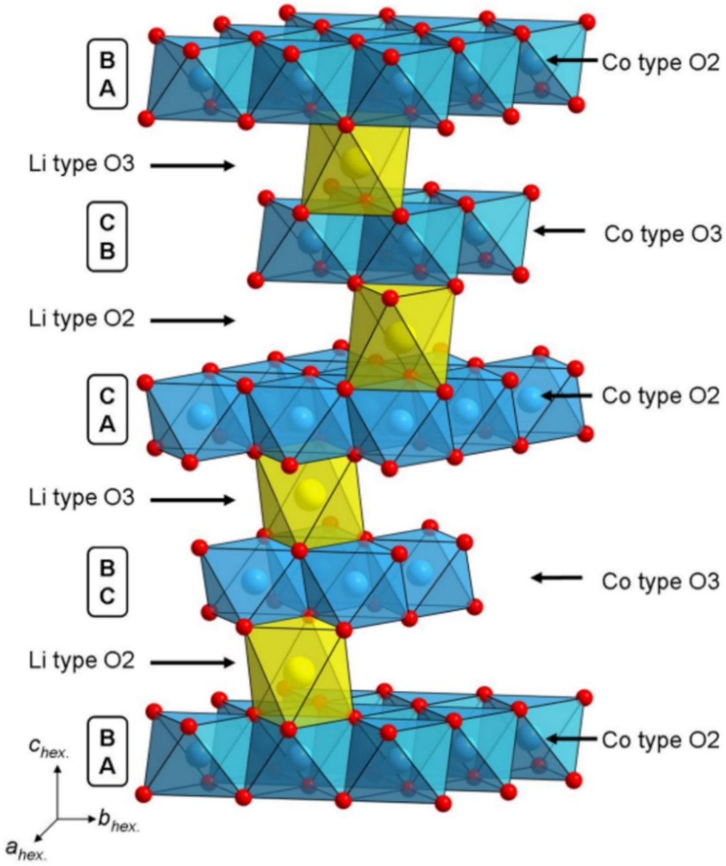

Figure III-3 : Representation of the O4-$LiCoO_2$ structure. From reference [43].

By using the ICP-AES technique to determine the chemical compositions of the synthetized phase, Berthelot *et al.*[42] suggested the presence of 0.8 Li^+ ions, Komaba *et al.*[100] showed the presence of 0.85 Li^+ ions in O4 structure and Yabuuchi *et al.*[83] determined 0.9 Li^+ ions with a negligible amount of remaining Na^+ ions from the OP4 phase in the O4-$LiCoO_2$ phase. Therefore, the Li interslab spaces are not completely filled and it is important to keep in mind that the alkali ions amount in the structure strongly depends of the exchange conditions.

Note that O*n*-Li_xCoO_2 (x < 1) phases with different stacking were also reported. The O1 stacking is obtained for structures largely deintercalated labelled $Li_{\varepsilon}CoO_2$ from O3-$LiCoO_2$[2,102]. An O6 polytype was introduced by Mendiboure *et al.*[103]. It is formed during the O2-Li_xCoO_2 Li^+ deintercalation[103,104]. Another polytype was reported by Paulsen *et al.*[101]. Thereafter, this stacking was labelled $T^{\#}2$[51,105] and its structure is derived from the O2 stacking which undergoes layers glidings along a (1/3, 1/6, 0) vector. This stacking is obtained for x values between 0.52 and 0.72 during Li^+ deintercalation from O2-Li_xCoO_2. The aim of this chapter is to obtain new information concerning the average structure and the local structure of the O4-$LiCoO_2$ phase. For this study, solid state NMR was used on two different samples prepared in two different ion-exchange conditions in order to isotopically mark the Li^+ ions in the different layers using ^6Li and ^7Li ions (**Figure III-4**). Again, the Li^+ ions mobility was tested on both samples after observing many signals by 1D NMR. ^{23}Na MAS NMR and ICP-OES were performed in order to confirm or not the presence of remaining Na^+ ions in the structure.

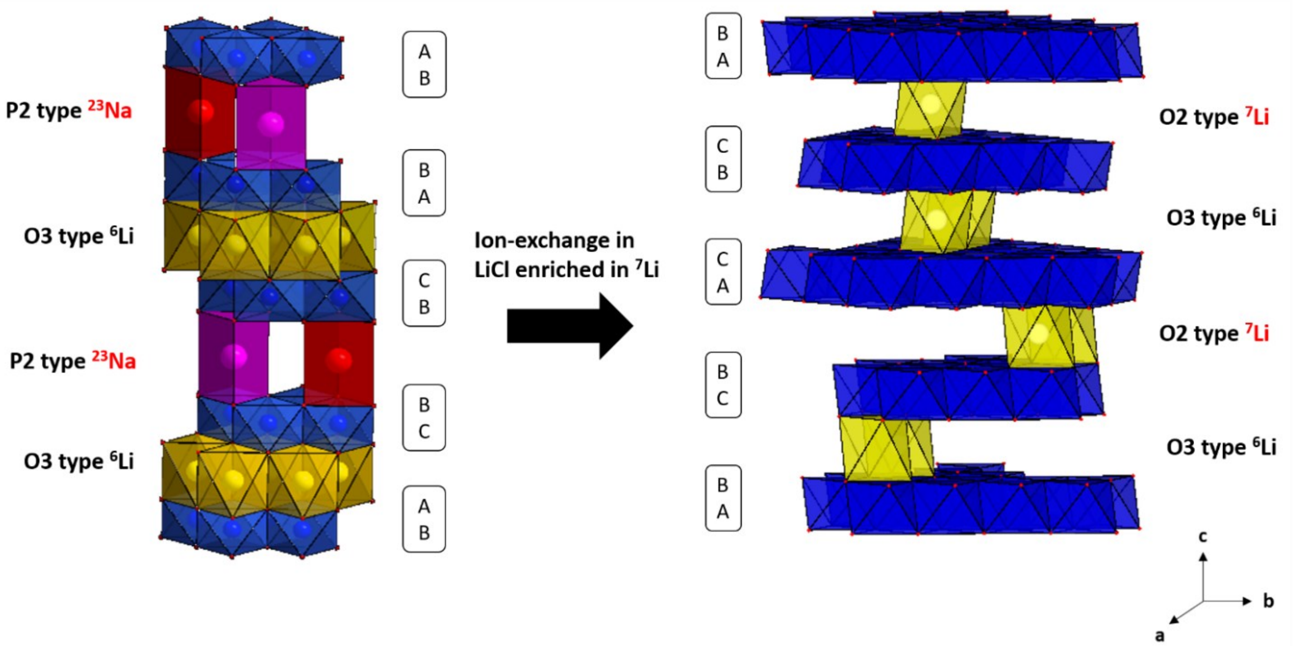

Figure III-4: *Representation of the expected O4 structure after ion-exchange from the OP4 phase enriched with ^6Li ions*

2. Synthesis conditions

Before realizing the ion-exchange, an OP4-(Li, Na)CoO_2 phase was synthetized enriched with ^{6}Li. The synthesis conditions were the same than those described in the chapter II except the use of Li_2CO_3 enriched in ^{6}Li instead of traditional Li_2CO_3.

We choose to synthetize two different O4 phases by ion-exchange with the "in solution" technique. Both syntheses were realized in a 1M LiCl solution and the synthesis conditions are summarized in **Table III-1.** The Li^+/Na^+ ratio corresponds to the molar amount of Li^+ ions in the LiCl solution over the molar amount of Na^+ ions present in the OP4 structure. After the reflux, the powders were cooled, washed in distilled water and filtered under vacuum many times. The powders were finally dried for 12 h at 110 °C. The two synthetized samples are labelled EIE (for Excess Ion-Exchange) and SIE (for Stoichiometric Ion-Exchange) and their synthesis conditions only differ from the use of different Li^+/Na^+ ratio. The expected structure after ion-exchange is represented on **Figure III-4.**

	Temperature	**Reflux duration**	**Li^+/Na^+ ratio**
EIE sample	105 °C	4 h	20
SIE sample	105 °C	4 h	1

Table III-1*: Synthesis conditions of the two O4-$LiCoO_2$ sample (EIE and SIE)*

3. Average structures and chemical compositions characterization

3.1 OP4 enriched with ^{6}Li phase XRD pattern

XRD was performed on the PANalytical X'Pert Pro diffractometer equipped with a Co anticathode from 12° to 90°. The Le Bail method was used to refine the XRD pattern.

The XRD pattern (**Figure III-5**) of the OP4 phase is similar to the patterns introduced in the previous chapter. However, the phase contains a small amount of OPP9 impurity and the cell parameters of the OP4 phase enriched with ^{6}Li ions are a_{hex} = 2.822(1) Å and c_{hex} = 20.26(1) Å in good agreement with the values obtained previously. This phase was, then, used as precursor in order to realize the ion-exchange.

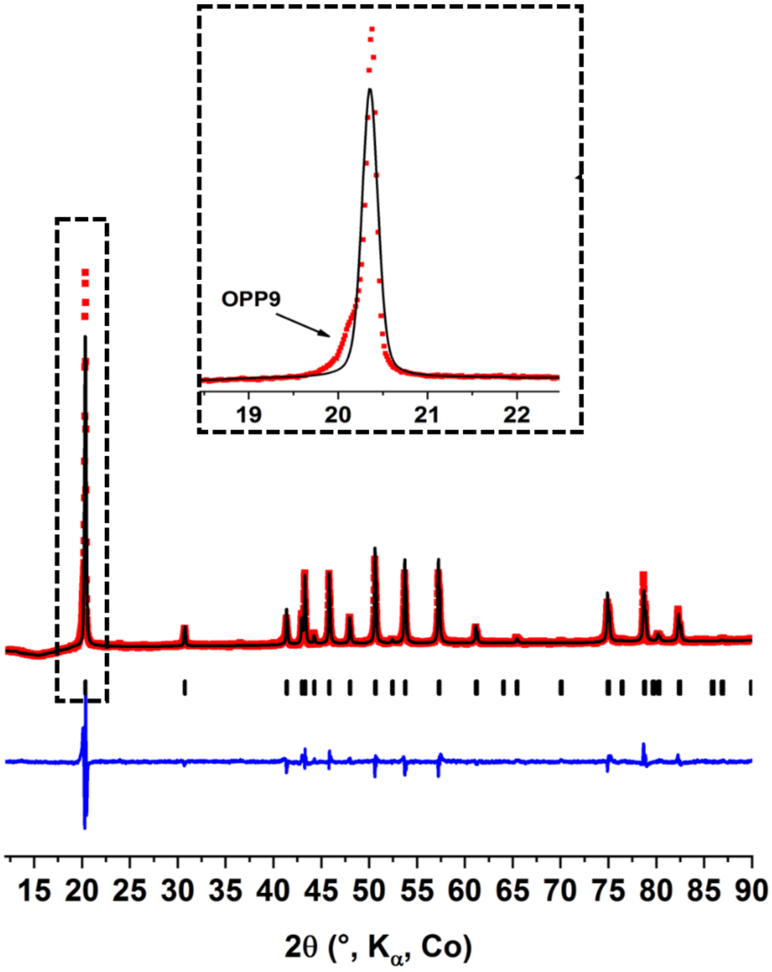

Figure III-5: *Refined XRD pattern of OP4-(^{6}Li/Na)CoO$_2$ phase used for the ion-exchanges.*

3.2 O4 samples average structures

The XRD acquisitions were performed on the PANalytical X'Pert Pro diffractometer equipped with a Co anticathode from 12° to 90°.

A comparison of the EIE sample, SIE sample and the simulated O4-$LiCoO_2$ XRD patterns is shown on **Figure III-6.** The broadening and the large asymmetry of the peaks prevent from refining correctly the patterns that's why we decided to compare the experimental patterns to a theoretical one. In order to check if we synthetized the O4 phase, and not a O2 or O3-$LiCoO_2$ phase, it was necessary to examine the presence of the O4 characteristic diffraction peaks: (103), (105) and (1010) as proposed in the literature[42]. While (103) peak is not intense enough to be observed, we can see the (105) and (1010) peaks on the experimental patterns indicating the synthesis of an O4 phase. Note that the EIE sample XRD pattern exhibits an additional peak highlighted by a red arrow on **Figure III-6.** This peak is assigned to the presence of a small amount of O3-$LiCoO_2$ and can also explained the shape of the (100) peak on the same pattern. By using the positions of the (004) and (100) peaks, an estimation of the lattice parameters was realized considering the hexagonal cell. For both samples, a_{hex} ~ 2.10 Å while c_{hex} is different in the two samples (EIE: c_{hex} ~ 19.2 Å, SIE: c_{hex} ~ 19.7 Å). The broadening of the peaks can be explained by the presence of many stacking faults in the structure created during the ion-exchange and especially during the $LiCo_2O_4$ block gliding from OP4 to O4 represented in **Figure III-2**.

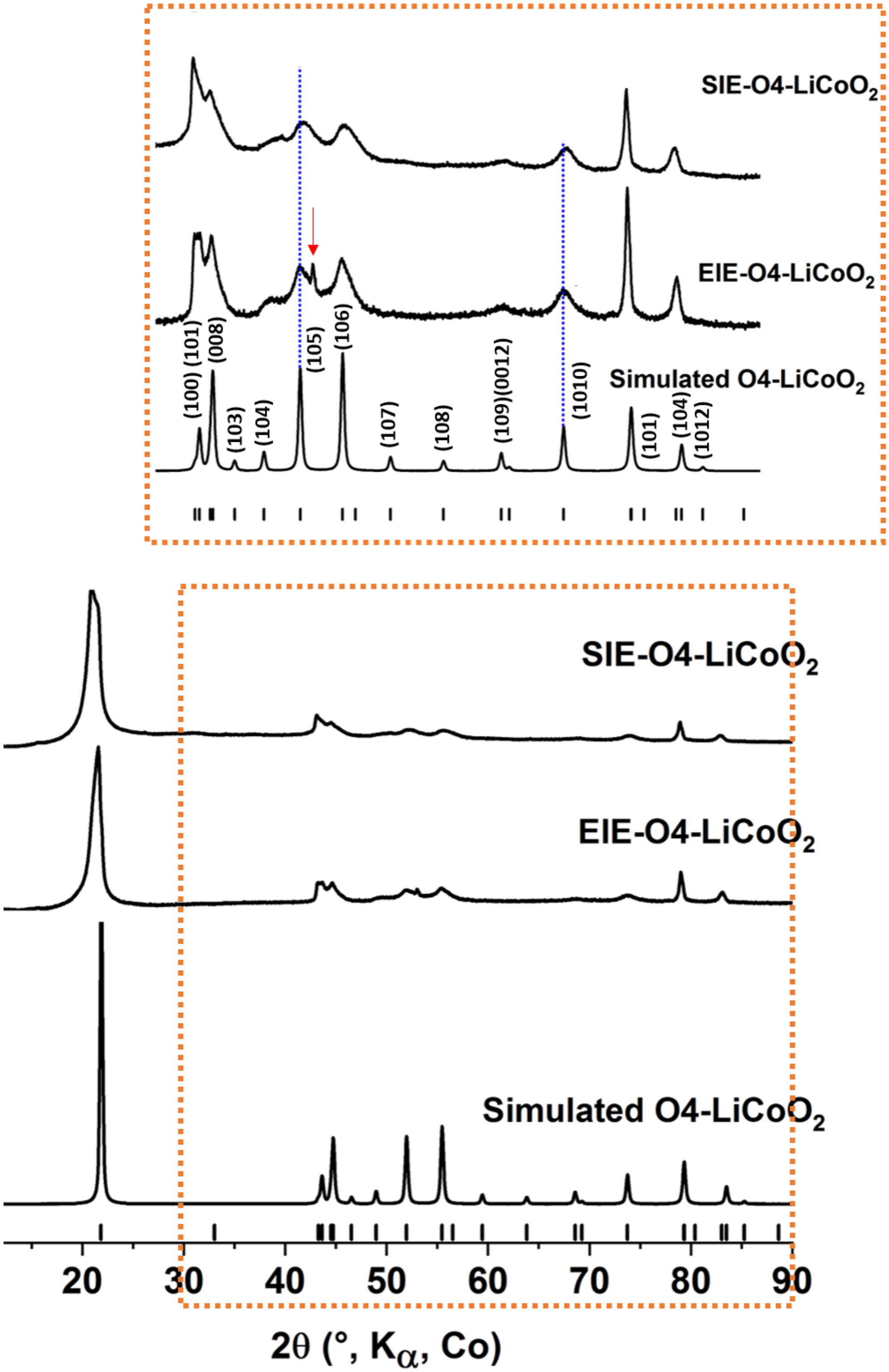

Figure III-6: *Experimental XRD patterns of both samples compared to the theoretical one using Berthelot et al. data*[43]

3.3 Chemical compositions

In order to determine the chemical compositions of both EIE and SIE samples, ICP-OES was performed. The samples were previously solubilized in a HCl/HNO_3 mixture before the measurement. The samples were tested in order to determine the Co and Li^+ ions amount but also the amount of eventual remaining Na^+ ions.

ICP-OES shows different Li/Co ratio for both samples in good agreement with the ion-exchange conditions used to synthetize the two samples. The Li^+ ions compositions are 0.79(4) and 0.68(7) for, respectively, EIE and SIE-O4-$LiCoO_2$ in good agreement with the synthesis conditions of the two samples. However, it is important to note that a small part of the Li^+ ions in the EIE sample can be due to O3-$LiCoO_2$ present as an impurity. Additionally, ICP-OES shows the presence of ~ 0.1(1) Na^+ ions in both samples but it is also to qualify because of the important uncertainty. The presence of Na^+ ions could be explained by the presence of local Na^+ ions which are still intercalated in the structure either in remaining P-type layers or in O-type layers. This point will be discussed later in this manuscript regarding the ^{23}Na MAS NMR spectra. A partial filling of the O4 structure is proposed regarding the ICP results with vacancies in the layers whatever the synthesis conditions in opposition with the synthesis by ion-exchange of the O2 polytype which proposes full Li interslab spaces. Regarding these results, the samples will be relabeled 'O4-Li_xCoO_2' until the end of this chapter.

4. $^{6/7}Li$ and ^{23}Na MAS NMR

4.1 Standard sample

Before showing the NMR spectra of the EIE and SIE samples, we studied a sample without any enrichment in ^6Li. The presence of potential ^6Li ions in this sample is only due to the natural abundance of this isotope (natural abundance ^6Li: 7.6 % vs ^7Li : 92.4 %). It had been synthetized before the beginning of my PhD using an "usual" OP4 phase as precursor and in the same synthesis condition than the EIE sample. This sample is labeled "standard" sample in this work.

Figure III-7 shows the ^{7}Li MAS NMR spectrum of this sample. ^{7}Li MAS NMR was realized on this sample and performed on a 7.05 T magnet with a Hahn Echo sequence. The spectral width was set to 1 MHz, and the recycle time D_0 = 10 s, is long enough to avoid T_1 saturation effects. The NMR spectrum exhibits three signals at -4, +32 and +66 ppm. The presence of such strongly shifted signals denote the presence of Co^{4+} ions. The signal located at -4 ppm could be assigned to diamagnetic domains: Li^+ ions surrounded by LS-Co^{3+} as 1st and 2nd neighbors, although influences by further paramagnetic neighbors as rather broad and not located at -0.4 ppm as observed for Li in O3-$LiCoO_2$ **(Figure III-7**)[91]. The presence of paramagnetic signals confirms the presence of a Li^+ ions amount different from 1 and therefore vacancies in the interslab spaces. For localized LS-Co^{4+} ions with unpaired electron in the t_{2g} orbitals one would have expected positive shift for 90° Co-O-Li interactions and negative shifts for 180° Co-O-Li by analogy with the study of Cr-doped $LiCoO_2$ samples[70]. However here only positive shifts are observed. A hypothesis to explain the presence of both positively shifted paramagnetic signals is the presence of delocalized electrons in the electronic structure of the phase (Knight shift contribution) leading to a “Curie-Weiss metallic” regime with the presence of both localized and delocalized electrons. For instance, Knight shift contributions are reported on the O3-Li_xCoO_2 system for $x < 0.74$[91] and on O2-Li_xCoO_2 for $x < 0.75$[104]. The origin of the different signals needs, however, further investigations.

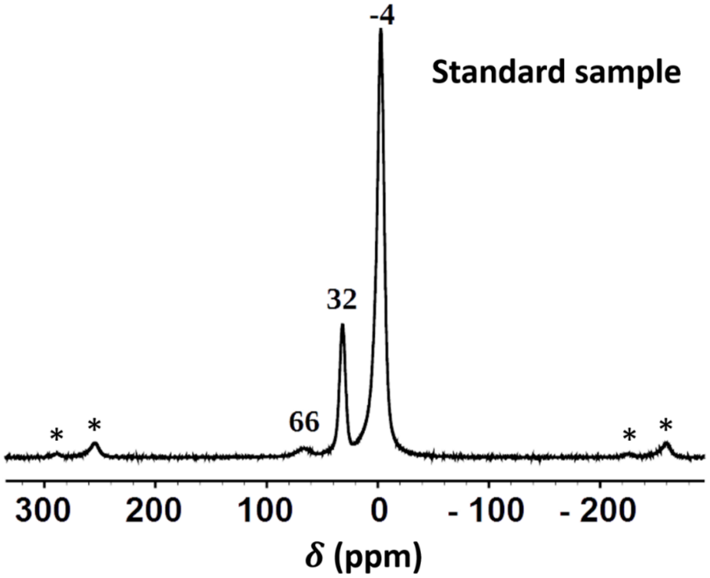

Figure III-7: *Experimental ^{7}Li MAS NMR spectrum obtained with a Hahn Echo sequence of the standard sample on a 7.05 T magnet with a spinning frequency of 30 kHz. * are the spinning side bands.*

4.2 A selective exchange?

^{7}Li and ^{6}Li MAS NMR were performed with the Hahn Echo sequence on the EIE- and SIE-O4-Li_xCoO_2 samples in order to check which Li sites are occupied by ^{6}Li and ^{7}Li ions. The spectral width was set to 1 MHz, and the recycle time $D_0 = 10$ s, is long enough to avoid T_1 saturation effects. The acquisitions were performed on a 7.05 T magnet using a spinning frequency of 30 kHz and with a Hahn echo sequence. **Figure III-8** allows to compare the MAS NMR spectra of the standard sample, the EIE sample and the SIE sample. Note that the spectra were normalized to the number of scans and to the mass of powder in each rotor on **Figure III-8b.** The comparison on the spectra of the standard sample and the EIE sample shows that the exchange isn't selective, in fact, the ^{7}Li and ^{6}Li ions are randomly distributed between the different Li sites. We are, therefore, not in presence of the expected structure proposed on **Figure III-4.** Moreover, the small difference between the shift values in the two samples, SIE and EIE is the consequence of the slight difference in the alkali ions composition regarding the compositions determined by ICP-OES.

Finally, another interesting point is the intensities of the signals depending of the probed Li nucleus and the analyzed sample. The lower intensity of the ^{6}Li signals on the EIE sample spectrum compared to those observed on the SIE sample spectrum suggests that a higher amount of the ^{6}Li ions are removed from the structure during the exchange in the case of the EIE sample. It is possible that an increase of the reflux duration would lead to a removal of the ^{6}Li ions to the amount corresponding to natural abundance. Moreover, the relative intensity between the three signals observed on the ^{7}Li MAS NMR spectra is different. In the case of the EIE sample, the intensity of the -4 ppm signal is relatively low compared to the intensities of this signal recorded on the standard sample and EIE sample. That could indicate that the exchange is not complete for the SIE sample because of the different Li^+/Na^+ ratio used to synthetize this sample. Therefore, it is possible that the Li sites which involve the two paramagnetic signals are the first to be filled during the exchange followed by the O3-$LiCoO_2$-like sites. As both ^{7}Li and ^{6}Li ions occupy the same sites, only dynamic MAS NMR for the ^{7}Li nucleus was performed in McMaster University, Hamilton, Canada.

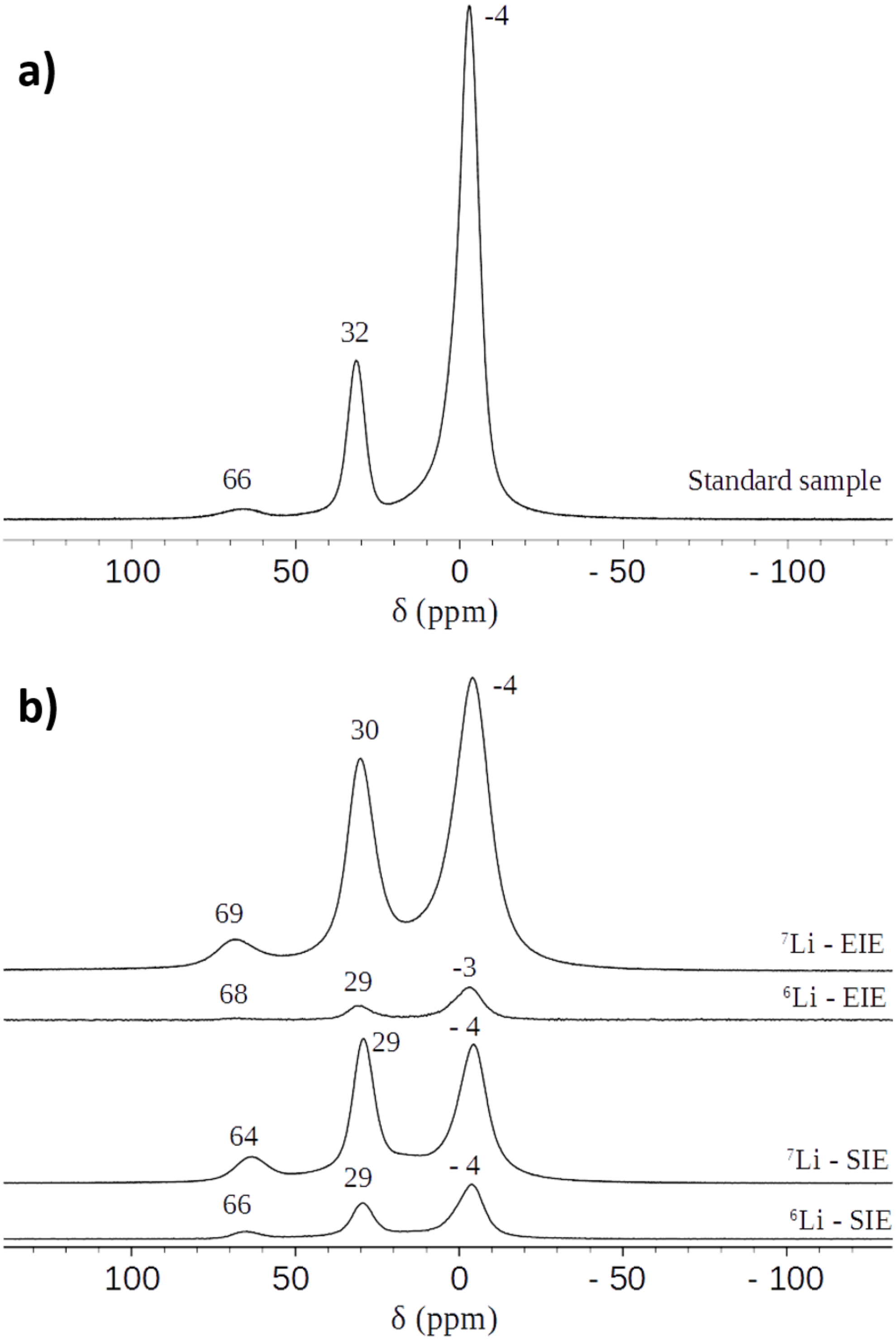

Figure III-8: *(a) Experimental ^{7}Li MAS NMR spectra of the standard sample (b) Experimental ^{7}Li and ^{6}Li MAS NMR spectra of EIE and SIE samples normalized by the number of scans and the mass in the rotor. All the spectra were realized on a 7.05 T magnet with a spinning frequency of 30 kHz.*

4.3 Evidence of Na^+ ions in the structure

ICP-OES introduced a potential presence of remaining Na^+ ions after the ion-exchange. However, due to the important uncertainty concerning the amount of Na^+ ions, it is important to confirm by another technique if some Na^+ ions remains or not in the O4 phases. ^{23}Na MAS NMR was also performed on both samples on a 7.05 T magnet using a simple pulse sequence and with a baseline removal on the software DMFit[65]. The spectral width was set to 1 MHz, and the recycle time $D_0 = 0.5$ s, is long enough to avoid T_1 saturation effects. ^{23}Na MAS NMR spectra (**Figure III-9**) highlight that a certain amount of Na^+ ions remains in the structure after the ion-exchange. Note that more Na^+ ions remain in the phase obtained in the stoichiometric exchange condition than with the Li^+ excess exchange condition as expected. Moreover, two environments can be evidenced by ^{23}Na MAS NMR as two signals at 176 ppm and around 400 ppm are observed. The 176 ppm signal is located at a similar position than the major signal recorded on the OP4 phase before the ion-exchange and could be due to a slight amount of remaining OP4 phase as impurity. The large shift value of the major signal around 400 ppm is not in agreement with Na^+ ions in prismatic sites. The value is more in agreement with local remaining Na^+ ions in octahedral sites and therefore in the O3-type Li interslab spaces. Three times more Na^+ ions remain in SIE sample than in EIE sample but it is still difficult to determine the chemical formulas including the Na^+ ions because of the high uncertainty of the ICP results.

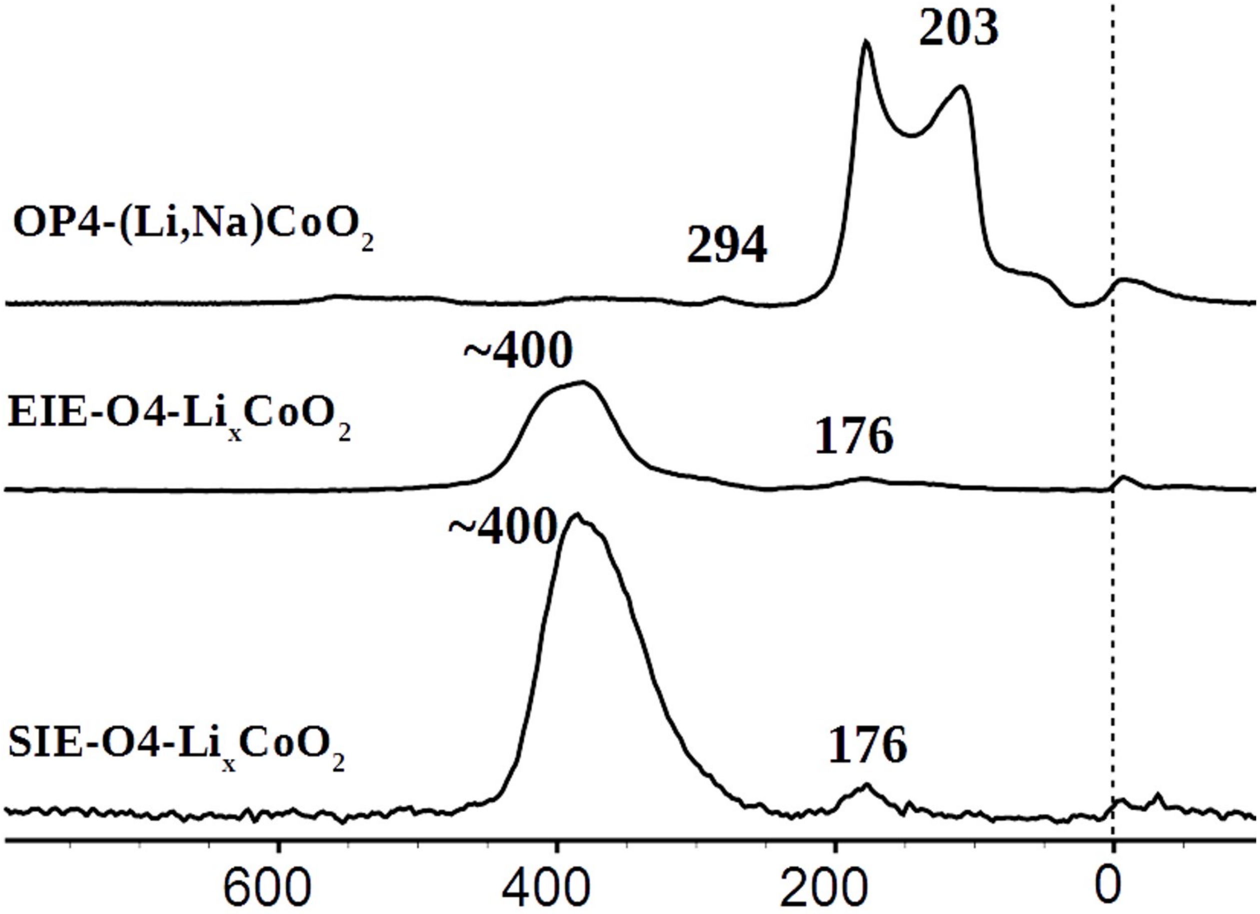

Figure III-9: *Experimental* ^{23}*Na MAS NMR spectra of both O4-phases compared to the OP4 phase. Only the spectra of the O4 materials were normalized to the number of scans and to the mass of powder in the rotor. NMR was performed on 7.05 T magnet with a spinning frequency of 30 kHz.*

5. Li^+ ions mobility in the interslab spaces

As the SIE sample was not synthetized when the measurements were processed in McMaster University, Exchange Spectroscopy (EXSY) and selective inversion were only performed only on the EIE sample on a 4.7 T magnet at 60 kHz. The selective inversion sequence was, then, incremented in Bordeaux and tested on the SIE sample but on a 2.35 T magnet at 30 kHz.

EXSY consists of the succession of three $\pi/2$ pulses separated by two times : t_1 and mixing time. EXSY is, for the 2D measurements, a basic acquisition and its pulse program in presented in the Chapter I (**Figure I-23**). Different mixing times were performed at 340 K: 50 ms, 100 ms and 300 ms on a 7 T magnet. A measurement was also realized at 320 K with a mixing time of 300 ms. Only the sample B was analyzed with this technique. EXSY was tested for many mixing times values from 10 µs to 0.4 s. No cross-peak was evidenced for values to 0.2 s however for 0.3 s, one can distinguish potential cross-peaks between the signals at ~ 30 ppm and -4 ppm (**Figure III-10**). It is however complicated to conclude something about the third signal because of its low intensity. We can't conclude clearly about the Li^+ ions mobility regarding the EXSY experimental results, indeed, it is not obvious if cross-peaks appear really or if it is just background noise.

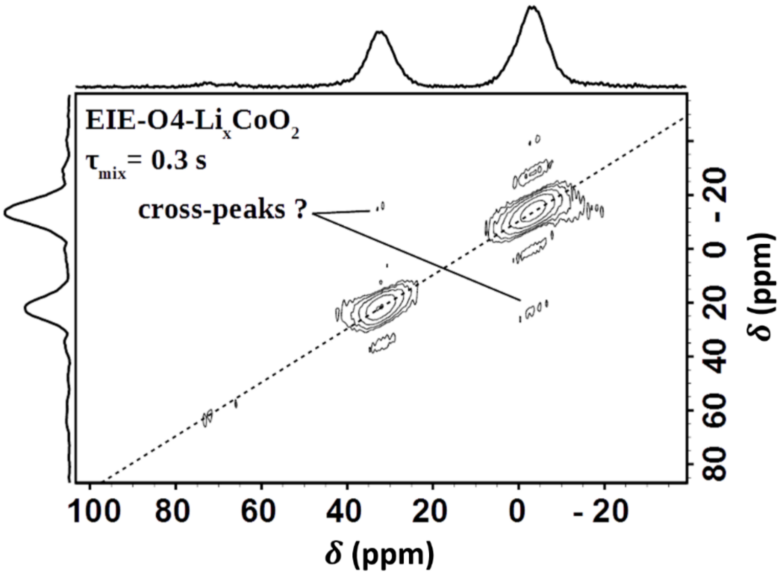

Figure III-10: ^{23}Na MAS NMR spectrum were only performed on sample SIE using an EXSY measurements of EIE at room temperature with a mixing time of 0.3 s (4.7 T magnet, spinning frequency of 60 kHz)

Selective inversion was introduced in the previous chapter and is a complementary technique to EXSY in order to confirm or deny that the cross-peaks are due to a Li$^+$ mobility in the layers. Moreover, the selective inversion measurements were easier to set up for this material as for the OP4 phase because of the higher separation between the signals. Selective inversion was performed for different mixing times from 50 ns to 6 s for each signal only at room temperature as the NMR spectrometer was not outfitted with a VT probe (**Figure III-11**). For the EIE sample, evidence of mobility is only observed on **Figure III-11b** between signals at 30 ppm and -4 ppm. In this case, the signals separation allows to avoid the overlapping of the soft pulse on none-probed sites as it was the case on the OP4 sample. However, the reversible phenomenon can't be observed when we probe the diamagnetic signal (**Figure III-11a**). That can be explained by the different relaxation times needed for diamagnetic signal, preventing spin exchanges with the other sites. **Figure III-11c** highlights that there is no spin exchange between the Li$^+$ ions involving signal at 60 ppm and the other Li$^+$ ions. Considering this point, one can suppose that both signals at 30 ppm and -4 ppm are due to Li$^+$ ions in same layers but in different environments (one paramagnetic and one diamagnetic) while Li$^+$ ions involving signal at 60 ppm are in a minor environment, without any interaction with the other Li sites. As no mobility of the Li$^+$ ions was observed in the OP4 structure contrary to the case of O4, it is possible that the O3 type and O2 type layers are not filled with the same amount of alkaki ions involving mobility for layers with the higher number of vacancies.

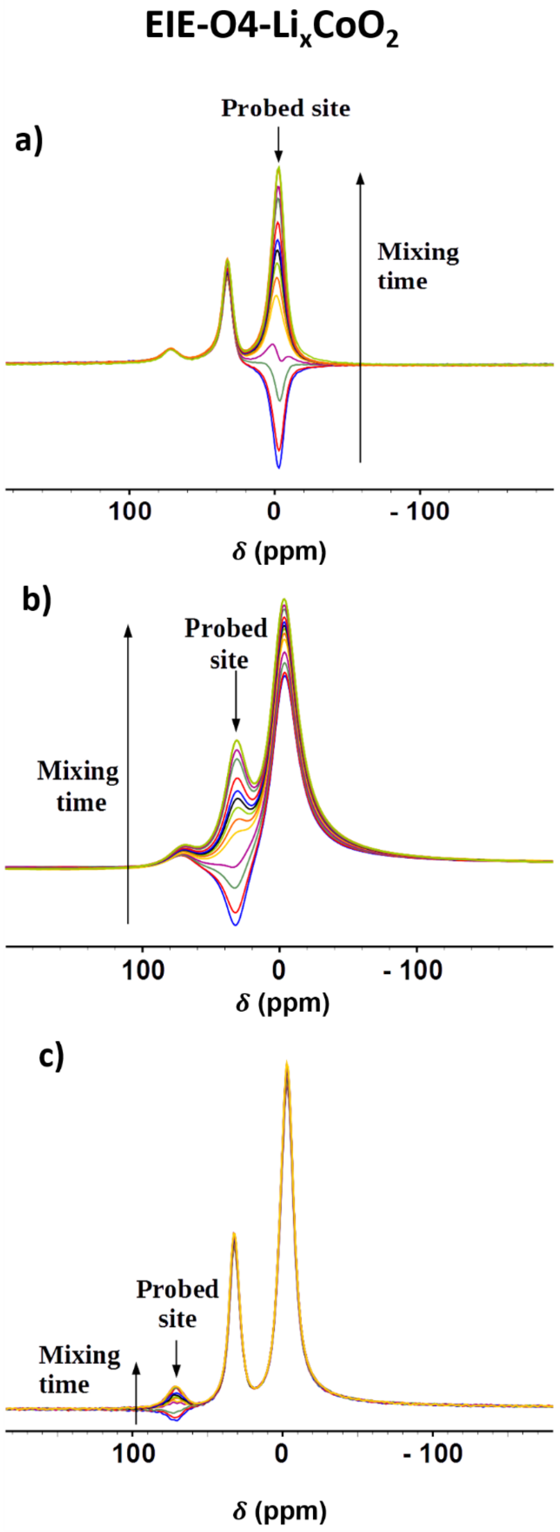

Figure III-11: *Experimental ^{7}Li MAS NMR selective inversion on EIE sample on a 4.7 T with a spinning frequency of 60 kHz. (a) -4 ppm signal is probed (b) 30 ppm site is probed (c) 68 ppm site is probed by the soft pulse*

After analyzing the EIE sample in McMaster University, we tried to implement the selective inversion sequence in Bordeaux on a 2.35 T magnet in order to, for the first time, study dynamics in Bordeaux by solid state NMR and also to study SIE sample synthesized after last journey in McMaster University. However, only selective inversion by probing the site at -4 ppm was realized for the moment (**Figure III-12).** By probing the diamagnetic site, an important build-up of signal at 30 ppm is observed contrarily to the phenomenon observed on the EIE sample (**Figure III-11a)** despite the use of the same mixing time values. Globally, the increase in the Li^+ ions mobility between both sites is characterized by an important build-up of the paramagnetic signal at 32 ppm when the diamagnetic signal is probed. It is the consequence of the weaker filling of the Li interslab spaces in the SIE sample than in the EIE sample according to the chemical compositions measured by ICP-OES, in fact, the interslab spaces are filled between 68 and 78 % (depending of the Na^+ ions real amount) for this sample versus 80 to 90 % for the EIE sample. However, regarding the NMR (1D and dynamics) results, it is still complex to assign each signal to a specific environment in the structure and the O4 structure needs further investigations.

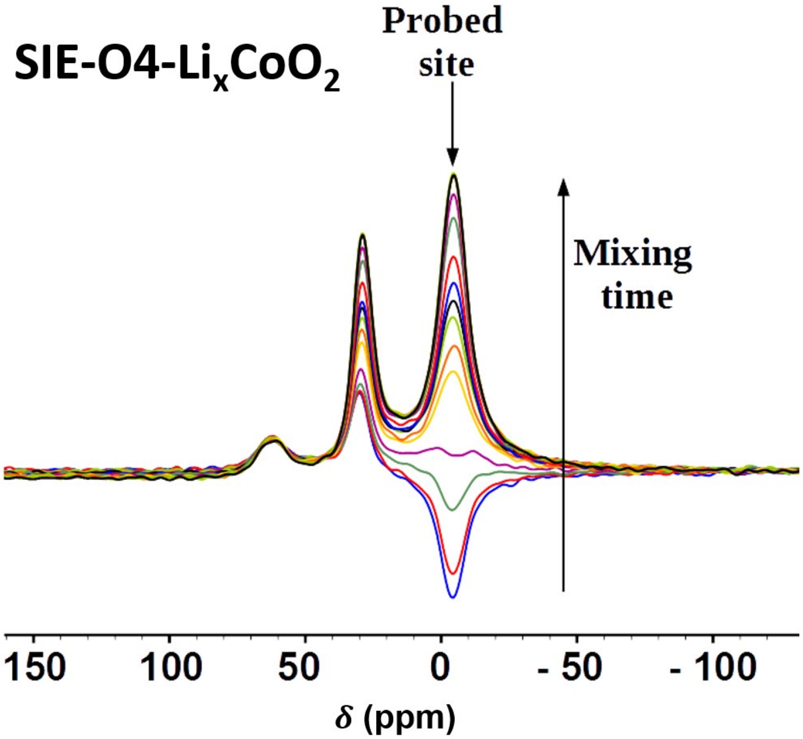

Figure III-12: *Experimental ^7Li MAS NMR selective inversion on a 2.35 T magnet with a spinning frequency of 30 kHz of SIE sample. We only probed the diamagnetic signal with the soft pulse.*

6. Conclusion

The O4 phase was successfully synthesized from OP4 phase with a solution route and proposed different amounts of Li^+ ions following the exchange conditions. It is, however, difficult to synthetize a phase with no stacking faults. During the ion-exchange, all the Li^+ ions are mobile and participate to the exchange as suggested by ^6Li and ^7Li MAS NMR spectra. ICP-OES, 1D NMR and 2D NMR suggest that Li layers are not completely filled and that a Li^+ ions amount limit is reached for longer exchanges. Moreover, Li^+ ions are present in three different sites: a diamagnetic environment, probably surrounded only by Co^{3+} and two paramagnetic environments due to a repartition of Co^{4+} in the CoO_2 layers. Selective inversion shows that two Li sites are in the same layer due to the possibility of Li^+ ions to hop from one site to the other. The origin of the signals is still complex to assign and needs more investigations for example by variable temperature NMR to observe or not delocalized electrons like on the OP4 phase. This point needs to be investigated more largely. Finally, ^{23}Na MAS NMR suggests that Na^+ ions occupy octahedral sites in Li interslab spaces as already observed in the OP4 phase. O4-phase structure and electronic structure are also difficult to understand and peak assignment needs to be investigate more carefully to explain their origin.

Part B:

Layered-Na_xMO_2 as positive electrode for Na-ion batteries

Chapter IV: The P2-$Na_x(Co,Mn)O_2$ phases electrochemical properties and structural evolution during cycling studied by *operando* Synchrotron X-Ray Diffraction

1. Introduction

Na_xCoO_2 was introduced in 1973 and investigated as positive electrode material, for the first time in 1981[1,76,106]. As shown in the general introduction, different polytypes of Na_xCoO_2 pristine phases can be synthetized depending on the Na^+ content and synthesis conditions[7] (**Figure GI-2)**. The investigation of the electrochemical performances of the different Na_xCoO_2 polytypes as positive electrode material for Na batteries highlighted the complexity of the different systems in the 2 V – 3.5 V voltage range[76]. By cycling the P'3, O'3 and O3 polytypes, the systems undergo a succession of structural changes involving for instance Na^+/vacancy ordering at specific Na^+ content highlighted by voltage jumps and drops during the charge and discharge (**Figure IV-1a**). Note that the Na^+ content in **Figure IV-1a** was incorrect. The P2-Na_xCoO_2 cycling curve (**Figure IV-1b**) exhibits also many voltage jumps or drops due to the existence of Na^+/vacancy ordering in the Na interslabs[47]. The phases diagram of the P2 polytype was investigated by *in-situ* XRD, recently by Berthelot *et al*. for $x > 0.6$[47] (**Figure IV-1b**). They monitored the evolution of the (008) diffraction line position which provides an insight of the c_{hex} lattice parameter change during the discharge. That also allowed to describe more precisely the different domains depending on the Na^+ content. The c_{hex} parameter decreases as the Na^+ intercalated amount increases due to the screening effect of the Na^+ ions which limits the O-O repulsions between the successive layers. Note that the a_{hex} lattice parameter slightly increases during the discharge because the Co^{3+} ion radius (0.545 Å) is larger than the Co^{4+} radius (0.53 Å)[3].

Concerning the peculiar phases, Cava and coworkers[107,108] were the first to highlight the superstructure peaks by electronic microscopy for the $x = 1/2$ composition. These particular structures can be, usually, described in a hexagonal or orthorhombic cell but sometimes modulation vectors are necessary to describe incommensurable superstructures. **Table IV-1** summarizes the peculiar phases observed for $x \geq 0.5$, their voltage vs Na^+/Na of formation and their superstructure expressed from the original hexagonal cell (in the *$P6_3/mmc$* space group). The $Na_{1/2}CoO_2$ and $Na_{2/3}CoO_2$ (described by Platova *et al.*[92]) phases and were also stabilized by electrochemical deintercalation by Berthelot *et al.*[47] and characterized by Rietveld refinement on synchrotron XRD data. For $Na_{4/7}CoO_2$, the superstructure was studied by Igarashi *et al.*[109] by neutron and electron diffraction. **Figure IV-2** shows the corresponding Na^+/vacancy ordering for these three phases.

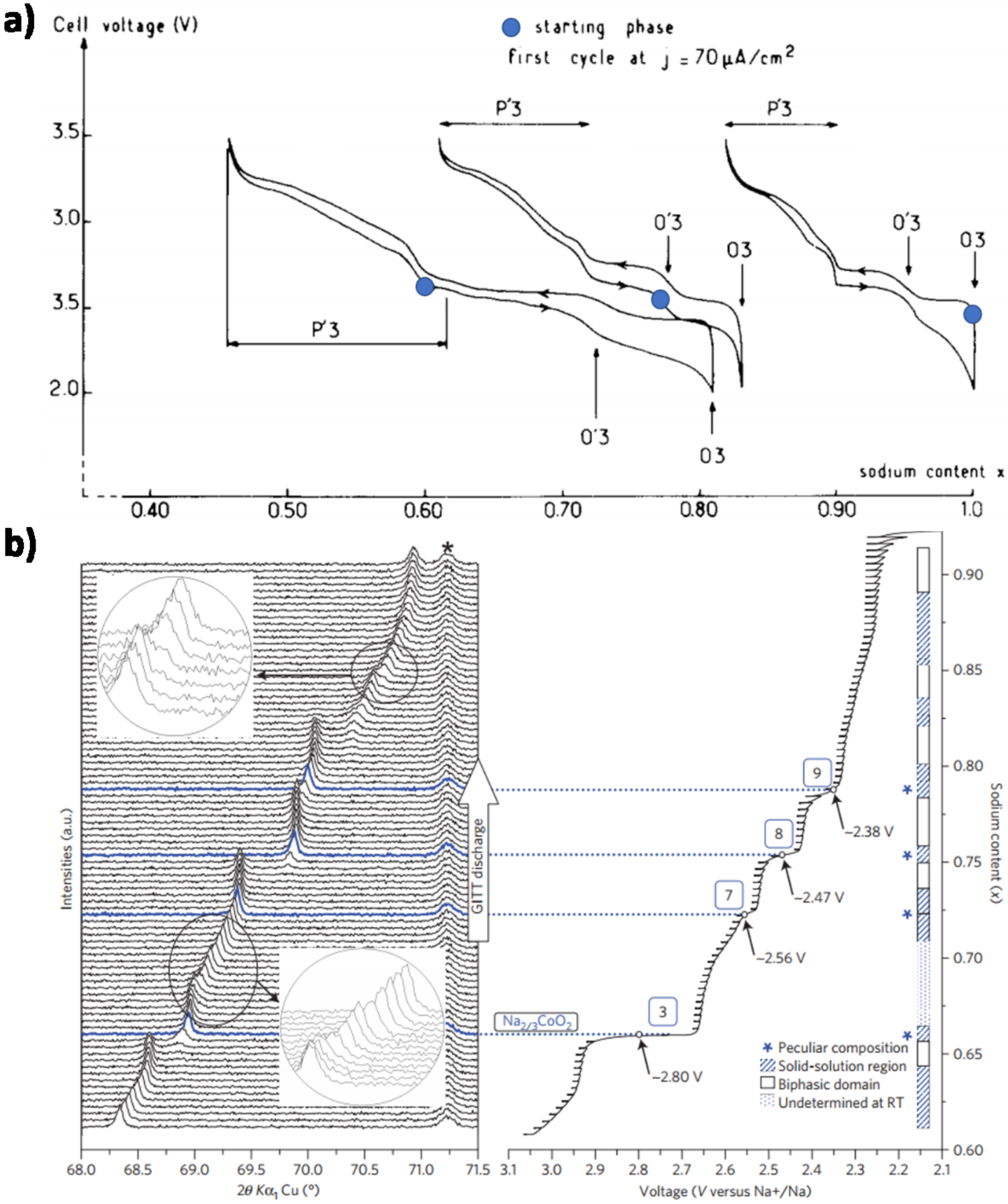

Figure IV-1: *a) Electrochemical cycling in the 2 V – 3.5 V range of the P3, O3 and O'3 Na_xCoO_2 polytypes. Reproduced from reference [76]. b) In-situ XRD patterns with the corresponding discharge from 3.1 V to 2.1 V of the P2 polytype. From reference [47].*

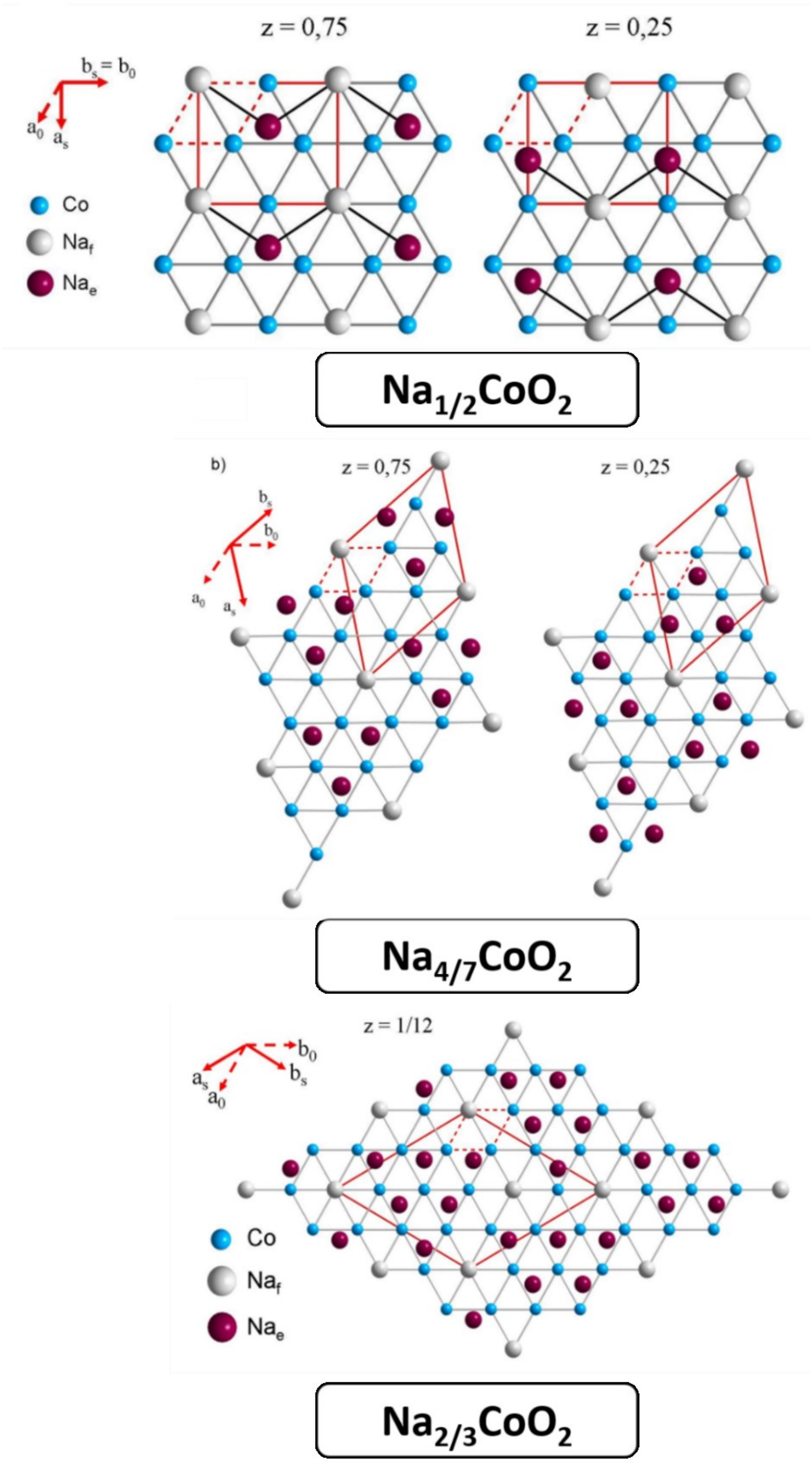

***Figure IV-2**: Representation, in the (a, b) plane, of the Na^+/vacancy ordering for $Na_{1/2}CoO_2$ (reference: [110]), $Na_{4/7}CoO_2$ (reference: [109]) and $Na_{2/3}CoO_2$ (reference: [92]). The purple dashed lines represent the initial hexagonal cell while the solid purple lines represent the superstructure cells. Extracted from reference [43].*

Peculiar phases	Voltages of formation (vs Na^+/Na)[43]	Superstructures	References
$Na_{3/4}CoO_2$	2.47 V	*Undefined*	[43]
$Na_{5/7}CoO_2$	2.56 V	*Undefined*	[43]
$Na_{2/3}CoO_2$	2.8 V	$R\bar{3}c$: $2\sqrt{3}a \times 2\sqrt{3}a \times 3c$	[47,72,92,111,112]
$Na_{4/7}CoO_2$	3.15 V	$P6_3/m$: $\sqrt{7}a \times \sqrt{7}a \times c$	[109]
$Na_{1/2}CoO_2$	3.45 V	$Pnmm$: $\sqrt{3}a \times 2a \times c$	[16,47,107,108,110,113–116]

***Table IV-1**: The peculiar phases already reported on the Na_xCoO_2 system for $x \geq 0.5$ with the associated voltages of formation, space groups and superlattices*

The Mn-substituted P2-Na_xCoO_2 phases are also interesting positive electrode materials for Na-ions batteries. The influence of the Co/Mn ratio had been largely studied by Paulsen and Dahn[117]. P2-$Na_xCo_{2/3}Mn_{1/3}O_2$ exhibits interesting electrochemical performances[45]. Contrary to P2-Na_xCoO_2, Carlier *et al*. highlighted the presence of only one voltage jump on its galvanostatic curve for x = 1/2 when charging to 4.0 V vs Na^+/Na. Cheng *et al.*[118] reported by X-Ray Absorption the redox couples involved during the charge and discharge of the system. They expected that the pristine phase, $Na_{2/3}Co_{2/3}Mn_{1/3}O_2$ contains only Co^{3+} and Mn^{4+} ions. During the discharge for $x > 2/3$, the Co^{3+} and Mn^{4+} ions are reduced into Co^{2+} and Mn^{3+} ions while during the charge for $x < 2/3$, only the Co^{3+} ions are oxidized into Co^{4+} ions. The change of the couple at x = 2/3 is associated with a change of the slope on the galvanostatic curve. Note that the electrochemical performances of other Co_yMn_{1-y} systems were reported in the literature (**Table IV-2**).

$Na_xMn_{1-y}Co_yO_2$ material	E range	Capacity (mA.h.g^{-1})	C-rate	Capacity retention	Electrolyte	Ref
P2-$Na_xMn_{0.89}Co_{0.11}O_2$	1.5 - 3.8 V	138	C/3	67 % (20 cycles)	$NaClO_4$ in PC	119
P2-$Na_xMn_{1/2}Co_{1/2}O_2$	1.5 - 4 V	123	C/8	69 % (30 cycles)	$NaClO_4$ in PC	120
P2-$Na_xMn_{0.3}Co_{0.7}O_2$	2.0 - 3.8 V	60	C/2	87 % (60 cycles)	$NaClO_4$ in EC/DEC	121
P2-$Na_xCo_{0.1}Mn_{0.9}O_2$	1.5 - 3.8 V	160	C/3	68 % (150 cycles)	$NaClO_4$ in PC/EC	4
P2-$Na_xMn_{0.25}Co_{0.75}O_2$	1.5 - 4.2 V	120	C/10	87 % (100 cycles)	$NaPF_6$ in PC/EC	122
P2-$Na_xMn_{1/2}Co_{1/2}O_2$	1.5 - 4.2 V	140	C/10	85 % (100 cycles)	$NaPF_6$ in PC/EC	122
P2-$Na_xMn_{0.75}Co_{0.25}O_2$	1.5 - 4.2 V	160	C/10	78% (100 cycles)	NaPF6 in PC/EC	122
P2-$Na_xMn_{0.2}Co_{0.8}0_2$	2.0 – 4.0 V	80	C/20	?	$NaClO_4$ in PC	123
P2-$Na_xMn_{0.3}Co_{0.7}O_2$	2.0 – 4.0 V	85	C/20	?	$NaClO_4$ in PC	123
P2-$Na_xMn_{0.6}Co_{0.4}O_2$	2.0 – 4.0 V	70	C/20	?	$NaClO_4$ in PC	123

Table IV-2: *Electrochemical performances of some $Na_xCo_yMn_{1-y}O_2$ systems reported in the literature*

The previous studies in our group and in most of the studies in the literature at the beginning of this PhD were realized using $NaClO_4$ in an organic solvent as electrolyte. Unfortunately, this electrolyte is not stable enough to investigate cycling above 3.8 V vs Na^+/Na. Preliminary studies realized by Cedric Constantin in collaboration with Anthony Baux, in 2015, in our group showed that rather good cycling properties in the 1.5 - 4.3V vs Na^+/Na voltage range could be achieved using $NaPF_6$ in 1M in PC + 2% wt FEC as electrolyte in a Na(s) // P2-Na_xCoO_2 cell (**Figure IV-3**). We, thus, decided to further investigate this system using this electrolyte, with a particular interest for the mechanisms occurring at high voltage. In **Table IV-3** we report the peculiar phases reported in the literature for $0.25 \leq x < 0.5$. $Na_{1/3}CoO_2$ formation was also investigated by *in-situ* XRD in this work. In this chapter, we were also interested to the structural changes of other $Na_xCo_yMn_{1-y}O_2$ systems for y = 1/3, 1/2 and 2/3 by *in-situ* XRD recorded during the Na^+ (de)intercalation and called *operando* XRD through this chapter.

Composition	Superstructure	Determined by	References
x = 0.43	Hex: $\sqrt{7}a$ x $\sqrt{7}a$ x c	TEM	124
x = 0.40	Hex: $\sqrt{5}a$ x $\sqrt{5}a$ x c	DFT Calculations	113
x = 0.33	Hex: $\sqrt{3}a$ x $\sqrt{3}a$ x c	DFT Calculations	113,115
	Hex: $3a$ x $3a$ x c	STM	124
x = 0.30	Ortho: $\sqrt{3}a$ x 5a x c	DFT Calculations	113
x = 0.25	Hex: $2a$ x $2a$ x c	DFT Calculations	113,115

***Table IV-3**: Peculiar P2-Na_xCoO_2 phases highlighted in the literature for $0.25 \leq x < 0.5$.*

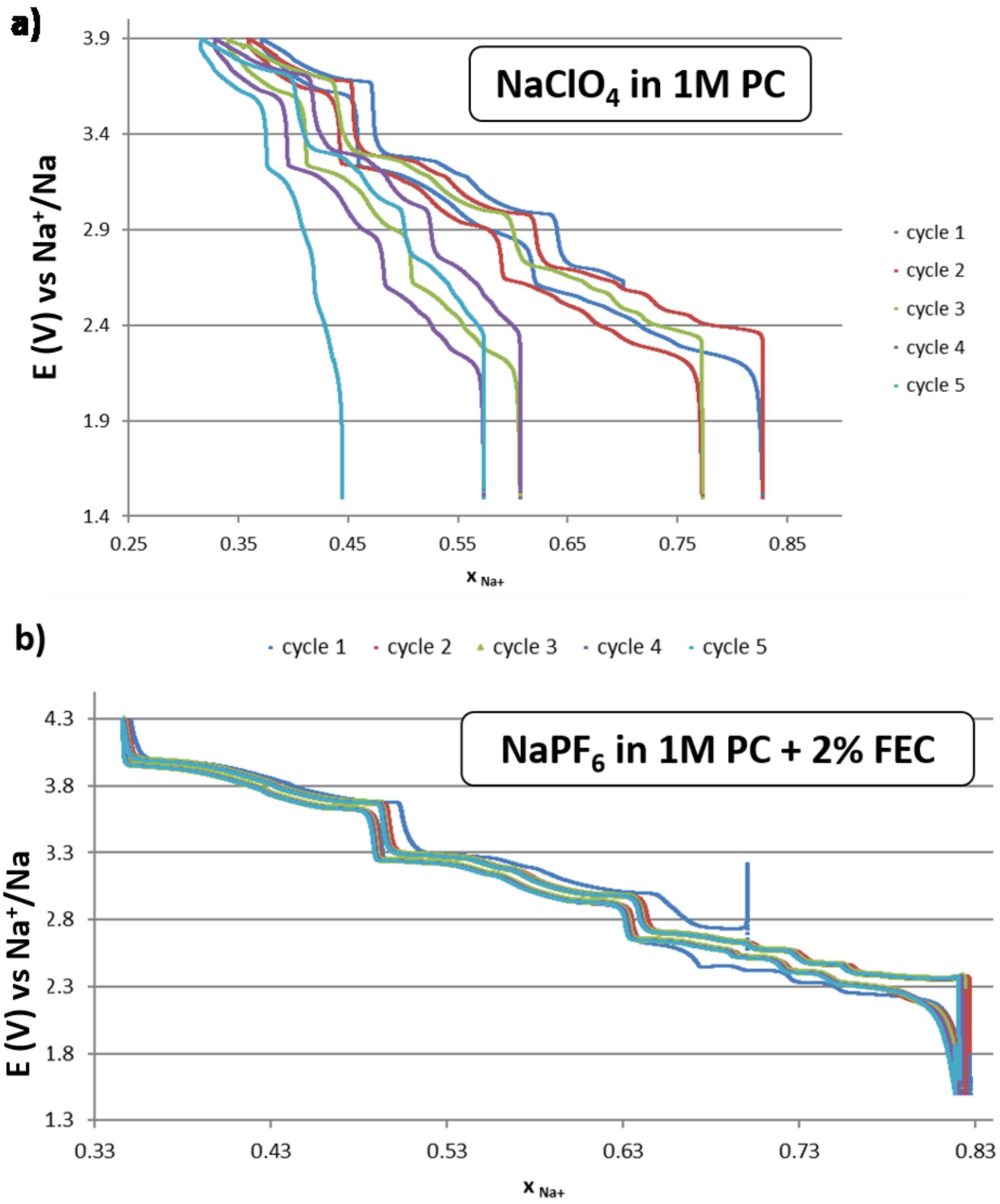

Figure IV-3: *a) Cycling curves of a Na/NaClO$_4$ in 1M PC/P2-Na$_x$CoO$_2$ cell in the 1.35 – 3.9 V vs Na$^+$/Na range at C/20 b) Cycling curves of a Na/NaPF$_6$ in 1M PC + 2% FEC/P2-Na$_x$CoO$_2$ cell in the 1.4 – 4.3 V vs Na$^+$/Na range at C/20*

2. Synthesis and characterization of the pristine phases

2.1 Synthesis of P2-pristine materials

P2-Na_xCoO_2 is synthetized using a solid state reaction while a co-precipitation technique was used to synthetize homogeneous Mn-substituted phases.

- **P2-$Na_{0.7}CoO_2$**

Na_2CO_3 (Sigma Aldrich, 99.9%, dried at 200°C) and Co_3O_4, (home prepared from cobalt nitrate decomposition at 400 °C) were used as precursors for the synthesis of P2-$Na_{\sim 0.7}CoO_2$. They were ground in an agate mortar in an Ar-filled glovebox before the thermal treatment. An excess of 5% of Na_2CO_3 was added to the Na/Co = 0.7 target composition because of the sodium high volatility at high temperature. The expected reaction is presented as **Equation IV-1**. The thermal treatment was made under a O_2 gas flux followed by a quench as presented on **Figure IV-4.**

$$^{0.7}/_{2}\,Na_2CO_3 + {}^{1}/_{3}\,Co_3O_4 + {}^{1.9}/_{12}\,O_2 \rightarrow Na_{0.7}CoO_2 + {}^{0.7}/_{2}\,CO_2 \qquad \text{eq(IV-1)}$$

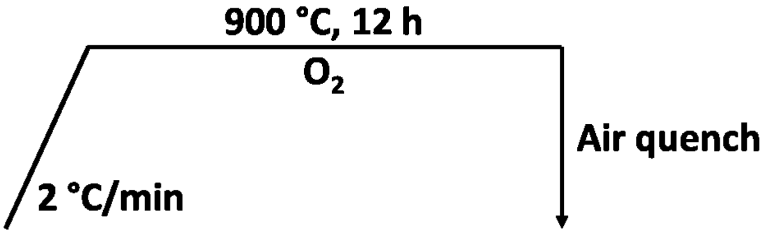

Figure IV-4: *Thermal treatment for the P2-$Na_{\sim 0.7}CoO_2$ synthesis*

- **P2-$Na_x(Co,Mn)O_2$**

To prepare the Mn-substituted phases, cobalt and manganese nitrates were solubilized in distilled water in stoichiometric proportions. A solution of NH_4OH and NaOH in 3:1 molar ratio was then slowly added to the mixture. NH_4OH was added in order to stabilize the solution pH during the slow NaOH addition. NH_4OH and water were then removed by using a rotary evaporator at 80 °C under vacuum. The mixture was dried in oven for 12h at 100 °C before the final thermal treatment. The powder was finally heated under O_2 flux using the following thermal treatment (**Figure IV-5**).

Figure IV-5: *Thermal treatment for the P2-*$Na_{x0}Co_yMn_{1-y}O_2$ *phases synthesis*

Due to the possible loss of Na^+ during the syntheses, the exact initial Na^+ composition x_0 is not accurately known at this stage, but is, usually, close to 0.70 for $Na_{x0}CoO_2$, close to 2/3 for the $Na_{x0}Co_{2/3}Mn_{1/3}O_2$ phases and 0.6 for $Na_{x0}Co_{1/2}Mn_{1/2}O_2$ and $Na_{x0}Co_{1/3}Mn_{2/3}O_2$.

2.2 Morphology of Na_xCoO_2

Figure IV-6 shows the Scanning Electron Microscopy (SEM) of P2-$Na_{\sim0.7}CoO_2$ phase. It shows the hexagonal shape of the structure with particles of 15 µm average diameter and 10 µm thickness. The hexagonal shape can be observed on many P2 phases in literature[125,126]. **Figure IV-6b** highlights the presence of an alternation of layers which characterizes the layered oxides structure. Small imperfections represented by white particles on the surface are due to an air exposure during the very short transit at air before the gold sputtering. These white particles can also correspond to remaining Na_2CO_3 precursor grown in air.

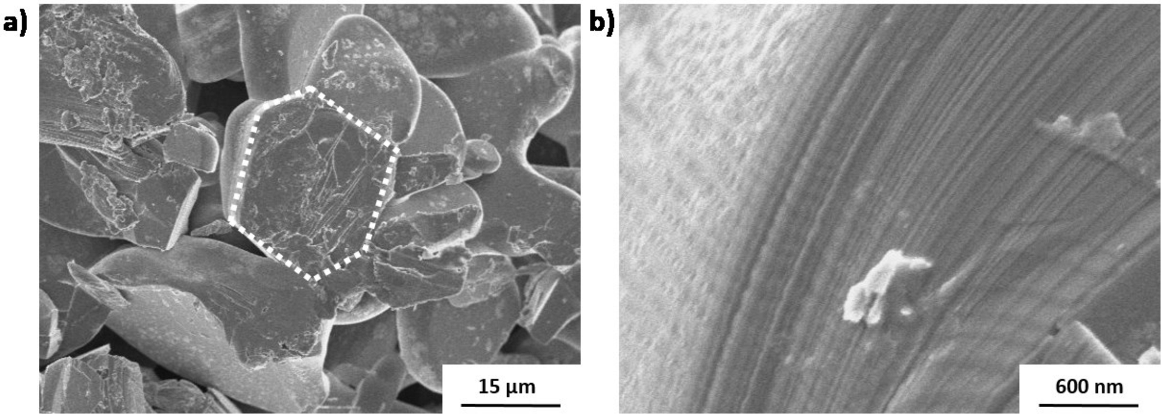

Figure IV-6: *SEM images of P2-$Na_{\sim0.7}CoO_2$ phase at two different magnifications.*

2.3 Structural characterization

The laboratory XRD study of the pristine materials (not shown here) indicated that all the phases were pure and crystallized in the *P6₃/mmc* space group. All the phases were also analyzed at ALBA Synchrotron facilities on the MSD04 beamline in a 2° to 73° 2θ range at a wavelength of $\lambda = 0.8261$ Å. The samples were packed in 0.5 mm diameter sealed capillaries as explained in chapter I. The XRD patterns were refined with the Le Bail method using the hexagonal cell described in *P6₃/mmc* without considering any Na^+/vacancy ordering (**Figure IV-7)**. The match is not perfect since some additional superstructure peaks can also be observed in the 15° - 23° range. Therefore, a correct indexation of the complete patterns could not be found in those cases. Note that the XRD pattern of the P2-$Na_{\sim2/3}Co_{2/3}Mn_{1/3}O_2$ exhibits a shoulder on the right side of the (002) peak indicating either an heterogeneity of the material or that the composition of the material falls in a biphasic domain.

The refined cell parameters (**Table IV-4**) are in good agreement with literature (Na_xCoO_2[127], $Na_xCo_yMn_{1-y}O_2$[120]). Note that a_{hex} is almost constant whatever the composition because of the slight difference between the Co^{3+} (0.545 Å),Co^{4+} (0.53 Å) and Mn^{4+} (0.53 Å) ions radii.

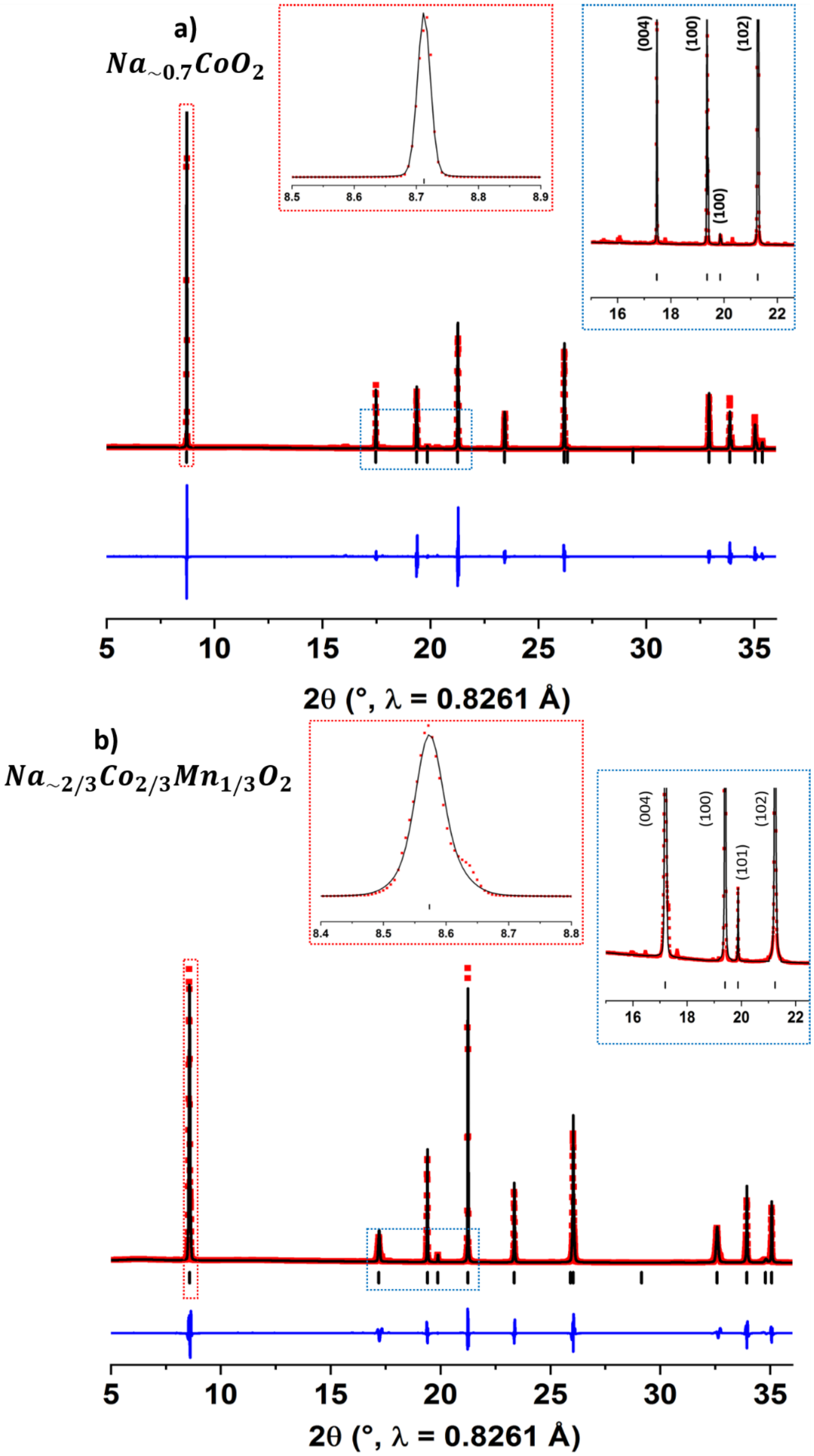
a)
$Na_{\sim 0.7}CoO_2$
8.5
8.6
8.7
8.8
8.9
(004)
(100)
(102)
(100)
16
18
20
22
5
10
15
20
25
30
35
2θ (°, λ = 0.8261 Å)
b)
$Na_{\sim 2/3}Co_{2/3}Mn_{1/3}O_2$
8.4
8.5
8.6
8.7
8.8
(004)
(100)
(101)
(102)
16
18
20
22
5
10
15
20
25
30
35
2θ (°, λ = 0.8261 Å)

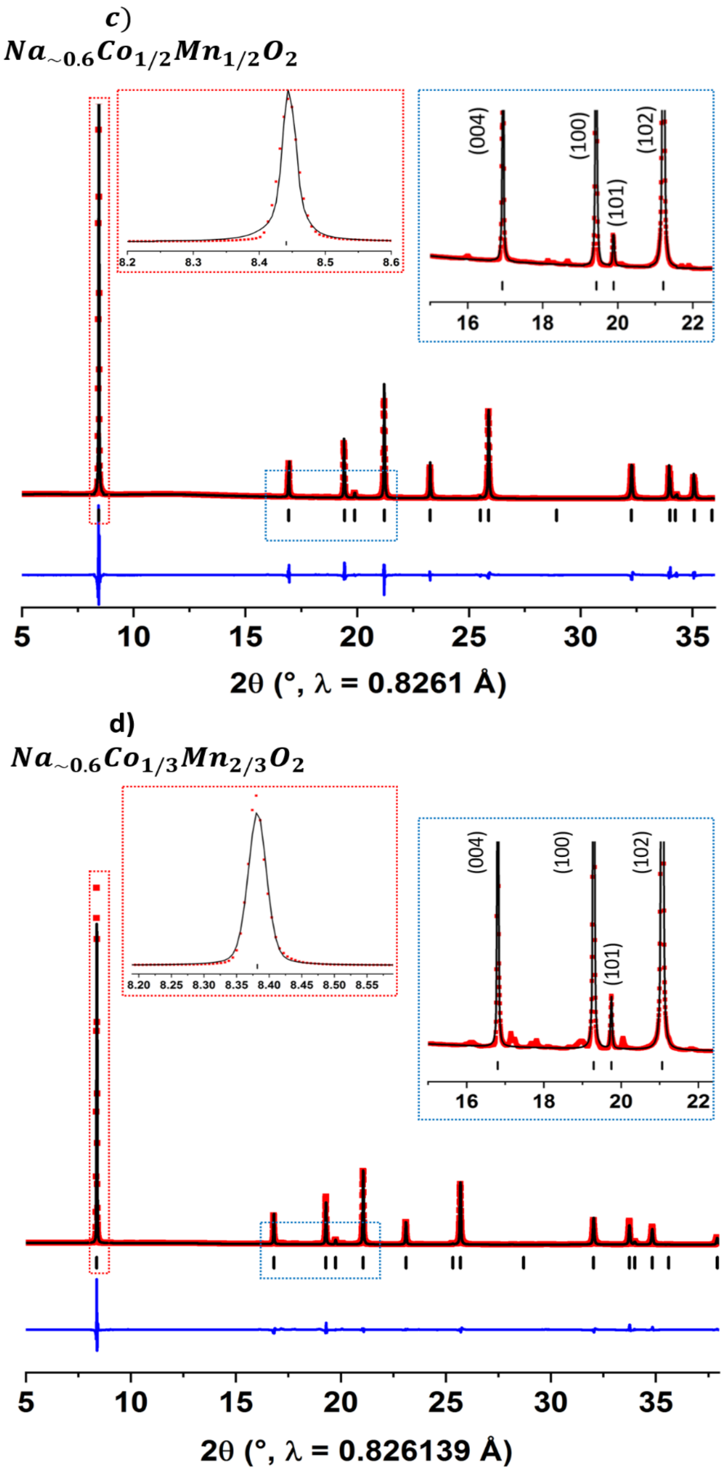

Figure IV-7: *SXRD patterns of the a) Na_xCoO_2 b) $Na_xCo_{2/3}Mn_{1/3}O_2$ c) $Na_xCo_{1/2}Mn_{1/2}O_2$ d) $Na_xCo_{1/3}Mn_{2/3}O_2$ pristine phases. Red points: experimental data, black lines: calculated curves, blue lines: difference between experimental and calculated data, black bars: Bragg positions. The two inserts are zooms on the (002) peak and in the 15°-23° range to evidence the presence of superstructure peaks.*

Space group : $P6_3/mmc$	a_{hex} (Å)	c_{hex}(Å)
$Na_{\sim0.7}CoO_2$	2.8363(2)	10.876(1)
$Na_{\sim2/3}Co_{2/3}Mn_{1/3}O_2$	2.8304(2)	11.052(3)
$Na_{\sim0.6}Co_{1/2}Mn_{1/2}O_2$	2.8291(1)	11.203(2)
$Na_{\sim0.6}Co_{1/3}Mn_{2/3}O_2$	2.8467(3)	11.304(4)

***Table IV-4**: Lattice parameters calculated by Le Bail refinements for each pristine phase. The exact Na^+ composition*

3. Electrochemical properties

All the materials were cycled in two different voltage ranges. The "low" voltage ranges correspond to the voltage windows where a good reversibility was observed for the Na_xCoO_2 and $Na_xCo_{2/3}Mn_{1/3}O_2$ system with an upper cutoff voltage value depending on the materials. The "high" voltage range involves irreversible cycling performances with the electrolyte described previously and is therefore, characterized by a drop in the specific capacity values between the first and the second cycle. The voltage ranges used in this manuscript are summarized in **Table IV-5**. The different galvanostatic curves (**Figure IV-8 and 11**) were performed at C/20. Each battery was assembled in a coin cell configuration using Na metal as negative electrode and $NaPF_6$ in 1M PC + 2% FEC as electrolyte.

	Voltages ranges (V vs Na^+/Na)	
Na_xCoO_2	Low	1.5 - 4.3 V
	High	1.5 - 4.6 V
$Na_xCo_{2/3}Mn_{1/3}O_2$	Low	1.25 - 4 V
	High	1.25 - 4.5 V
$Na_xCo_{1/2}Mn_{1/2}O_2$	Low	1.25 - 4 V
	High	1.25 - 4.6 V
$Na_xCo_{1/3}Mn_{2/3}O_2$	Low	1.25 - 4.3 V
	High	1.25 - 4.6 V

***Table IV-5:** Voltage ranges used in this manuscript for each system*

3.1 Galvanostatic cycling in the low voltage range

Figure IV-8 shows the evolutions of the cell voltage as a function of Na^+ content (x) in the material for the four systems cycled in their low voltage range. The Na_xCoO_2 and $Na_xCo_{2/3}Mn_{1/3}O_2$ systems exhibit a low polarization (**Figure IV-8a and b**) and a good capacity retention upon cycling (**Figure IV-9**). Note that the Na_xCoO_2 pristine phase was not the same than the refined one and it seems that its composition was close to 0.76 which is possible due the large P2 existence domain[7]. For $Na_xCo_{1/2}Mn_{1/2}O_2$ and $Na_xCo_{1/3}Mn_{2/3}O_2$, the polarization is higher and the capacity retention is worse (**Figure IV-8c, 8d and 9**). Among all the systems, P2-Na_xCoO_2 exhibits the best capacity retention (97 % in 40 cycles) compared to the Co-Mn systems (95 % in 35 cycles for $Na_xCo_{2/3}Mn_{1/3}O_2$ and 90 % in 13 cycles for $Na_xCo_{1/2}Mn_{1/2}O_2$). Concerning the redox couples involved during the $Na_xCo_{1/2}Mn_{1/2}O_2$ and $Na_xCo_{1/3}Mn_{2/3}O_2$ systems charges, one can expect that all Mn^{3+} (and Co^{2+} ions possibly) are first oxidized into Mn^{4+} (and Co^{3+}) for x = 1/2 and 1/3, respectively, before the oxidation of Co^{3+} into Co^{4+} as observed for the $Na_xCo_{2/3}Mn_{1/3}O_2$ system at x = 2/3[118]. A tiny slope change can be observed on both $Na_xCo_{1/2}Mn_{1/2}O_2$ and $Na_xCo_{1/3}Mn_{2/3}O_2$ galvanostatic curves and could be due to this redox couple change. The larger polarization observed for those two phases can be due to a lower electrical conductivity due to the lower amount of Co^{4+} ions during the electrochemical cycling compared to the amount in the Na_xCoO_2 and $Na_xCo_{2/3}Mn_{1/3}O_2$ systems.

Another interesting point is the shape of the electrochemical curve of the different systems. Whereas, the Na_xCoO_2 galvanostatic curve shows many accidents, the Co-Mn systems exhibit much less slope breaks. Only one is clearly observed on the $Na_xCo_{2/3}Mn_{1/3}O_2$ system for x = 1/2 that might correspond to a phase with a specific Na^+/vacancy ordering[45]. The voltage evolution of the $Na_xCo_{2/3}Mn_{1/3}O_2$, $Na_xCo_{1/2}Mn_{1/2}O_2$ and $Na_xCo_{1/3}Mn_{2/3}O_2$ systems suggests solid solution behaviors in their low voltage range.

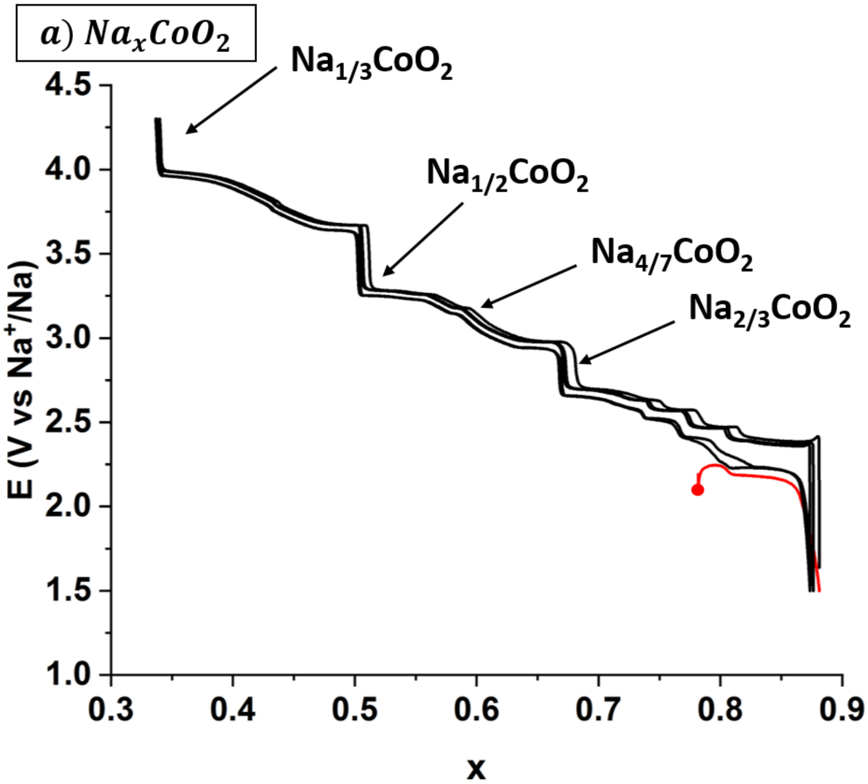
$a)\ Na_xCoO_2$
$Na_{1/3}CoO_2$
$Na_{1/2}CoO_2$
$Na_{4/7}CoO_2$
$Na_{2/3}CoO_2$
E (V vs Na^+/Na)
4.5
4.0
3.5
3.0
2.5
2.0
1.5
1.0
0.3
0.4
0.5
0.6
0.7
0.8
0.9
x

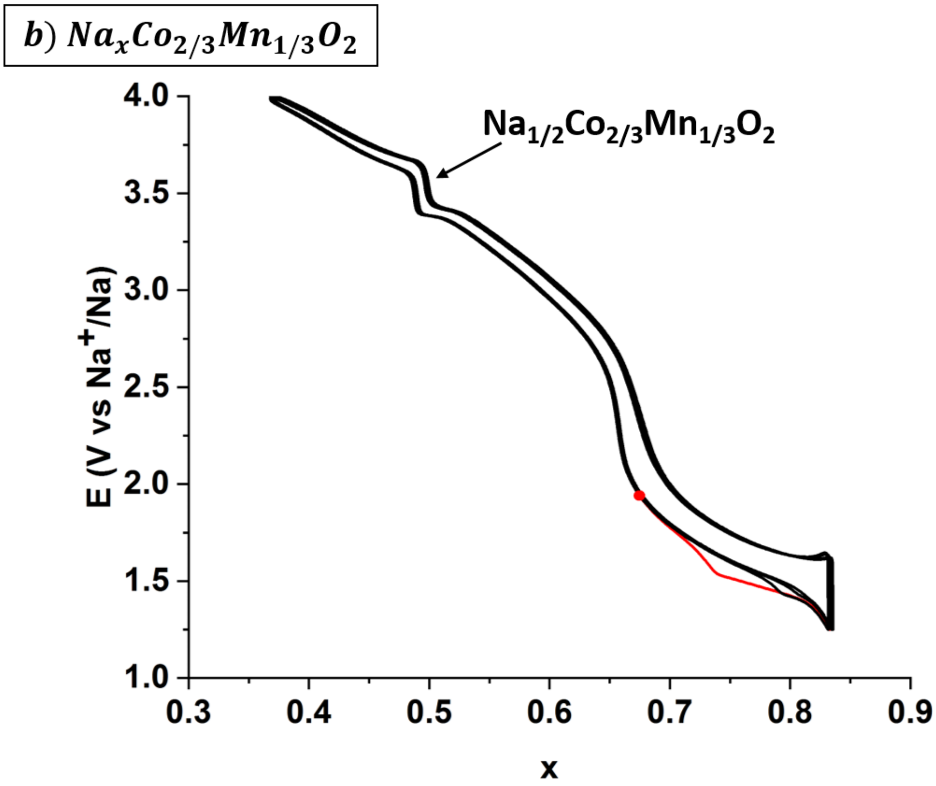
$b)\ Na_xCo_{2/3}Mn_{1/3}O_2$
$Na_{1/2}Co_{2/3}Mn_{1/3}O_2$
E (V vs Na^+/Na)
4.0
3.5
3.0
2.5
2.0
1.5
1.0
0.3
0.4
0.5
0.6
0.7
0.8
0.9
x

c) $Na_xCo_{1/2}Mn_{1/2}O_2$

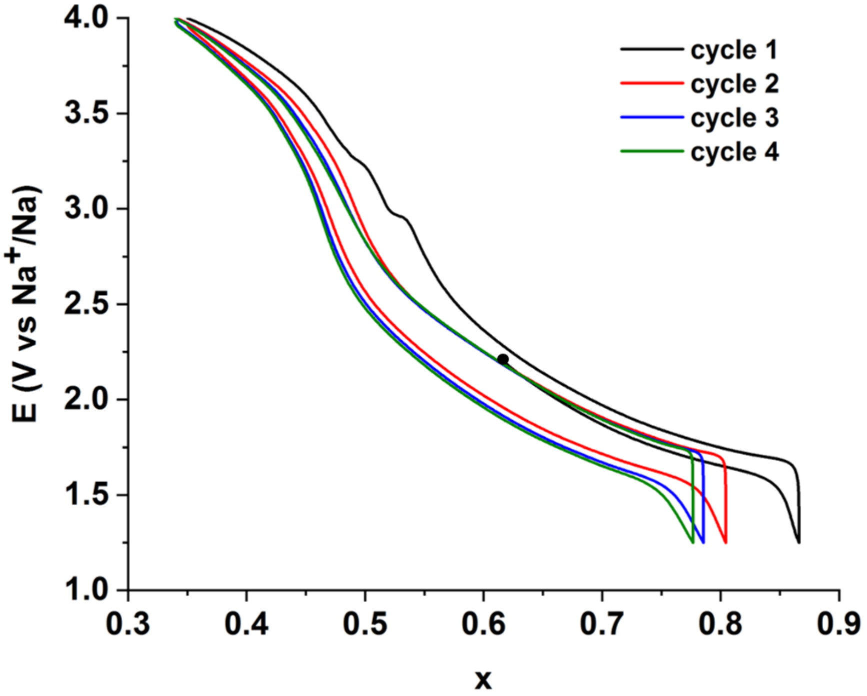

d) $Na_xCo_{1/3}Mn_{2/3}O_2$

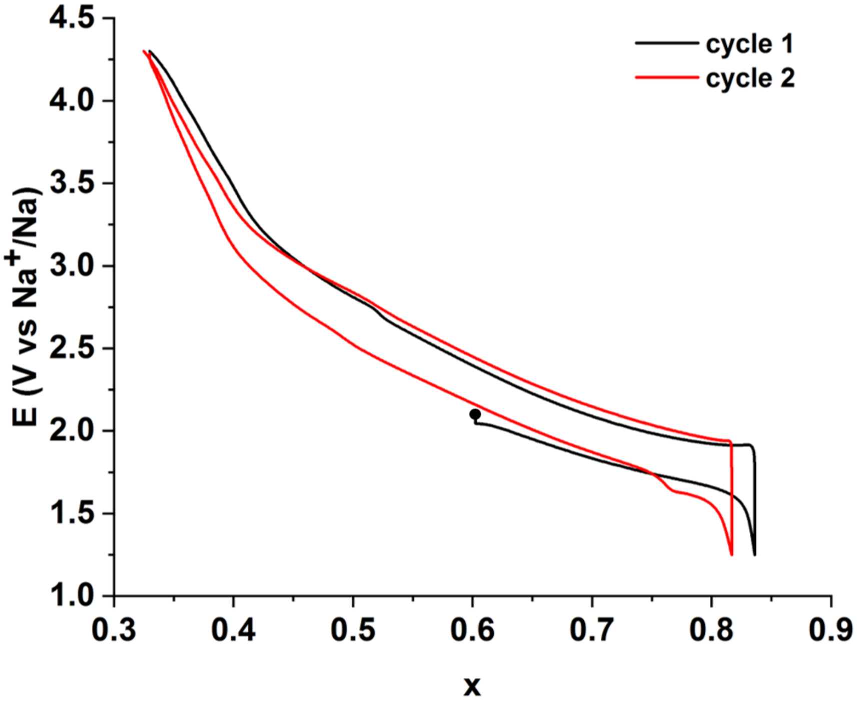

Figure IV-8*: Galvanostatic curves of the Na(s)/P2-Na_xMO_2 cell at C/20 in their low voltage range for a) Na_xCoO_2 b) $Na_xCo_{2/3}Mn_{1/3}O_2$ c) $Na_xCo_{1/2}Mn_{1/2}O_2$ d) $Na_xCo_{1/3}Mn_{2/3}O_2$*

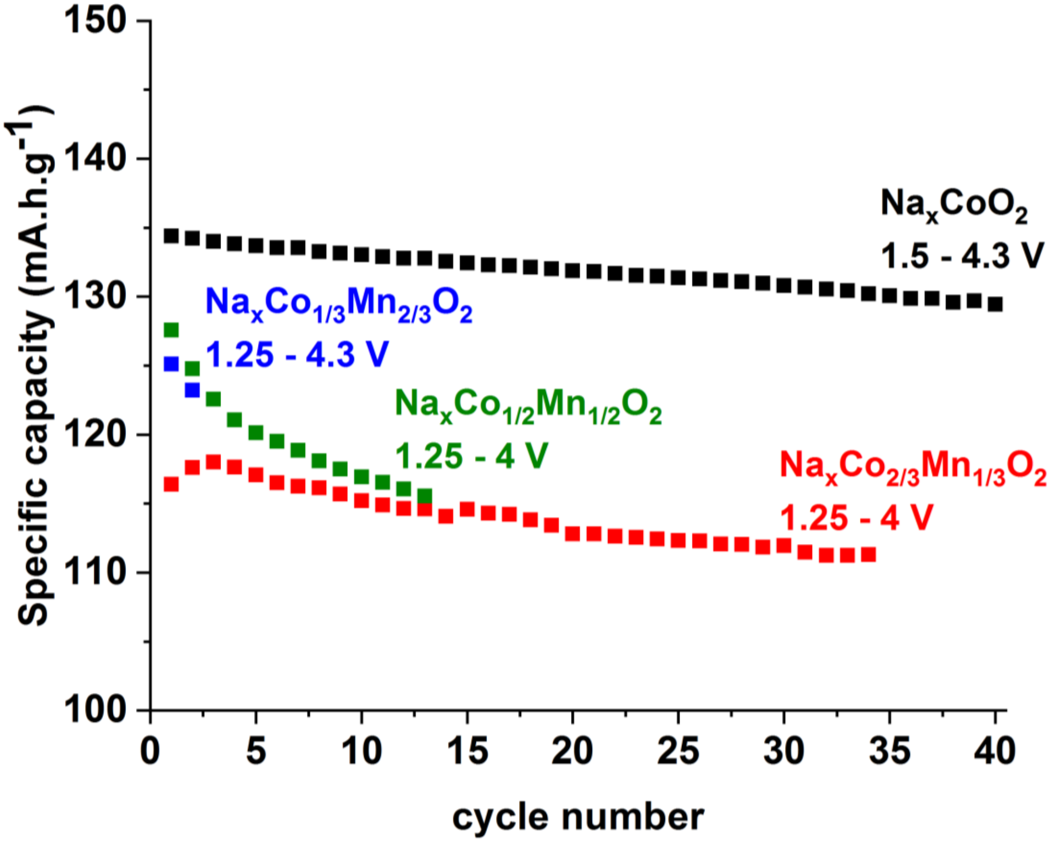

Figure IV-9: *Evolution of the specific capacities in their low voltage window when cycling in their low voltage range at C/20*

Figure IV-10 displays the 1st and the 40th cycle performed on the Na(s)/P2-Na$_x$CoO$_2$ cell at C/20 between 1.5 V and 4.3 V vs Na$^+$/Na. The shape of the galvanostatic curve of the 40th cycle in similar in charge and discharge than the curve observed during the 1st cycle. The same domains can be distinguished on both curves indicating the good reversibility of the system. Only a Δx shift to the lower Na$^+$ content occurs due to a possible small amount of reactions with the electrolyte at high voltage after many cycling.

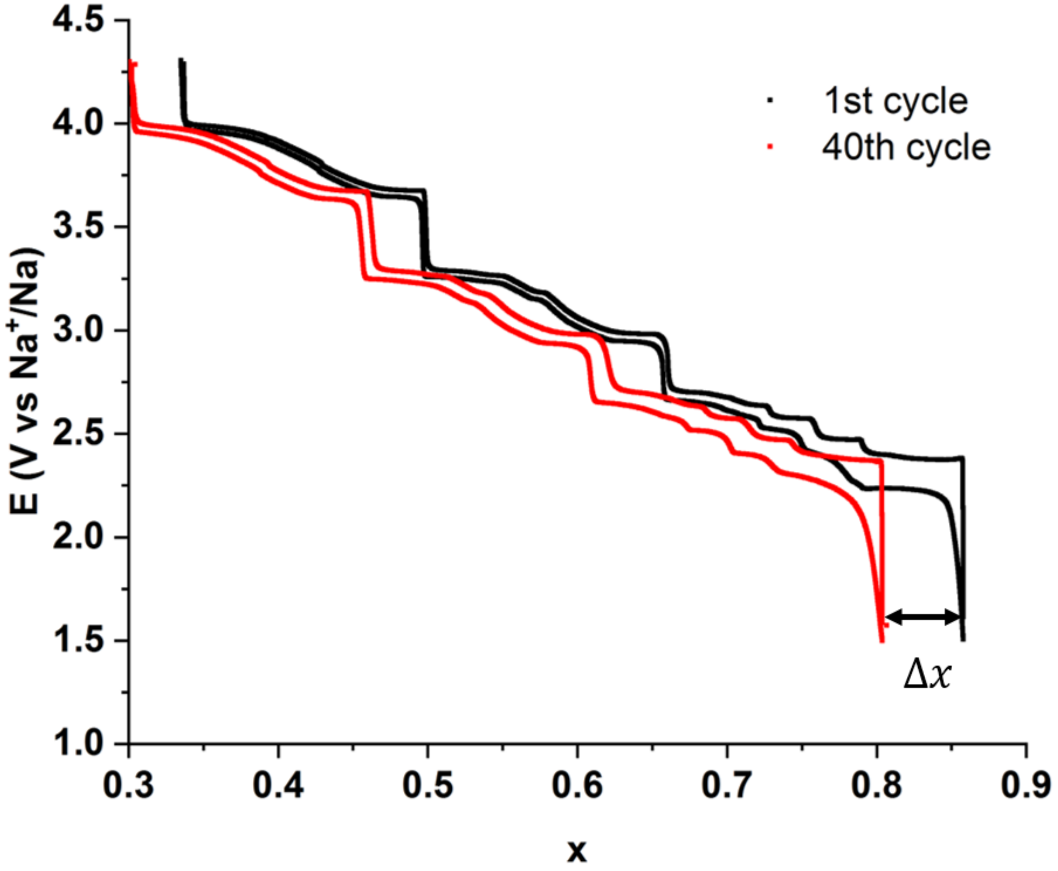

Figure IV-10: *Comparison between the first and the 40th cycle realized on the same Na(s) / P2-Na_xCoO_2 cell at C/20 in the low voltage range.*

3.2 Galvanostatic cycling in high voltage range

In order to investigate the performances under "extreme" conditions of the systems, the batteries were cycled at C/20 up to 4.6 V vs Na^+/Na for Na_xCoO_2 and 4.5 V for $Na_xCo_{2/3}Mn_{1/3}O_2$ (**Figure IV-12a and b**). The evolutions of their specific capacities are plotted in **Figure IV-11** and compared to the capacities obtained in the low voltage ranges. **Figure IV-11** shows a very fast decrease after only 2 cycles of the Na_xCoO_2 specific capacity (black crosses). The capacity retention is only 78 % after 40 cycles and the capacity becomes after few cycles lower than in the low voltage range (black square). For the $Na_xCo_{2/3}Mn_{1/3}O_2$ system, a relatively fast capacity decrease is also observed (87 % capacity loss in 7 cycles). A cycling to 4.6 V involves, thus, irreversible phenomena for both systems which, significantly, reduces the capacity and the performances of both batteries upon cycling.

The two other systems were cycled to 4.6 V, in order to check the eventual presence of voltage jumps at high voltage, voltage plateau or solid solution domains (**Figure IV-12c and d**). Two new peculiar phases for x = 1/3 on the $Na_xCo_{2/3}Mn_{1/3}O_2$ and $Na_xCo_{1/2}Mn_{1/2}O_2$ systems are highlighted by the presence of voltage jumps. No obvious ordered phases can be identified on the $Na_xCo_{1/3}Mn_{2/3}O_2$ system. Except for the specific compositions which correspond to these peculiar phases, the curve shape suggests the presence of solid solution domains for the three systems (Co,Mn) during charge and discharge in their “high” voltage ranges.

For Na_xCoO_2, a peculiar phase for x = 1/3 is observed when cycling to 4.6 V due to the presence of a voltage jump at this specific composition. The first discharge after a charge to 4.6 V involves a smoothing of the discharge galvanostatic curve without any voltage drops at the expected peculiar phases compositions as observed when cycled to 4.3 V (**Figure IV-8a**). However, the voltage jumps reappear during the next charge, mainly, for x = 2/3, 1/2 and 1/3 but globally disappear from the 3rd charge. The origin of this behavior is still unclear and could be due to a strong difference in kinetics during the discharge compared to the charge. For $Na_xCo_{2/3}Mn_{1/3}O_2$, the voltage drops/jumps are still observed during the following discharges/charges despite the decrease of the specific capacity when cycling to 4.5 V (**Figure IV-12b**). Note that the voltage drop at x = 1/2 remains over almost 20 cycles.

At high voltage, it is possible that, a proportion of the P2-Na_xMO_2 phase is, irreversibly, disordered due to some sheets glidings. By charging the battery and therefore by removing Na^+ ions, O-O repulsions increase and sheets glidings occur to stabilize the structure[128]. This point will be investigated in the following using *operando* XRD measurements and in the next chapter using ^{23}Na MAS NMR spectroscopy.

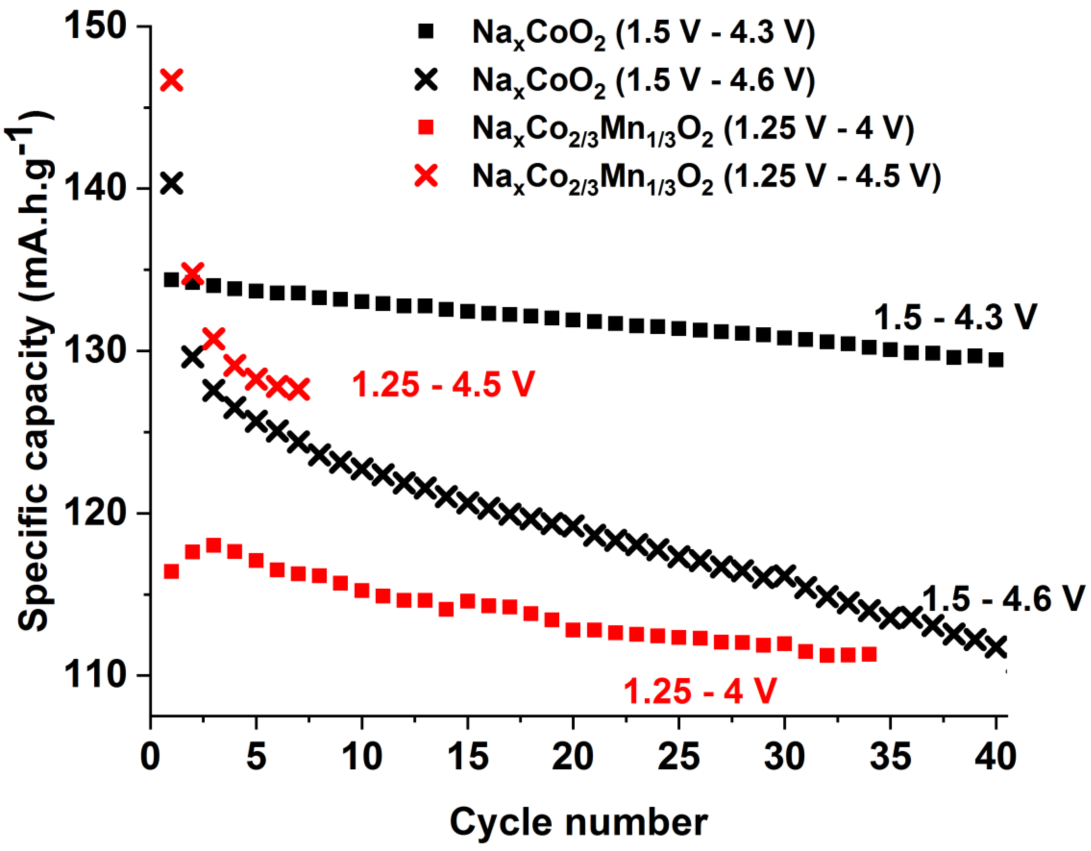

Figure IV-11: *Capacity as a function of cycle number for Na_xCoO_2 and $Na_xCo_{2/3}Mn_{1/3}O_2$ system in both voltage ranges at C/20.*

$a)\ Na_xCoO_2$

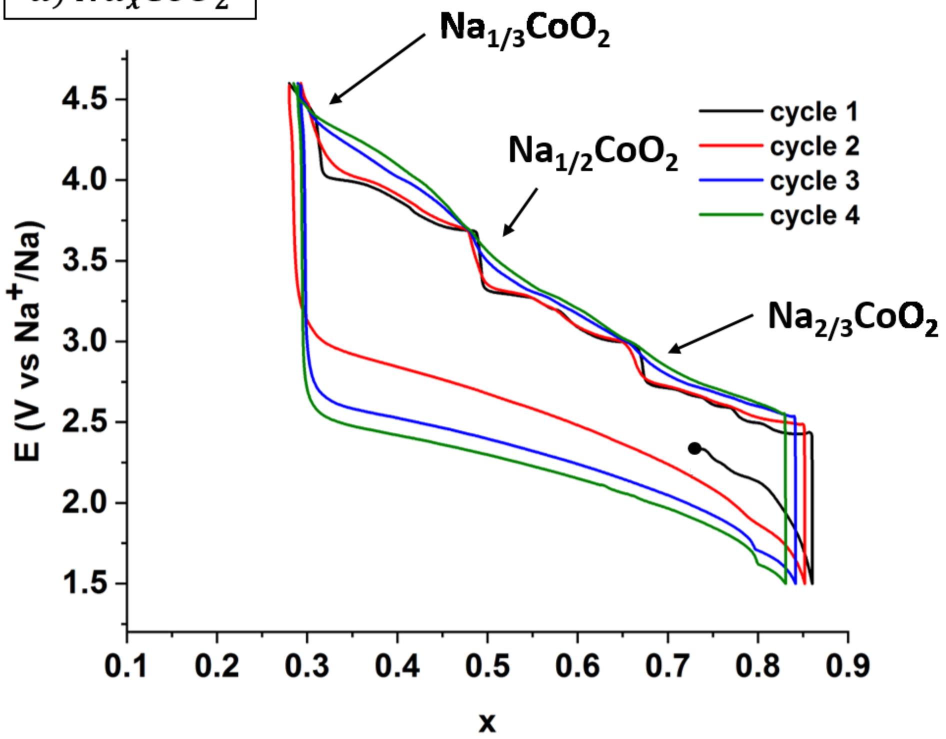

$b)\ Na_xCo_{2/3}Mn_{1/3}O_2$

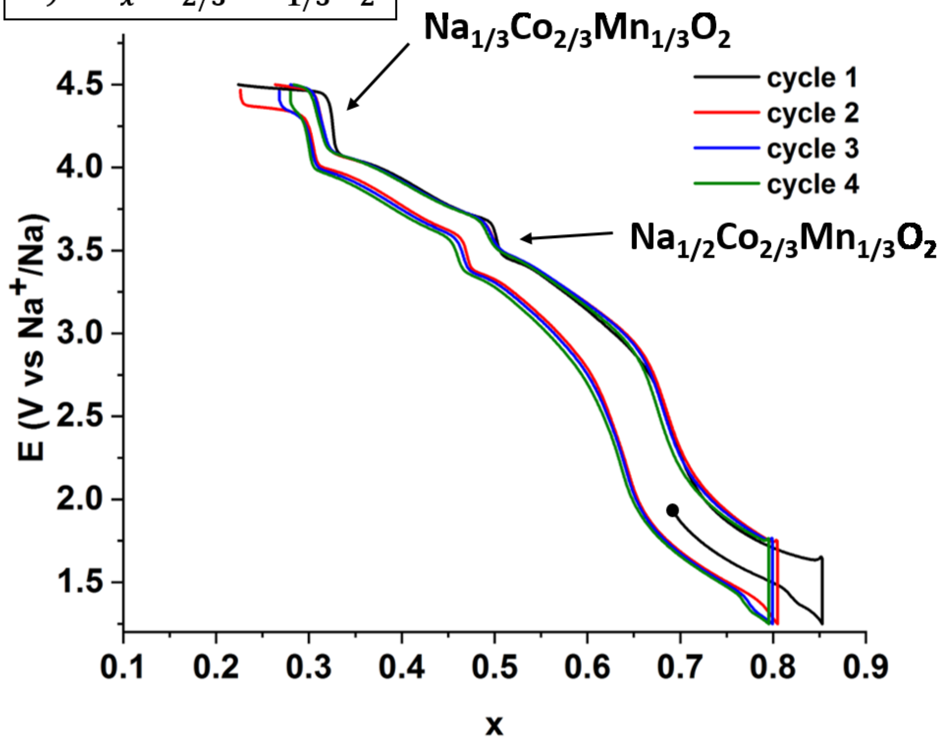

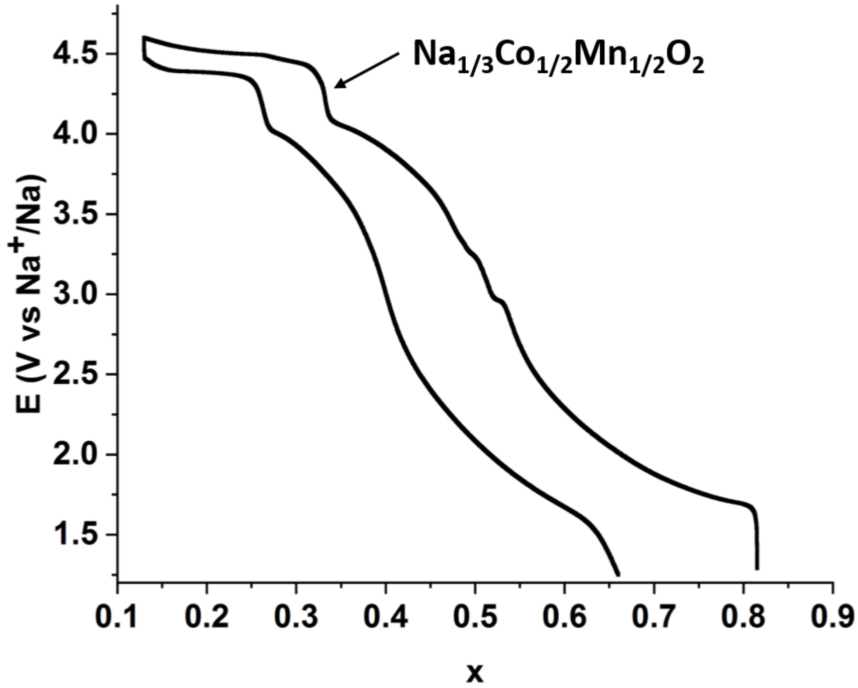

$c)\ Na_xCo_{1/2}Mn_{1/2}O_2$

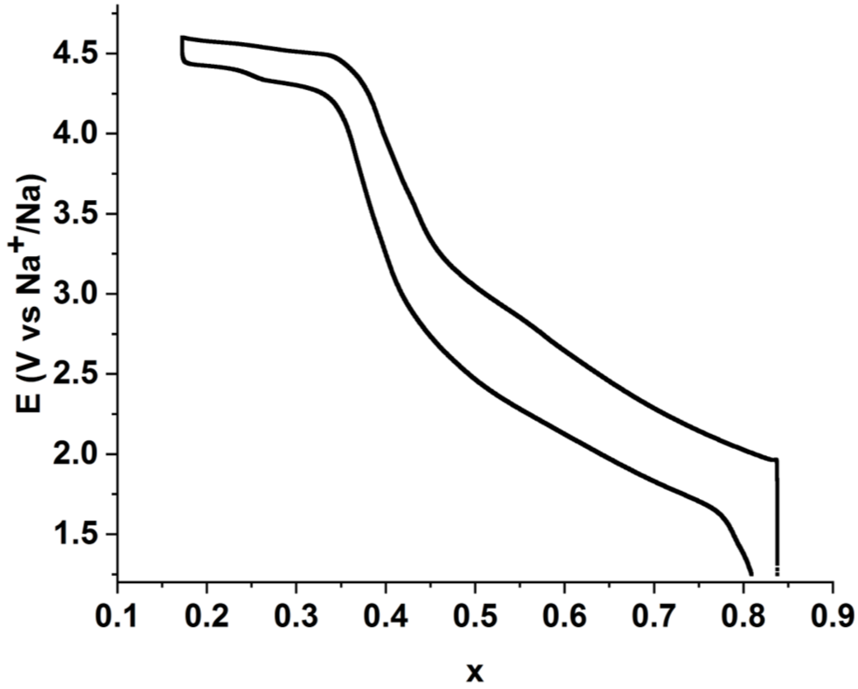

$d)\ Na_xCo_{1/3}Mn_{2/3}O_2$

***Figure IV-12**: Galvanostatic curves of the Na(s)/P2-Na_xMO_2 cell at C/20 in their high voltage range for a) Na_xCoO_2 b) $Na_xCo_{2/3}Mn_{1/3}O_2$ c) $Na_xCo_{1/2}Mn_{1/2}O_2$ d) $Na_xCo_{1/3}Mn_{2/3}O_2$*

4. Structural evolution by *in-situ* Synchrotron XRD

The structural evolution of the different P2 phases were investigated by *operando* XRD on the BL-04-MSPD beamline of the ALBA synchrotron (Barcelona, Spain) with the collaboration of François Fauth. Each system was cycled at a C/10 rate using drilled coin cells as described in the first chapter and *operando* measurements were realized up to 4.6 V or 4.5 V using the fast MYTHEN detector[129]. Moreover, a PITT (Potentiostatic Intermittent Titration Technique) was realized on the P2-Na_xCoO_2 system for different high voltages from 4.1 V to 4.8 V vs Na^+/Na.

4.1 Na_xCoO_2 system

4.1.1 *Operando measurements*

Starting from a Na(s)//P2-$Na_{\sim 0.7}CoO_2$ cell, the first charge and second discharge were investigated in the 1.5 V – 4.6 V range at C/10. **Figure IV-13** shows the XRD patterns recorded *operando* during the first charge and **Figure IV-13b** focus in the 16.2-18° range in order to follow the (004) peak evolution and to observe the appearance of the superstructure peaks. During the charge, the (004) peak shifts to lower angles indicating the increase of the c_{hex} lattice parameter as expected. Up to 3.1 V, the structural evolution is in agreement with the study conducted by Berthelot *et al.*[43] using laboratory XRD: an important number of peculiar phases is observed in the $0.6 < x < 0.92$ range with an alternation of biphasic and solid solution domains as well as peculiar phases. The Le Bail refinements realized on the Synchrotron XRD patterns of the $Na_{1/2}CoO_2$, $Na_{4/7}CoO_2$ and $Na_{2/3}CoO_2$ phases are given in the Appendix section. The colored lines indicate which patterns were extracted to realize the refinements on **Figure IV-13**. The calculated lattice parameters with the reported supercells are in good agreement with the previous works (**Table IV-1**). *Operando* experiments at a C/10 rate enable, thus, to study the formation of ordered phases in this system.

We focused then our study on the phases evolution at high voltage. For $0.45 < x < 1/3$, the P2 structure is still maintained and the (004) peak 2θ position is almost constant on the XRD patterns, suggesting that the structure has reached a maximal c_{hex} lattice parameter value (11.20(1) Å) despite further Na^+ ions deintercalation. Moreover, an additional peak appears at 17.7° on **Figure IV-12b** for $x = 0.4$. Its position shifts toward low angles when the voltage increases indicating a pseudo-solid solution domain probably due to the presence of incommensurate structures. For the XRD patterns recorded at the highest voltages, this peak has disappeared and the (004) peak intensity slightly decreases which could be the sign of the beginning of sheets glidings. In order to investigate further the phases at high voltage, another battery was studied using a Potentiostatic Intermittent Titration Technique and recorded the XRD patterns after relaxation.

Note that the discharge of the cell following the *operando* experiment is given in the Appendix part (**A-4**). Surprisingly the (004) peak position remains unchanged up to $x \sim 0.5$. We believe it highlights the problem of kinetics during the discharge following a charge at 4.6 V that can be at the origin of the limited cycle life. But we do not understand so far the origin for it: surface modification, role of the remaining stacking faults, cracks due to the large volume change …

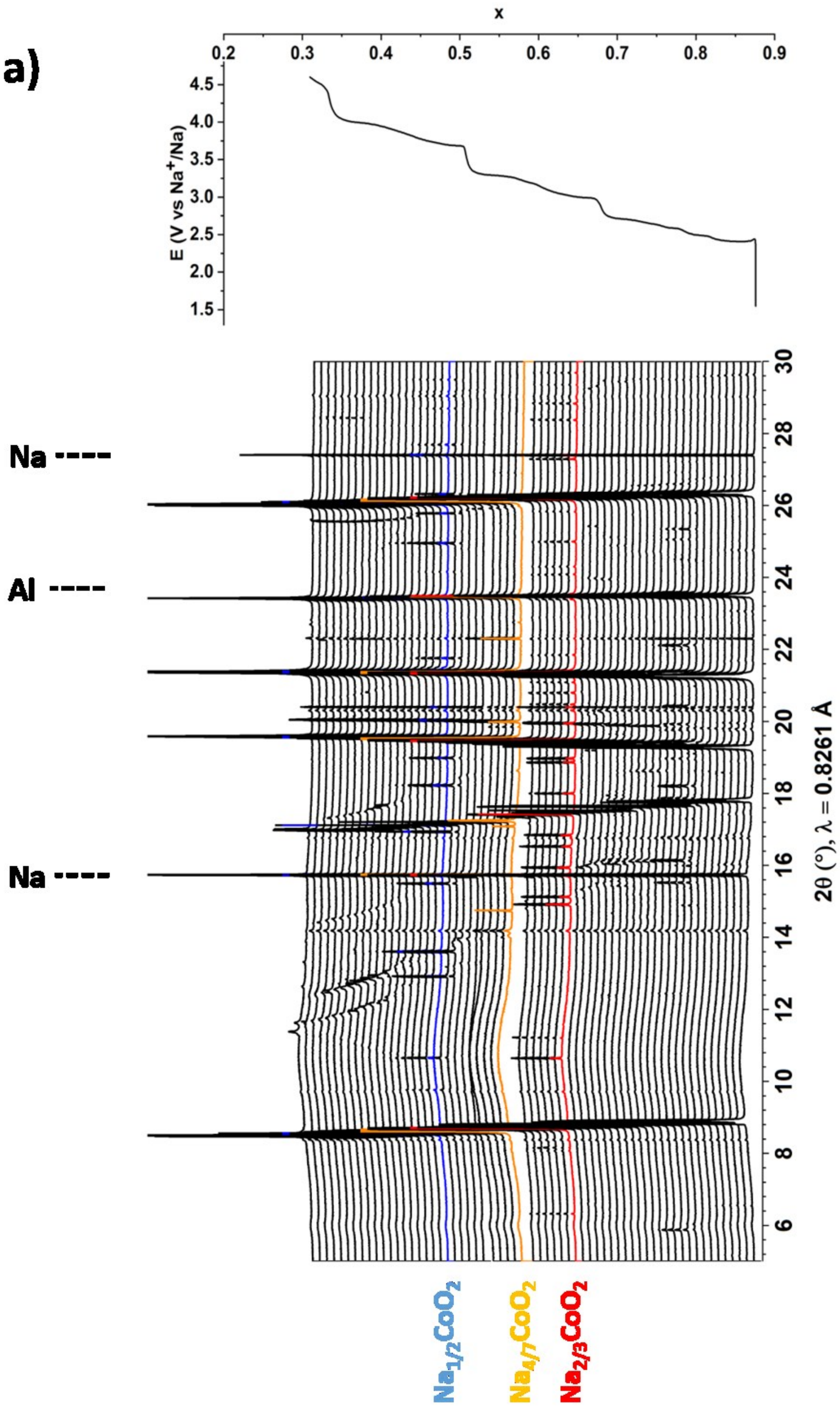
a)
x
0.2
0.3
0.4
0.5
0.6
0.7
0.8
0.9
E (V vs Na$^+$/Na)
4.5
4.0
3.5
3.0
2.5
2.0
1.5
Na ----
Al ----
Na ----
30
28
26
24
22
20
18
16
14
12
10
8
6
2θ (°), λ = 0.8261 Å
$Na_{1/2}CoO_2$
$Na_{4/7}CoO_2$
$Na_{2/3}CoO_2$

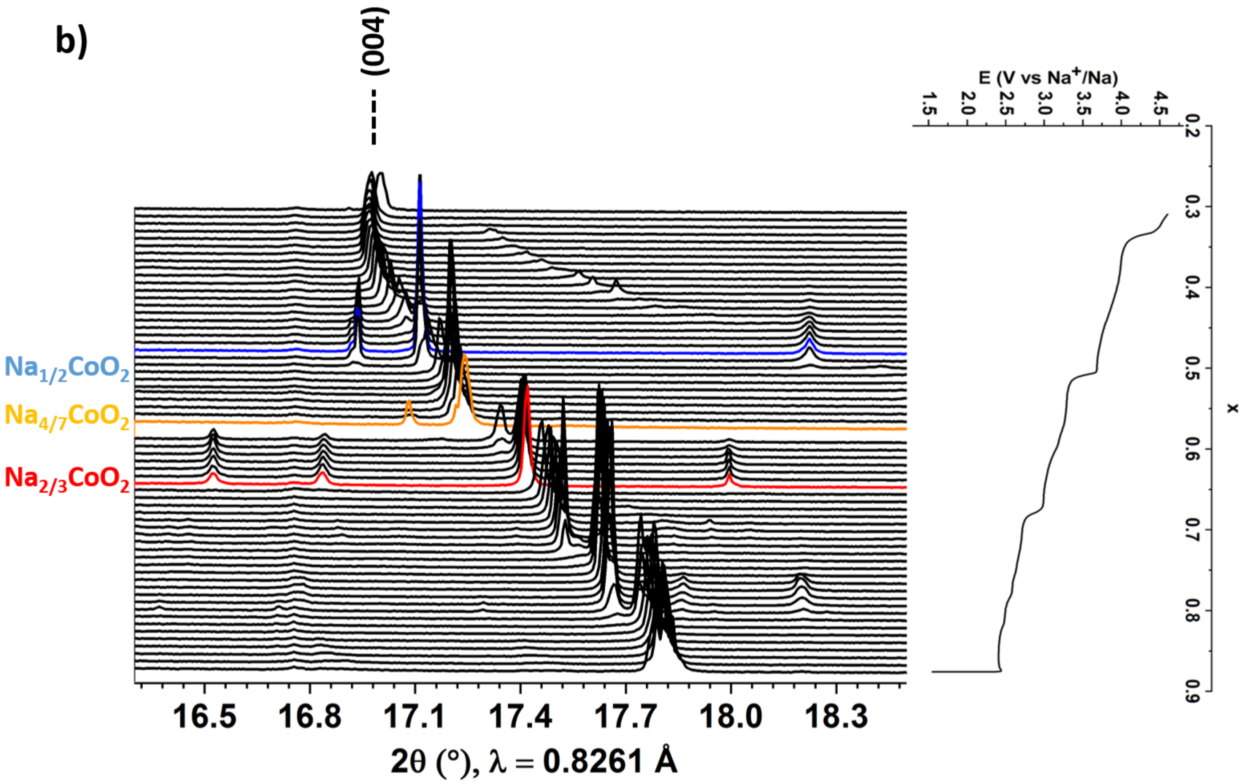

Figure IV-13: *XRD patterns obtained by operando XRD on the* Na_xCoO_2 *system on the first charge from 1.5 V to 4.6 V at C/10 (a) in the 5 – 30° range (b) in the 16.3 – 18.5° range. The colored lines represent the XRD patterns of the peculiar phases* $Na_{2/3}CoO_2$*,* $Na_{0.57}CoO_2$ *and* $Na_{1/2}CoO_2$*.*

4.1.2 PITT

The cell for this study was first charged using a C/10 regime until 4.1 V and then, different voltages from 4.1 V to 4.8 V with a step of 0.05 V were applied. The reported XRD patterns are the last one recorded at each voltage corresponding to a maximal relaxed phase (**Figure IV-14**). Note that the used cell was not the same than for the *operando* acquisitions introduced before.

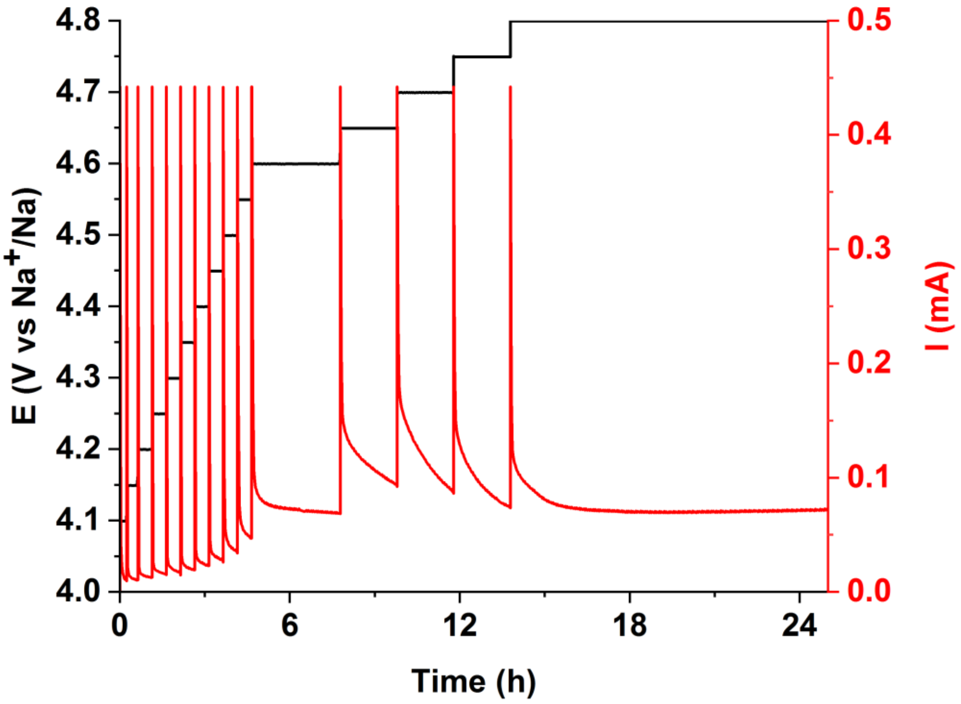

***Figure IV-14**: Voltage (in black) and current (in red) evolution during the PITT measurements on Na_xCoO_2 as a function of time*

Figure IV-16 shows the influence of the increasing voltage on the (002) peak 2θ position and lineshape and on the peaks in the 6-30° range in order to investigate possible sheets glidings. From 4.1 V to 4.55 V (black lines), the average structure remains in the P2 structure as shown by the presence of a thin P2 peak at a constant 2θ position. Note the presence of two contributions to the (002) peak from 4.3 V to 4.55 V. At 4.6 V, the P2 structure is still maintained but the (002) lines starts to broaden probably due to some "O"-type stacking faults formation. In fact, the XRD pattern traced in blue is the first to show a strong broadening of its (00ℓ) and (10ℓ) peaks. For voltages from 4.65 to 4.8 V (in red), (00ℓ) peaks almost disappear and (10ℓ) peaks are broadened and become asymmetric. Moreover, the (002) peak is largely broadened and shifted to larger angle values characteristic of a decrease of the c_{hex} lattice parameter. The peaks asymmetry and the decrease of the c_{hex} lattice parameter highlight the presence of sheets glidings leading to a strong disorder. The sheets glidings were already reported by Komaba and coworkers[128] and more recently by Billaud[130] *et al.* on other P2-systems by *ex-situ* XRD. Note that in these papers, these phases were determined in an OP4 structure considering that the Na^+ ions are intercalated in prismatic and octahedral sites after the P2-OP4 phase transition. In our study, the phase obtained at high voltage is called "OP" phase and not OP4 due to the absence of a good ordering along the c axis contrary to the phase studied in the chapter II. **Figure IV-15** shows the transition between the ideal P2 structure and the faulted "OP" one involving the formation of O-type intercalation sites. Moreover, the decrease of the c lattice parameter of the "OP" phase suggests that the thickness of the O-type interslab spaces is smaller than the thickness of the P-type interslab spaces.

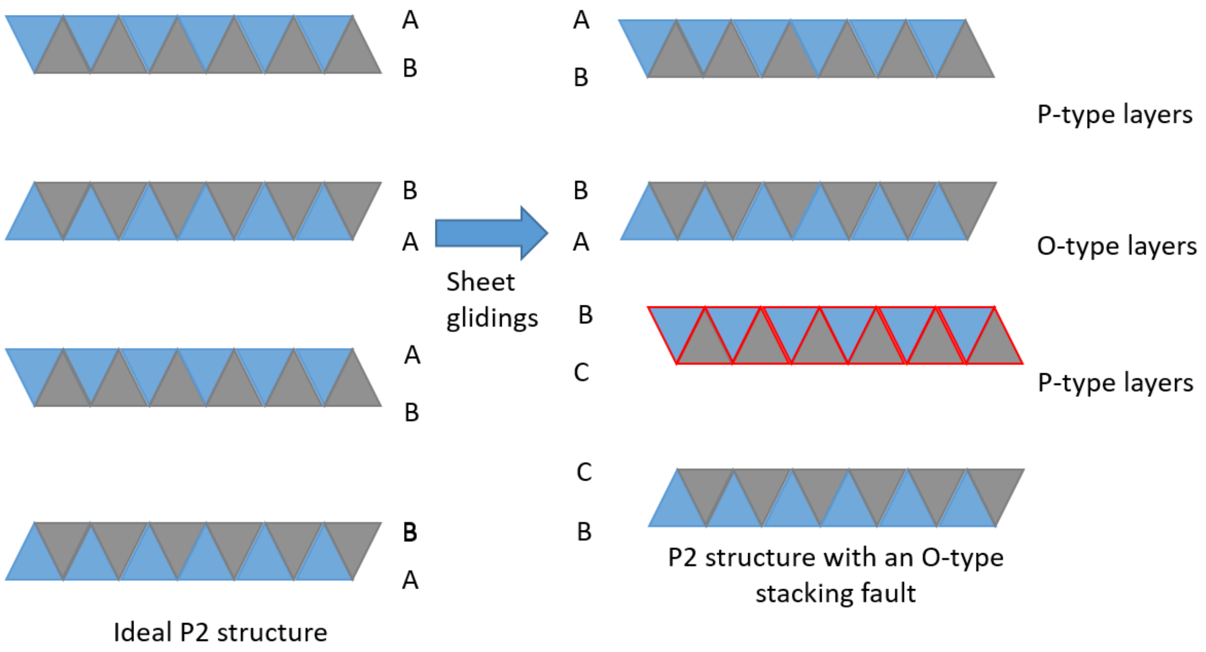

***Figure IV-15**: Representation of the CoO_2 stacking in ideal P2 structure and P2 structure with an O-type stacking fault after sheets glidings.*

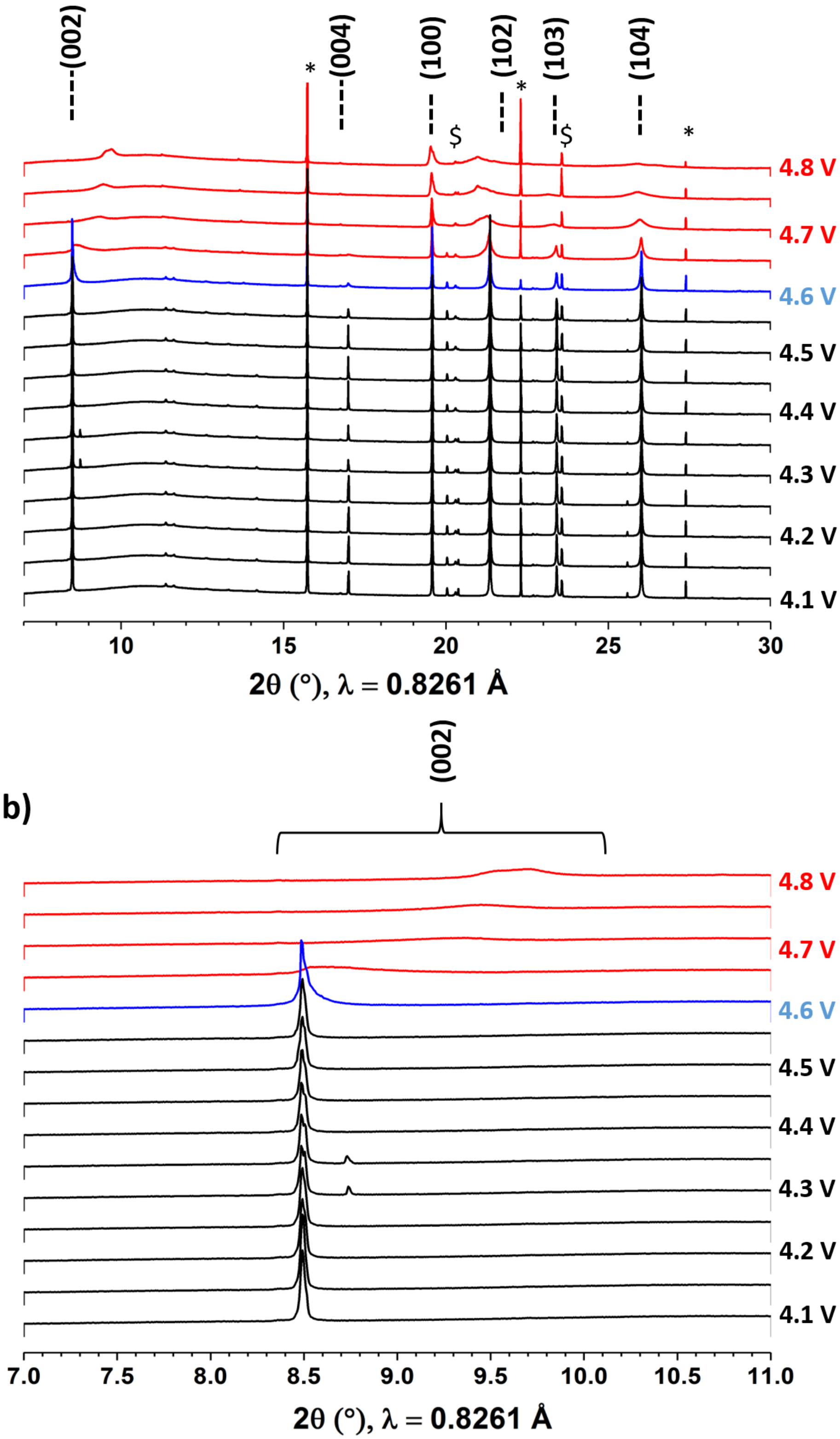

***Figure IV-16**: XRD patterns of stabilized Na_xCoO_2 phases by PITT at different voltages from 4.1 V to 4.8 V for a) $7 < 2\theta < 30°$ and b) $7 < 2\theta < 11°$. $ = Al, * = Na.*

The XRD patterns recorded during the PITT measurements allow to extract a XRD pattern of the relaxed $Na_{1/3}CoO_2$ phase before the glidings which was never reported before. The refinement was first performed in the *$P6_3/mmc$* space group representing the P2 structures (**Figure IV-17a**). The lattice parameters in the hexagonal cell are a_{hex} = 2.809(1) Å and c_{hex} = 11.20(1) Å. However, as expected, the superstructure peaks are not indexed with this space group. These peaks are highlighted by arrows on **Figure IV-17a**. In order to include the superstructure peaks in the refinement, we performed a Le Bail refinement by using the *$P6_1$* space group which also described a hexagonal cell. A good match is obtained between the refined pattern and the experimental one with a $\sqrt{3}\, a_{hex} \times \sqrt{3}\, a_{hex} \times 3\, c_{hex}$ supercell (**Figure IV-17b**). The calculated lattice parameters are: a_s = 4.867(1) Å and c_s = 33.61(1) Å. The representation in the (a,b) plane of the supercell compared to the initial hexagonal cell in the *$P6_3/mmc$* space group is plotted on **Figure IV-18**. Despite intensities not correctly refined and especially in the 10° - 14° range, it is possible to confirm than $Na_{1/3}CoO_2$ crystallizes in a hexagonal superlattice cell as predicted by many papers[113,114,124] even if the structure needs more investigations concerning its real superstructure, atomic positions …

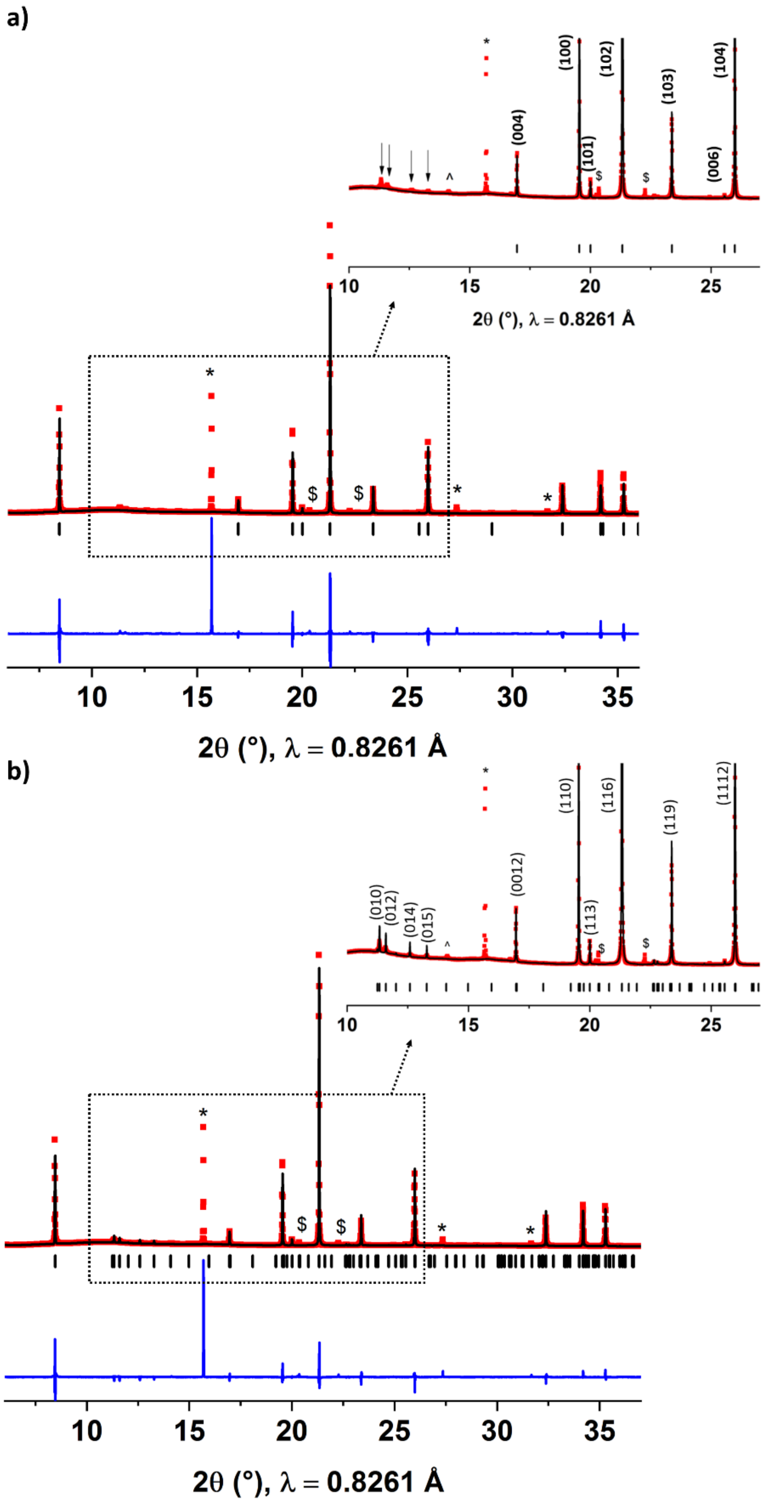

Figure IV-17: *SXRD pattern of $Na_{1/3}CoO_2$ in the (a) $P6_3/mmc$ space group (b) $P6_1$ space group. Red points = Yobs, black line = Ycalc, blue line = Yobs – Ycalc, black ticks = Bragg positions. Insert highlights the presence of superstructure peaks. $ = Al, * = Na, ^ = C.*

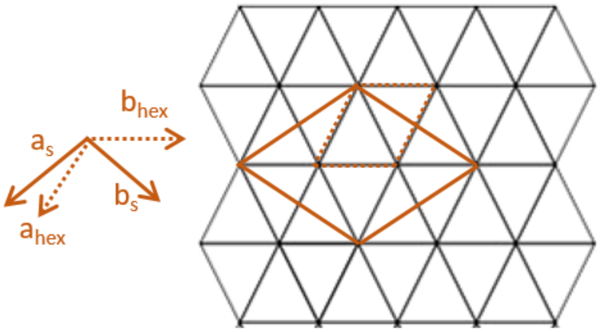

Figure IV-18: *Representation in the (a,b) plane of the initial hexagonal cell (solid line) and the superstructure hexagonal cell (dashed line)*

4.2 $Na_xCo_{2/3}Mn_{1/3}O_2$ system

The first charge following the first discharge from a P2-$Na_{\sim 2/3}Co_{2/3}Mn_{1/3}O_2$ // Na cell has also been studied by *operando* synchrotron XRD from 1.25 V to 4.5 V at a rate of C/10. As for the Na_xCoO_2 system, the 2θ positions of the (002) and (004) peaks decrease during the Na^+ ions deintercalation indicating a global increase of the c_{hex} lattice parameter during the charge (**Figure IV-19**). The system also reaches a limit c_{hex} value for x = 0.4 (11.30(1) Å). This system is less complex than Na_xCoO_2, in fact, only few superstructure peaks appear during the charge to 4.5 V. For $0.67 < x < 0.8$ many contributions are observed as seen in the red frame zooms. The ionic and electronic conductivities in this composition are probably worth than for $x < 0.67$ leading to composition heterogeneities in the electrodes. Indeed, for $x > 2/3$, no Co^{4+} is present that usually leads to conductivity improvement and the system exhibits less Na vacancies. Globally, $Na_xCo_{2/3}Mn_{1/3}O_2$ has a solid solution behavior with only one clear ordered phase at x = 1/2. $Na_{1/2}Co_{2/3}Mn_{1/3}O_2$ (red XRD pattern), in first approximation, was Le Bail refined in the same space group than $Na_{1/2}CoO_2$ (*Pnmm)* and with same relation between the hexagonal lattice parameters and the orthorhombic one ($\sqrt{3}\, a_{hex}$ x 2 a_{hex} x c_{hex}). **Figure IV-20** shows the refinement of the SXRD data recorded on this phase. The calculated lattice parameters with the *Pnmm* space group are a_s = 4.8848(6) Å, b_s = 5.6171(9) Å and c_s = 11.257(2) Å. All the diffraction peaks are indexed with this supercell except one tiny additional peak on the right of (123) and (203) peaks corresponding probably to the formation of another phase. It is the first time, that an XRD pattern of an ordered phase on this system is reported.

Note that no obvious superstructure peak appears for x = 1/3 in our conditions while the voltage jump is well-defined on the galvanostatic curve. The blue arrow represents the appearance of an additional peak at 2θ = 9.2°. This peak indicates probably the formation of a defected "OP" phase due to the CoO_2 sheet glidings as also observed on **Figure IV-16.** The discharge of the cell following the experiment presented is given in the Appendix part (**A-5**).

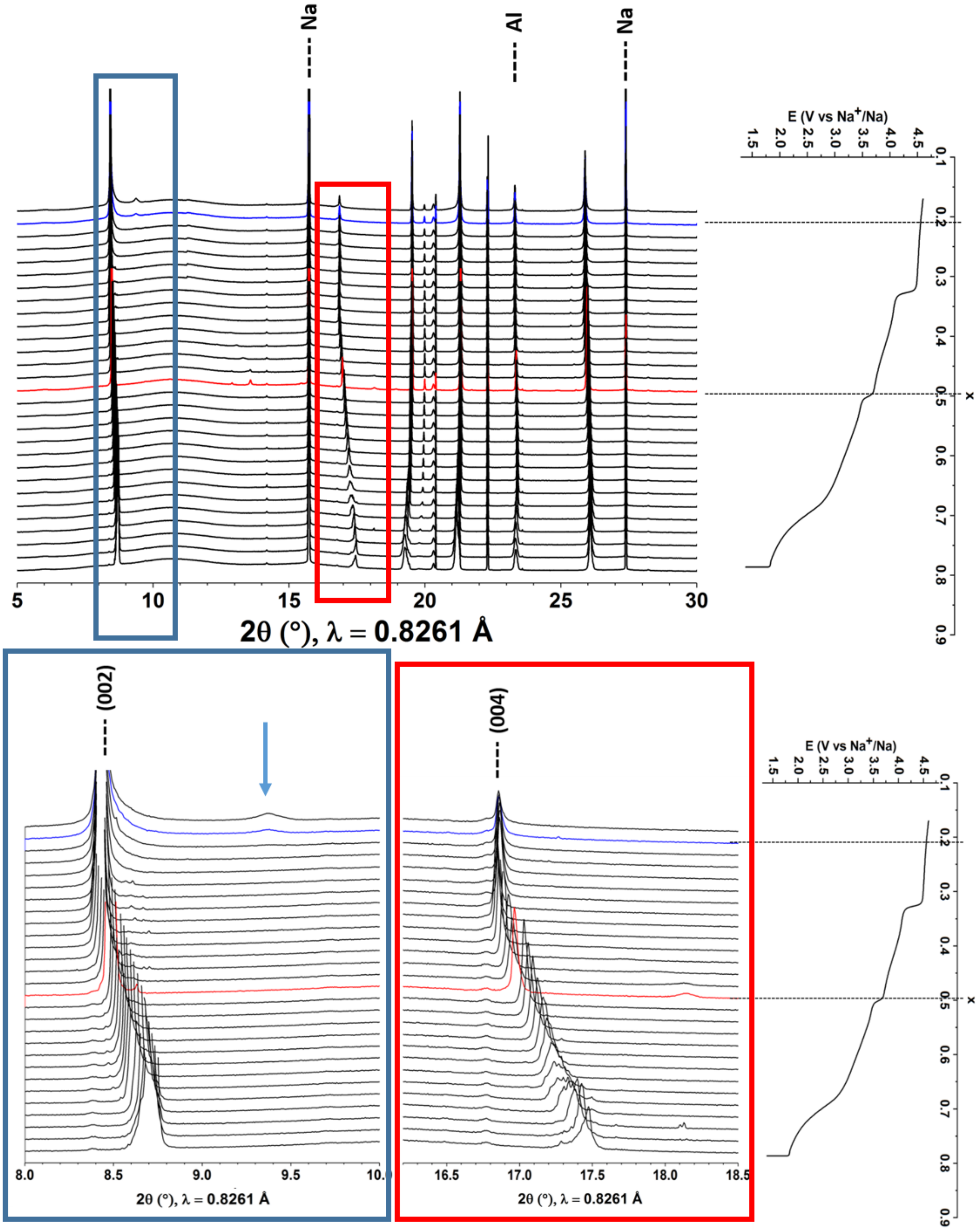

Figure IV-19: *XRD patterns obtained during the operando measurements on the* $Na_xCo_{2/3}Mn_{1/3}O_2$ *system on the first charge from 1.25 V to 4.5 V at C/10*

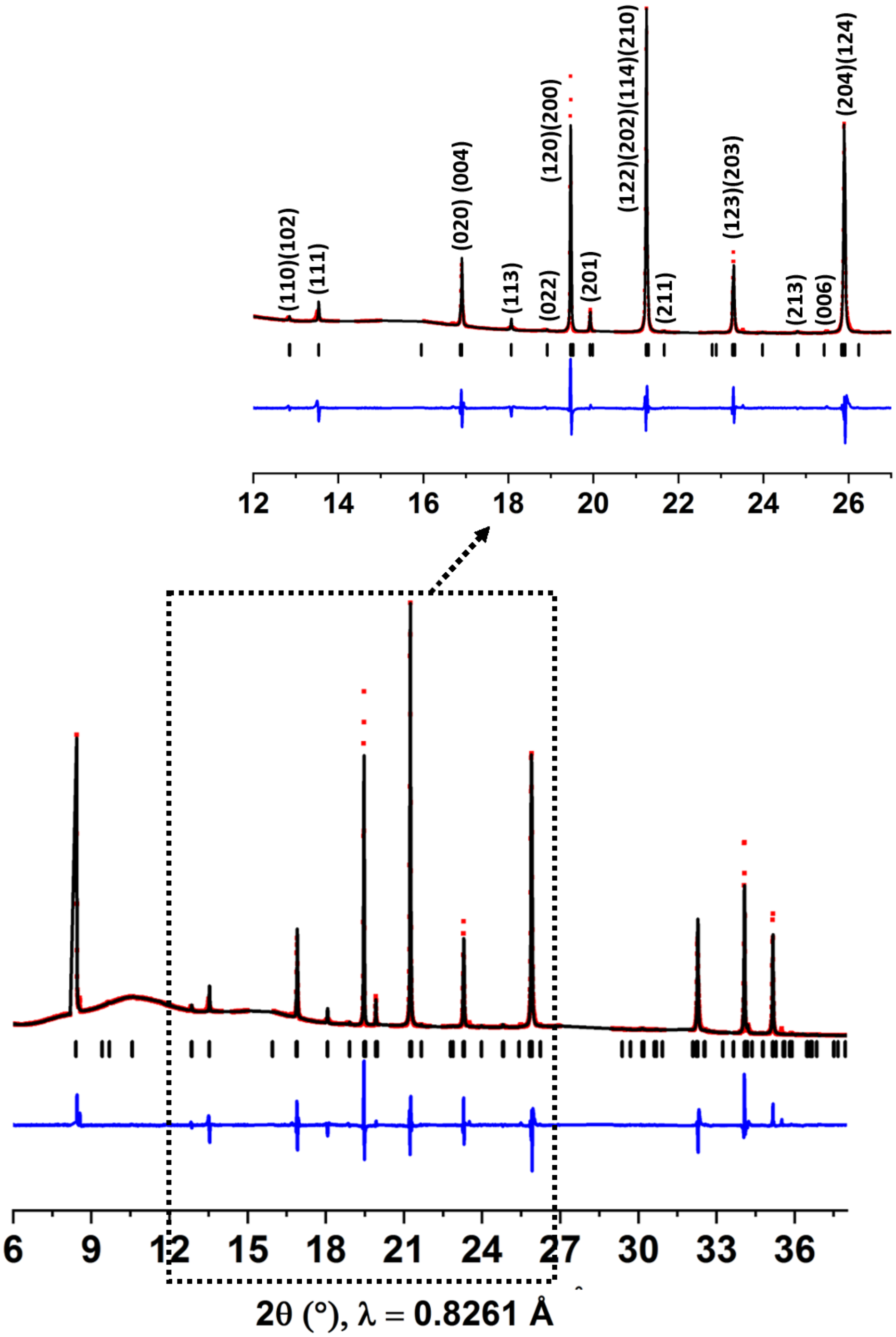

Figure IV-20: *SXRD pattern of $Na_{1/2}Co_{2/3}Mn_{1/3}O_2$ in the Pnmm space group. Red points = Yobs, black line = Ycalc, blue line = Yobs – Ycalc, black ticks = Bragg positions. Insert highlights the the presence of superstructure peaks.*

4.3 $Na_xCo_{1/2}Mn_{1/2}O_2$ system

The first charge following the first discharge from a P2-$Na_{\sim 0.6}Co_{1/2}Mn_{1/2}O_2$ // Na cell has also been studied by *operando* synchrotron XRD from 1.25 V to 4.5 V at a rate of C/10. The first charge is reported in this manuscript (**Figure IV-21**). Again, the P2-structure is maintained in the $0.18 < x < 0.7$ range. As previously showed, the galvanostatic curve only exhibits one voltage jump for $x = 1/3$ and a slope change around $x = 1/2$. Globally, the (002) and (004) peaks evolution denotes an increase of the c_{hex} lattice parameter during the charge. For $0.45 < x < 0.7$, an important heterogeneity in the electrodes is also at the origin of the presence of many contributions as seen in the red framed zoom. As for the $Na_xCo_{2/3}Mn_{1/3}O_2$ system, no Co^{4+} should be present in this particular range involving bad ionic and electronic conductivities. For $x < 0.45$, the expected presence of Co^{4+} ions improves the conductivity in the electrode and leads to the observation of one well-defined (004) peak (blue framed zoom). Moreover, a solid solution behavior can be observed. The system reaches a c_{hex} lattice parameter maximal value at $x \approx 0.4$ (11.33(1) Å). The zoom in the 13.5 – 14° range highlights the presence of a superstructure peak appearance for x around 1/3 on the red XRD pattern which corresponds to the formation of the $Na_{1/3}Co_{1/2}Mn_{1/2}O_2$ peculiar phase. A Le Bail refinement was realized on the XRD data of this phase using the same space group than for $Na_{1/3}CoO_2$. However, we are not able to refine correctly the XRD pattern of this phase with the *$P6_3/mmc$* space group due to a possible distortion of the corresponding cell.

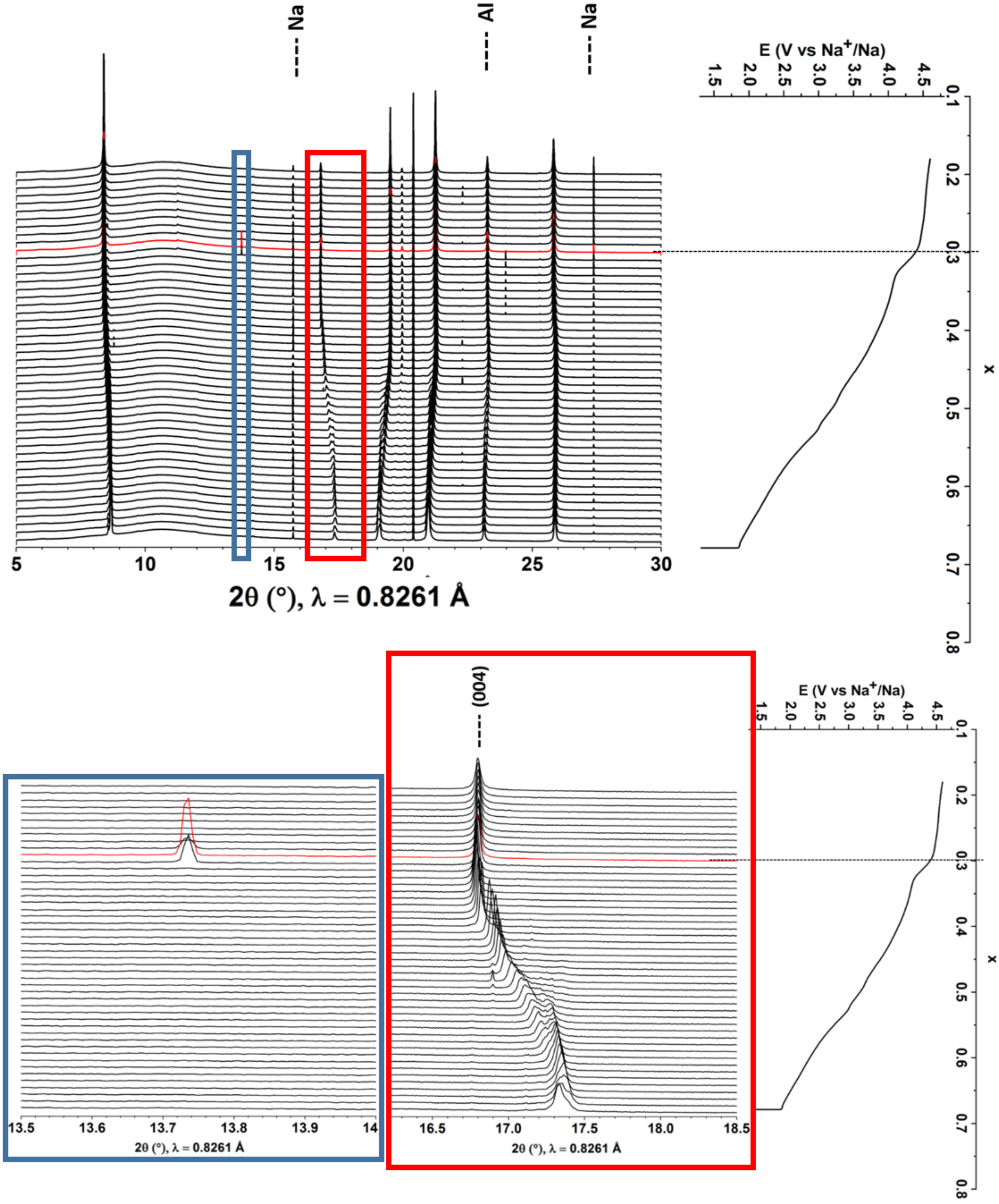

***Figure IV-21**: XRD patterns obtained by operando measurements on $Na_xCo_{1/2}Mn_{1/2}O_2$ system on first charge from 1.25 V to 4.5 V at C/10.*

4.4 $Na_xCo_{1/3}Mn_{2/3}O_2$ system

The first charge following the first discharge from a P2-$Na_{\sim 0.6}Co_{1/3}Mn_{2/3}O_2$ // Na cell has also been studied by *operando* synchrotron XRD from 1.25 V to 4.5 V at a rate of C/10. **Figure IV-22** displays the XRD patterns obtained *operando*. As expected, the c_{hex} lattice parameters globally increases until a limit value reached for $x \approx 0.4$ (11.35(1) Å). The (004) peak evolution suggests that this system has a solid solution behavior during all the charge. The presence of many contributions on the XRD patterns suggests an important heterogeneity as observed on the previously studied Co,Mn systems. This heterogeneity can be observed in the $0.71 < x < 0.36$ range. For $x < 0.36$, a well-defined (004) peak is visible on the XRD patterns, probably to the appearance of Co^{4+} ions. As expected, regarding the galvanostatic charge, no superstructure peak appears during the charge on any pattern.

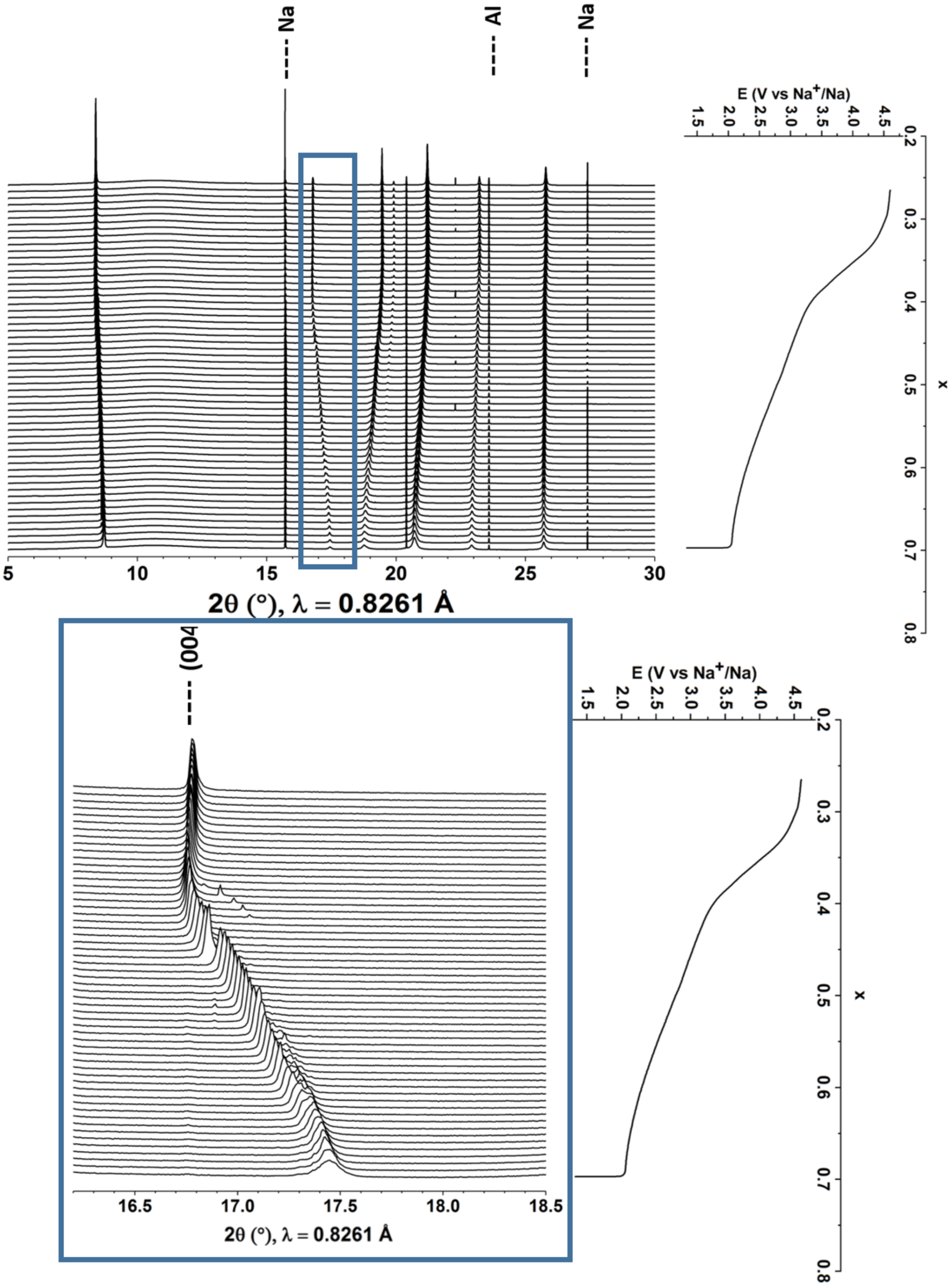

Figure IV-22: *XRD patterns obtained by operando measurements on* $Na_xCo_{1/3}Mn_{2/3}O_2$ *system on first charge from 1.25 V to 4.5 V at C/10.*

4.5 Discussion

To summarize the results extracted from this study for the four P2-Na_xMO_2 (M = Co,Mn) systems: the P2-structures remain during the Na^+ deintercalation with our acquisition conditions at C/10. For each system, a maximal c_{hex} value is reached for x around 0.4. The lattice parameters in **Table IV-6** correspond to the calculated values from Le Bail refinements realized on the XRD patterns on which the (004) peaks is at its minimal 2θ position. As expected, the c_{hex} lattice parameters has increased and the a_{hex} lattice parameters has decreased compared to their initial values (**Table IV-4**). In **Figure IV-23**, the evolution of the c_{hex} lattice parameters is plotted as a function of x for the four systems. Concerning the Co,Mn phases, the evolution of c_{hex} confirms the presence a solid solution behavior while for Na_xCoO_2, many breaks in the Vegard law can be observed due to the presence of different kinds of domains. Moreover, the Na_xCoO_2, $Na_xCo_{1/2}Mn_{1/2}O_2$ and $Na_xCo_{1/3}Mn_{2/3}O_2$ XRD patterns don't exhibit any obvious sheets glidings during the *operando* measurements even at high voltage. However, for $Na_xCo_{2/3}Mn_{1/3}O_2$, the additional peak observed at 9.2° shows that sheets glidings occur for x ≈ 0.2.

	Na_xCoO_2	$Na_xCo_{2/3}Mn_{1/3}O_2$	$Na_xCo_{1/2}Mn_{1/2}O_2$	$Na_xCo_{1/3}Mn_{2/3}O_2$
Studied voltage range	1.5 V – 4.6 V	1.25 V – 4.5 V	1.25 V – 4.5 V	1.25 V – 4.5 V
Minimal a_{hex} (Å)	2.810(1)	2.818(1)	2.822(1)	2.828(1)
Maximal c_{hex} (Å)	11.20(1)	11.30(1)	11.33(1)	11.35(1)
Maximal c_{hex} value reached for x ≈	0.4	0.4	0.4	0.4
Maximal c_{hex} value reached for V ≈	4 V	4 V	3.8 V	3.5 V

***Table IV-6**: Lattice parameters calculated from refinements on the last XRD patterns data and the voltage and x values corresponding to the reach of the maximal c_{hex} value for each system.*

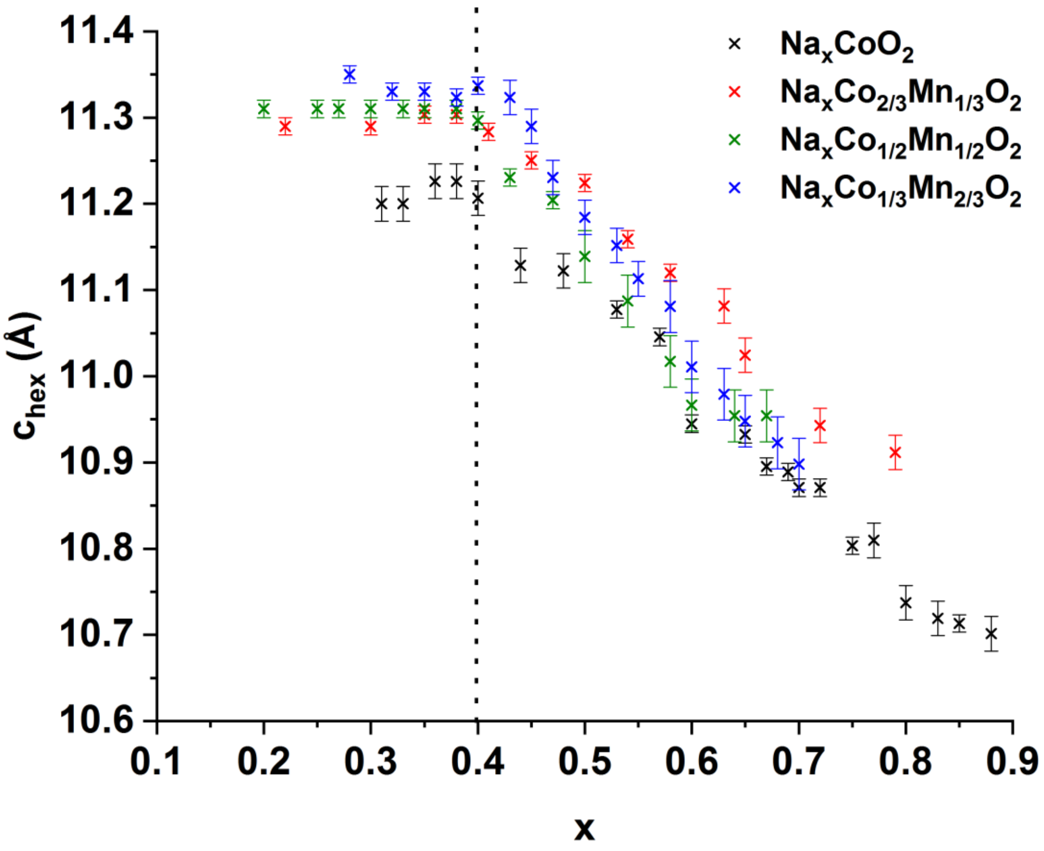

Figure IV-23: *Evolution of c_{hex} lattice parameter as a function of x for the four systems*

5. Conclusion

In this chapter, we studied the electrochemical performances and the evolution of the average structures of four systems $Na_xCo_yMn_{1-y}O_2$ for y = 2/3, 1/2, 1/3 and 1 by *operando* high-resolution XRD. The recent addition of FEC in electrolyte formulation allows to reach higher voltages on these systems than in the previous studies. The *operando* measurements showed the remaining of the P2 structure for each system in the studied voltage ranges at C/10. The presence of sheets glidings was also highlighted on relaxed Na_xCoO_2 phases for $x < 1/3$. Concerning the P2-Na_xCoO_2 system, previously, 9 monophasic domains were determined for x between 0.5 and 1. For $x < 0.5$, the system remains complex and one obvious peculiar phase can be highlighted for $x = 1/3$. The Co_yMn_{1-y} systems have a solid solution behavior during all the Na^+ deintercalation despite an important heterogeneity in the electrodes before the oxidation of Co^{3+} into Co^{4+}. For specific compositions, peculiar phases were also observed. These new peculiar phases were evidenced for $Na_{1/3}CoO_2$, $Na_{1/3}Co_{1/2}Mn_{1/2}O_2$ and $Na_{1/2}Co_{2/3}Mn_{1/3}O_2$ by voltage jumps on the galvanostatic curves and by the appearance of superstructures peaks on the XRD patterns. The refinements need to be performed again on relaxed phases to have a better insight of the real structure of these phases but it seems that the $x = 1/2$ phases crystallize in an orthorhombic cell in the *Pnmm* space group. $Na_{1/3}CoO_2$ was also successfully refined in the $P6_1$ space group.

After focusing on the average structures, we will study the local structure evolution, in the next chapter, thanks to ^{23}Na MAS NMR, of the P2-Na_xCoO_2 and P2-$Na_xCo_{2/3}Mn_{1/3}O_2$ systems.

Chapter V: ^{23}Na MAS NMR Study of P2-Na_xMO_2 (M = Co, $Co_{2/3}Mn_{1/3}$) phases: new insight on the intercalation/deintercalation mechanisms

1. Introduction

The previous chapter proposed a study of the average structural evolution of $Na_xCo_yMn_{1-y}O_2$ systems upon cycling. In this chapter, we focus on the study of the local structure and electronic structure evolution of P2-Na_xCoO_2 and P2-$Na_xCo_{2/3}Mn_{1/3}O_2$ systems upon charging.

MAS NMR has been shown to be a key tool to investigate the deintercalation mechanisms in many battery materials[29,30,33,40,131–136]. In 1999, Ménétrier *et al.*[91] in our group, proposed a deep investigation of the Li_xCoO_2 system by ^7Li MAS NMR (**Figure V-1**). They assigned the signal at 0 ppm of O3-$LiCoO_2$ to Li^+ surrounded by diamagnetic Co^{3+} (t_{2g}^6 e_g^0) in their low spin configuration. They synthesized the different Li_xCoO_2 phases in the $0.5 \leq x < 1$ by electrochemical deintercalation in order to perform *ex-situ* ^7Li MAS NMR. They showed that the 0 ppm signal remains the only one in the $0.94 \leq x < 1$ range despite the oxidation of the Co^{3+} into paramagnetic Co^{4+} (t_{2g}^5 e_g^0). However, its intensity strongly decreases when x decreases in this particular range. The single electron in the electronic configuration of Co^{4+} is in one of the t_{2g} orbital pointing directly in the direction of the 2s orbital of the first Li^+ ions neighbor through a common edge of the LiO_6 and CoO_6 octahedra (**Figure V-1c**). In this case, the strong hyperfine interaction leads to the loss of the signal on the NMR spectra. Therefore, ^7Li MAS NMR showed, that in the $0.94 \leq x \leq 1$ composition range, the electrons have a localized behavior. Moreover, an additional signal can be observed at 57 ppm on the x = 0.94 spectra. In the $0.75 < x < 0.94$ range, the intensity of the 0 ppm and 57 ppm signals, respectively, decreases and increases when x decreases indicating the presence of a two-phase region. This biphasic behavior is also visible on the Li_xCoO_2 galvanostatic curve by the presence of a voltage plateau in this particular range. For $x < 0.75$, the signal at 0 ppm disappears and the 57 ppm signal is shifted to higher values when x decreases indicating the presence, in the material, of delocalized electrons with an increasing participation of the Li 2s orbital to the Knight shift. ^7Li MAS NMR highlighted in this study the modification of the hyperfine interaction nature from a paramagnetic contact shift to a Knight shift upon Li^+ deintercalation. Note that ^7Li MAS NMR has been successfully applied to study the deintercalation mechanisms in many other systems[74,137].

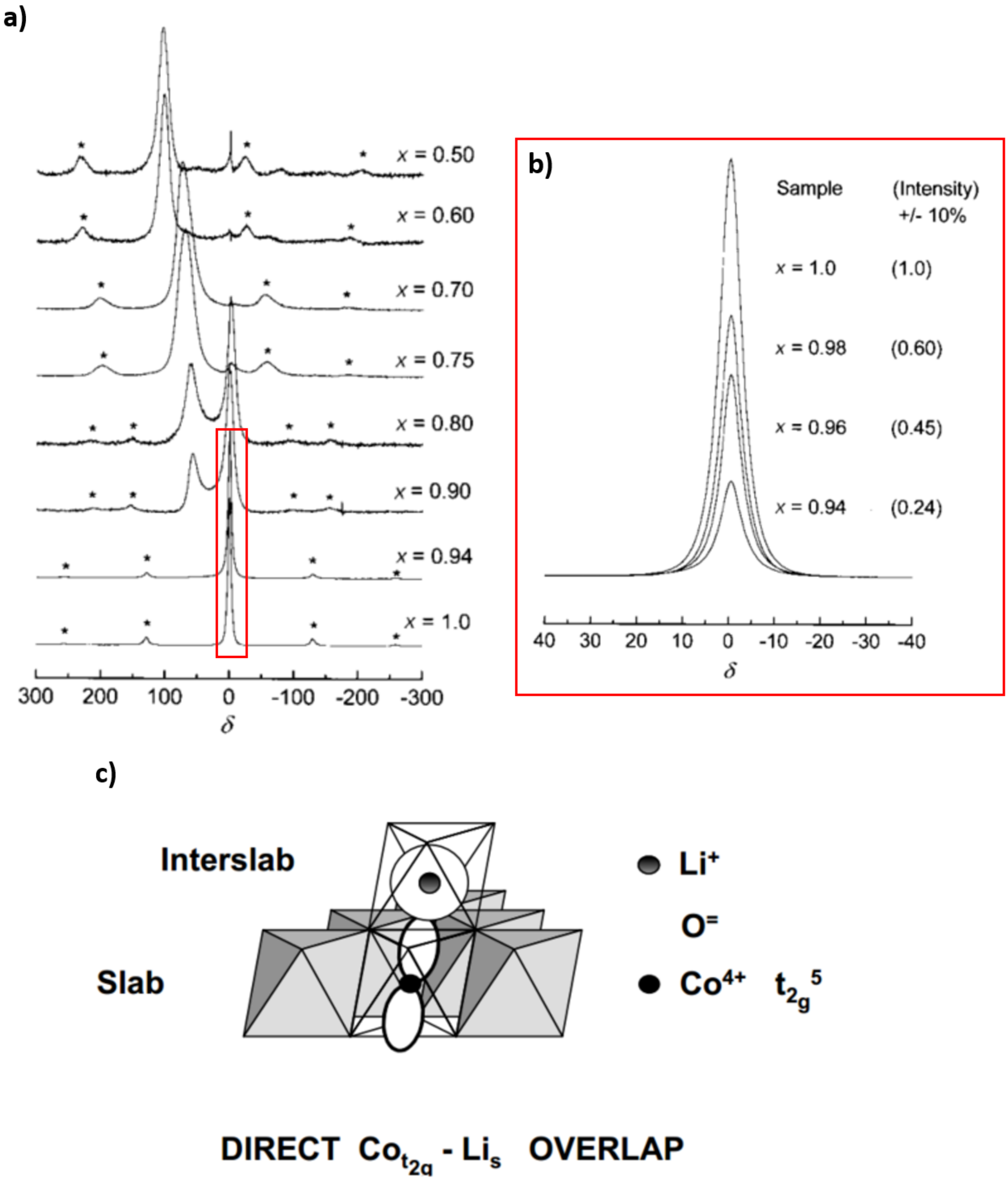

Figure V-1: *(a) ^{7}Li MAS NMR spectra of the Li_xCoO_2 phases for $0.5 \leq x \leq 1$. * represents the spinning side bands. (b) ^{7}Li MAS NMR spectra from x = 0.94 to x = 1 in the -40 - 40 ppm range. Reported from reference [91]. (c) Representation of the direct overlap between a single electron from the t_{2g} orbital of Co^{4+} and the 2s Li orbital*

^{23}Na MAS NMR can be also used to probe the local structure and electronic structure in battery materials eventhough the resolution of the spectra is not as good as obtained for ^{7}Li due to the strong quadrupolar moment of ^{23}Na compared to ^{7}Li (**Table I-2**). In 2009, Carlier *et al.*[94] reported a NMR study of the P2-Na_xCoO_2 system for $0.55 \leq x \leq 0.75$. All the phases were obtained by direct powder synthesis. The shape of the signal is governed by the 2nd order quadrupolar interaction whereas the position is governed by the hyperfine interaction. Moreover, the P2-structure is characterized by the presence of two signals for Na^+ intercalation: Na_e and Na_f (**Figure I-3**). As depicted on **Figure V-2b**, each site has its own Electric Field Gradient value with the main contribution (V_{zz}) along the c axis. When moving from a site to another, the Na^+ ions are surrounded by three other sites. Therefore, the presence of this 3-fold axial symmetry with the same direction than V_{zz} leads to an average chemical shift between both V_{zz} contributions. Note that the phase for $x_0 = 0.88$ is out of range of the P2 existence. Therefore, the diamagnetic signal is due to an important amount of remaining precursors. The real composition of this phase is, however, unclear. They showed that the NMR shift values increase when x decreases in good agreement with the oxidation of diamagnetic Co^{3+} into paramagnetic Co^{4+} considering the phases in a Curie-Weiss regime with localized electrons and delocalized electrons at the Fermi level. (**Figure V-2a**).

The ^{23}Na NMR MAS spectra of P2-$Na_{2/3}Co_{2/3}Mn_{1/3}O_2$ pristine material has been studied, in our group by Carlier *et al.*[45], and compared to P2-$Na_{2/3}CoO_2$ (**Figure V-3**). As also observed on P2-$Na_{2/3}CoO_2$, the P2-$Na_{2/3}Co_{2/3}Mn_{1/3}O_2$ spectra has a broad lineshape because of the 2nd order quadrupolar interaction. Moreover, the NMR shift value is higher as Mn^{4+} ions (t_{2g}^3 eg^0) carries 3 unpaired electrons vs 1 electron for Co^{4+}.

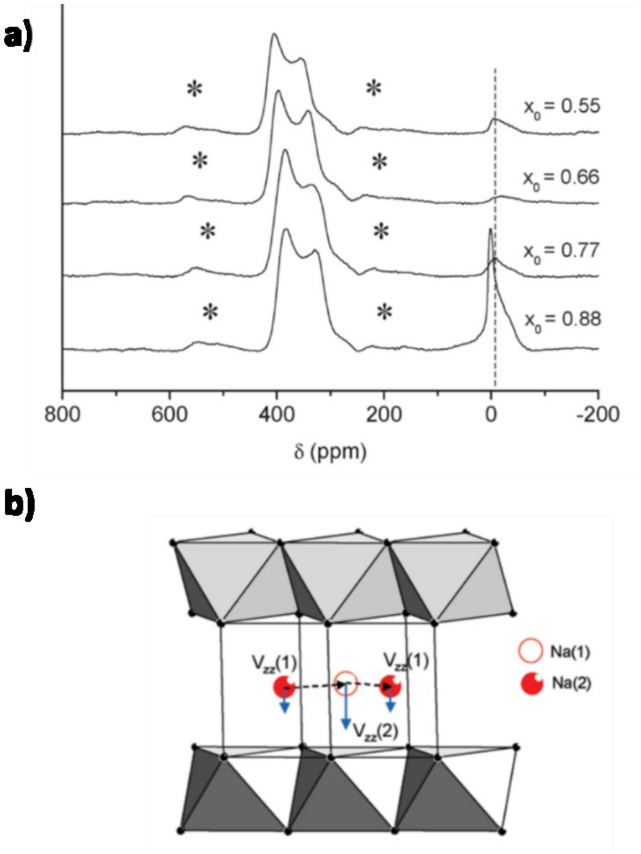

Figure V-2: *(a) ^{23}Na MAS NMR spectra of the P2-Na_xCoO_2 samples (b) Diffusion pathway of the Na^+ ions in the P2 stacking. From reference [94].*

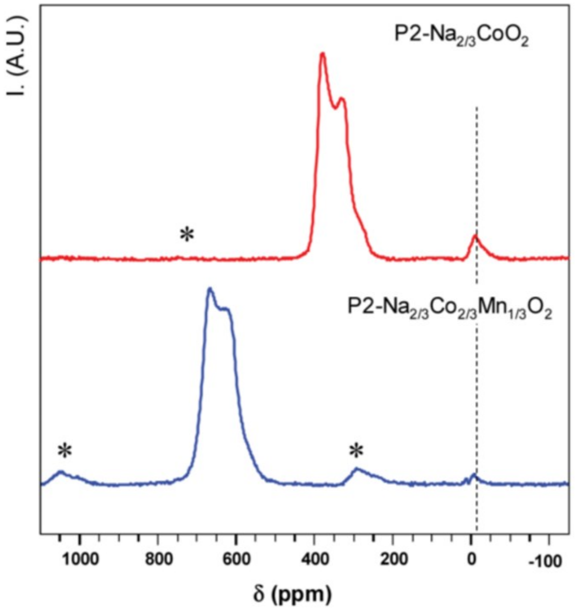

Figure V-3: *^{23}Na MAS NMR spectra of both pristine phases recorded on a 7.05 T magnet with a spinning frequency of 30 kHz. * are the spinning side bands. From reference [45].*

More recently, Raphaële Clément and collaborators (C. Grey group) investigated different systems that can be used as positive electrode materials for Na-ion batteries. They studied different phases with various Na^+ content by *ex-situ* ^{23}Na MAS NMR in order to understand the mechanisms occurring during the Na^+ (de)intercalation and to have an insight of the local structure and electronic structure evolution of the different materials[39,138–141]. The particularity of their works is that the different phases were synthetized by electrochemical (de)intercalation for different Na^+ contents in order to characterize them. They studied, for example, different amounts of Mg^{2+} ion doping in P2-Na_xMnO_2 by *ex-situ* MAS NMR in order to understand the mechanisms involved by this doping and why its leads to a significant enhancement of the electrochemical properties[140]. Moreover, they also studied high voltage Na_xMnO_2 phases ($x < 0.3$) that underwent some sheet glidings: the signals are largely broadened due to the panel of new environments involved by the glidings. They investigated the role of the dopants on these high voltage phase transitions: Li as dopant in $Na_xNi_zMn_{1-z}O_2$ systems[39] or Mg in Na_xMnO_2[140]. In this chapter, the P2-Na_xCoO_2 and P2-$Na_xCo_{2/3}Mn_{1/3}O_2$ systems were investigated in the same vein. In fact, we synthetized different phases by electrochemical deintercalation and we analyzed them by *ex-situ* XRD and *ex-situ* ^{23}Na MAS NMR in order to investigate the mechanisms occurring during the charge of both systems.

2. P2-Na_xCoO_2 and P2-$Na_xCo_{2/3}Mn_{1/3}O_2$ systems

2.1 ^{23}Na MAS NMR spectra of the pristine phases

Figure V-4 displays the ^{23}Na MAS NMR spectra of both pristine phases discussed in the previous chapter. The measurements were performed using a single pulse sequence on a 7.05 T magnet with a spinning frequency of 30 kHz in the conditions than in reference [45]. The spectral width was set to 1 MHz, and the recycle time $D_0 = 0.5$ s, is long enough to avoid T_1 saturation effects. The same lineshape due to the 2nd order quadrupolar interaction are observed for the $Na_{\sim 0.7}CoO_2$ spectrum than in the previous work. **Table V-1** summarizes the shift position, the quadrupolar constant and the anisotropy value for our $Na_{\sim 0.7}CoO_2$ sample, fitted on the experimental spectrum using the software DMFit[65]. **Figure V-5** shows a relative good match between the experimental and the fitted spectrum with a quadrupolar lineshape. η reaches a non-negligible value meaning that the sites exhibit a low axial dissymmetry: the Na^+ ions are not exactly in the center of the prismatic sites in average. Moreover, the position of the signal at 351 ppm is in agreement with the previous data (around 350 ppm at RT[94]) (**Figure V-3)**. Concerning the P2-$Na_{\sim 2/3}Co_{2/3}Mn_{2/3}O_2$ phase, the signal is broader and the lineshape is different than in **Figure V-3**, possibly due a highest distribution of the Na^+ environments in our phase due to less random distribution of the Co^{3+} and Mn^{4+} ions in the transition metal layers. Moreover, on the synchrotron XRD pattern of this phase (**Figure IV-7b**), the (002) peak exhibits a shoulder on its right indicting a heterogeneity in the pristine material or a composition slightly different from 2/3 in a biphasic domain. The lineshape observed on the NMR spectrum (**Figure V-4**) is therefore, due to a more important number of environments than on spectrum showed in **Figure V-3.**

	$\boldsymbol{Na_{\sim 0.7}CoO_2}$	$\boldsymbol{Na_{\sim 2/3}Co_{2/3}Mn_{2/3}O_2}$
δ_{iso}(ppm)	351(1)	569(1)
ν_Q (MHz)	2.04(1)	-
η	0.18(1)	-

Table V-1: *NMR parameters of both pristine phases calculated by two fits on the spectra shown in* ***Figure V-4***

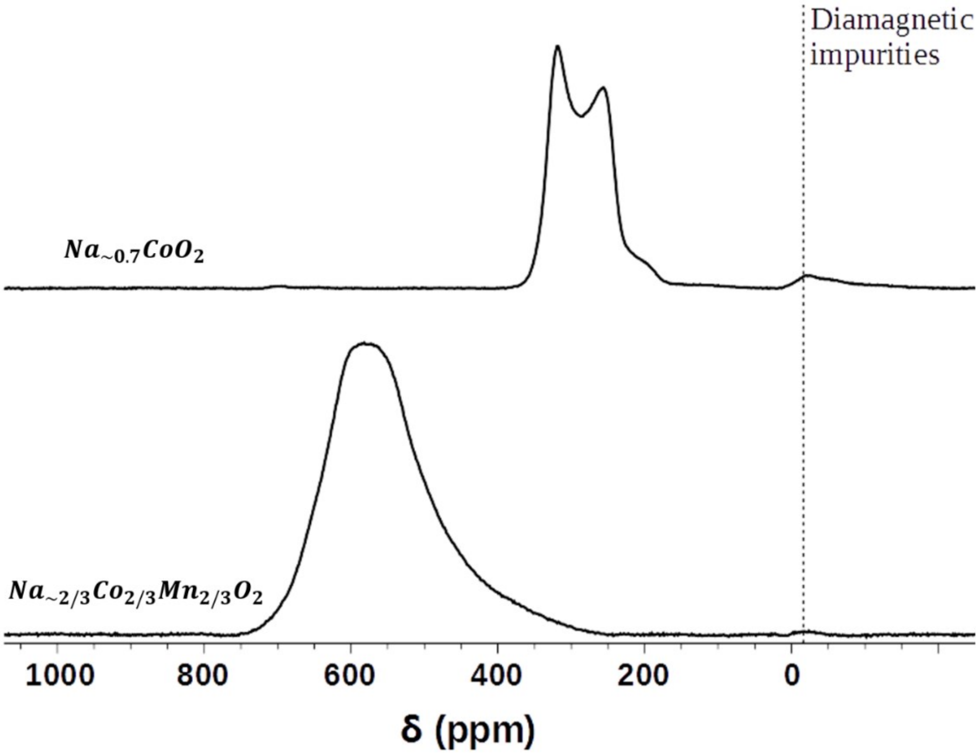

Figure V-4: *^{23}Na MAS NMR spectra of P2-$Na_{\sim 0.7}CoO_2$ and P2-$Na_{\sim 2/3}Co_{2/3}Mn_{2/3}O_2$ on a 7.05 T magnet at a spinning frequency of 30 kHz with a single pulse sequence.*

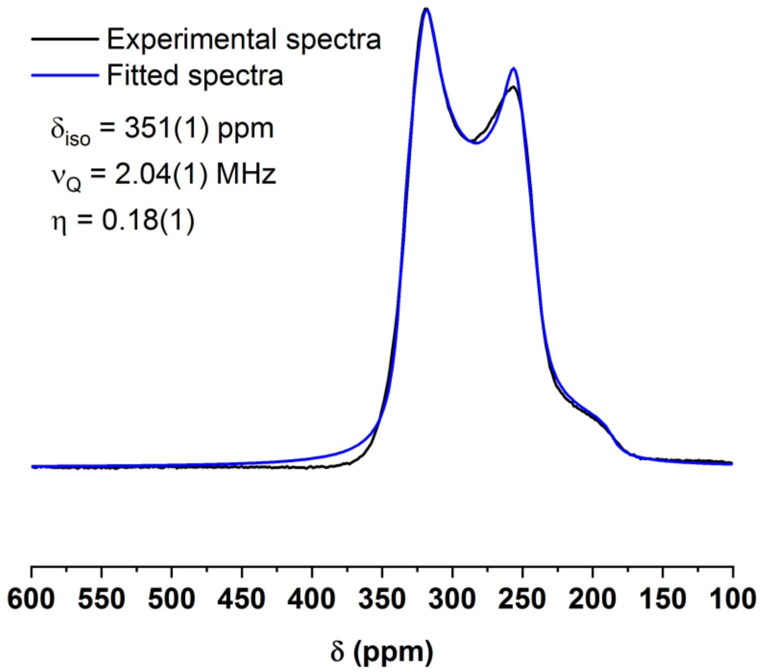

Figure V-5: *Experimental and fitted NMR signal using a 2nd order quadrupolar lineshape realized on the Na_xCoO_2* pristine phase *spectrum*

2.2 Synthesis of the Na_xMO_2 phases

In order to study the mechanisms involved during the Na^+ deintercalation by *ex-situ* ^{23}MAS NMR, different Na_xCoO_2 and $Na_xCo_{2/3}Mn_{1/3}O_2$ phases were synthetized by electrochemical (de)intercalation with a precise control of the voltage. These syntheses were performed in an airtight electrochemical cell represented on **Figure V-6.** The positive electrode, negative electrode and the electrolyte were assembled in the cell and tightened between two screws which were also the current collectors. The assembly was realized in an Ar-filled glovebox. This kind of cell is easier to open after the electrochemical (de)intercalation than the sealed coin cells. Usually, the positive electrodes were a mixture of 90 mg of active material and 10 mg of black carbon. PTFE as binder couldn't be used due to the impossibility to pack correctly a capillary for the XRD characterizations. As no binder was used, the mixture was pressed into pellets in the glovebox to form a dense positive electrode. The electrolyte was $NaPF_6$ in 1 M PC + 2 % FEC and the negative electrode was metal sodium. The electrochemical syntheses were realized in two steps as already described on **Figure I-13**. The galvanostatic step was performed at C/20 to the targeted voltage. **Figure V-7** displays an example of typical curves obtained on the P2-Na_xCoO_2 system. In this example, the new phase was synthetized at 4.2 V from $Na_{\sim 0.7}CoO_2$ to reach the x = 1/3 composition. The black curve represents the voltage evolution as a function of time with a similar shape than the galvanostatic curve introduced in the previous chapter. In fact, the same voltage jumps and domains than on **Figure IV-8a** are seen. The red curve shows the current evolution and its relaxation during the potentiostatic step. Once this second step finished, the cell was disconnected and entered in the glovebox where its voltage was measured to be assured that the synthetized phase didn't evolve after the battery disconnection. The cell was, then, opened and the positive electrode powder was washed with DiMethyl Carbonate. Note that, usually, the half of the 100 mg of initial powder was lost during the pelleting or in the separators. The remaining amount of powder was enough to fill, at least, a 0.3 mm diameter capillary for XRD acquisitions and a 2.5 mm diameter rotor for ^{23}Na MAS NMR acquisitions, so that the characterizations presented in this chapter have been done on a same electrode material for a given voltage. Note that for the $Na_xCo_{2/3}Mn_{1/3}O_2$ synthesis, the carbon additive was only composed of soot that's why the graphite impurities are only observed on the Na_xCoO_2 XRD patterns.

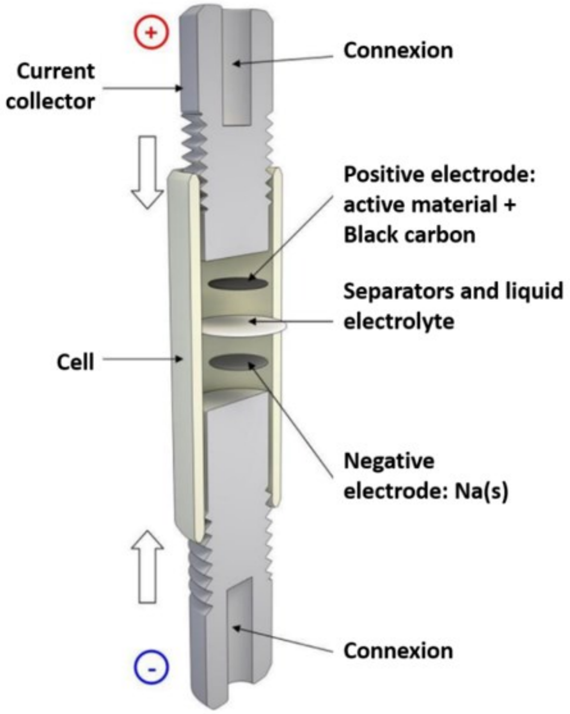

Figure V-6: *Representation of the electrochemical cell used for the synthesis of (de)intercalated phases*

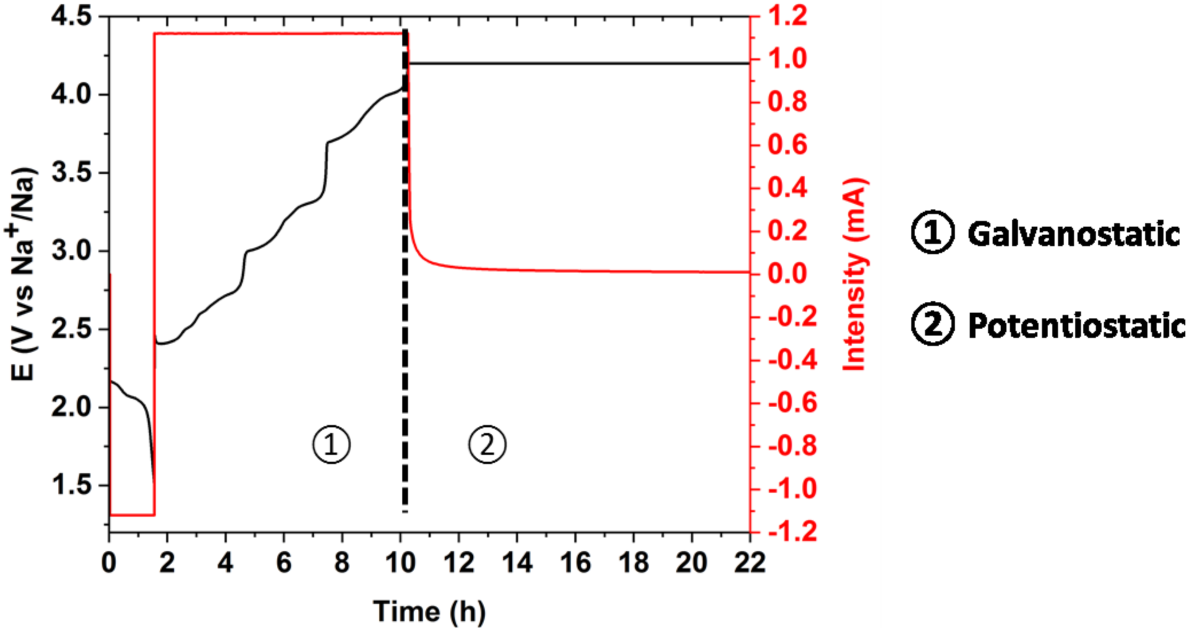

Figure V-7: *Example of a floating curve. The red line represents the current evolution and the black line the voltage evolution as a function of time. This example was realized on the* Na_xCoO_2 *system and the phase was stabilized at 4.2 V.*

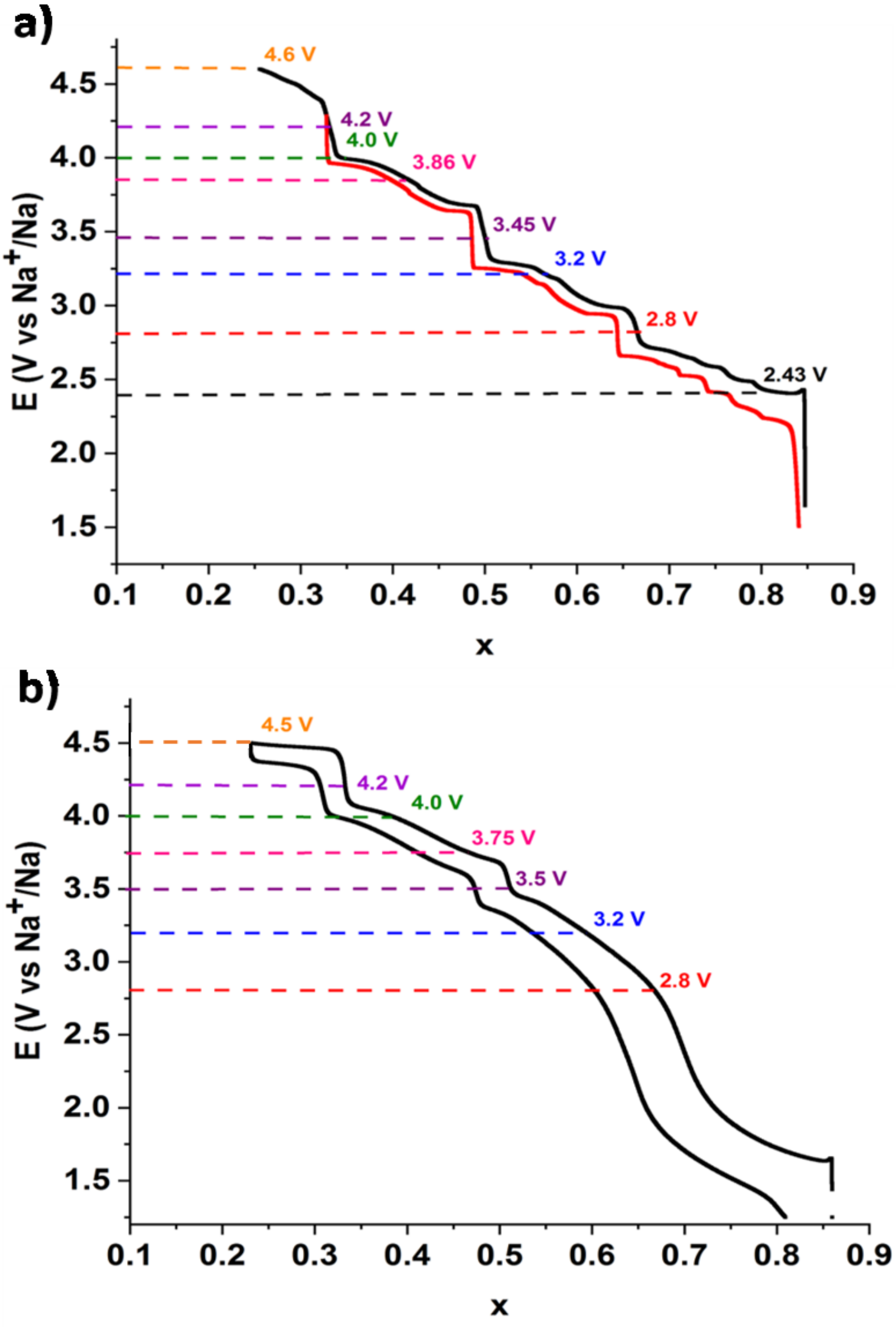

:

Figure V-8: *Charge and discharge at C/20 of (a) Na_xCoO_2 (1.5 - 4.6 V (black) 1.5 V – 4.3 V (red)) and (b) $Na_xCo_{2/3}Mn_{1/3}O_2$ (1.25 - 4.5V) (black lines). The colored dashed lines correspond to the voltage applied during the potentiostatic step to synthetize the phases on both systems*

2.3 Structural characterization

As the amount of material is limited, we used sealed capillaries set-up available only on our Panalytical X'Pert Pro diffractometer equipped with a Cu anticathode. Due to the presence of Co ions in the materials, as significant fluorescence was observed and the overall quality of the XRD patterns is weak. **Figure V-9** displays the different XRD patterns of the Na_xCoO_2 and $Na_xCo_{2/3}Mn_{1/3}O_2$ phases prepared at different voltages.

In agreement with our *in-situ* XRD experiments, the P2 structure is maintained for x values up to 1/3 in both systems. Moreover, the low resolution of the patterns prevents from observing any superstructure peaks. Therefore, all the XRD patterns were refined using the $P6_3/mmc$ space group with, first, the Le Bail method. Note that no splitting of the peaks due to the orthorhombic distortion highlighted in the previous chapter, can be observed for the x = 0.5 phases. It is possible that the targeted voltages were not exactly correct or that the phases slightly changed after the disconnection of the battery.

As observed in the previous chapter, the c_{hex} and a_{hex} lattice parameters, respectively, increase and decrease before reaching limit values around x = 0.4. The evolution of these values are plotted on **Figure V-10** as a function of x and is in good agreement with the values determined in the previous chapter for a_{hex} and c_{hex} limit values (**Table IV-6**).

Concerning the XRD patterns of the two phases synthetized at high voltage: $Na_{0.25}CoO_2$ and $Na_{0.22}Co_{2/3}Mn_{1/3}O_2$ (**Figure V-11**), most of the peaks assigned to the P2 structure disappears while others, broadened, appears in good agreement with the XRD patterns obtained with the PITT on Na_xCoO_2 (**Figure IV-15**). By comparing the two XRD patterns of the phases synthetized at high voltage, peaks at similar positions can be observed and therefore, confirms that sheets glidings also occur in the $Na_xCo_{2/3}Mn_{1/3}O_2$ system. The (002) peak of the two systems is shifted to the $2\theta \approx 17.5°$ position indicating an important decrease of the c lattice parameter to c ≈ 10.1 Å. This value was estimated from the position of the first diffraction peak. Moreover, in the chapter IV, we showed the Na_xCoO_2 XRD pattern of the phase relaxed at 4.6 V (blue pattern on **Figure IV-15).** This pattern is strongly different from the pattern obtained in this chapter by electrochemical deintercalation (orange XRD pattern). It is, therefore, possible that a longer relaxation during the PITT would involve a similar XRD pattern than on **Figure V-9** and that 4.6 V corresponds to the voltage of sheets glidings beginning on the Na_xCoO_2 system. Note that the small shift between the peaks observed on $Na_{0.25}CoO_2$ and $Na_{0.22}Co_{2/3}Mn_{1/3}O_2$ XRD patterns is due to the slight difference in Na^+ content between the two materials.

P2-domain	a_{hex} (Å)	c_{hex} (Å)
$Na_{0.82}CoO_2$	2.845(1)	10.90(1)
$Na_{0.33}CoO_2$	2.809(1)	11.20(1)
$Na_{0.67}Co_{2/3}Mn_{1/3}O_2$	2.829(1)	11.05(1)
$Na_{0.33}Co_{2/3}Mn_{1/3}O_2$	2.817(1)	11.29(1)

Table V-2: *Lattice parameters of the P2-phases synthetized at the lowest and highest voltages for the two systems. The lattice parameters of the other phases are plotted on* ***Figure V-10****.*

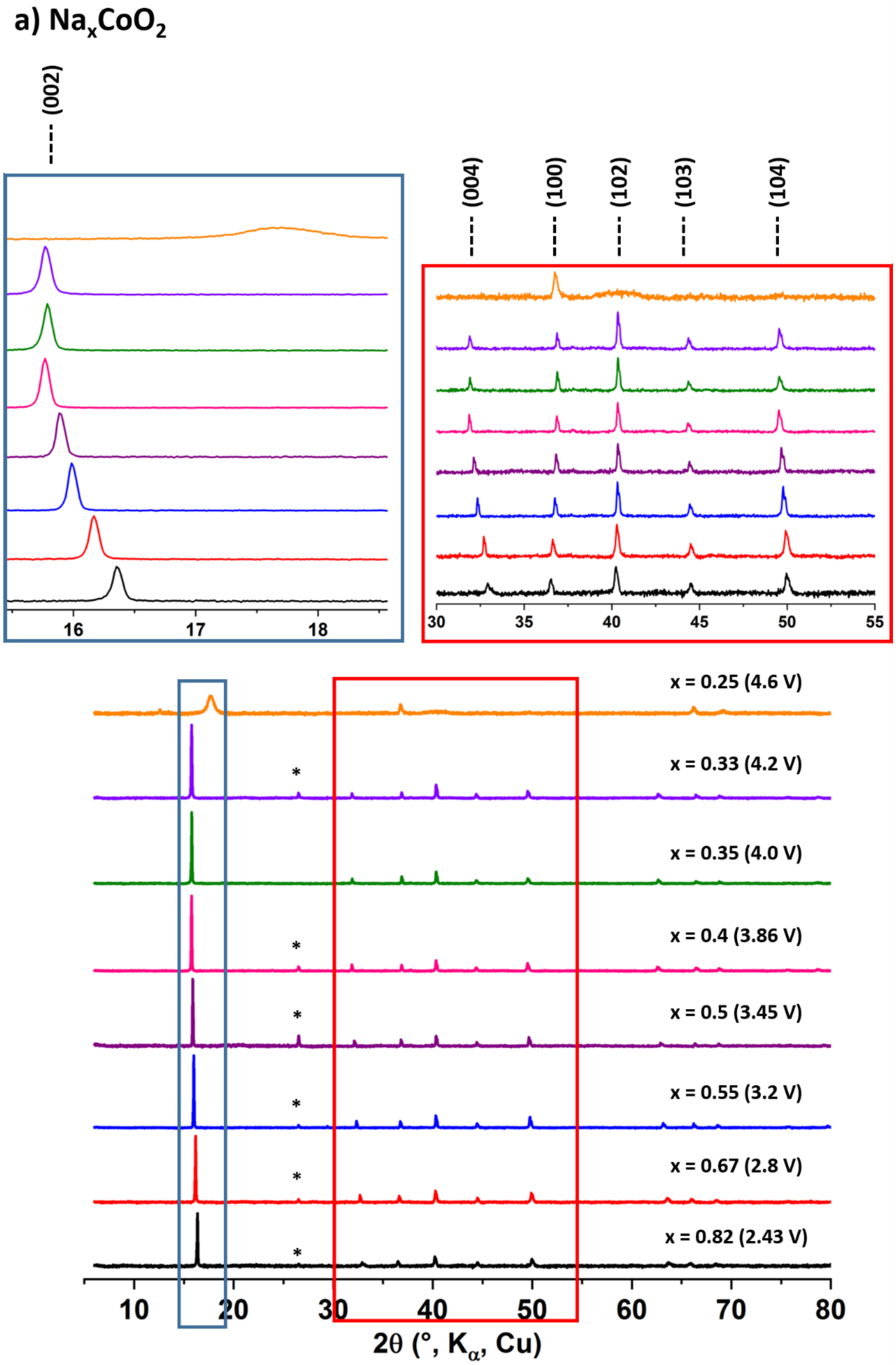
a) Na_xCoO_2
(002)
(004)
(100)
(102)
(103)
(104)
16
17
18
30
35
40
45
50
55
x = 0.25 (4.6 V)
x = 0.33 (4.2 V)
x = 0.35 (4.0 V)
x = 0.4 (3.86 V)
x = 0.5 (3.45 V)
x = 0.55 (3.2 V)
x = 0.67 (2.8 V)
x = 0.82 (2.43 V)
*
10
20
30
40
50
60
70
80
2θ (°, K_α, Cu)

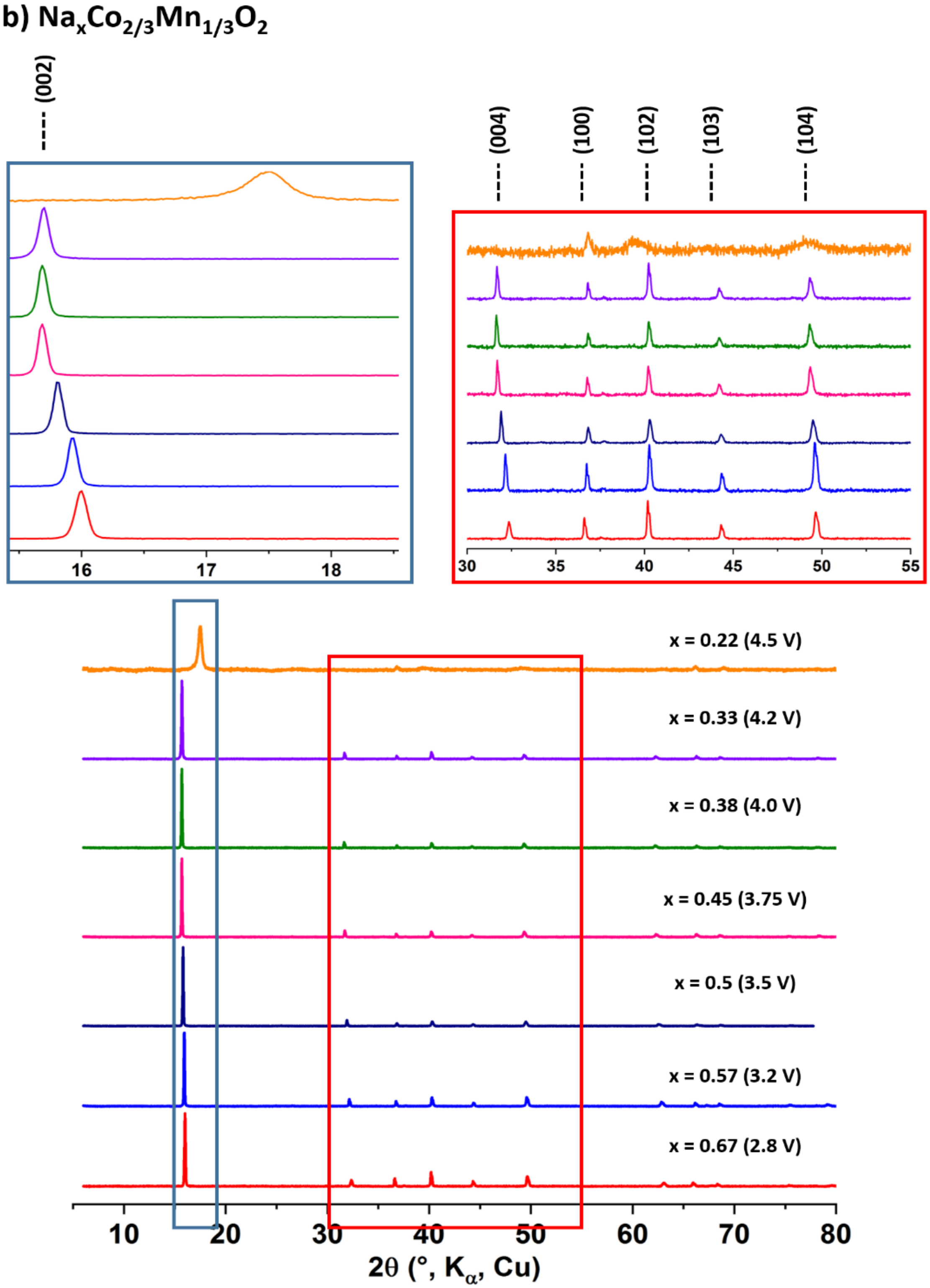

Figure V-9: *Experimental XRD patterns of the (a) Na_xCoO_2 (b) $Na_xCo_{2/3}Mn_{1/3}O_2$ phases. * represents the graphite peak used in the electrode formulation.*

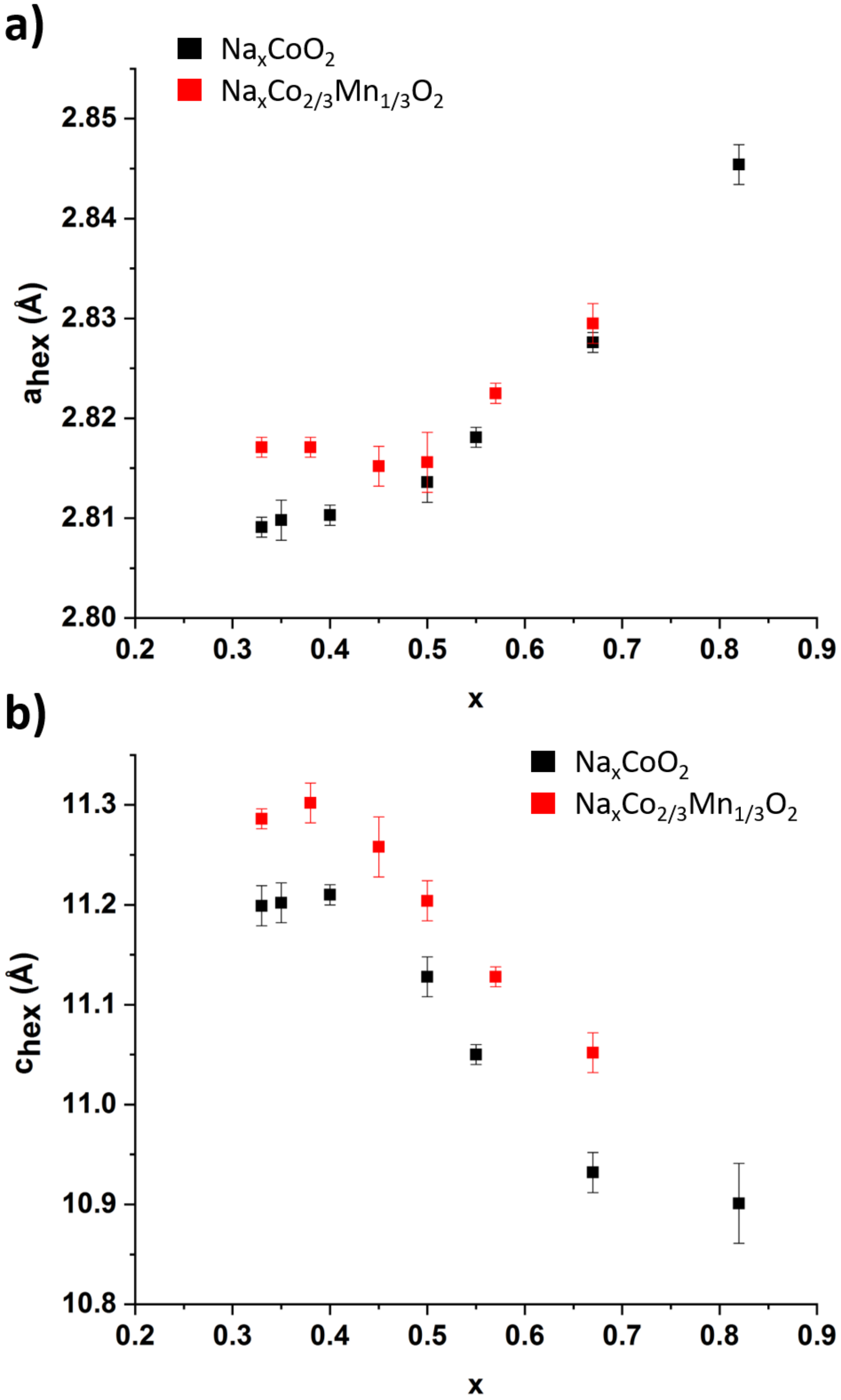

Figure V-10: *Evolution of the (a) a lattice parameter (b) c lattice parameter for P2-*Na_xCoO_2 *and P2-*$Na_xCo_{2/3}Mn_{1/3}O_2$ *phases studied in this chapter*

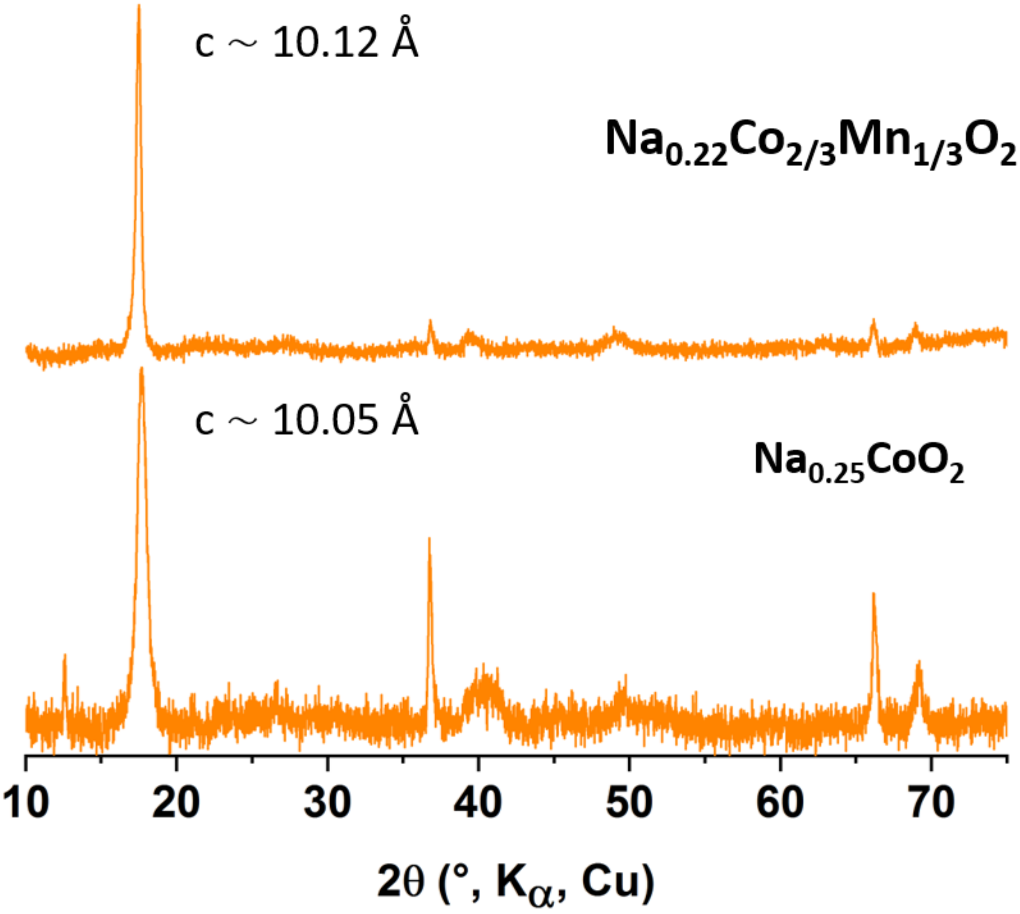

Figure V-11: *XRD patterns of the "OP" phases:* $Na_{0.25}CoO_2$ *and* $Na_{0.22}Co_{2/3}Mn_{1/3}O_2$ *stabilized at, respectively, 4.6 and 4.5 V vs* Na^+/Na

Despite, the low quality of the XRD acquisitions, we were able to perform Rietveld refinements on the P2-Na_xCoO_2 phases using some constraints as discussed below. An example of refined pattern is given in **Figure V-12** (refinement of the XRD pattern of $Na_{0.4}CoO_2$): a good match is observed between the experimental and the calculated patterns. The resulting fitted parameters are given in **Table V-3.** The Rietveld refinements of the P2-$Na_xCo_{2/3}Mn_{1/3}O_2$ patterns could not be performed as the calculated profiles with the Le Bail method could not allow a satisfactory fit of the experimental line width.

In order to perform the Rietveld refinements of the XRD patterns of the P2-Na_xCoO_2 phases, we fixed the B_{iso} values to 0.5 Å² for the Co and O ions and 1.0 Å² for the Na ions. We also fixed the global Na^+ content in the different P2 phases according to value obtained from the electrochemical experiment. Therefore, we only refined the z position of the oxygen ions and the occupancies of the Na_e and Na_f sites. The two Na sites are represented on **Figure I-3**.

The refined data allowed to extract the layers thickness for the different P2-phases (**Figure V-13b). Figure V-13a** shows the structure of a P2 material and defines clearly what will be called the Na^+ ions layers and the MO_2 layers in **Figure V-13b.** Globally, the Na^+ ions layers thickness increases during the charge up to a maximal value reached around x = 0.4 while the CoO_2 slabs thickness slightly decreases to the same x values. The increase of the Na^+ ion layers thickness is in agreement with the Na^+ deintercalation and the increase of the O-O repulsions between the layers. The decrease of the CoO_2 slabs thickness is coherent with the oxidation of Co^{3+} to Co^{4+} that increases the Co-O covalency. Note that the $Na_{0.82}CoO_2$ phase layers thickness is not shown on the **Figure V-13b** due to the impossibility to perform a proper Rietveld refinement of its XRD pattern. As the c_{hex} lattice parameters evolution is rather similar for the two systems (**Figure V-10)**, and as the ionic radii of Co^{3+} (0.545 Å), Co^{4+} (0.53 Å) and Mn^{4+} (0.53 Å)[3] are also rather similar, we expect a similar evolution of the slabs thickness for the P2-$Na_xCo_{2/3}Mn_{1/3}O_2$ phases.

	Space group : P6_3/mmc					
	$a_{hex.}$ = 2.810(1) Å			$c_{hex.}$ = 11.21(1) Å		
Atom	**Site**	**x**	**y**	**z**	**B (Å^2)**	**Occ.**
Co	2a	0	0	0	0.5	1
Na_f	2d	0	0	0.25	1.0	0.16(1)
Na_e	2b	2/3	1/3	0.25	1.0	0.24(1)
O	4f	1/3	2/3	0.083(1)	0.5	1
	Rp = 12.2 % Rwp = 12.4 %			U = 0.14(1) V = -0.05(1) W = 0.008(1) X = 0.007(1) η = 0.45(1)		

***Table V-3**: Calculated parameters, atomic positions and atomic occupancies obtained for the refined XRD data performed on $Na_{0.4}CoO_2$ (XRD pattern in **Figure V-12**) with the P6_3/mmc space group.*

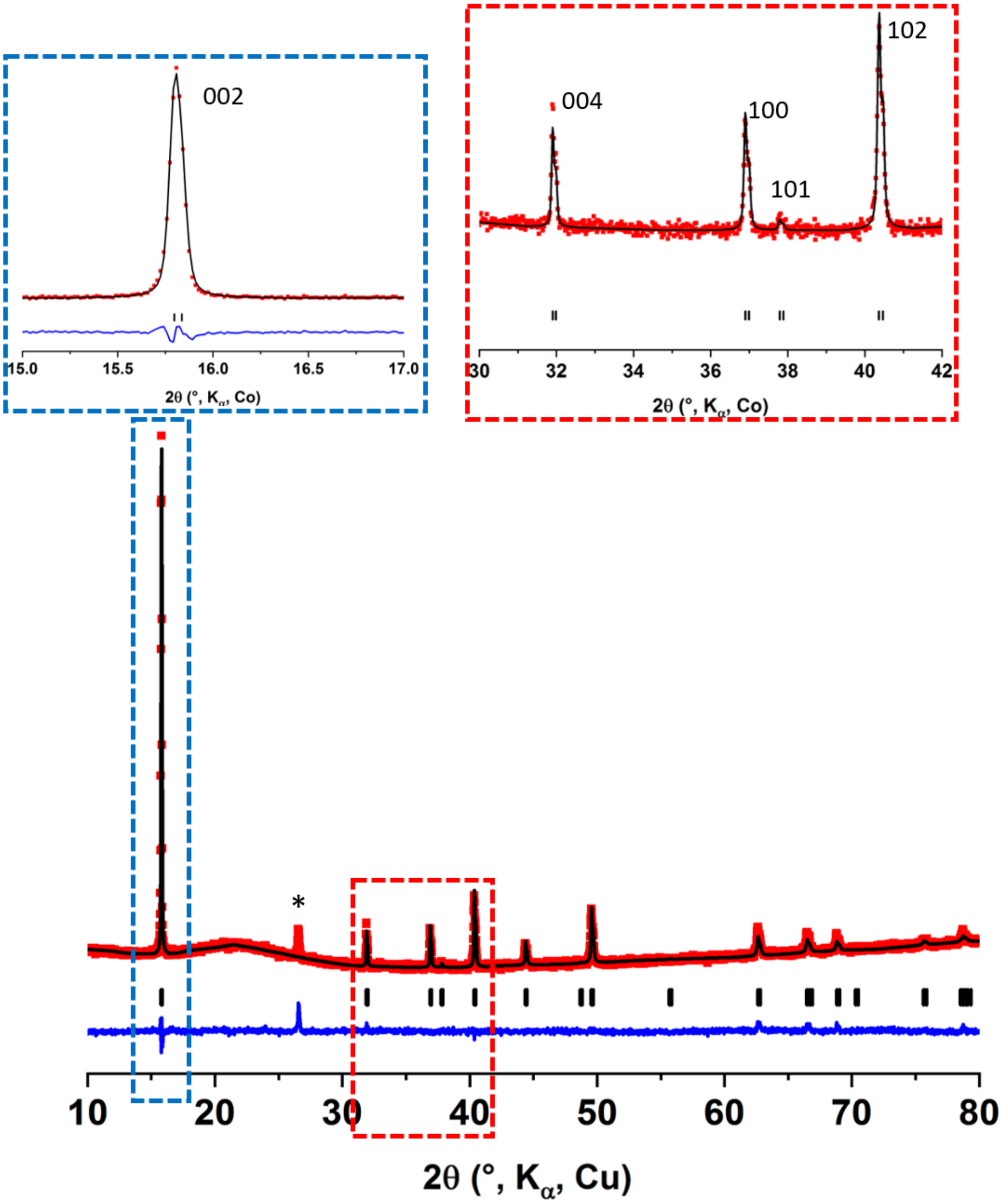

Figure V-12: *Refined XRD pattern as a function of 2θ position of* $Na_{0.4}CoO_2$*. Black bars correspond to the Bragg positions of the phase. Red points correspond to experimental XRD pattern while black line is the calculated one obtained by Rietveld refinement. The blue line is the difference between experimental and calculated lines. * is a peak due to the graphite present in the mixture.*

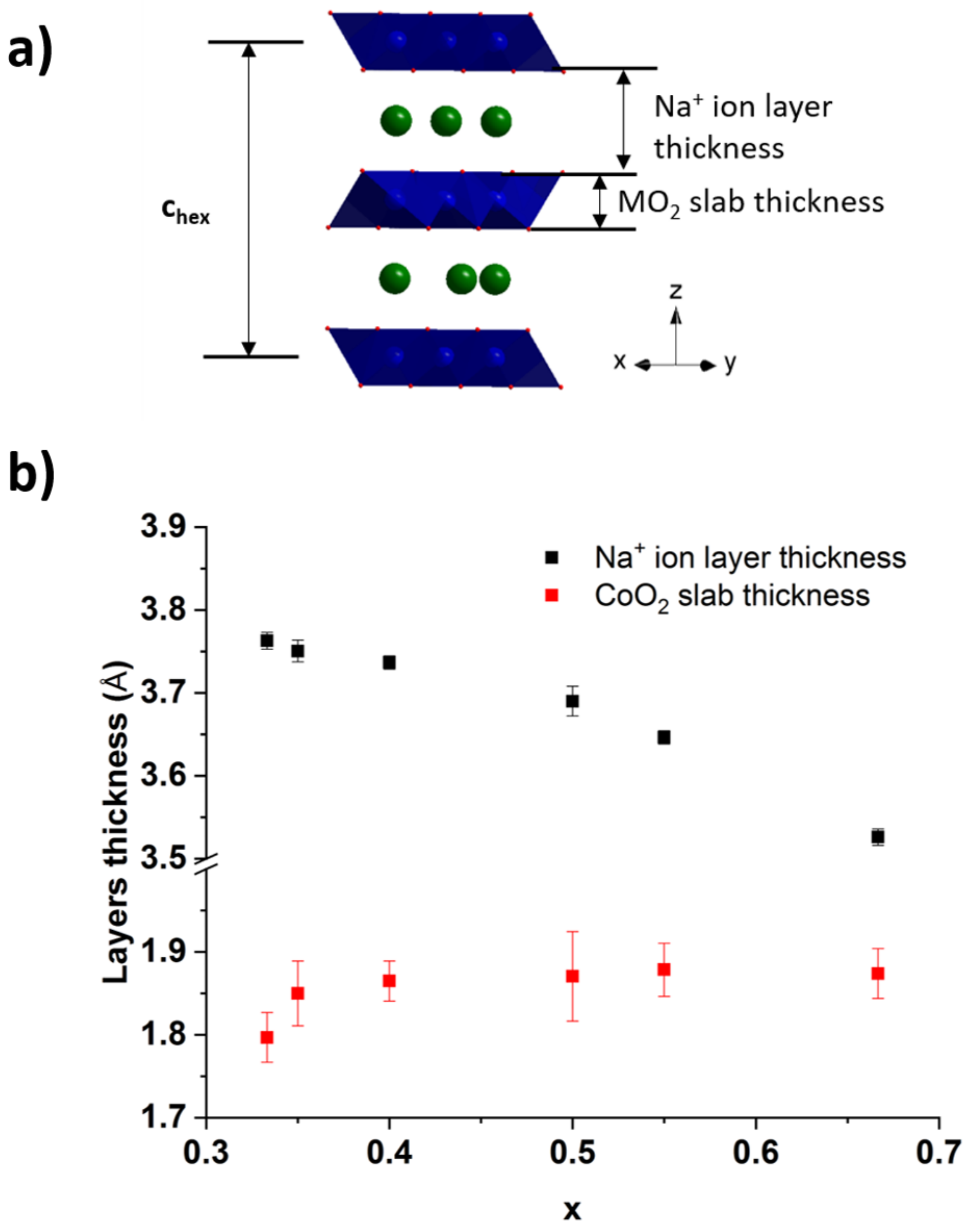

Figure V-13: *(a) Schematic representation of the P2-stacking (b) Evolution of the layers thicknesses in the P2-structure for P2-*Na_xCoO_2

Table V-4 shows the repartition between the two different Na intercalation sites for the P2 phases determined with the Rietveld refinements. During the charge, the amount of Na^+ ions in the Na_f sites stays constant while the amount of Na^+ ions in the Na_e sites largely decreases until reaching the x = 0.5 composition. For x = 0.5, the amounts of Na^+ ions are almost the same in both sites for the two systems. In the $1/3 < x < 0.5$ range, the Na^+ ions in Na_f sites are mainly removed. Another interesting point is that the Na ions occupy almost only the Na_e sites in the $Na_{1/3}CoO_2$ phase.

x	Na_e	Na_f
0.82	-	-
0.67	0.44(1)	0.23(1)
0.55	0.34(1)	0.23(1)
0.50	0.27(1)	0.23(1)
0.40	0.24(1)	0.16(1)
0.35	0.31(1)	0.04(1)
0.33	0.31(1)	0.02(1)

Table V-4: *Repartition of the Na^+ ions in the interslab spaces between both intercalation sites for the P2-Na_xCoO_2 phases*

Figure V-14 compares the different bonds distances in the NaO_6 and CoO_6 octahedra for P2-$Na_{0.33}CoO_2$ and P2-$Na_{0.67}CoO_2$. As expected the Co-O distance decreases because of the distortion of the CoO_6 octahedra during Na^+ deintercalation. Moreover, the Na-O distance increases during Na^+ deintercalation which is coherent with the global increase of the Na^+ layer thickness.

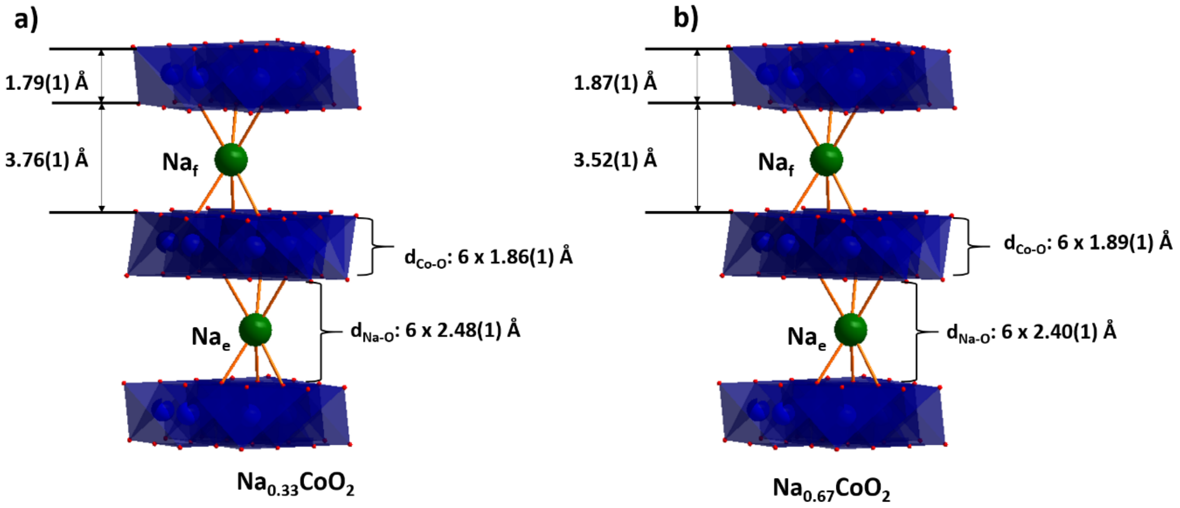

Figure V-14: *Comparison of the different distances in (a) P2-*$Na_{0.33}CoO_2$ *and (b) P2-*$Na_{0.67}CoO_2$

2.4 Magnetic properties on Na_xCoO_2 system

In order to better understand the NMR shift evolution discussed in the following paragraph, we also analyzed the magnetic properties of some of our Na_xCoO_2 phases, compared with literature. The magnetic measurements were performed from 7 K to 300 K without an application of a magnetic field during the cooling and with the application of 1 T during the acquisitions on a Super Quantum Interference Device (SQUID) magnetometer MPMS5. As the powders were used for the XRD and NMR characterizations, we only get enough powder for the magnetic measurements of four samples: x = 0.67, x = 0.55, x = 0.4 and x = 0.33. **Figure V-15a** shows the evolution of the susceptibility as a function of temperature obtained on these samples. Igarashi *et al.*[75] already reported the susceptibility of some Na_xCoO_2 phases but only for $0.7 \leq x \leq 0.5$ compositions (**Figure V-15b**). They highlighted that the Na_xCoO_2 samples have a Curie-Weiss behavior ("Curie-Weiss metal regime") in the 0.64-0.7 range in good agreement with our experimental magnetic measurement realized on the $Na_{0.67}CoO_2$ phase. In the $0.52 < x < 0.58$ range, the magnetic properties turns to a Pauli paramagnetic regime due to the delocalized character of the electrons. For our samples, the Pauli paramagnetic behavior can be observed, experimentally, on the phases synthetized with $x \leq 0.55$. Note that the Na^+ content corresponding to transition from the "Curie-

Weiss metal regime" to the Pauli paramagnetic regime is not completely clear for the moment in fact, some previous studies show the transition for x = 0.5[108] or around 0.6[142]. **Figure V-16** represents the magnetic phase diagram of P2-Na_xCoO_2 proposed by Foo *et al.*[108].

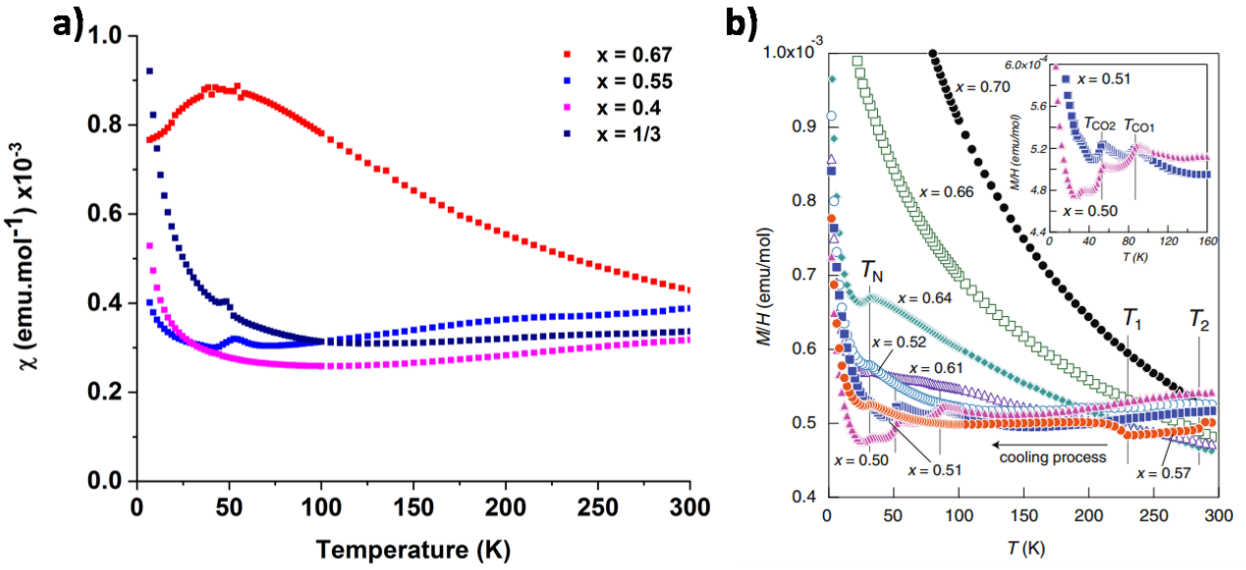

***Figure V-15**: (a) Magnetic measurements of some Na_xCoO_2 phase as a function of temperature from 7 K to 300 K (a) synthetized in this work under a 1T magnetic field (b) from reference [75] under a 0.8 T magnetic field.*

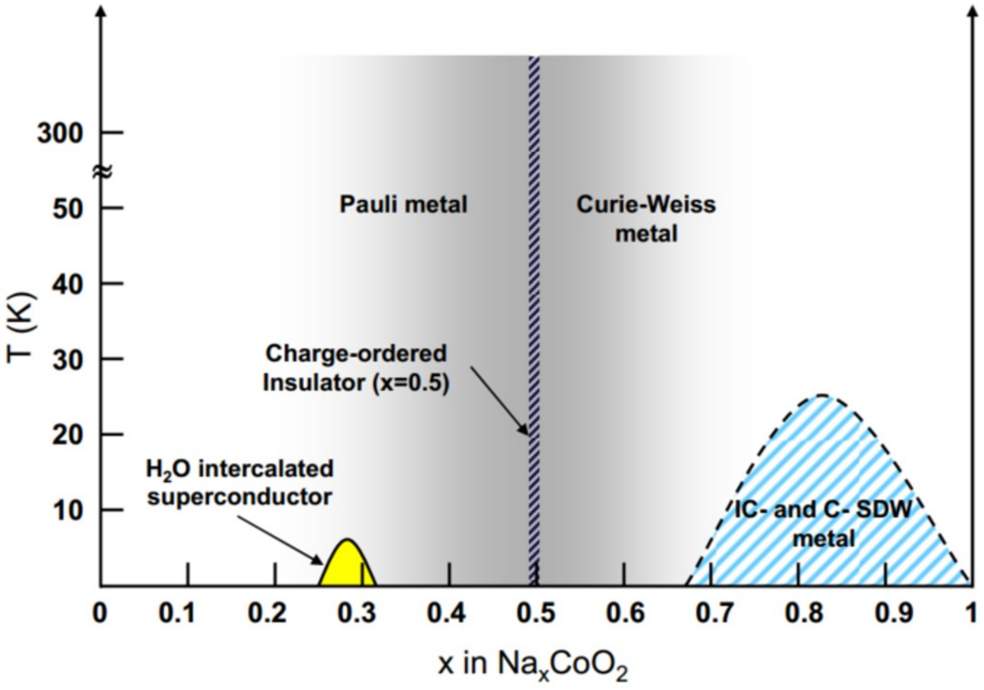

***Figure V-16:** Magnetic phases diagram of P2-Na_xCoO_2. Data are extracted from [108].*

This change in behavior of the magnetic susceptibility vs the Na^+ content can be understood considering the specific band structure expected for the Co^{n+} ion in a distorted CoO_6 octahedra flattened along the c direction as discussed in the first chapter. The t_{2g} orbital degeneracy is lift in two groups: a_{1g} and e_g' orbitals, resulting from a recombination of the d orbitals (as described in the first chapter section 1.3.2). **Figure V-17a** proposes the band structure of the P2-Na_xCoO_2 phases expected in the "Curie-Weiss metal regime" and in the "Pauli regime". In the "Curie-Weiss metal regime", the phases also exhibit a metallic behavior[54], we thus expect some localized (heavy) electrons as well as some delocalized (light) electrons respectively occupying the a_{1g} and e_g bands. In the Pauli paramagnetic regime, no localized electrons are expected in the localized a_{1g} orbitals anymore: the Fermi level is thus located in the e_g' orbitals below the a_{1g} states (**Figure V-17b**). The change in position of the Fermi level, can be understood by the oxidation of Co^{3+} to Co^{4+} ions and by the increase of the CoO_6 distortion when the Na^+ content decreases, resulting in an increase in energy of the a_{1g} band and decrease of the e_g' one. We can define a θ angle between the z axis and an axis along a Co-O direction (**Figure I-5**). Due to the D_{3d} distortion, this angle is supposed to become higher than 54.74° (value in the case of a regular octahedra). **Table V-5** summarizes the θ values calculated in our phases. As expected, the θ value increases with decreasing x involving that the octahedra are flattened during the Na^+ deintercalation involving the expected increase of the a_{1g} band.

x	**θ** (°)
0.67	59.3(1)
0.55	59.3(1)
0.50	60.1(1)
0.40	60.1(1)
0.35	60.3(1)
0.33	60.5(1)

Table V-5: *Evolution of the θ angle in the different P2-Na_xCoO_2 phases*

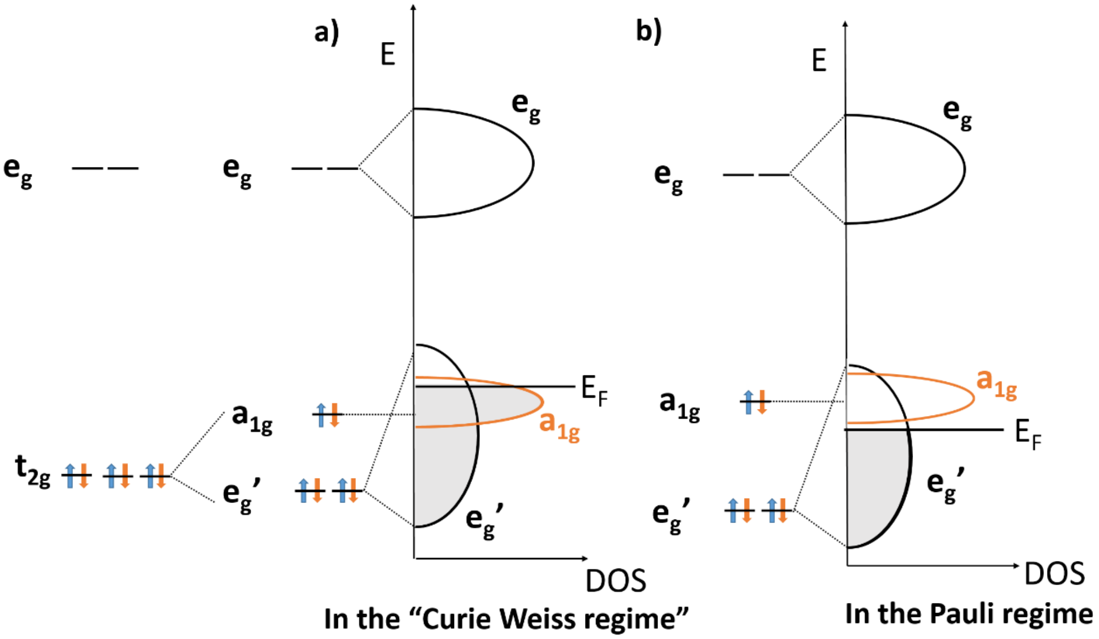

Figure V-17: *Representation of the band structure of the P2-Na_xCoO_2 phases with the D_{3d} symmetry in the (a) "Curie-Weiss metal regime" (b) in the Pauli paramagnetic regime*

2.5 ^{23}Na MAS NMR study

Figure V-18 represents the ^{23}Na MAS NMR spectra recorded for each phase under a 7.05 T magnetic field with a spinning frequency of 30 kHz using a single pulse sequence. The spectral width was set to 1 MHz, and the recycle time $D_0 = 0.5$ s, is long enough to avoid T_1 saturation effects. The discussion below will be divided in two points: the first concerning the lineshape of the signals followed by a discussion concerning the shift value evolution. The spectra of both pristine phases are also shown. Note that the signal position of the pristine $Na_{\sim 2/3}Co_{2/3}Mn_{1/3}O_2$ phase, is larger than the one reported previously [45] and would rather reflect a Na composition slightly higher for x ~0.68.

2.5.1 Lineshape evolution

- **Na_xCoO_2**

The lineshape, as already mentioned, is due to the 2nd order quadrupolar interaction in the $0.33 \leq x \leq 0.82$ range. The software DMFit allows us to fit the signals using a quadrupolar simulated lineshape. Moreover, we decided to fit also the signal in the $0.33 \leq x \leq 0.55$ with a 2nd order quadrupolar lineshape signal in order to extract the isotropic position of the signals, the ν_Q quadrupolar constants and the anisotropy value η (**Table V-6).** An example of fit on $Na_{0.67}CoO_2$ is depicted in **Figure V-19** showing a good match between the experimental and fitted curves. All the fits for the other phases are reported in the Appendix section (**A-6**). The NMR spectra of Na^+ content larger than 0.82 are not presented here, since the spectra are really larger, probably due a strong decrease in the ionic mobility, resulting in several contributions.

x	δ_{iso} (ppm)	ν_Q (MHz)	η
0.82	298(1)	2.10(1)	0.083(1)
0.7 (pristine)	351(1)	2.04(1)	0.18(1)
0.67	395(1)	1.93(1)	0.22(1)
0.55	386(1)	1.66(1)	0.24(1)
0.5	361(1)	1.55(1)	0.51(1)
0.4	292(1)	1.40(1)	0.47(1)
0.35	286(1)	1.19(1)	0.36(1)
0.33	280(1)	1.18(1)	0.5(1)

Table V-6: *NMR parameters for P2-Na_xCoO_2 samples from fitting spectra*

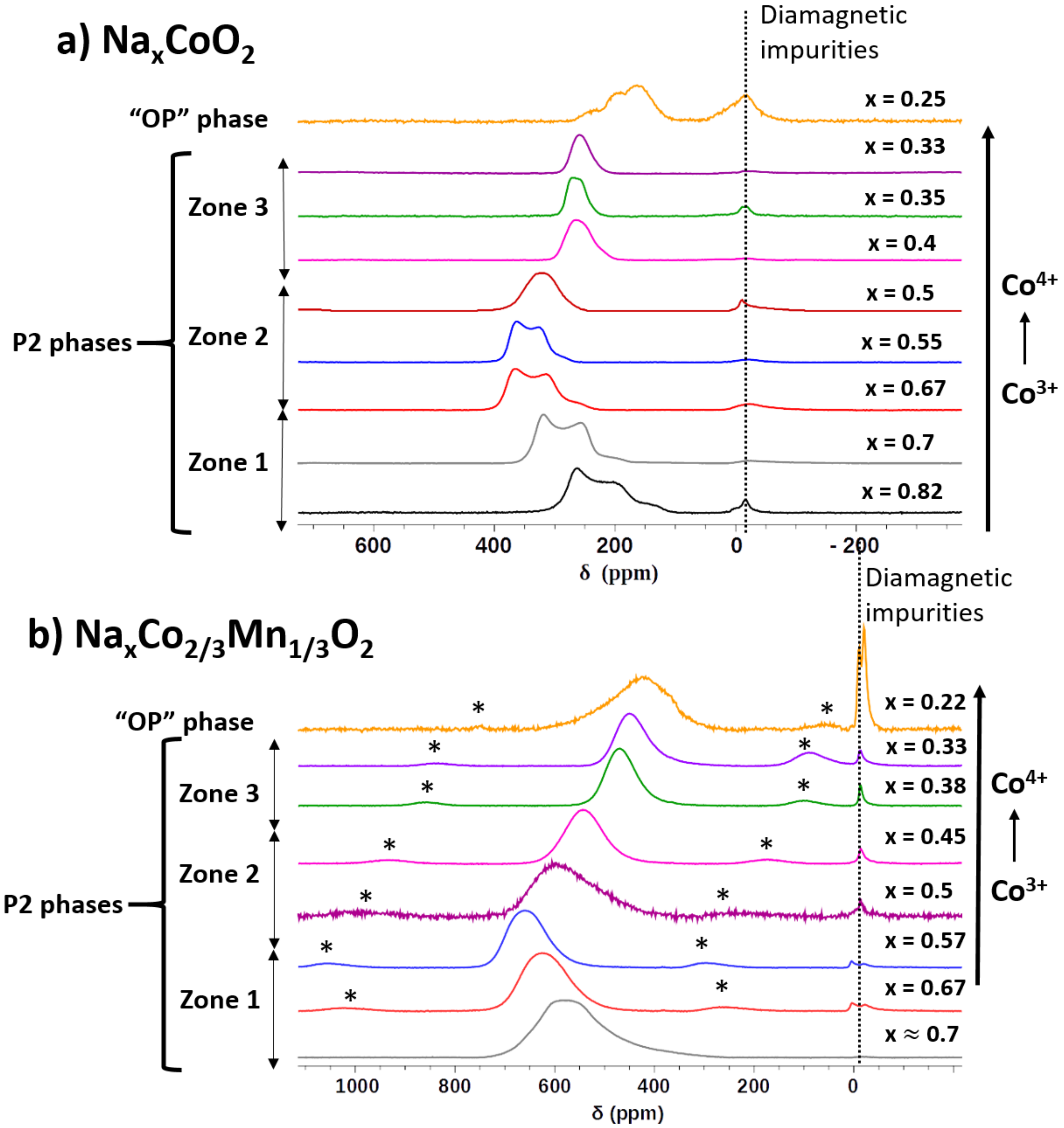

.

Figure V-18: *Evolution of the* ^{23}Na *MAS NMR shifts for (a)* Na_xCoO_2 *and (b)* $Na_xCo_{2/3}Mn_{1/3}O_2$ *systems. The acquisitions were realized on a 7.05 T magnet with a spinning frequency of 30 kHz and a simple pulse sequence. * = spinning side bands.*

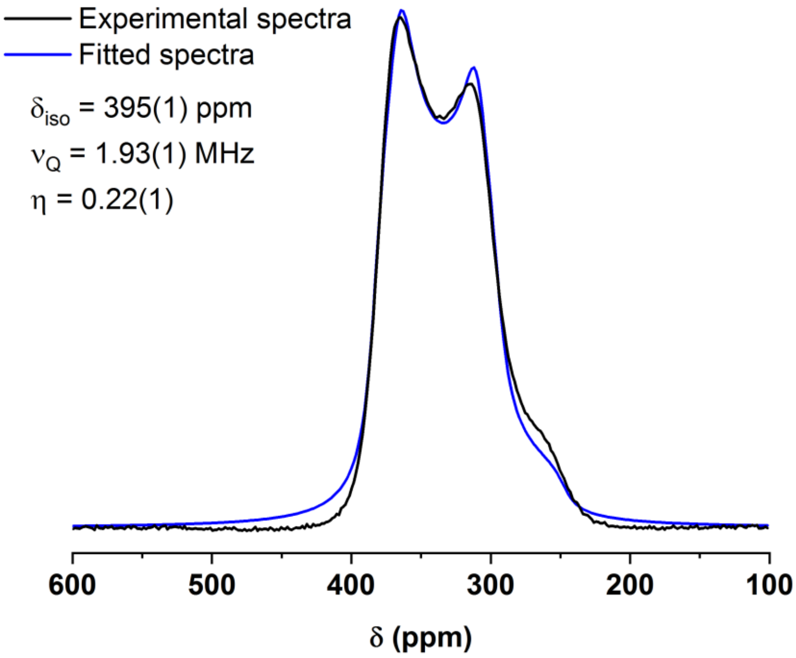

Figure V-19: *Experimental and fitted using a 2^{nd} order quadrupolar lineshape NMR signals realized on the $Na_{0.67}CoO_2$ spectrum*

The ionic mobility does not lead to a same averaged signal as the Na^+ content is decreasing. Moreover, the quadrupolar constant is decreasing whereas the anisotropy value is increasing as x decreases. This is the result of many changes: Na_e/Na_f site occupation, diffusion path, hopping rate, Co-O covalency, Co mean oxidation state, increase of the Na^+ layer thickness …

For the “OP” phase ($Na_{0.25}CoO_2$), the signal is largely broadened and three contributions can be observed on **Figure V-18a.** The appearance of a broad signal observed on the ^{23}Na MAS NMR spectrum is in agreement with the Clément *et al.*[140] study on Na_xMnO_2.The presence of these new environments are due to the sheets which have already glided and which involve the presence of many stacking faults additionally to the appearance of octahedral and prismatic sites for Na^+ ions intercalation. The broadening of the signals is due to the decrease of the overall ionic mobility evidenced by the decrease of the c_{hex} lattice parameter (**Figure V-10**). It is also possible that in a same Na^+ layer, some Na^+ ions are in octahedral sites and others are in prismatic sites.

- **$Na_xCo_{2/3}Mn_{1/3}O_2$**

The 2nd order quadrupolar lineshape is less clear for this system due to a distribution of the Na environments, as already observed on the pristine phase (**Figure V-4**), because of the random distribution of the Co and Mn ions in the metal transition layers. Therefore, the local ionic mobility depends on the local distribution in the $Co_{2/3}Mn_{1/3}O_2$ slabs. The global narrowing of the signals with decreasing x (except for x = 1/2) is due to the increase of the ionic mobility of the Na^+ ions in the interslab spaces. In order to fit the isotropic signal, we used a Gaussian-Lorentzian lineshape on DMFit. For x = 1/2, the lineshape is unclear for the moment, in fact, in the case of a peculiar phase, the ionic mobility would be low enough, due to the Na^+/vacancy ordering, to allow to slightly distinguish the Na_e and Na_f sites. But in our case, no orthorhombic distortion of the peaks can be observed on $Na_{0.5}Co_{2/3}Mn_{1/3}O_2$ XRD pattern indicating that our phase is not ordered (**Figure V-9**).

For the "OP" phases, a broadening of the signals is also observed due to the decrease of the ionic mobility in the phase. As discussed for $Na_{0.25}CoO_2$, the presence of many intercalation sites and stacking faults involved the presence of many contributions.

2.5.2 Signal shift evolution

For both systems, the shift position is mainly governed by the hyperfine interaction. But, for the Na_xCoO_2 phases (and especially for x > 0.5), the quadrupolar interaction contributes also to the isotropic position as seen in **Table V-6.**

In order to discuss the evolution of the shift in the P2 structure domain, we separated the spectra on **Figure V-18** in three zones:

- in the zone 1, the NMR shift strongly increases
- in the zone 2, the NMR shift decreases. For Na_xCoO_2, we decided to limit the zone 2 to x = 0.5 because of the magnetic transition reported by Foo *et al.*[108]
- in the zone 3, the NMR shift stays constant (or slightly decreases), with a much lower shift that observed in zone 2

The x ranges of these zones are not fixed but their introduction allows to simplify the discussion. As already discussed in the chapters I and II, the hyperfine interaction in NMR depend on the nature of the unpaired electrons.

- Localized electrons leads to a Fermi contact shifts which represents the amount of electronic spin transferred from metal transition ions to the probed nucleus through the chemical bonds. This interaction, therefore, strongly depends of the number of single electrons in the electronic configuration of the metal transition ions. The Fermi contact shift δ^{i}_{Fermi} is described with the following equation:

$$\delta^{i}_{Fermi} = \frac{1}{3SN_A}\rho^{i}(0)\chi_M$$

χ_M: magnetic molar susceptibility

S: spin quantum number

$\rho^{i}(0)$: spin density on the probed nucleus

- Delocalized electrons lead to Knight shifts. Similarly, to the Fermi contact shift, it involves the presence of electronic spin density on the s orbitals of the probed nucleus. However, in that case, the spin density comes from the participation of the s electrons at the Fermi level. Here, then the Knight shift depends on the contribution of the Na 3s orbital at the Fermi level. The Knight shift (δ_{Knight}) equation is the following:

$$\delta_{Knight} = \frac{8\pi}{3}\langle|\psi_{r=0}|^2\rangle\chi^{e}_{s}$$

χ^{e}_{s}: Pauli susceptibility of conduction electrons at Fermi level

$\langle|\psi_{r=0}|^2\rangle$: contribution of “s” orbitals at Fermi level of probed nucleus

❖ For the Na_xCoO_2 system

In order to interpret the NMR shift evolution and to make the link with the mechanisms involved during the Na^+ deintercalation, we need to consider two factors: the local geometric evolution represented by the evolution of the Na-O distance and the c_{hex} lattice parameter in **Figure V-20a** and the local electronic structure evolution considering the oxidation of diamagnetic Co^{3+} (t_{2g}^6 e_g^0) into paramagnetic Co^{4+} (t_{2g}^5 e_g^0) and the Curie-Weiss metal – Pauli paramagnetic transition for x = 0.5 (**Figure V-20b)**. Note that a change in the average position for Na^+ ions is also linked to the Na_e and Na_f site occupancy (**Table V-4**), but as one does not expect a strong shift difference for those two environments[39], this effect won't be therefore discussed below. The shift evolution versus the Na^+ content is also plotted in **Figure V-20c** and each zone introduced previously is depicted with a specific blue contrast color.

- In zone 1 ($0.67 \leq x \leq 0.82$), the NMR shift increase can be explained by the oxidation of diamagnetic Co^{3+} (LS, t_{2g}^6 e_g^0) into paramagnetic Co^{4+} (LS, t_{2g}^5 e_g^0) while a majority of the electrons have a localized behavior. The more paramagnetic species are formed the more shifted is the signal. The position of the signal in this composition domain probably results from a sum of a Fermi contact shift and a Knight shift as discussed already in the chapter II for the OP4 phase. Therefore, the shift can be expressed as:

$$\delta_{tot} = \delta_{Fermi,a_{1g}}^{Co^{4+}} + \delta_{Knight,e_g'}^{Co^{n+}}$$

- In zone 2 ($0.5 \leq x \leq 0.67$), the NMR shift significantly decreases when x decreases despite the oxidation of Co^{3+} to Co^{4+} ions (still in a "Curie-Weiss metal domain" $x > 0.5$). As shown on **Figure V-13b** and **Figure V-20a**, the thickness of the Na^+ layers and the Na-O distance increase when x decreases. This increase leads to a weaker overlap between the Na 3s and the O 2p orbitals and thus to a weaker overall spin transfer from the Co^{4+} ions to the Na 3s orbital, reducing the Fermi contact shift. Thus, for $\delta_{Fermi,a_{1g}}^{Co^{4+}}$, two antagonist effects occurring as x decreasing: an increase of the amount of unpaired electrons and a decrease of the efficiency of the spin transfer mechanisms. It seems that in this composition domain, the modification of the local geometry is predominant.

- In zone 3 ($0.33 \leq x \leq 0.5$), an important decrease of the NMR shifts, compared to the values in the zone 2, is observed and is due to the change of regime which probably occurs in the 0.4 – 0.5 x range. In this zone, the NMR shift evolution is mostly governed by the Knight shift contribution due to the establishment of the Pauli paramagnetic regime with only delocalized electrons in the electronic structure and no significant evolution of the Na-O distance (**Figure V-20a).** Therefore, $\delta_{Fermi,a_{1g}}^{Co^{4+}} \sim 0$ ppm and the Na 3s orbital participation to the Knight shift seems to be almost constant during the Na^+ deintercalation.

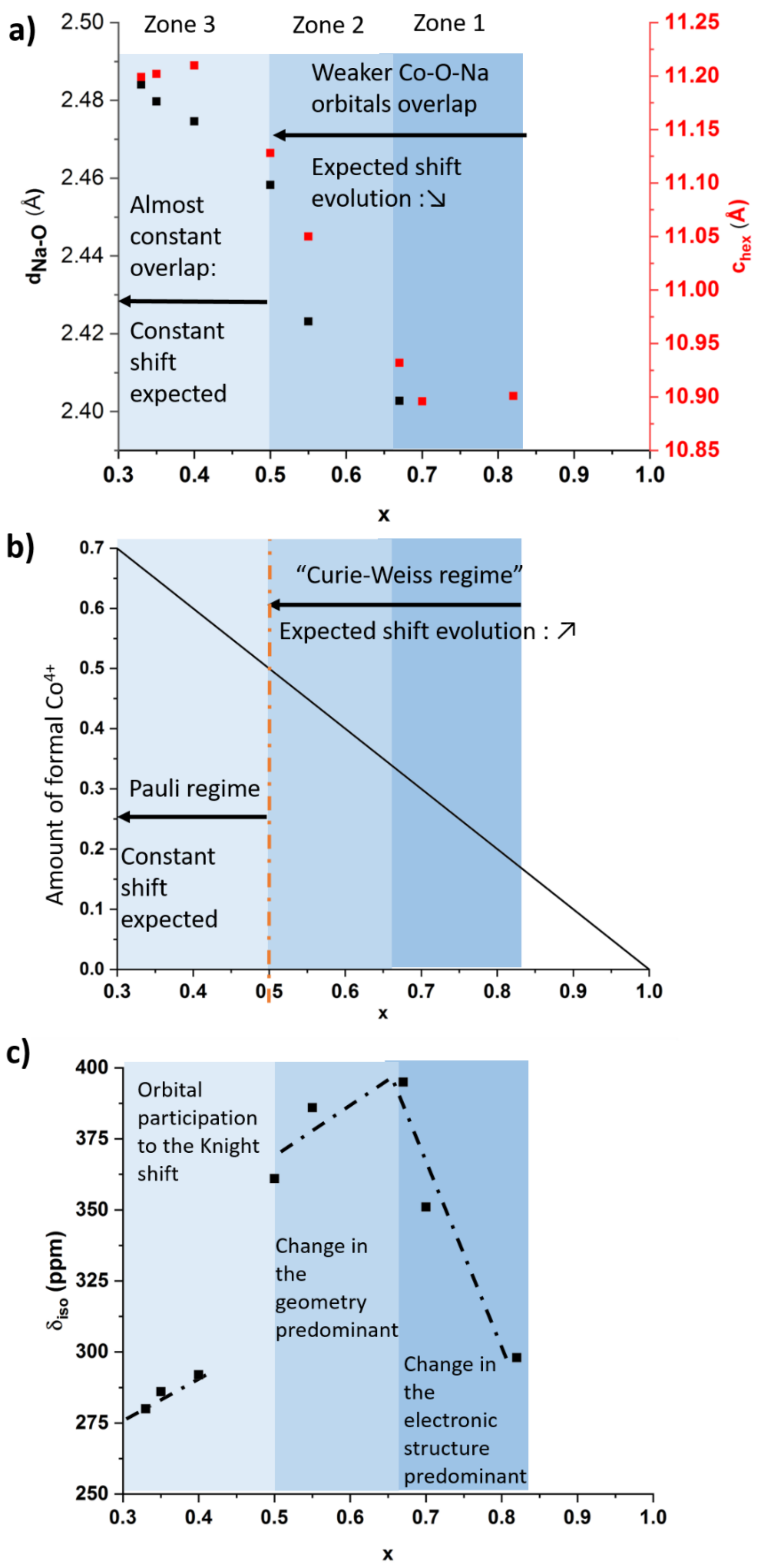

Figure V-20: *For the P2-Na_xCoO_2 system: (a) Evolution of the Na-O distance and c lattice parameter as a function of x. (b) Evolution of the amount of formal Co^{4+} ions as a function of x. "Curie-Weiss metal regime" and "Pauli paramagnetic regime" are separated by an orange dashed line (c) ^{23}Na MAS NMR isotropic shift evolution as a function of x.*

❖ For the $Na_xCo_{2/3}Mn_{1/3}O_2$ system

The impossibility to refine the XRD patterns with the Rietveld method prevents from studying the geometry point of view with the Na-O distances. We can assume that the Na^+ layers evolution is following the c_{hex} lattice evolution since no severe modification of the CoO_2 layer thickness is expected form the oxidation of Co^{3+} to Co^{4+} ions. Note the overall shifts are larger than observed for the Na_xCoO_2 phases due to the presence of Mn^{4+} (t_{2g}^3 e_g^0) ions that leads to a higher Fermi contact shift contribution. This system is more complex than Na_xCoO_2 because we need to consider the contribution of the Mn^{4+} ions to the total shift value. Moreover, a transition from a "Curie-Weiss metal" regime to a Pauli paramagnetism is not necessarily occurring at $x = 0.5$ on this system. Cheng *et al.*[118] reported the partial DOS on $Na_{2/3}Co_{2/3}Mn_{1/3}O_2$ and highlighted the presence of the D_{3d} distortion for the Mn^{4+} ions. They also reported that the filled t_{2g} orbitals of the Mn^{4+} ions have a lower energy that the t_{2g} orbitals of the Co ions. **Figure V-22b** displays the schematic band diagram of $Na_xCo_{2/3}Mn_{1/3}O_2$ in the "Curie-Weiss metal regime" considering the D_{3d} distortion and the up and down populations. Regarding the energy of the Fermi level, we expect some localized electrons as well as some delocalized electrons respectively occupying the a_{1g} and e_g' bands of the $Co^{3+/4+}$ and some localized electrons in the levels of the Mn^{4+} ions in the "Curie-Weiss metal regime". The total NMR shift can be expressed as:

$$\delta_{tot} = \delta_{Fermi}^{Mn^{4+}} + \delta_{Fermi,a_{1g}}^{Co^{4+}} + \delta_{Knight,e_g\prime}^{Co^{n+}}$$

$\delta_{Fermi}^{Mn^{4+}}$ is supposed to remain constant as only the Co^{3+}/Co^{4+} redox couple is involved in the redox process for $x < 2/3$ from an electronic point of view. However, from a geometric point of view, its contribution decreases when x decrease due to the Na^+ layer thickness increase.

$\delta_{Knight,e_g\prime}^{Co^{n+}}$: the contribution of the Na 3s orbital participation to the Knight shift is almost constant

The evolution of $\delta_{Fermi,a_{1g}}^{Co^{4+}}$ depends if we consider the electronic structure or the geometric point of view as already discussed for Na_xCoO_2. Note that from a geometric point of view $\delta_{Fermi,a_{1g}}^{Co^{4+}}$ evolves in the same way than $\delta_{Fermi,a_{1g}}^{Mn^{4+}}$.

- In zone 1 ($0.57 \leq x \leq 0.68$), the shift increases is due to the change in the electronic structure due to the formation of Co^{4+} ions (t_{2g}^5 e_g^0) as x decreases (**Figure V-21b**) involving an increase of $\delta_{Fermi,a_{1g}}^{Co^{4+}}$ not compensated by the probable slight decrease of $\delta_{Fermi,}^{Mn^{4+}}$ due to increase of the c_{hex} lattice parameter in this zone (**Figure V-21a**).

- As observed for Na_xCoO_2, the shift decreases in the zone 2 ($0.45 \leq x \leq 0.57$) (**Figure V-21c**). Therefore, the geometric point of view is also predominant for this system in the zone 2. This point is strengthened by the important increase of c_{hex} lattice parameter in the zone 2 (**Figure V-21a**). In this zone, both $\delta_{Fermi,a_{1g}}^{Co^{4+}}$ and $\delta_{Fermi,a_{1g}}^{Mn^{4+}}$ contributions increase due to the D_{3d} distortion of the MO_6 octahedra. Then, a change in position of the Fermi level, as x decreases, is expected and can be understood by the oxidation of Co^{3+} to Co^{4+} ions in a same way than for Na_xCoO_2, resulting in an increase in energy of the a_{1g} band of the Co and Mn ions when the system reaches the zone 3 (**Figure V-22b).** In this system, a magnetic transition probably occurs between $0.4 \leq x \leq 0.45$. However, this magnetic state can't be completely considered as metallic due to the participation of the localized electrons of the Mn^{4+} ions to the total shift. That's why we called this magnetic state, "Pauli regime".

- In the zone 3 ($0.33 \leq x \leq 0.4$), as the shift is almost constant, the $\delta_{Fermi,a_{1g}}^{Co^{4+}}$ should be null due to empty a_{1g} band as depicted on **Figure V-21c**. Moreover, the low evolution of the c_{hex} lattice parameter in this zone (**Figure V-21a**) suggests that $\delta_{Fermi}^{Mn^{4+}}$ should stay almost constant in the zone 3. Therefore, the participation of the 3s Na orbital to the "Knight shift" should be almost constant in good agreement with the shift evolution of the Na_xCoO_2 phases in the same zone.

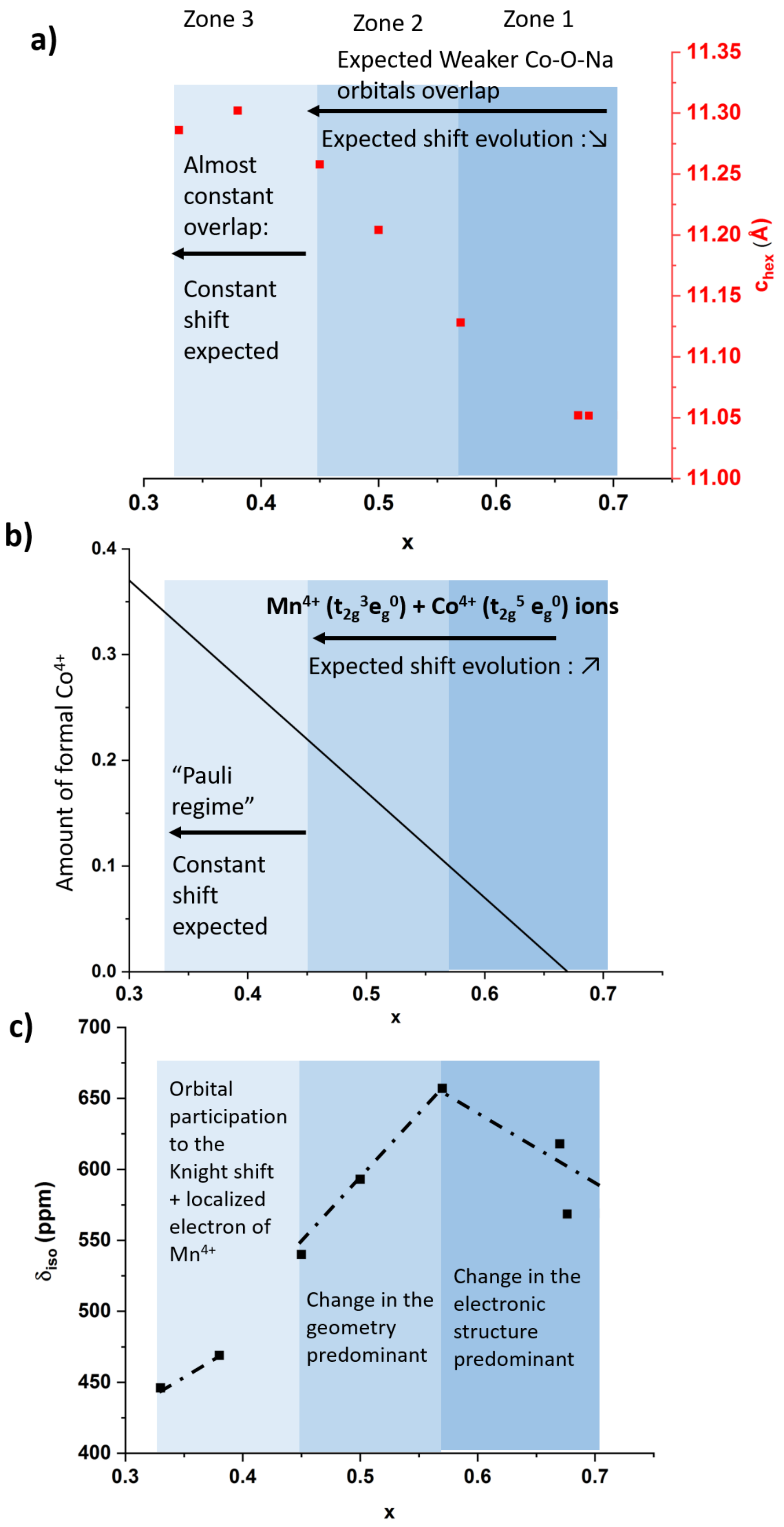

Figure V-21: *(a) Evolution of the c lattice parameters as a function of x for* $Na_xCo_{2/3}Mn_{1/3}O_2$ *phases (b) Evolution of the amount of formal* Co^{4+} *ions as a function of x. (c) Isotropic shift evolution obtained after the fit of the spectra as a function of x. The Zone 1, 2 and 3 are separated by black dashed lines.*

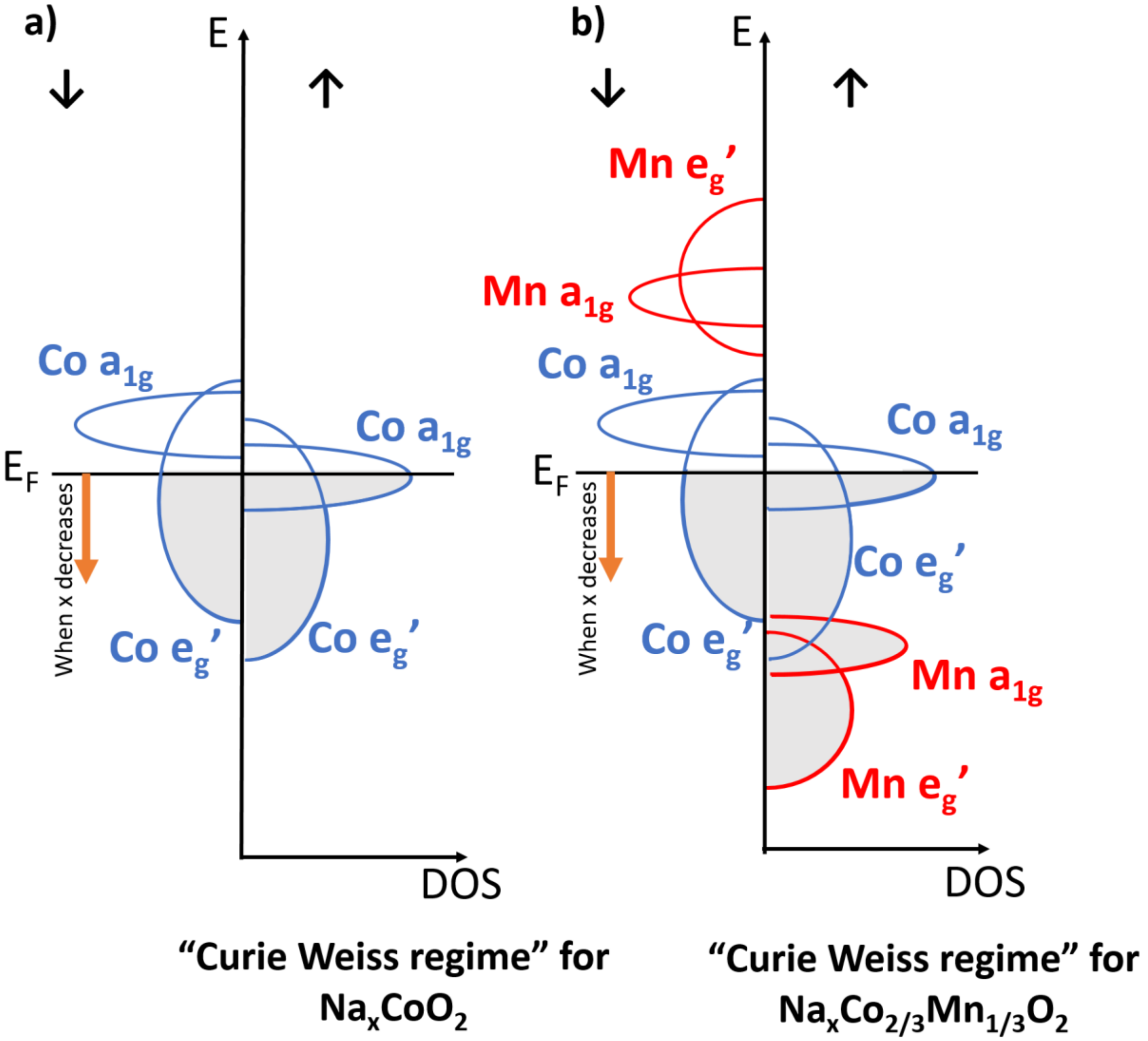

Figure V-22: *Schematic representation of the band structure of the t_{2g} levels of the (a) P2-Na_xCoO_2 and (b) P2-$Na_xCo_{2/3}Mn_{1/3}O_2$ phases with the D_{3d} symmetry in the "Curie-Weiss metal regime" considering up and down DOS.*

3. Conclusion

In this chapter, we studied the local structure and electronic structure and the mechanisms occurring during the Na^+ deintercalation by *ex-situ* ^{23}Na MAS NMR in two different systems. Rietveld refinements on the Na_xCoO_2 phases patterns showed a global increase of the Na^+ ion layers thickness. Moreover, Le Bail refinements showed an increase of the c lattice parameter during the Na^+ deintercalation in $Na_xCo_{2/3}Mn_{1/3}O_2$. For the phases with compositions, $x < 0.33$, the XRD patterns suggested an important decrease of the c lattice parameters compared to the value in the P2 structures due to the sheets gliding and "OP" phase formation.

The ^{23}Na MAS NMR shift evolution can be interpreted considering different effects: the structural and electronic structure modifications occurring upon charging for x values corresponding to a "Curie-Weiss metal regime". During the Na^+ deintercalation, the consecutive predominance of both effects explains why the NMR shift, first, increases and then, decreases. For the lowest Na^+ contents, the localized electrons of the Co^{4+} ions are no more involved in the total shift value. Therefore, Na_xCoO_2, for $x < 0.5$ has a metallic behavior with a constant Knight shift contribution of the delocalized electrons to the total NMR shift while the NMR shift in $Na_xCo_{2/3}Mn_{1/3}O_2$, for $x < 0.45$, is due to a "Knight shift" with a constant contribution of the localized electrons of the Mn^{4+} ions.

Finally, for the two disordered "OP" phases formed at high voltage, the intercalation in octahedral or prismatic sites for the Na^+ ions leads to the observation of many contributions on both spectra. Syntheses by electrochemical (de)intercalation is, therefore, an accurate technique in order to study the mechanisms involved during the Na^+ (de)intercalation by *ex-situ* MAS NMR and XRD.

Chapter VI: Study of mechanisms involved during Na^+ (de)intercalation in the O3-Na_xRuO_3 system

1. Introduction

In this chapter, we report the ^{23}Na MAS NMR study of the O3-Na_xRuO_3 phases used as positive electrode in Na-ion batteries. The particularity of this layered oxide system is to propose an extra capacity due to the participation of the oxygen ions to the redox process and to propose a good stability in cycling. This work was done in collaboration with the Pr. Yamada group at the University of Tokyo. The main goal was to characterize the modification in the electronic structure upon Na^+ deintercalation in a system where O-redox is involved at high voltage. For this study, all the syntheses were realized in Tokyo by Benoit Mortemard de Boisse and sent in airtight containers to Bordeaux in order to perform the NMR acquisitions. The samples were directly entered in a glovebox before the powder packing in rotors.

In 2004, Mogare *et al.*[143] are the first to propose a synthesis of the pristine O3-Na_2RuO_3 (**Figure VI-1**) phase *via* a thermal decomposition of Na_2RuO_4. Rozier *et al.*[144] reported a capacity of almost 180 mA.h.g^{-1} which largely exceeds the value that the oxidation of Ru^{4+} (t_{2g}^4 e_g^0) into Ru^{5+} (t_{2g}^3 e_g^0) can deliver. Mortemard de Boisse *et al.*[46] reinvestigated the material in the aim to understand this extra capacity. They showed that 1.5 electrons can be removed from the phase upon charging to 4.0 V. They reported that this extra capacity is due to the participation of the oxygen ions in the redox process in the $0.5 \leq x < 1$ range. In fact, the O-O distance (2.580(4) Å) is short enough, when the system reaches the O1-Na_1RuO_3 composition, to raise the antibonding σ^* orbitals of the O-O bonds at the Fermi level involving the oxygen redox reaction. The extra capacity allows the system to reach the $Na_{1/2}RuO_3$ compositions with an O1 structure (**Figure VI-2**). Note that this phenomenon is observed on other systems and involved extra capacity and for example in systems for Li-ion batteries[145–148]. The O3-Na_2RuO_3 formula can be rewritten as O3-$Na[Na_{1/3}Ru_{2/3}]O_2$ in a more usual lamellar oxide nomenclature: the transition metal layers are composed of a honeycomb ordering with one Na^+ ion surrounded by 6 Ru^{4+} ions as shown in **Figure VI-1**.

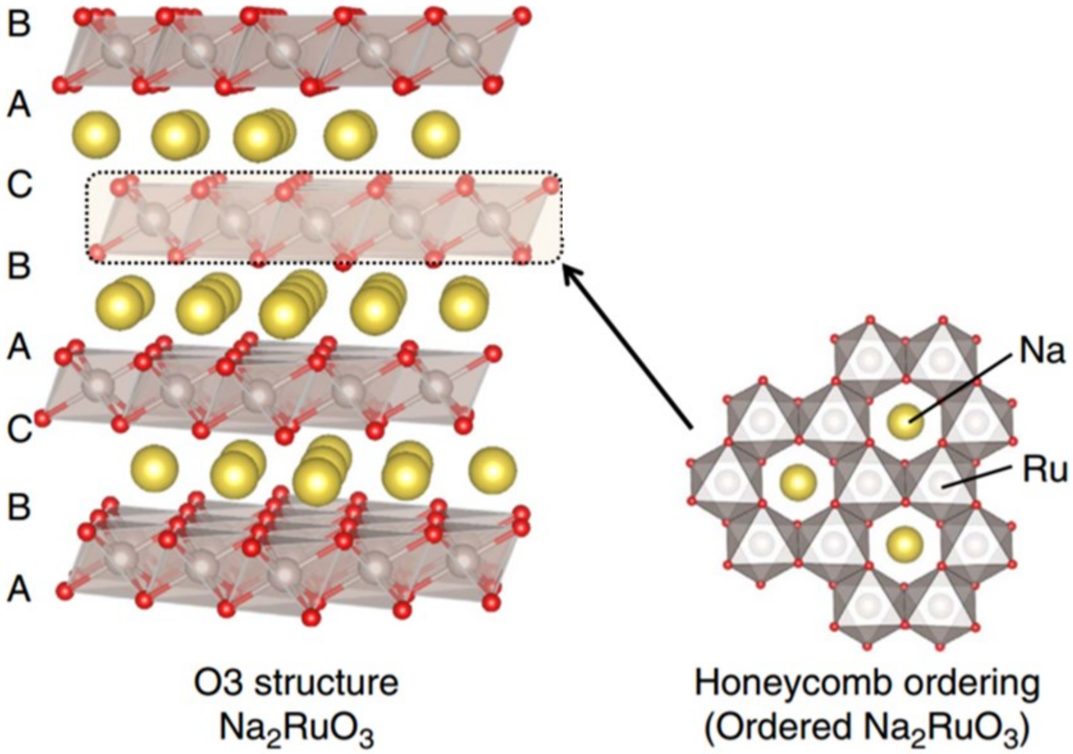

Figure VI-1: *Structure of O3-Na_2RuO_3 with the oxygen ions in red, the Na^+ ions in yellow and the Ru^{4+} ions in grey. Extracted from reference* [46].

In 2019, Mortemard de Boisse *et al.*[48] reinvestigated the O3-Na_xRuO_3 system. They showed that Na_2RuO_3 presents 40 % of stacking faults due to occasional shifts of the $[Na_{1/3}Ru_{2/3}]O_2$ slabs perpendicularly to the stacking direction. Note that the amount of stacking faults strongly decreases during the Na^+ deintercalation (to 2%) but increases again to its initial value (40 %) at the end of each cycle. The O1-Na_1RuO_3 and O1'-$Na_{1/2}RuO_3$ phases have characteristic Ru^{5+}/vacancy ordering in the transition metal layers and Na^+/vacancy ordering in the interslab spaces meaning that the Na^+ ions from the transition metal layers are the first to be deintercalated during the charge of the battery (**Figure VI-2b**).

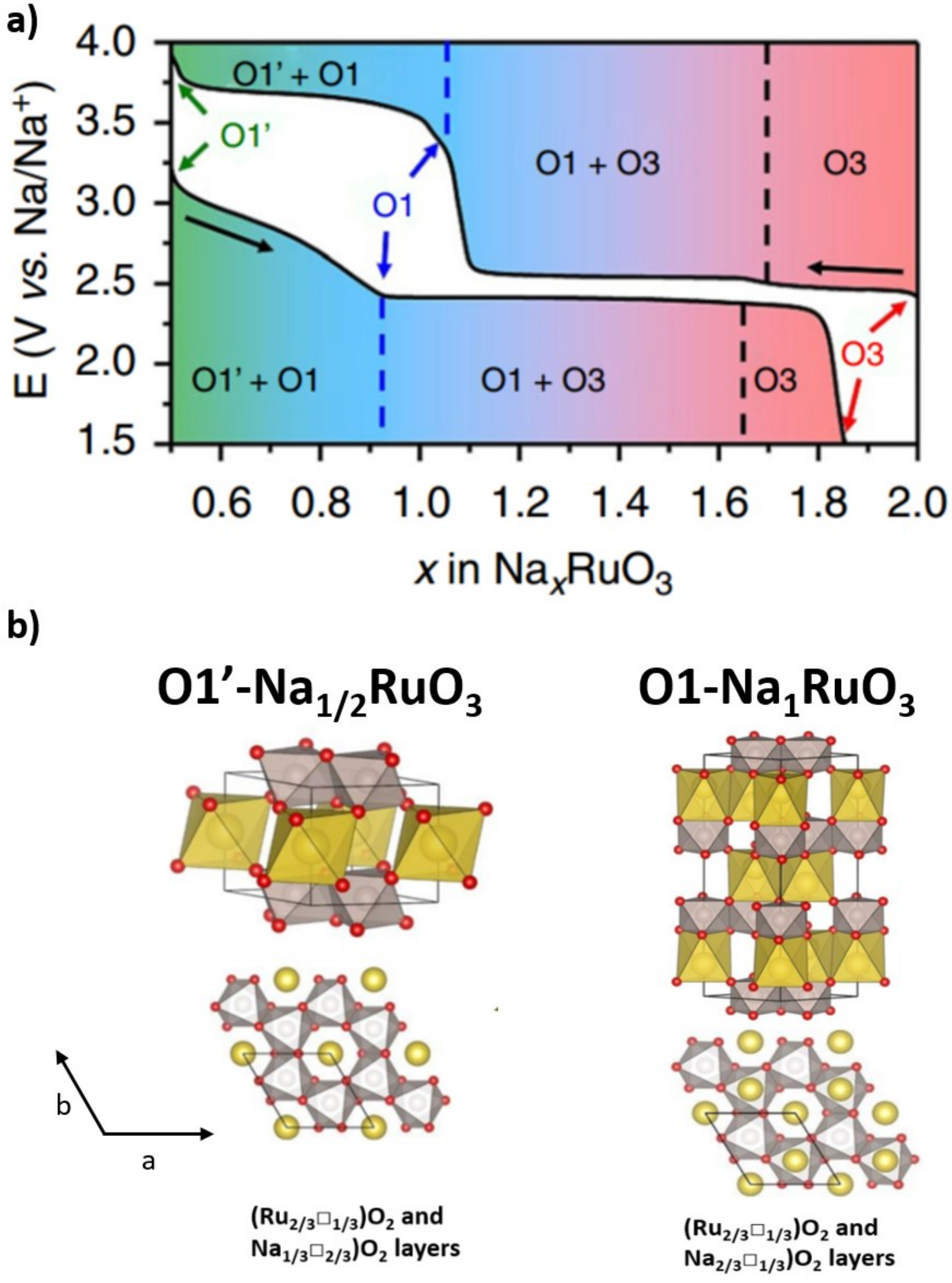

Figure VI-2: *(a) Electrochemical performances between 1.5 and 4 V of the O3-Na_xRuO_3 system at C/10 (b) Representation of the O1-Na_1RuO_3 and O1'-$Na_{1/2}RuO_3$ structures and the corresponding Ru ions, Na ions and vacancies repartition in the layers. From reference* [48].

2. ^{23}Na MAS NMR results

Single pulse ^{23}Na MAS NMR spectra were recorded on a Bruker 500 Avance spectrometer at 132.302 MHz (B_0= 11.75 T). A spinning frequency of 30 kHz was used. The sample were placed in zirconia rotors in a dry box and studied by NMR immediately after taking the rotors out of the glovebox. An XRD pattern taken after the RMN studies ensured that the samples did not evolved during the NMR acquisitions, indicating satisfactory air-tightness of the rotors. As ^{23}Na is a quadrupolar nucleus with I = 3/2, a short pulse length of 1 µs corresponding to a selective π/8 pulse determined using an aqueous 0.1 mol.l^{-1} NaCl solution was employed. In these conditions, we ensure that the main signal observed is due to the -½→+½ central transitions. The spectral width was set to 1 MHz, and the recycle time D_0 = 0.2 s, is long enough to avoid T_1 saturation effects. The baseline distortions resulting from the spectrometer dead time (8 µs) were computationally removed using a polynomial baseline correction routine. The external reference was a 0.1 mol.L^{-1} NaCl aqueous solution.

2.1 Pristine phase

Figure VI-3 represents the three Na sites environments in O3-Na_2RuO_3. O3-Na_2RuO_3 crystalizes in the *C2/m* space group leading to two Na sites in the interslab space which are relatively similar and label Na2 and Na3 in this work. They only differ because of the monoclinic distortion of the cell. **Figure VI-4a** shows the ^{23}Na MAS NMR spectra of two O3-Na_2RuO_3 phases prepared in the same way as described in reference[48]. Both spectra of O3-Na_2RuO_3 clearly exhibits two isotropic shifts located at ~2400 and 877 ppm while one spectrum exhibits an additional signal at 750 ppm. Such large shift values are typically resulting from Fermi contact shift interactions expected between Ru^{4+} ($t_{2g}^4e_g^0$) ions and ^{23}Na nucleus. By analogy with the NMR spectra of Li_2MnO_3 that exhibits also a honeycomb ordering (Li/Mn in the layers)[149], we can assign the most shifted signals to Na1 (site: 2a) in the Ru plane, interacting with 6 Ru^{4+} as 1st neighbors (90° Ru-O-Na) and the less shifted ones to Na2 and Na3 (**Figure VI-3**). Both Na2 (site: 4h) and Na3 (site: 2d) sites have 4 Ru^{4+} as first neighbors (90° Ru-O-Na) and 4 Ru^{4+} as second neighbors (180° Ru-O-Na interactions). They result in really similar Fermi contact shifts around ~877 ppm. This signal assignment was confirmed by DFT calculations performed by Eriko Watanabe from the University of Tokyo, who spent 3 months in our group. The presence of two contributions ~877 ppm, can be detected by the slight asymmetry of the signal on the left side. We attempted to decompose the signal using two contributions as shown in **Figure VI-4b and c**. First fit (**Figure VI-4b**) was performed by fixing the width at half maximum to 42.7 ppm and the Gaussian/Lorentzian proportion to 0.57 because both Na2 and Na3 sites are in similar environments. Therefore, only the intensity and the position of the signals can be refined. We thus determined the presence of two contributions located at 877 ppm and 925 ppm, with proportions different from the expected ones for Na in Na2 (site 2d) and Na3 (site 4h)[48]. By releasing all the parameters (**Figure VI-4c**), we obtained the expected two for one proportion between Na3 and Na2. However, the signals have different widths (40 and 77 ppm) and different Gaussian/Lorentzian proportions (0.72 for the less shifted signal and 0.67 for the other) which is surprising for Na nucleus in really similar environments. Consequently, this slight asymmetry could be due to some different Na environments because of the stacking faults. The 750 ppm one may also be assigned to the presence of some stacking faults evidenced in this material that may modify slightly locally the bond distances and angles[48].

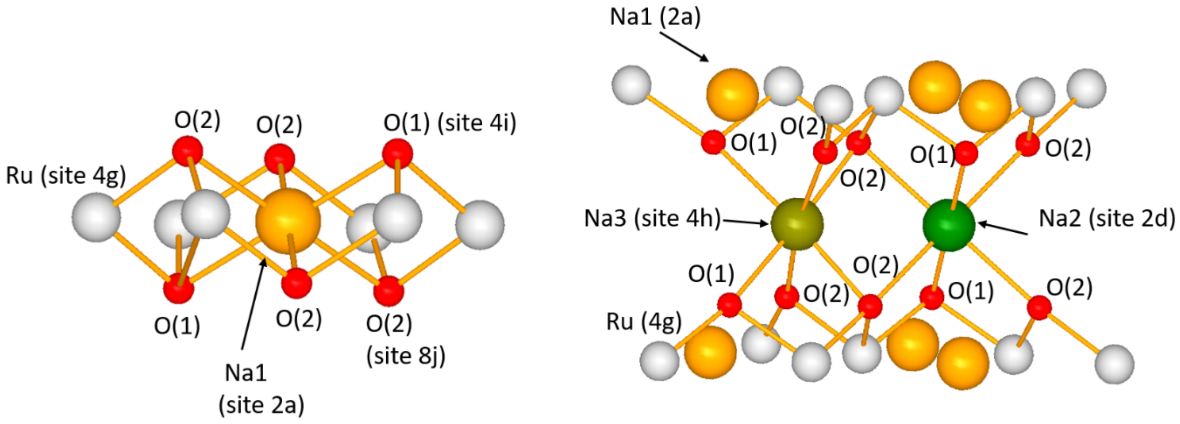

Figure VI-3: *Representation of the different Na site environments in O3-Na_2RuO_3.*

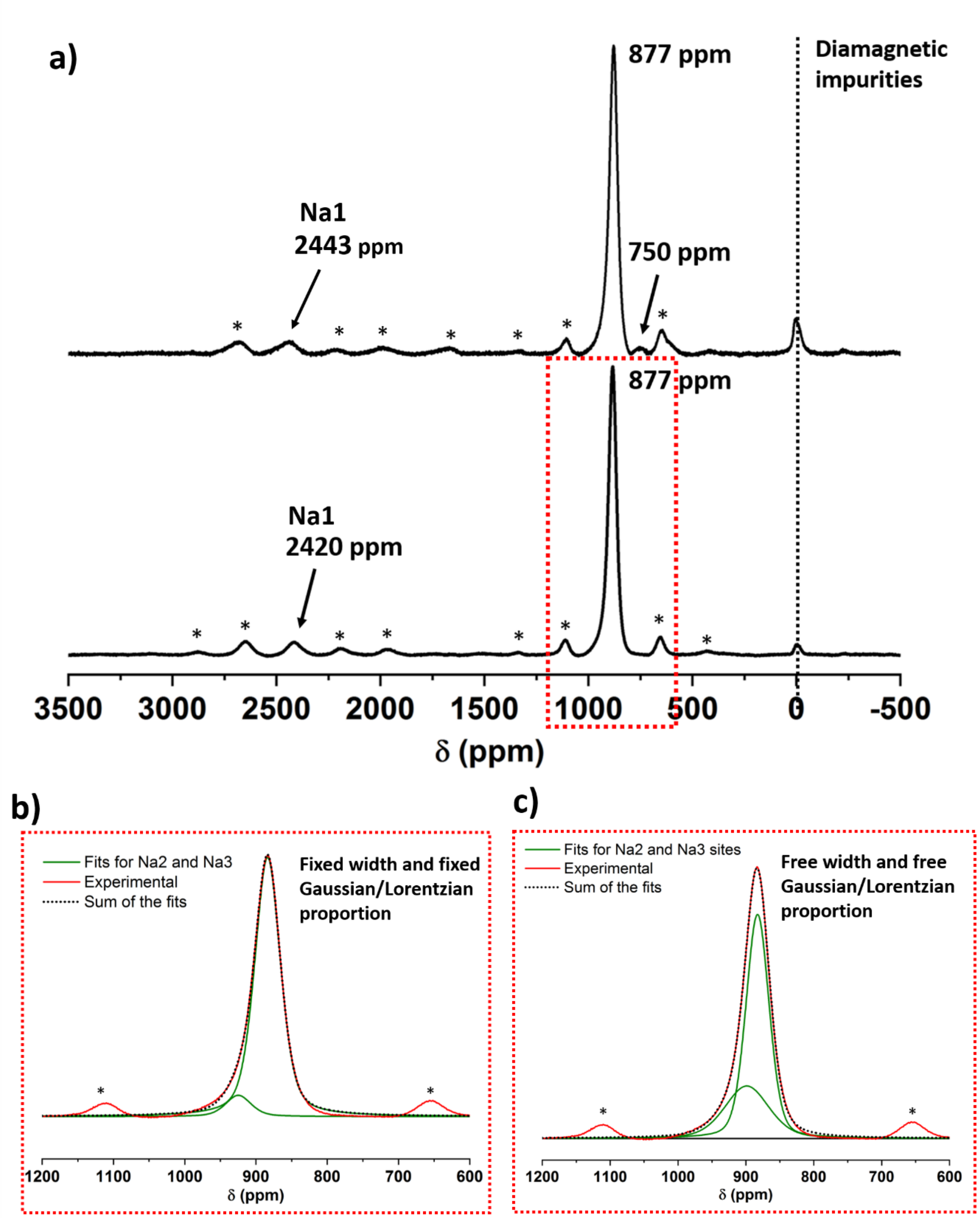

***Figure VI-4**: (a) ^{23}Na MAS NMR spectra of two O3-Na_2RuO_3 phases. The measurements were realized on a 11.75 T magnet with a spinning frequency of 30 kHz and a single pulse sequence. (b) Fits realized on DMFit of the signal at 877 ppm using two Na contributions corresponding to Na2 and Na3 using fixed widths and fixed Gaussian/Lorentzian proportions. (c) Fits realized on DMFit of the signal at 877 ppm using two Na contributions corresponding to Na2 and Na3 and free parameters. * represents the spinning side bands*

2.2 Deintercalated phases and reversibility of the system

In order to check the reversibility of the cycling process of O3-Na_2RuO_3 depending on the upper cutoff voltage, we investigated the local structure by ^{23}Na MAS NMR of two phases recovered at the end of the discharge and synthetized by electrochemical reintercalation at 1.5 V. The first one was charged up to 3.07 V (Na_1RuO_3) and the second one up to 4 V ($Na_{1/2}RuO_3$). **Figure VI-6** displays the NMR spectra of these two phases. Additionally, **Figure VI-6** shows the NMR spectra of the Na_xRuO_3 materials recovered after the Na^+ electrochemical deintercalation at 3.07 V (O1-Na_1RuO_3) and at 4 V (O1'-$Na_{1/2}RuO_3$) compared to the one of the pristine O3-Na_2RuO_3. In **Figure VI-6**, the signal located around 0 ppm is assigned to Na carbonates, or other Na diamagnetic species (remaining electrolyte salt, SEI). The acquisitions were performed in the same conditions than for the pristine phase. All the spectra were normalized to the number of scans.

No significant differences are observed for the two materials recovered after a charge up to 3.07 V (Na_1RuO_3) or up to 4 V ($Na_{1/2}RuO_3$) followed by a discharge at 1.5 V: their spectra exhibit two signals (around 895 ppm and one around 2550 ppm), showing that the deintercalation process is overall reversible and the Na^+ ions can be reintercalated in the transition metal layers (signal at 2550 ppm). Those spectra are, however slightly different from the one of the pristine phase. The slight difference in the shift values is probably due to some slight differences in distances and angles due to the reformation of stacking faults and to the overall Na composition that might be slightly lower than 2, although no evidence of an extra signal possibly assigned to Na next to Ru^{5+} (t_{2g}^3 e_g^0) ions is observed. No signal at 750 ppm is clearly observed in the discharged phases but the signal at 895 ppm is larger than the one of the pristine material, probably also due to the reformation of stacking faults that may differ from the pristine materials. As a conclusion, the cycling at 4 V that involves the O-redox mechanism is mostly reversible and do not imply Ru irreversible migration in the interslab space. This point confirms the previous results obtained by XRD for the same phases after cycling and the good reversibility of the electrochemical process.

O1-Na_1RuO_3 and O1'-$Na_{1/2}RuO_3$ were also studied by ^{23}Na MAS NMR. **Figure VI-5** shows the Na site environments in both phases. Mortemard de Boisse et al.[48] reported that Na_1RuO_3 crystallizes in the $R\overline{3}$ space group while $Na_{1/2}RuO_3$ crystallizes in the $P\overline{3}{:}1m$ space group. Surprisingly, the O1-Na_1RuO_3, does not exhibit any shifted signal in our acquisition conditions

(**Figure VI-6)** suggesting a complex behavior of the Fermi contact shift (link to the structure and electronic structure) for this composition. From a geometric aspects, Mortemard de Boisse *et al*.[48] reported that the interlayer distance continuously decreases from x = 2 to x = 1. This can be explained by the presence of non-centered Na^+ ions in their octahedra as depicted on **Figure VI-5**, as Na^+ is located in an octahedron sharing a face with Ru^VO_6 on one side and with $\square O_6$ on the other side. These particular positions lead to Ru-O-Na angles different than the usual 90° and 180° for 1st and 2nd neighbors interactions. By only considering the distance between the Na^+ and the Ru^{5+}, there are 6 Ru^{5+} as 2nd neighbor with ~126° Ru-O-Na interactions, 3 Ru^{5+} interact as 3rd neighbor at ~137° and only 1 Ru^{5+} interacts at ~82° as 1st cationic neighbor (**Figure VI-5)**. The presence of these particular angles shows an uncommon and complex behavior of this system. The Ru^{5+} as 1st cationic neighbor (red arrow on **Figure VI-5**) shares one face of its RuO_6 octahedron with one NaO_6 octahedron. The distance between this Ru^{5+} and the Na^+ ions, in this case, is 3.149 Å. Moreover, the θ angle, defined in the first chapter (**Figure I-6**) between the z axis and a Ru-O direction, is equal to ~60° indicating a possible D_{3d} distortion and lift of degeneracy of the t_{2g} orbitals into the a_{1g} and e_g' orbitals. In this case, it is possible that the localized behavior of the electrons in 4d orbitals leads to a the loss of the observability of the signal due to a direct overlap mechanism in a similar way than for Li_xCoO_2 in the 0.94 – 1 range[91]. Moreover, another possibility is the that the Ru^{5+} as first neighbors (126° interactions) are mainly involved in the spin transfer mechanism due to the short Na-O distance (2.129 Å) shown in **Figure VI-5**. Therefore, this short Na-O distance could lead to an important spin transfer from the Ru^{5+} to the 3s Na orbital and the loss of observability of the NMR signal, which would be too shifted, too broad or associated with a very short T1 or T2 relaxing times.

For $Na_{1/2}RuO_3$, a ^{23}Na MAS NMR signal is observed around a major contribution located at 30 ppm. The presence of an additional signal at 100 ppm can be due to the 2 % of stacking faults highlighted in the previous work. **Figure VI-2** exhibits the Na^+/vacancy ordering in the interslab spaces and **Figure VI-5** depicts the environment of the unique Na site in this phase. No Na^+ ions is located in octahedral sites with a common face with RuO_6 anymore. Therefore, no direct overlap between the a_{1g} Ru orbitals and 3s Na orbital is possible anymore, what would prevent the loss of observability of the NMR shift. The Na^+ ions occupy the center of one octahedra site as depicted in **Figure VI-5** sharing only edges or corner with RuO_6. Mortemard de Boisse *et al*[48]. showed that the interslab spaces thickness still decreases from x = 1 to x = 1/2 but the Na-O distance increases by considering the oxygen ions involved in the 126° interactions for Na_1RuO_3. Moreover by using the calculated parameters obtained by a Rietveld refinement and reported in reference [48] for $Na_{1/2}RuO_3$, we determined that $\theta \sim 57°$ which indicates that the RuO_6 octahedra are less distorted than in the case of Na_1RuO_3. For this specific composition, O-redox has occurred and is associated to the formation of relatively short O-O bonds. If paramagnetic O were formed, one could have expected a large Fermi contact shift for the adjacent Na^+ ions. As the shift observed is relatively small, it more likely corresponds to either a Knight shift or a Fermi contact shift with small spin transfer from Ru to Na. As no magnetic measurements were performed for the Na_1RuO_3 and $Na_{1/2}RuO_3$ phases, it is, for the moment, difficult to understand their electronic structure. Magnetic measurements could inform about the presence of localized or delocalized electrons. Note that the magnetic properties of Li_xRuO_3 had been investigated by Kobayashi *et al.*[150]. They reported that Li_1RuO_3 has a temperature independent susceptibility evolution suggesting the presence of only delocalized electrons which is not in agreement with the behavior of Na_1RuO_3 observed with ^{23}Na MAS NMR.

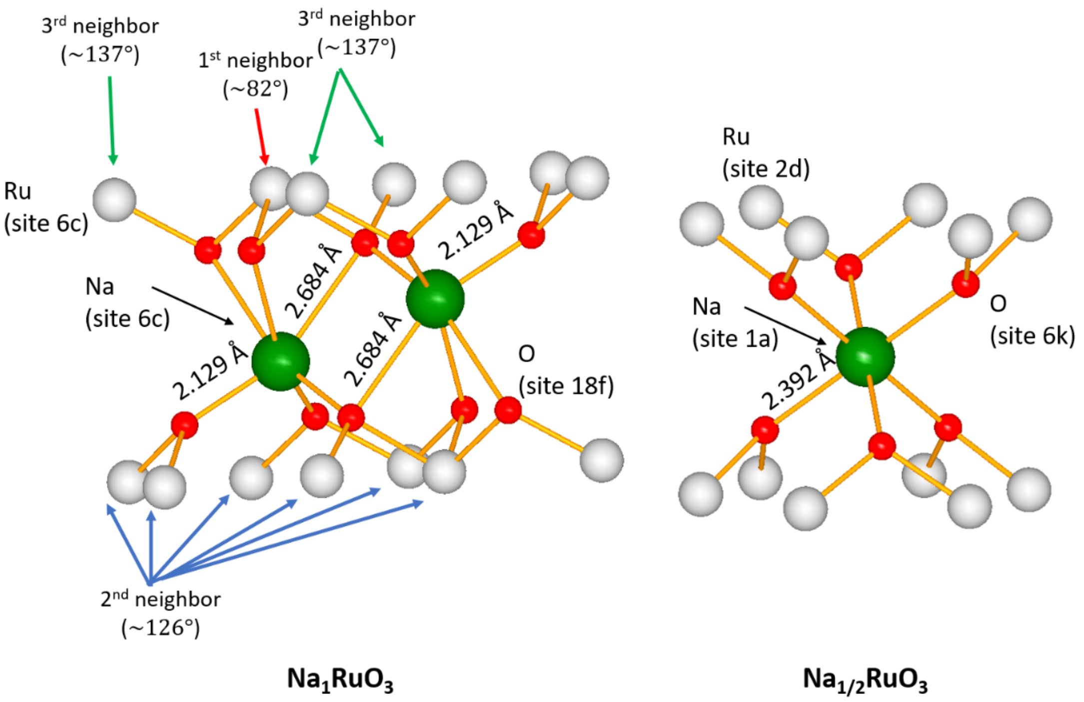

Figure VI-5: *Representation of the different Na sites environments in Na_1RuO_3 and $Na_{1/2}RuO_3$.*

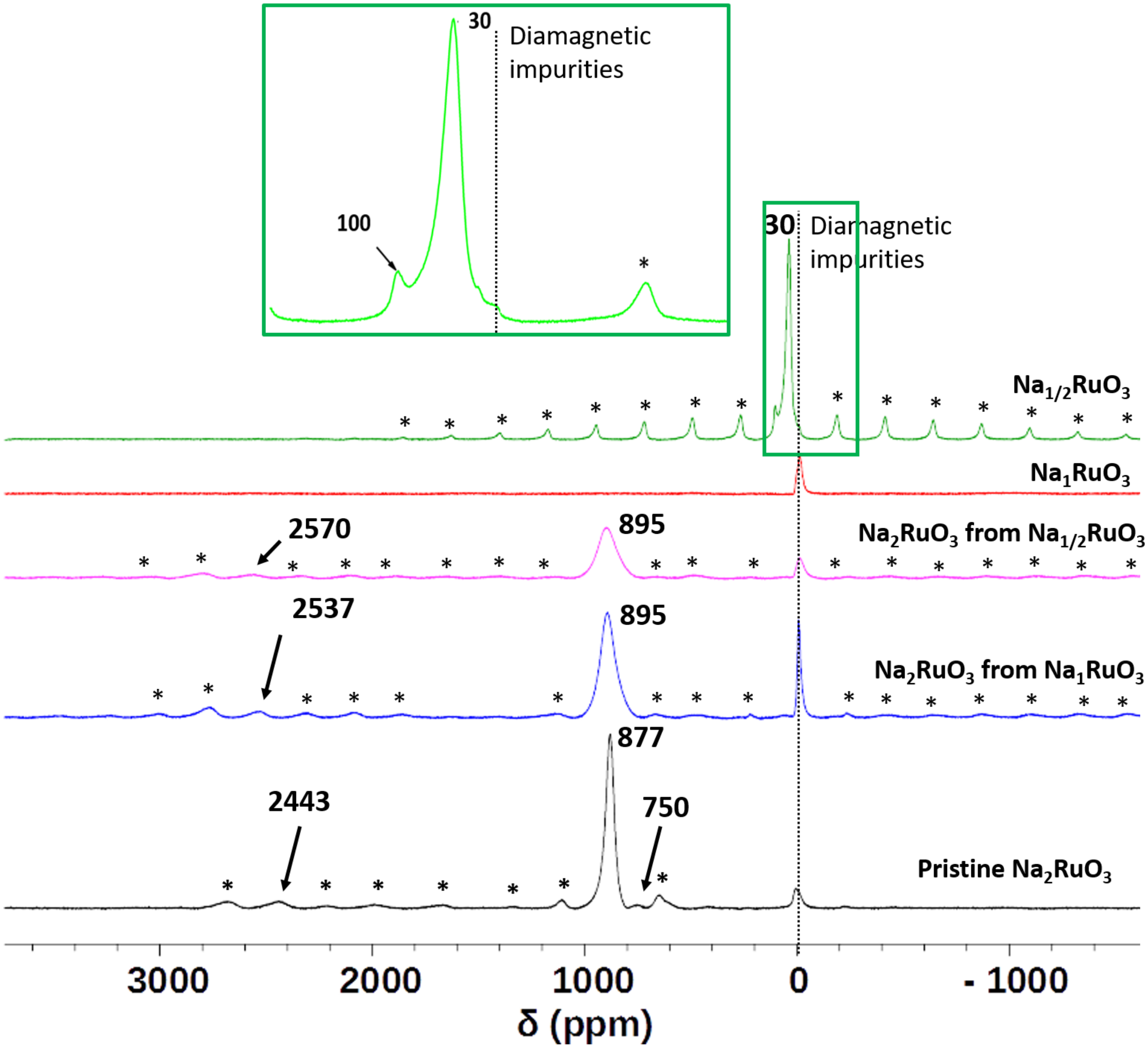

***Figure VI-6**: ^{23}Na MAS NMR spectra of the pristine Na_2RuO_3 (black line), Na_2RuO_3 after one cycle (magenta and blue lines), Na_1RuO_3 (red line) and $Na_{1/2}RuO_3$ (green line). The spectra were recorded on a 11.75 T magnet with a spinning frequency of 30kHz and using a single pulse sequence. * are the spinning side bands.*

3. Conclusion

In this chapter, we studied the evolution of the local structure of O3-Na_xRuO_3 by *ex-situ* ^{23}Na MAS NMR on phases synthetized by electrochemical (de)intercalation and confirmed its good reversibility of the redox process even using an upper cutoff voltage involving O-redox. The participation of the oxygen ions to the redox process is very interesting for the development of new materials positive electrode materials with high energy densities. Nowadays, the number of studies concerning this kind of materials is drastically increasing. These systems are usually composed of Mg^{2+}, Na^+ ions or □ in their transition metal layers. We can mention $Na_x(Mg_yMn_{1-y})O_2$[151], $Na_x(□_{1/7}Mn_{6/7})O_2$[152], $Na_xRu_{0.75}Sn_{0.25}O_3$[144] or Na_xIrO_3[153] which are systems that were studied as positive electrode materials for Na-ion batteries where an anionic redox process participates to the global redox process at high voltages.

Concerning the NMR study of the deintercalated phases shows that the NMR evolution is more complex to understand without complementary magnetic properties or electrical conductivity measurements. A loss of signal observation is obtained for O1-Na_1RuO_3, while a 30 ppm signal is observed for $Na_{1/2}RuO_3$ suggesting a magnetic transition between x = 1/2 and x = 1. For the future, it would be interesting to study other compositions in order to have a better insight of the global evolution of the shift and the mechanisms involved during the Na^+ deintercalation.

General Conclusion/Perspectives

During this work, solid state NMR has been used as a key tool to characterize, as a complementary technique to XRD, the atomic structure of several lamellar oxides. In addition, thanks to the hyperfine coupling, solid state NMR allowed to investigate the local electronic structure of the materials and its modification upon cycling. We were also interested in the ionic dynamics of the Li^+ ions in the interslab spaces for two specific layered oxides.

The first part of this work concerned an OP4-$(Li,Na)CoO_2$ phase which proposes a very unusual structure because of an 1:1 alternation of interslab spaces filled with Li^+ in octahedral sites and Na^+ in prismatic sites. As a misunderstanding existed between the chemical formula of the phase and its structure, we decided to investigate the local structure of the phase. ^7Li MAS NMR showed the presence of five different environments for the Li^+ ions in the material. Moreover, we highlighted that the NMR signal shifts are due to two contributions: a Knight shift and a Fermi contact shift due to the presence of, respectively, electrons with a localized behavior and electrons with a delocalized behavior in the electronic structure. This “Curie Weiss metallic regime” involves that the electronic structure is difficult to be modelled by DFT calculations. Based on the ^{23}Na MAS NMR results, we further considered the presence of Na^+ ions in the Li interslab spaces in our Rietveld refinement and we thus determined OP4-$[Li_{0.42}Na_{0.05}]Na_{0.32}CoO_2$ as chemical formula. Finally, the Li^+ ions exhibited no obvious dynamics in the interslab spaces, for the probed timescale, as revealed by the selective inversion technique due to the almost 95 % filling of the Li interslab spaces with Li^+ and Na^+ ions in octahedral sites.

Note that also that during this PhD, we published, in collaboration with Romain Berthelot (ICGM, Montpellier), the study of a layered oxide $Li_{3-x}Na_xNi_2SbO_6$ with a honeycomb ordering in the Ni_2SbO_2 slabs[154]. Contrary to the OP4 phase, this phase proposes a random occupancy of the interslab spaces with the Na^+ and Li^+ ions in octahedral geometries. NMR was used as a local characterization technique to reach this conclusion and is a powerful technique to study the distribution and localization of the different ions in a material.

The dynamics of the Li^+ ions was evidenced by solid-state MAS NMR (selective inversion technique) in another phase synthetized during this work, O4-Li_xCoO_2. In fact, vacancies are thus present in the Li interslab spaces making easier the Li^+ ions mobility. This material was obtained by a “in solution” ion-exchange technique from the OP4 phase. The idea was to synthetize a phase with ^{6}Li ions in the O3-type layers and ^{7}Li ions in the O2-type layers by considering a possible selective exchange. However, ^{6}Li and ^{7}Li MAS NMR showed that the exchange isn’t selective and both Li^+ ions types occupy, randomly, the two different crystallographic sites. Moreover, we showed that a small amount of Na^+ ions remains in the structure after the ion-exchange. We suggested that this Na^+ ions are located in octahedral sites in the Li interslab layers.

The mechanisms occurring upon cycling have been studied by *in-situ* Synchrotron XRD and ^{23}Na MAS NMR for different P2-$Na_xCo_yMn_{1-y}O_2$ (y = 1/3, 1/2, 2/3 and 1) phases used as positive electrode materials in Na batteries. We determined that P2-Na_xCoO_2 can be cycled at C/20 reversibly up to 4.3 V vs Na^+/Na and shows a complex phases diagram with a succession of solid solution and two-phase reactions upon Na deintercalation. While the P2 structure is maintained for $x > 1/3$, for $1/3 < x < 1/2$, we showed a solid-solution behavior despite that “in average” the presence of possible incommensurable structures associated to ion and charge ordering are observed. A new ordered phase $Na_{1/3}CoO_2$ was also evidenced and it was shown to crystallize in a hexagonal cell with a $\sqrt{3}\,a_{hex} \times \sqrt{3}\,a_{hex} \times 3\,c_{hex}$ superlattice. However, this phase needs further investigations to get a description of its actual structure. Moreover, we showed that sheets glidings occur for $x < 1/3$ with the transformation of the P2-type structure into an “OP”-like one with different intercalation sites for the Na^+ ions and many stacking faults. Sheets glidings are associated with a decrease of the c lattice parameter due to the formation of octahedral sites. For future works, it would be interesting to investigate more carefully the discharge following the charge up to 4.6 V in order to understand the reason of the strong polarization observed on the galvanostatic curve at C/20.

Concerning the Co,Mn systems, we highlighted that P2-$Na_xCo_{2/3}Mn_{1/3}O_2$ can be cycled reversibly at C/20 up to 4 V (vs Na^+/Na) and that the two other studied systems (for y = 1/3 and 1/2) show an important polarization when cycled, respectively, up to 4 V and 4.3 V. Globally these systems reveal a solid solution behavior with one or two peculiar phases for specific compositions (x = 1/2 and/or x = 1/3). The presence of sheets glidings at high voltage was also highlighted on the $Na_xCo_{2/3}Mn_{1/3}O_2$ system. Additionally, we determined that $Na_{1/2}Co_{2/3}Mn_{1/3}O_2$ crystallizes in the *Pnmm* space group like the $Na_{1/2}CoO_2$ phase. The discharge following the charge up to 4.5 V would be also interesting to be investigated in order to understand the mechanisms involved even if the polarization is weaker than in the case of Na_xCoO_2.

As just mentioned, the mechanisms involved during the Na^+ deintercalation were studied in the P2-Na_xCoO_2 and P2-$Na_xCo_{2/3}Mn_{1/3}O_2$ systems. For each system, the formation of intermediate phases was identified. They were thus synthesized by electrochemical deintercalation at specific voltages. in order to be analyzed *ex-situ* by XRD and ^{23}Na MAS NMR. Rietveld refinements of the XRD patterns showed that the Na layers' thickness increases during the battery charge for P2-Na_xCoO_2 until reaching a limit value for x = 0.4. ^{23}Na MAS NMR exhibited a complex behavior for both systems during the Na^+ deintercalation in fact, the shift values first increase and then decrease before reaching an almost constant value for the lower x values. It is, therefore, impossible to only consider the Co^{3+} ($t_{2g}^6\ e_g^0$) ions oxidation into paramagnetic Co^{4+} ions ($t_{2g}^5\ e_g^0$) to explain the shift evolution, two effects have to be considered: the evolution of the structure geometry (increase of the Na-O distance when x decreases) and the evolution of the electronic structure (increase of the amount of formal Co^{4+} ions when x decreases). We showed that both effects are consecutively predominant when the Na^+ content in both systems decreases and we highlighted the presence of a "Curie-Weiss metallic regime" for $x > 0.5$ with localized and delocalized electrons. Finally, for the lowest x values ($x < 0.5$), the presence of only delocalized electrons (Pauli paramagnetic regime) in the electronic structure of P2-Na_xCoO_2 and the constant NMR shift suggest that the participation of the Na 3s orbital to the Knight shift is almost constant. For P2-$Na_xCo_{2/3}Mn_{1/3}O_2$, the evolution of the NMR shift is due to a "Knight shift" with an additional constant participation of the localized electrons of the Mn^{4+} ($t_{2g}^3\ e_g^0$) ions for the lowest x compositions. It should be interesting to study both $Na_xCo_{1/2}Mn_{1/2}O_2$ and $Na_xCo_{1/3}Mn_{2/3}O_2$ systems in the same vein in order to confirm the presence of a magnetic transition occurring for $x < 0.5$ in the Co,Mn systems. Concerning the "OP" phases resulting from sheets glidings and obtained at high voltage, ^{23}Na MAS NMR confirmed the presence of a panel of different environments for both systems.

In the last chapter, O3-Na_xRuO_3 was instigated by *ex-situ* ^{23}Na MAS NMR, in collaboration with the Pr. Yamada group and B. Mortemard de Boisse, a former PhD student of the group. The particularity of this system is to propose an extra capacity due to the participation of the oxygen ions in the redox process because of a short enough O-O distance due to the honeycomb ordering in the transition metal layers. O3-Na_2RuO_3 after one cycle, O1-Na_1RuO_3 and O1'-$Na_{1/2}RuO_3$ were synthetized by electrochemical (de)intercalation. We showed a good reversibility of this system at the local scale and a reintercalation of the Na^+ ions in the transition metal layers after one cycle. The electronic structure evolution of this system is relatively complex to understand while no sheets glidings occurs even for the lowest Na^+ contents. The evolution of the NMR shifts during the Na^+ deintercalation seems to be mainly correlated with the geometry of the structure and especially, the distance between the Na^+ and the Ru ions as first neighbors leading to a strongly shifted signal for Na_1RuO_3. However, for $Na_{1/2}RuO_3$, the shift can either be due to a Knight shift or a Fermi contact shift but without magnetic measurements, it is, for the moment, difficult to conclude about the magnetic state of these phases. Moreover, it would be interesting to synthetize more phases with different Na^+ compositions in order to have a better insight of the evolution of the local structure.

The systems with extra capacity due to the participation of the oxygen couple to the redox process are very interesting and promising for the future, in the battery field as no structural transition due to layers glidings seems to occur in these systems at high voltage allowing a better stability in cycling. These kinds of system would be interesting to be studied for different amounts of Na^+ ions in order to understand the different mechanisms occurring during the charge with ^7Li and/or ^{23}Na MAS NMR. For instance, Yang *et al*[155]. reported that the $Na_xLi_{0.18}Fe_{0.12}Mn_{0.7}O_2$ system have an interesting capacity of 190 mAh.g^{-1} with a relatively good capacity retention.

Appendix

A.1 $Na_{2/3}CoO_2$

The most intense diffraction peaks are those indexed with the *P6₃/mmc* space group, only the superstructure peaks allow to determine the superstructure lattice for the peculiar phase. Platova *et al.*[92] suggests a cationic order in an orthorhombic cell with the $R\bar{3}c$ space group and cell parameters bigger than in the corresponding hexagonal cell ($\sqrt{12}a_{hex}$ x $\sqrt{12}a_{hex}$ x $3c_{hex}$). Berthelot *et al.*[47] managed to index each peak with the cell described by Platova *et al*. We will only check if a Le Bail refinement is possible with the patterns obtained during the *operando* measurements (**Figure A-1**). Note that peaks impurities (Na, Al or graphite) were manually removed from the XRD pattern for the refinements. The lattice parameters (a_s = 9.797(1) Å and c_s = 32.81(1) Å) calculated are in good agreement with those determined by theoretically by Platova *et al.*[92] and experimentally by Berthelot *et al.*[47].

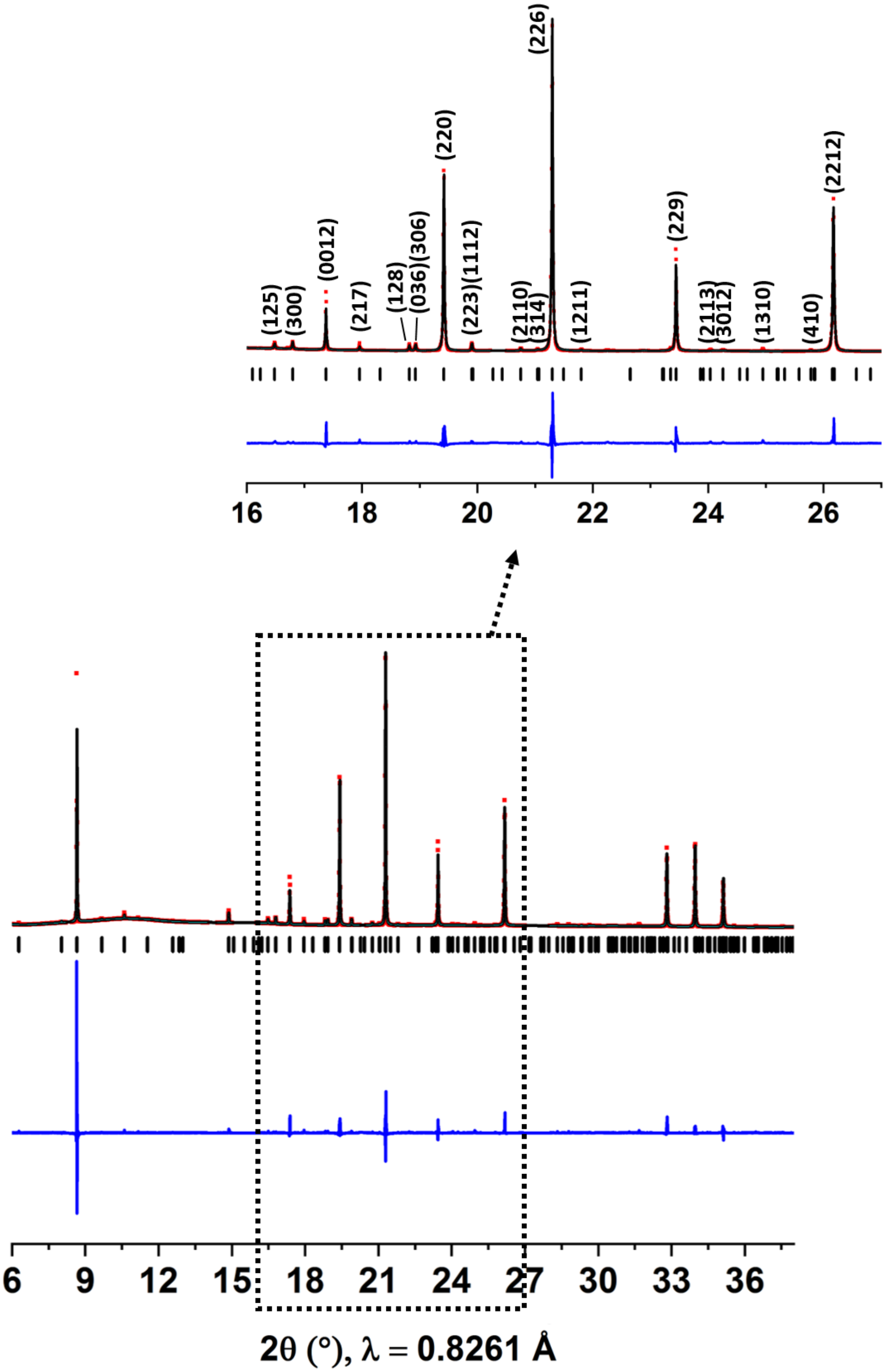

Figure A-1: *SXRD pattern of Na$_{2/3}$CoO$_2$ in the R$\bar{3}$c space group. Red points = Yobs, black line = Ycalc, blue line = Yobs – Ycalc, black ticks = Bragg positions. Insert highlights the presence of the superstructure peaks.*

A.2 $Na_{1/2}CoO_2$

The XRD pattern is shown in **Figure A-2** and most of the peaks are the same than for the P2 structure phase with the *$P6_3/mmc$* space group. Additional peaks appear (in insert) and can be refined in an orthorhombic cell as proposed by Huang *et al.*[16] with an order ($\sqrt{3}a_{hex}$ x $2a_{hex}$ x c_{hex}) in the Na interslab spaces. This phase, as $Na_{2/3}CoO_2$, was already refined by Berthelot *et al.* in the *Pnmm* space group. In this manuscript, calculated lattice parameters are a_s = 4.865(1) Å, b_s = 5.626(1) Å and c_s = 11.12(1) Å, in good agreement with those determined in former studies.

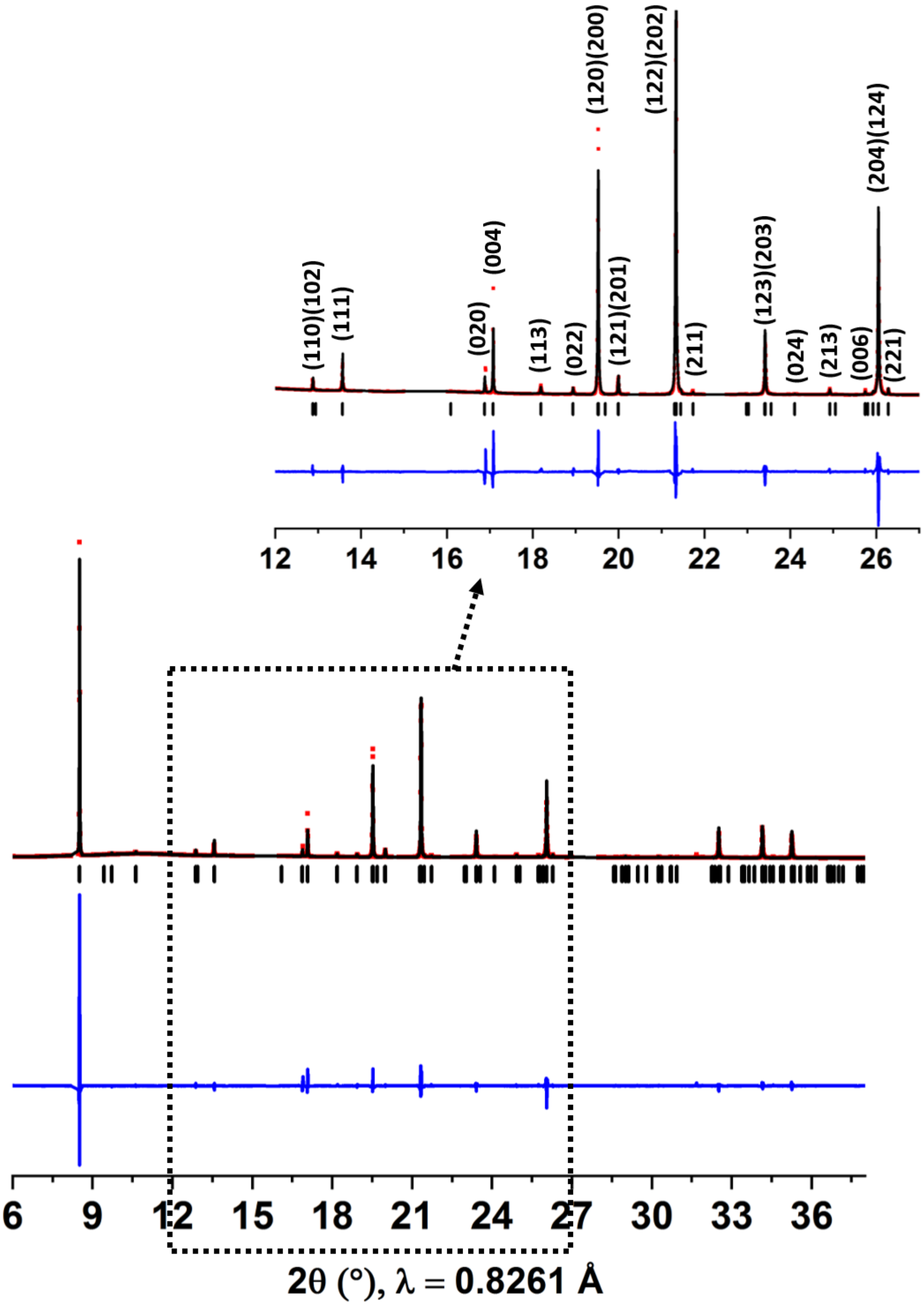

Figure A-2: *SXRD pattern of $Na_{1/2}CoO_2$ in the Pnmm space group. Red points = Yobs, black line = Ycalc, blue line = Yobs – Ycalc, black ticks = Bragg positions. Insert highlights the presence of the superstructure peaks.*

A.3 $Na_{4/7}CoO_2$

This phase was described, previously, by Igarashi *et al.*[109] in the hexagonal cell with a different space group than P2 structure. They realized electron and neutron diffraction in order to exhibit the superstructure ordering and determined a *P6₃/m* space group with a $\sqrt{7}a_{hex}$ x $\sqrt{7}a_{hex}$ x c_{hex} superlattice. In this manuscript, we show the refined XRD pattern of this phase (**Figure A-3**). The calculated lattice parameters are in good agreement with the superstructure determined by Igarashi *et al.*[109] (a_s = 7.459(1) Å and c_s = 11.04(1) Å).

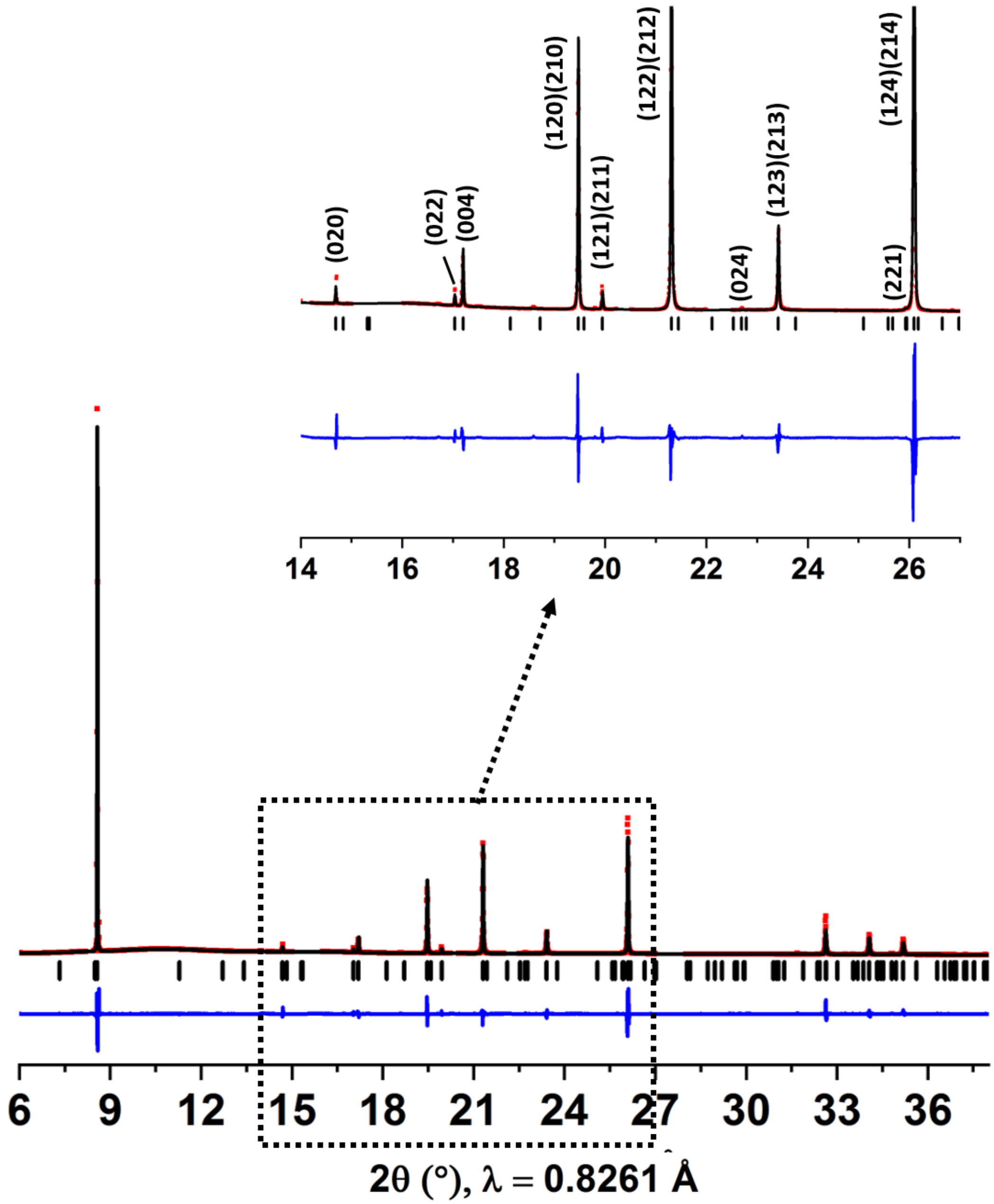

***Figure A-3**: SXRD pattern of $Na_{4/7}CoO_2$ in $P6_3/m$ space group. Red points = Yobs, black line = Ycalc, blue line = Yobs – Ycalc, black ticks = Bragg positions. Insert highlights the presence of superstructure peaks.*

A.4 First discharge on the Na_xCoO_2 system

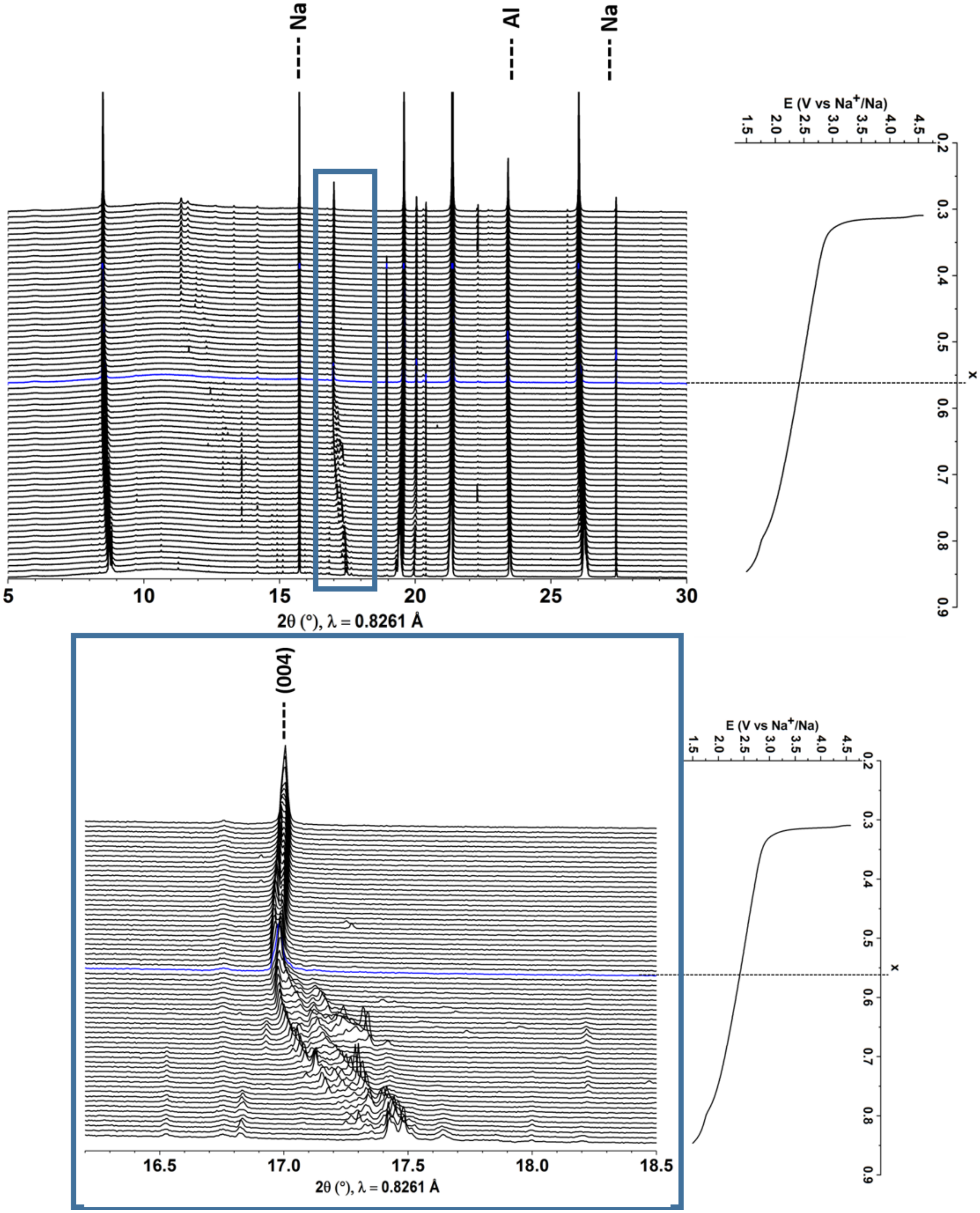

Figure A-4: *XRD patterns obtained by operando measurements on Na_xCoO_2 system on first discharge from 4.6 V to 1.5 V.*

A.5 First discharge on the $Na_xCo_{2/3}Mn_{1/3}O_2$ system

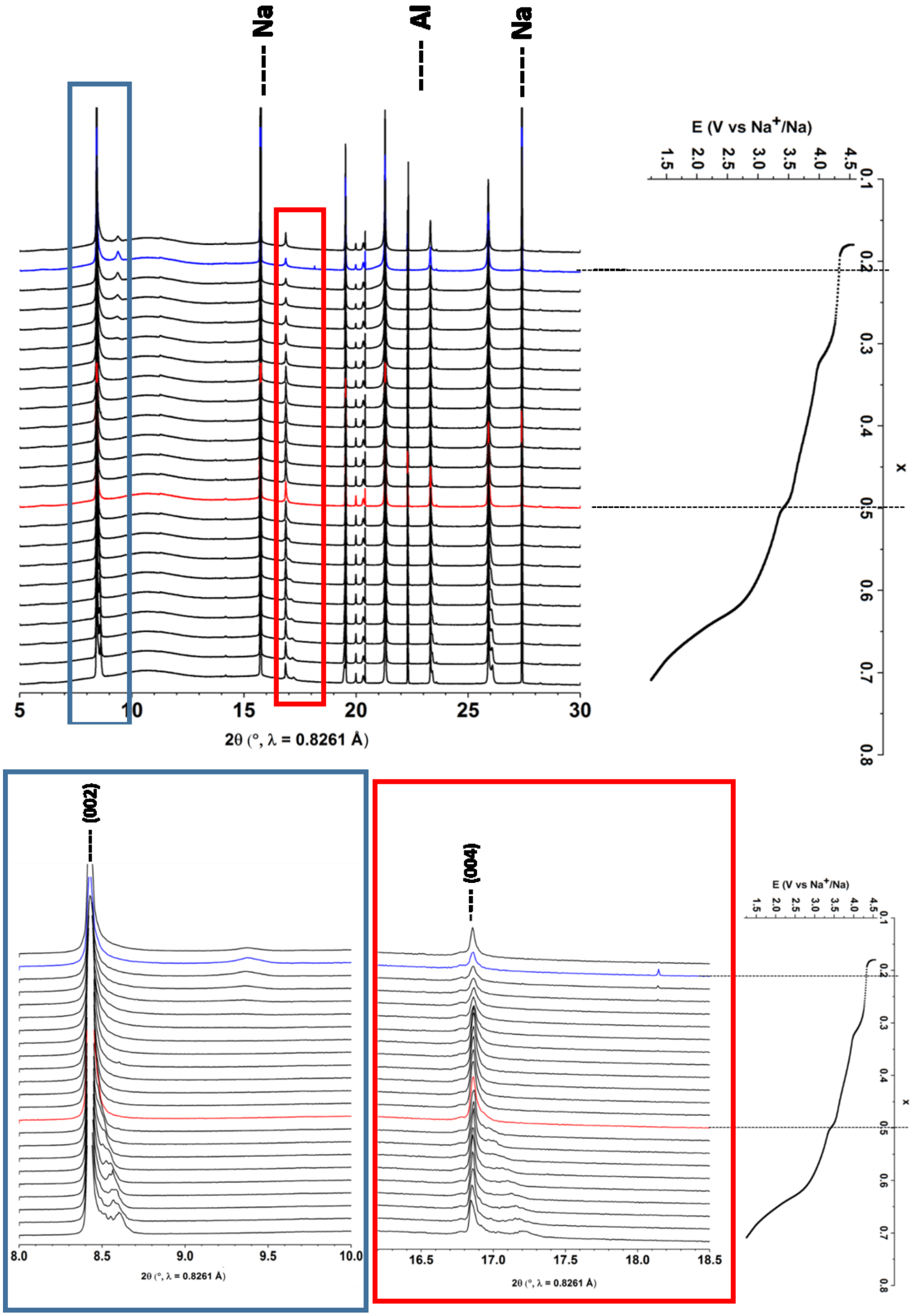

Figure A-5: *XRD patterns obtained by operando measurements on $Na_xCo_{2/3}Mn_{1/3}O_2$ system on first disc*

A.6 Fits of the ^{23}Na MAS NMR spectra on the Na_xCoO_2 phases

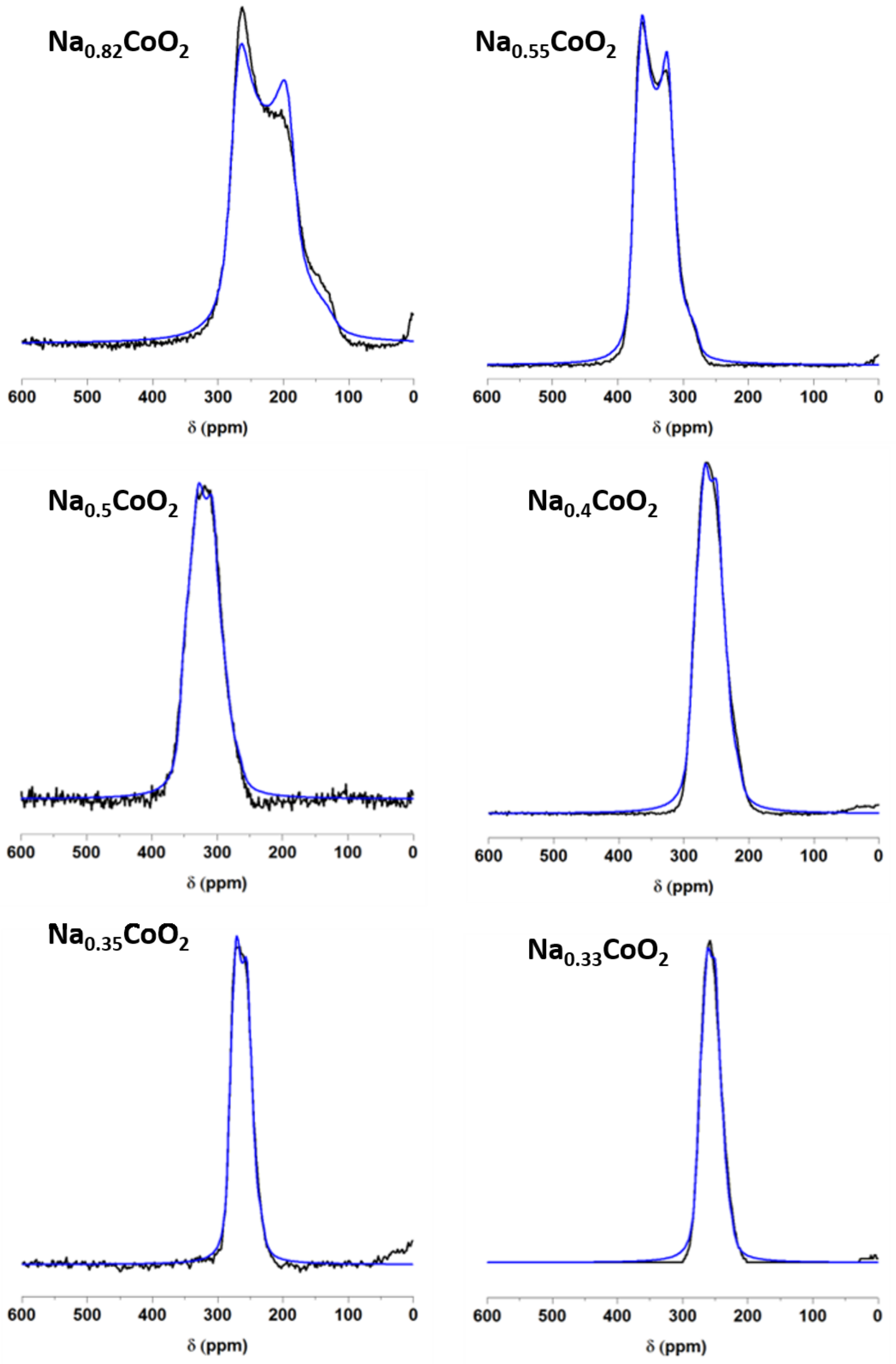

Figure A-6: *Fits of the MAS NMR spectra of the* Na_xCoO_2 *phases using a* 2^{nd} *order quadrupolar lineshape*

Résumé étendu

1. Introduction générale

Les oxydes lamellaires sont des matériaux de formule chimique A_xMO_2 où A représente un ion alcalin et M un ou des ions métaux de transition. Ils sont largement étudiés en chimie du solide et entre autre comme matériaux d'électrode positive pour batteries.

Ils peuvent se décrire comme un empilement de feuillets MO_2 formés par des octaèdres MO_6 et d'espaces interfeuillets où s'intercalent x ions A^+ avec une alternance un feuillet MO_2 pour un interfeuillet. Une nomenclature spécifique existe pour décrire les oxydes lamellaires[1]. Elle est composée d'une lettre et d'un chiffre représentant respectivement, la géométrie du site d'intercalation des ions alcalins (O pour octaédrique, P pour prismatique …) et le nombre de feuillets nécessaire à la représentation de la maille élémentaire. Il faut également noter que le symbole ' est utilisé lorsque la maille subit une distorsion monoclinique ou orthorhombique. En général, la structure des phases $LiMO_2$ est de type O3 signifiant que les ions Li^+ sont intercalés dans des sites de géométrie octaédrique. Pour les oxydes lamellaires de type Na_xMO_2, la variété de structures pouvant être synthétisée est plus large selon les conditions de synthèse utilisées (température, rapport initial Na^+/M ou encore la nature de M)[7]. Les ions Na^+ sont alors intercalés soit dans des sites octaédriques ou prismatique. La **Figure RE-1** représente les structures P2, P3 et O3 ainsi que les environnements locaux des ions Na^+ partageant soit les arrêtes soit les faces (ou bien deux) avec les octaèdres MO_6 des feuillets supérieurs et inférieurs. Il faut remarquer que pour la structure P2, il existe deux sites d'intercalation prismatiques différents partageant soit les faces ou les arrêtes des octaèdres MO_6 et noter, respectivement, Na_f et Na_e.

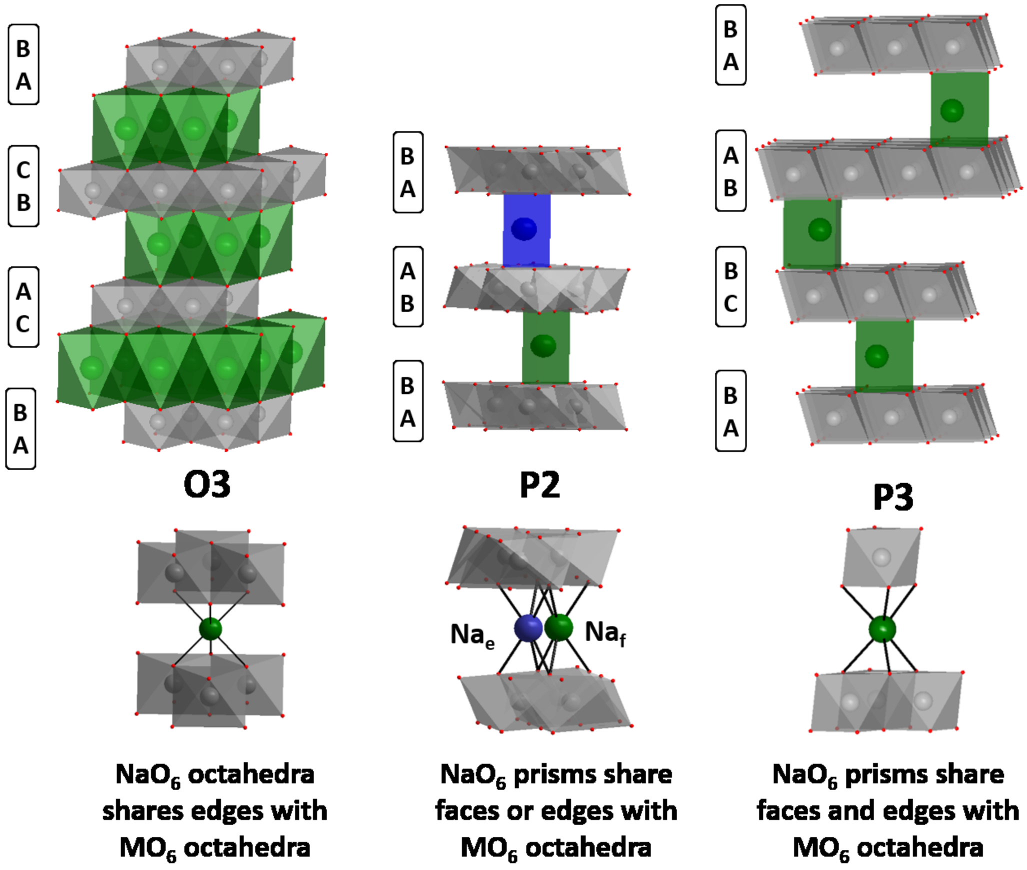

NaO_6 octahedra shares edges with MO_6 octahedra

NaO_6 prisms share faces or edges with MO_6 octahedra

NaO_6 prisms share faces and edges with MO_6 octahedra

***Figure RE-1**: Représentation des structures O3, P2 et P3 et environnements locaux respectifs des ions Na^+*

L'étude des phases Na_xMO_2 comme matériaux d'électrode positive pour batterie Na-ion a connu une forte recrudescence depuis 10 ans à cause de la diminution drastique[9] de la quantité de ressources en Li. En particulier, le système P2-Na_xCoO_2 présente un intérêt tout particulier car certaines phases présentent des propriétés physiques intéressantes telles que des propriétés thermoélectrique ou encore supraconductrice[10–15]. Dans ce manuscrit, nous avons étudier la structure moyenne de différentes phases de différents systèmes, comme P2-Na_xCoO_2, par diffraction des rayons X (DRX). De plus, la Résonance Magnétique Nucléaire avec rotation à l'angle magique (MAS RMN) du ^{23}Na a été utilisée comme technique de caractérisation afin d'étudier la structure locale, électronique et la structure électronique locale des différentes phases synthétisées lors de ce travail de thèse. La RMN a déjà largement été utilisées dans le domaine des batteries[29,30] pour l'étude des matériaux d'électrodes, de l'électrolyte ou encore des interfaces. La RMN du ^{23}Na est sensible à la présence d'électrons célibataires dans l'environnement du noyau de ^{23}Na via les interactions hyperfines. Deux interactions sont, dans ce travail, principalement responsables des déplacements chimiques observés sur les différents spectres RMN obtenus : le contact de Fermi et le déplacement de Knight. Le contact de Fermi est proportionnel à la quantité de densité de spin transférée de l'ion M vers l'orbitale s du noyau de ^{23}Na à travers les liaisons chimiques et donc via l'orbitale 2p de l'ion oxygène. Cette interaction concerne ainsi les électrons de type localisées. Le déplacement chimique impliqué par cette interaction peut s'écrire[62] :

$$\delta^{i}_{Fermi} = \frac{1}{3SN_A}\rho^{i}(0)\chi_M(T)$$

S: nombre de spin

$\chi_M(T)$: susceptibilité magnétique molaire

$\rho^{i}(0) = \sum_j(\left|\psi_j \uparrow (0)\right|^2 - \left|\psi_j \downarrow (0)\right|^2)$ avec $\left|\psi_j \uparrow (0)\right|^2$ la probabilité de présence de spin positif sur l'orbitale s et $\left|\psi_j \downarrow (0)\right|^2$ la probabilité de présence de spin négative sur l'orbitale s.

Le déplacement de Knight implique la présence d'une densité électronique de spin sur le noyau s sondé, cependant pour cette interaction, la densité de spin provient de la participation des électrons s au niveau de Fermi et implique ainsi les électrons de type délocalisés.

Le déplacement chimique total correspond ainsi à la somme des contributions des électrons localisés et des électrons délocalisés.

$$\delta_{tot} = \delta^{M^{n+}}_{Fermi} + \delta^{M^{n+}}_{Knight}$$

La présence d'électrons localisés et délocalisés provient d'une distorsion trigonale D_{3d} des octaèdres CoO_6 dans le cas des cobaltates. Cette distorsion implique une compression des octaèdres suivant l'axe z comme représenté sur la **Figure RE-2a**. Cette distorsion implique la levée de dégénérescence des orbitales t_{2g} en une orbitale a_{1g} et deux orbitales e_g'[54]. La **Figure RE-2b** représente la structure de bande du système P2-Na_xCoO_2 après la distorsion D_{3d} et montrant le niveau de Fermi à la fois dans une bande étroite a_{1g} et une bande large e_g' impliquant respectivement la présence des électrons localisés et délocalisés.

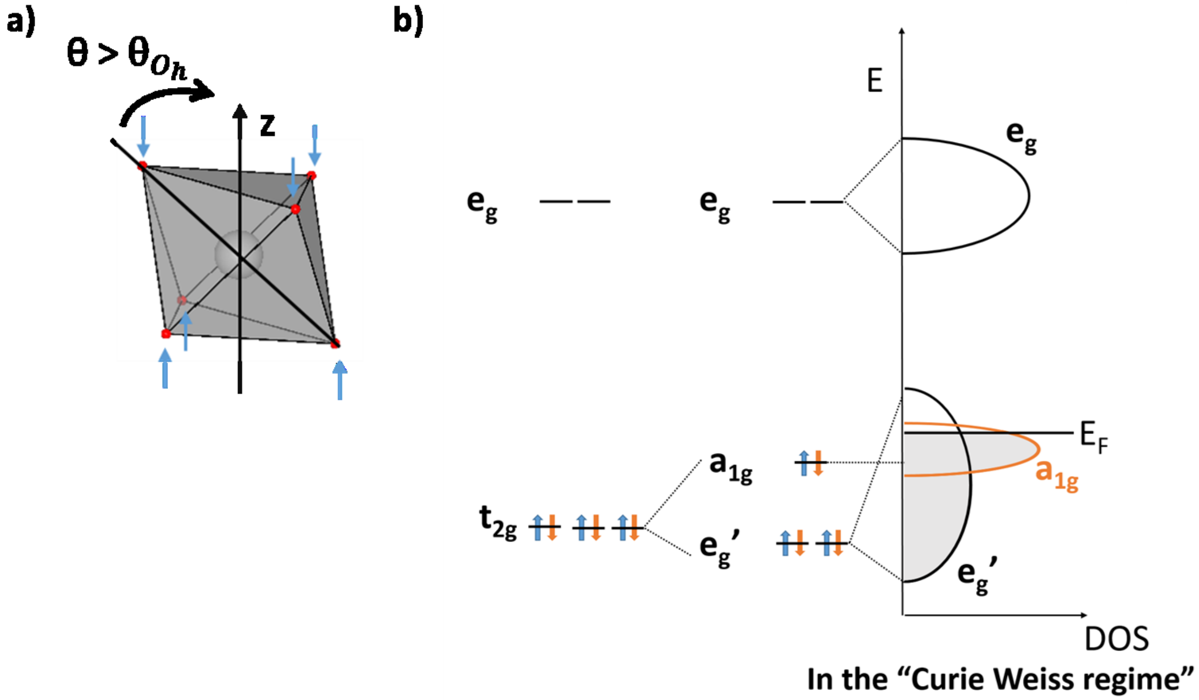

***Figure RE-2**: (a) Représentation de l'octaèdre CoO_6. Les flèches bleues indiquent la direction de la distorsion D_{3d} impliquant la compression des octaèdres suivant z. (b) Représentation de la levée de dégénérescence des orbitales t_{2g} en 2 orbitales e_g' et 1 orbitale a_{1g}. Représentation schématique du diagramme de bandes de P2-Na_xCoO_2 après distorsion D_{3d}.*

Lors de cette thèse, différentes phases P2-Na_xCoO_2 ont été synthétisées et analysées par DRX *ex-situ* et MAS RMN du ^{23}Na afin de comprendre les mécanismes impliqués lors de la charge et de la décharge d'une batterie Na-ion. Cette thèse fait suite aux travaux de thèse de Romain Berthelot qui a étudié le diagramme de phase du système P2-Na_xCoO_2 pour $x > 0.5$ par DRX *in-situ* mettant en évidence la présence de nombreux domaines selon la quantité d'ions Na^+ intercalés au sein du matériau[43,47].

2. Synthèse et caractérisation de P2-$Na_{\sim 0.7}$CoO2

2.1 Voie de synthèse

Cette phase est obtenue par voie solide en utilisant deux précurseurs Na_2CO_3 (Sigma-Aldrich, 99.9 %, séché à 200°C) et Co_3O_4 (synthétisé au laboratoire à partir de nitrates de cobalt décomposés à 400°C). Les deux précurseurs sont mélangés et broyés dans un mortier en agate au sein d'une boîte à gants remplie d'argon. A noter qu'un excès de 5 % massique en Na a été ajouté au rapport initial Na :Co = 0.7 en raison de l'évaporation du Na à haute température. Le mélange est placé dans une nacelle en or puis dans un four tubulaire. Le traitement thermique est réalisé sous flux d'O_2 à 900°C pendant 12h. La rampe de montée en température est de 2°C/min alors qu'une trempe est réalisée à la fin du traitement thermique.

Le rapport Na :Co a été mesuré par ICP-OES et confirme la synthèse de $Na_{0.70(8)}CoO_2$ comme matériau initial.

La **Figure RE-3** représente le diffractogramme obtenu après analyse DRX de la phase initiale. Cette acquisition a été réalisée au Synchrotron d'ALBA sur la ligne MSD04 en collaboration avec F. Fauth. Les affinements (trait noir) ont été obtenus par la méthode de Le Bail. Les pics les plus intenses sont indexés dans le groupe d'espace $P6_3/mmc$, caractéristique des empilements P2. Les paramètres de maille a_{hex} = 2.8363(2) Å et c_{hex} = 10.876(1) Å et sont en accord avec les valeurs obtenues dans la littérature[127]. Cependant, des pics de faible intensité dans la zone 15° - 23° ne peuvent pas être indexés dans ce groupe d'espace. Ils correspondent à des pics de surstructure dus à un ordre Na^+/lacunes dans les espaces interfeuillets pour la composition synthétisée.

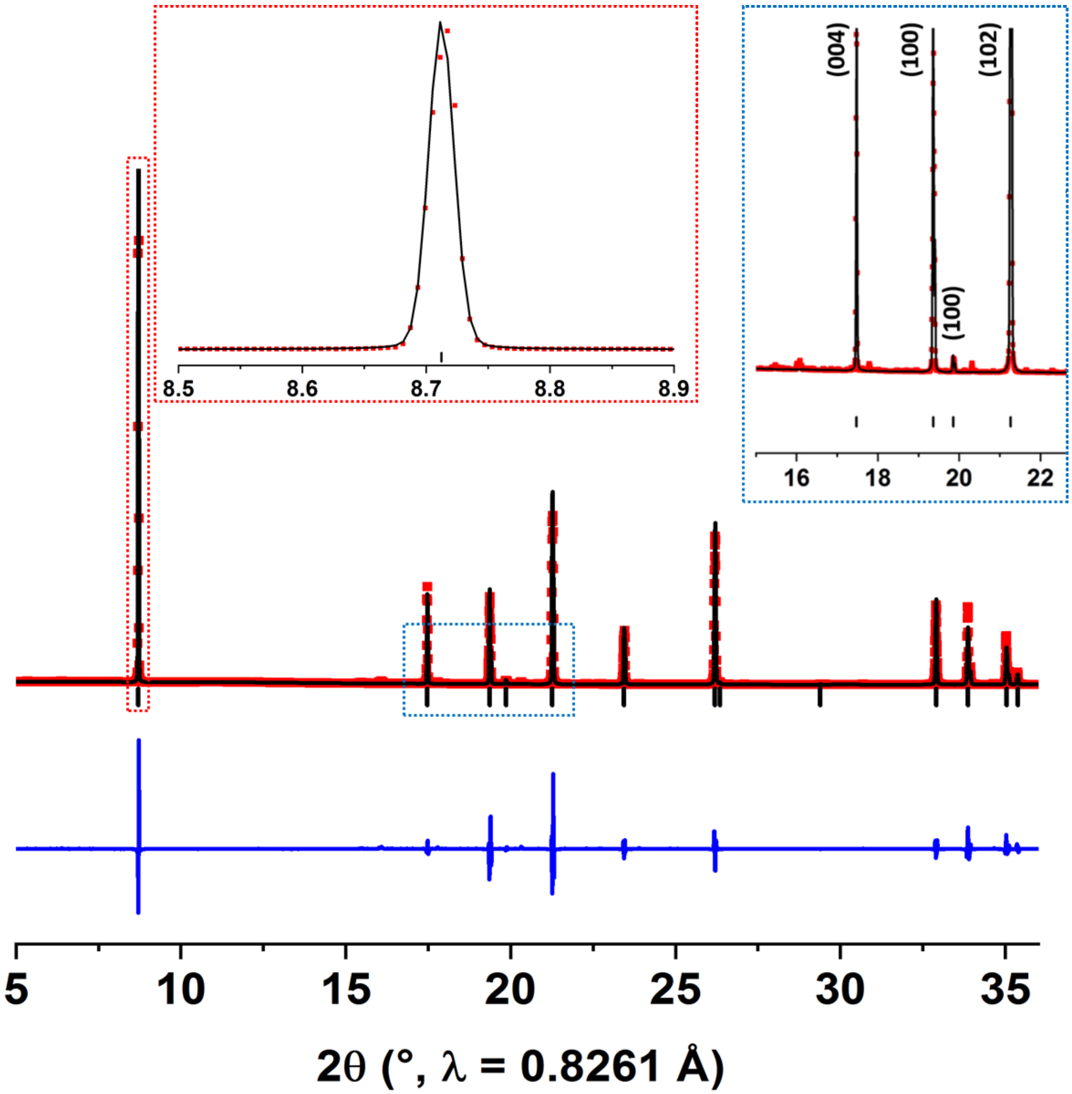

Figure RE-3: *Diffractogramme RX enregistré sur P2-$Na_{0.7}CoO_2$. Points rouges : données expérimentales, trait noir : données affinées, trait bleu : différence entre le profil expérimental et affinée, traits noirs : positions de Bragg. Les zooms ont été réalisés sur la raie (002) et entre 15° et 23° afin de mettre en évidence les pics de surstructure.*

2.2 Electrochimie

Des mesures en cyclage ont été réalisées en batterie Na(s) / $NaPF_6$ dans 1 M de Propylène Carbonate (PC) + 2% FluoroEthyl Carbonate (FEC) / P2-Na_xCoO_2 à un régime de C/20. Deux fenêtres de potentiel ont alors été étudiées : 1.5 – 4.3 V et 1.5 – 4.6 V vs Na^+/Na (**Figures RE-4**).

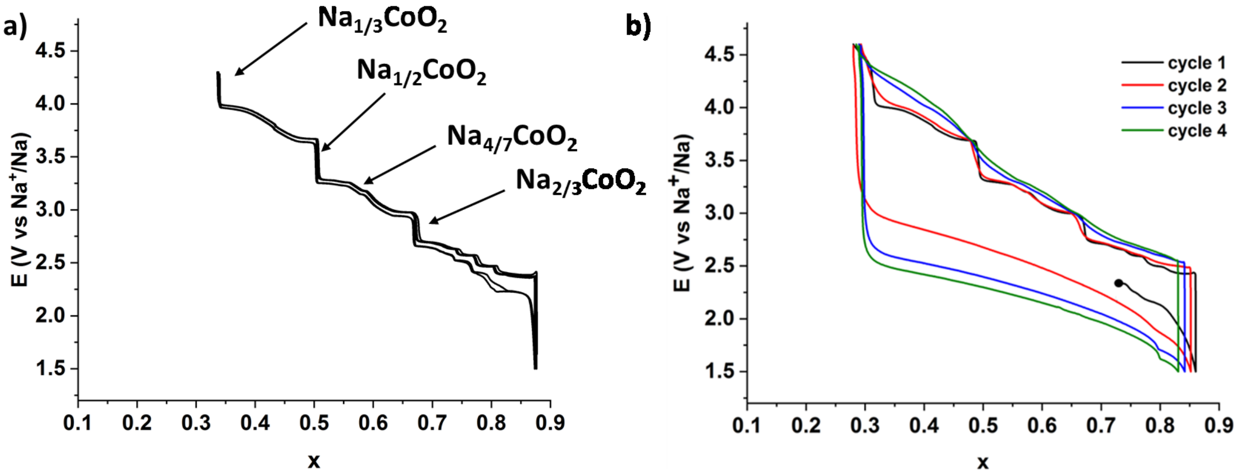

Figure RE-4: *Courbe de cyclage galvanostatique à C/20 entre (a) 1.5 et 4.3 V (b) 1.5 V et 4.6 V*

Le cyclage entre 1.5 V et 4.3 V montre que le système polarise très peu avec une bonne rétention de la capacité (97 % sur 40 cycles). Il faut noter que pour obtenir cette courbe, un autre matériau initial, que celui étudié par ICP, a été utilisé et que ce dernier a une composition en Na^+ proche de 0.75. De plus, la courbe électrochimique souligne la présence de nombreux domaines caractérisée par de nombreux changements de pente observable en charge et en décharge. Les sauts de potentiels visibles lors de la charge de la batterie traduisent la présence de composés définis pour des compositions spécifiques en Na^+ mises en évidence sur la **Figure RE-4a**.

Dans la gamme de potentiel 1.5 – 4.6 V, la courbe électrochimique souligne un comportement différent que celui observé dans la gamme 1.5 – 4.3 V. En effet, la (des)intercalation des ions Na^+ n'est plus réversible dans la gamme 1.5 – 4.6 V et une forte chute de la capacité est observable dès que le second cycle avec une faible rétention de la capacité (78 % après 40 cycles). De plus, les courbe de décharge sont lissées après charge à 4.6 V. En effet, les chutes de potentiel ou encore plateaux ne sont plus visibles alors qu'ils l'étaient lorsque le système était chargé jusque 4.3 V. Cependant, ce comportement n'est pour le moment pas totalement clair et pourrait être dû à une différence de cinétique pendant la décharge par rapport à la charge.

2.3 Synthèse par voie électrochimique de différentes phases

Afin d'étudier les mécanismes impliqués pendant la désintercalation des ions Na^+ par DRX et RMN du ^{23}Na ex-situ mais aussi de comprendre les phénomènes se produisant entre 4.3 et 4.6 V, différentes phases P2-Na_xCoO_2 ont été synthétisées par une technique électrochimique pour différents potentiels entre 1.5 et 4.6 V.

Ces synthèses ont été réalisées dans des cellules électrochimiques étanches et assemblées en boîte à gants. Le matériau d'électrode positif est un mélange de 90 % massique de matériau actif et 10 % massique de noir de carbone. A noter que nous ne pouvions pas utiliser de liants (PTFE) pour ces synthèses car il aurait alors été impossible de remplir un capillaire pour les acquisitions DRX. C'est pour cette raison que nous avons pastillé le mélange utilisé comme matériau d'électrode positive afin d'obtenir une électrode dense. Une fois la cellule assemblée, la synthèse par voie électrochimique se fait en deux étapes : une étape galvanostatique à C/20 jusqu'au potentiel cible puis une étape potentiostatique où le potentiel cible est maintenu alors que l'intensité diminue jusqu'à une valeur faible voire nulle. Une fois la batterie relaxée, elle peut être débranchée puis entrée en boîte à gants. Les potentiels cibles sont représentés sur la **Figure RE-5a**. La **Figure RE-5b** montre l'évolution du courant et du potentiel en fonction du temps dans le cas de la synthèse de $Na_{0.33}CoO_2$ pour à un potentiel cible de 4.2 V.

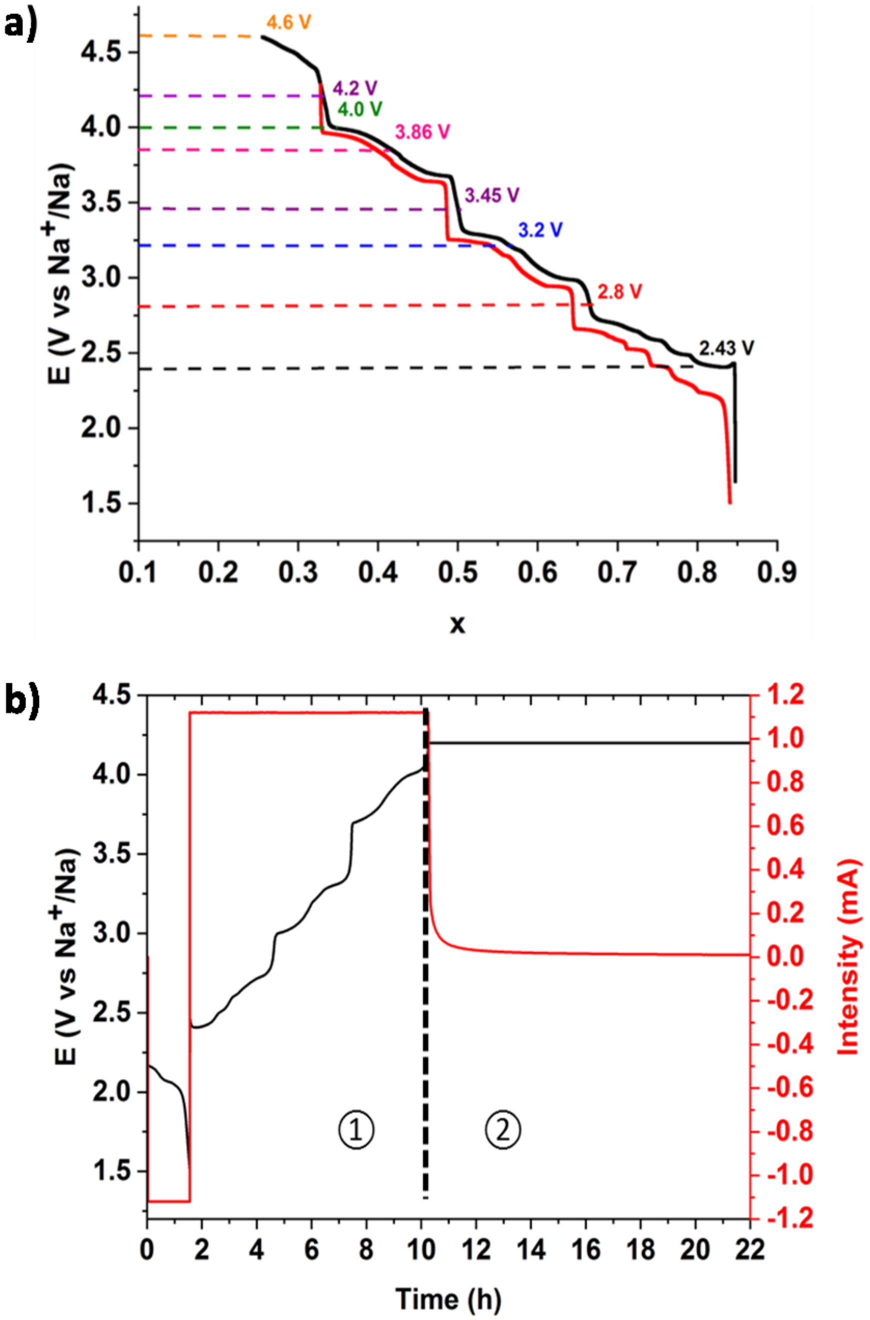

Figure RE-5: *(a) Charge entre 1.5 et 4.6 V (trait noir) et décharge entre 4.3 et 1.5 V (trait rouge) à C/20. Les traits en pointillés indiquent les potentiels cible pour les synthèses par voie électrochimique des phases* Na_xCoO_2*. (b) Evolution du potentiel (en noir) et du courant (en rouge) afin de réaliser la synthèse de* $Na_{0.33}CoO_2$ *par voie électrochimique.*

Le potentiel de la batterie est à nouveau mesuré afin de s’assurer que le système n’a pas évolué le temps de l’entrée en boîte à gants. La poudre synthétisée est enfin placé dans un capillaire en verre de 0.3 mm de diamètre pour analyse DRX et dans un rotor de 2.5 mm de diamètre pour analyse RMN du ^{23}Na à l’angle magique.

3. Caractérisation des phases synthétisées par électrochimie

3.1 Caractérisation de l’évolution de la structure moyenne

La **Figure RE-6** représente les diffractogrammes RX enregistrés sur les phases obtenues par voie électrochimique. Nous pouvons constater que la structure P2 est maintenue pour des valeurs de x supérieures ou égales à 1/3. En effet, les pics caractéristiques de cette structure sont observables sur les différents diffractogrammes. De plus, les affinements des diffractogrammes par la méthode de Rietveld[59], dans le groupe d’espace $P6_3/mmc$, ont permis de calculer l’évolution des paramètres et des épaisseurs des différents feuillets en fonction du taux d’ions Na^+ dans les différentes phases (**Figure RE-7**).

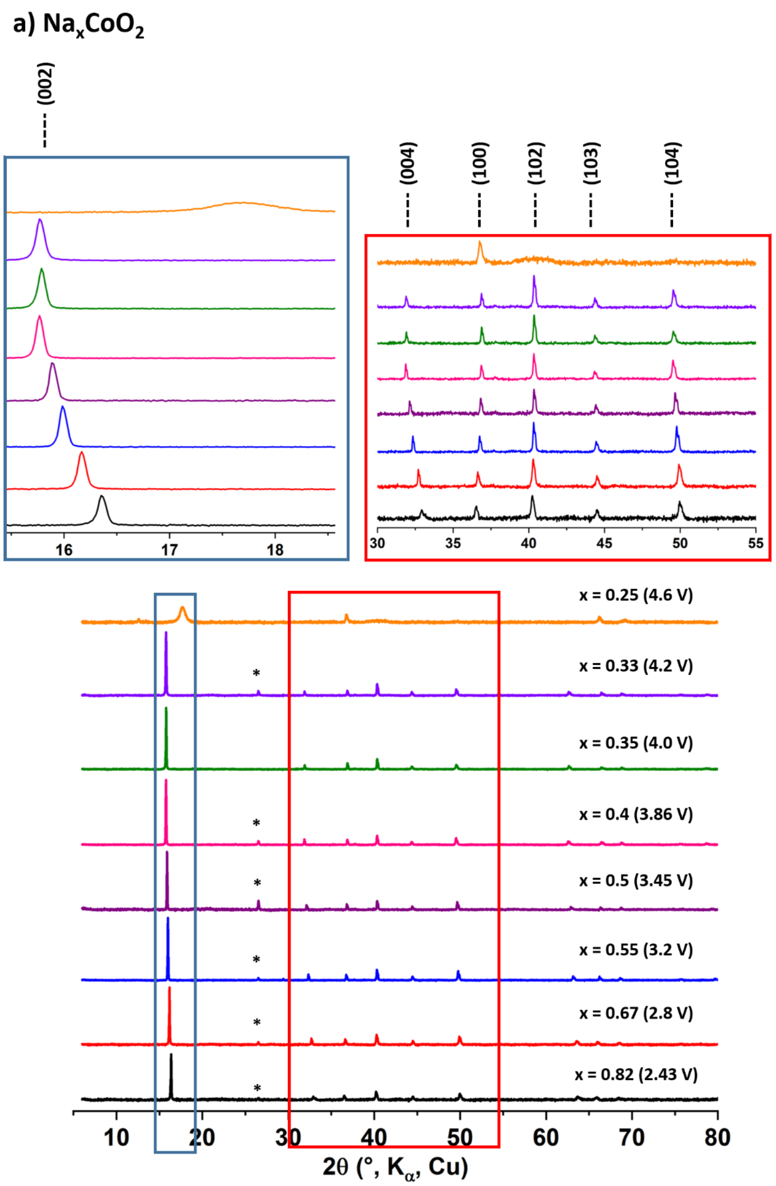

Figure RE-6: *Diffractogrammes enregistrés sur les phases synthétisée par voie électrochimique. Cadre bleu : zoom sur la raie (002). Cadre rouge : zoom sur la zone 30° - 55°. * représente le pic dû au graphite présent dans la formulation du matériau d'électrode positif.*

Il a été calculé que le paramètre de maille c_{hex} augmente lorsque x diminue ce qui est en accord avec l'augmentation des répulsions O-O entre les feuillets lors de la désintercalation des ions Na^+. A noter que le paramètre de maille a_{hex} diminue faiblement lorsque x diminue car l'ion Co^{3+} (0 .545 Å de rayon) est légèrement plus grand que l'ion Co^{4+} (0.53 Å de rayon)[3]. Les deux paramètres de maille atteignent une valeur limite pour x = 0.4 en charge.

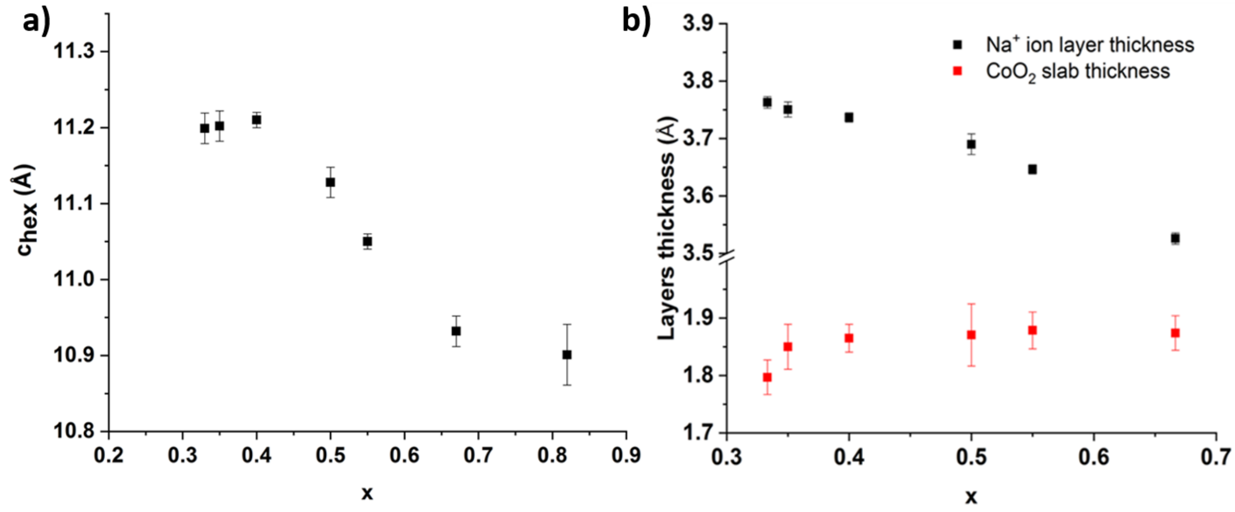

Figure RE-7: *(a) Evolution du paramètre de maille c_{hex} en fonction de x. Ces valeurs sont obtenues par affinement de type Le Bail. (b) Evolution des épaisseurs de feuillets en fonction de x. Ces valeurs ont été déterminées par affinement de type Rietveld.*

Concernant l'évolution des épaisseurs de feuillets, nous pouvons déterminer à l'aide des affinements Rietveld que l'épaisseur du feuillet CoO_2 diminue légèrement lorsque x diminue ce qui est cohérent avec l'oxydation des ions Co^{3+} en ions Co^{4+} augmentant la covalence des liaisons Co-O. L'épaisseur de l'interfeuillet augmente lors de la charge de la batterie en raison de l'augmentation des répulsions O-O interfeuillets. Ceci souligne l'écrasement progressif des octaèdres CoO_6, à l'origine de la distorsion D_{3d} lorsque x diminue et par conséquent, la présence d'électrons localisés et délocalisés dans la structure électronique de P2-Na_xCoO_2. La désintercalation des ions Na^+ lors de la charge de la batterie implique alors deux phénomènes : l'augmentation du niveau de la bande a_{1g} (due à l'aplatissement des octaèdres) et la diminution du niveau de Fermi (due à l'oxydation des ions Co^{3+} en Co^{4+}). Ces deux phénomènes sont en accord avec une transition magnétique mis en évidence par Foo *et al.*[108] pour x = 0.5. Pour x > 0.5, il a été montré que les phases sont dans un régime de type « Curie-Weiss métallique », régime dans lequel les électrons localisés et délocalisés occupent, respectivement, les bandes a_{1g} et e_g'. Pour x < 0.5, les phases sont dans un régime de type Pauli ou métallique où plus aucun électron localisé n'est présent dans la structure électronique impliquant uniquement la présence d'électrons délocalisés. Les structures de bande dans les deux régimes des P2-Na_xCoO_2 sont représentés de façon schématique sur la **Figure RE-8** dans les deux régimes magnétiques mis en évidence par Foo *et al.*[108].

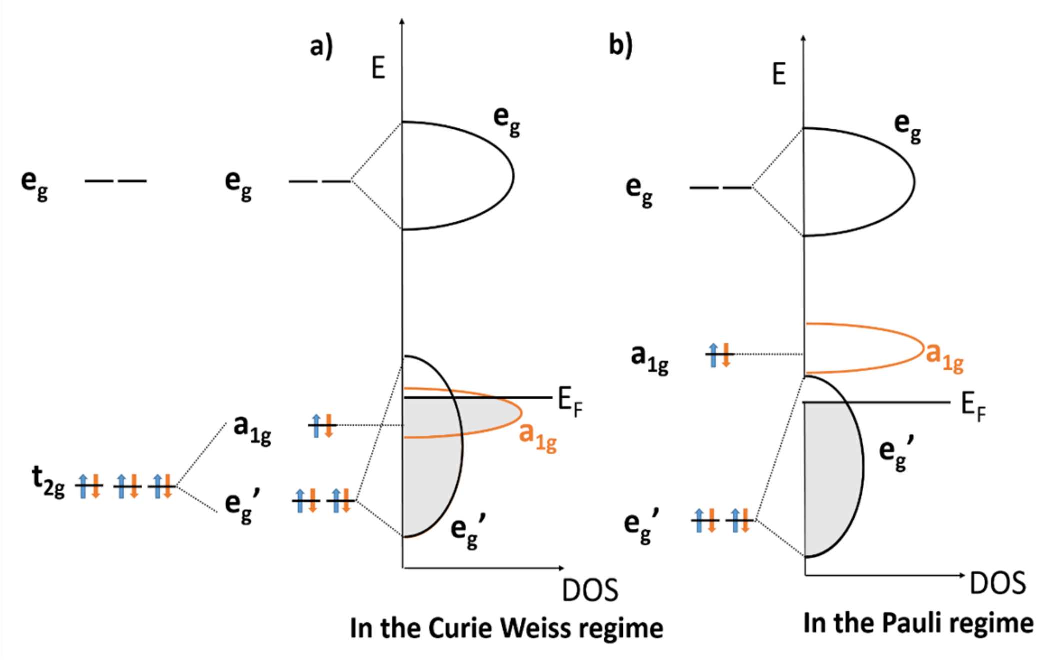

Figure RE-8: Représentation de la structure de bande des phases Na_xCoO_2 (a) dans un régime de type « Curie-Weiss métallique » pour $x > 0.5$ (b) dans un régime métallique pour $x < 0.5$.

Enfin, le diffractogramme enregistré sur la phase synthétisée à 4.6 V vs Na^+/Na souligne que la structure du matériau $Na_{0.25}CoO_2$ est désordonnée et n'est plus de P2 puisque le diffractogramme ne peut pas être affiné dans le groupe d'espace *P6₃/mmc*. En effet, des pics caractéristiques de cette structure ne sont plus visibles sur le diffractogramme alors que d'autres sont élargis et asymétriques. Par exemple la raie (002) est élargie et décalée vers les plus grands angles en accord avec la présence de glissement de feuillets. Ce phénomène peut s'expliquer par la présence des répulsions O-O devenues trop importantes pour stabiliser uniquement des feuillets de type P[128,130]. Certains feuillets glissent alors afin de stabiliser la les ions oxygènes menant à la présence de feuillets de type O (octaédrique) (**Figure RE-9**). Cependant, l'allure du diffractogramme suggère que l'alternance entre les feuillets de type O et P n'est pas régulière et semble aléatoire. C'est pour cela que par la suite de ce résumé, cette phase est nommée « OP ». A noter que ces glissements de feuillets ont déjà été mise en évidence sur d'autres systèmes par d'autres groupes de recherche sur des matériaux différents[128,140].

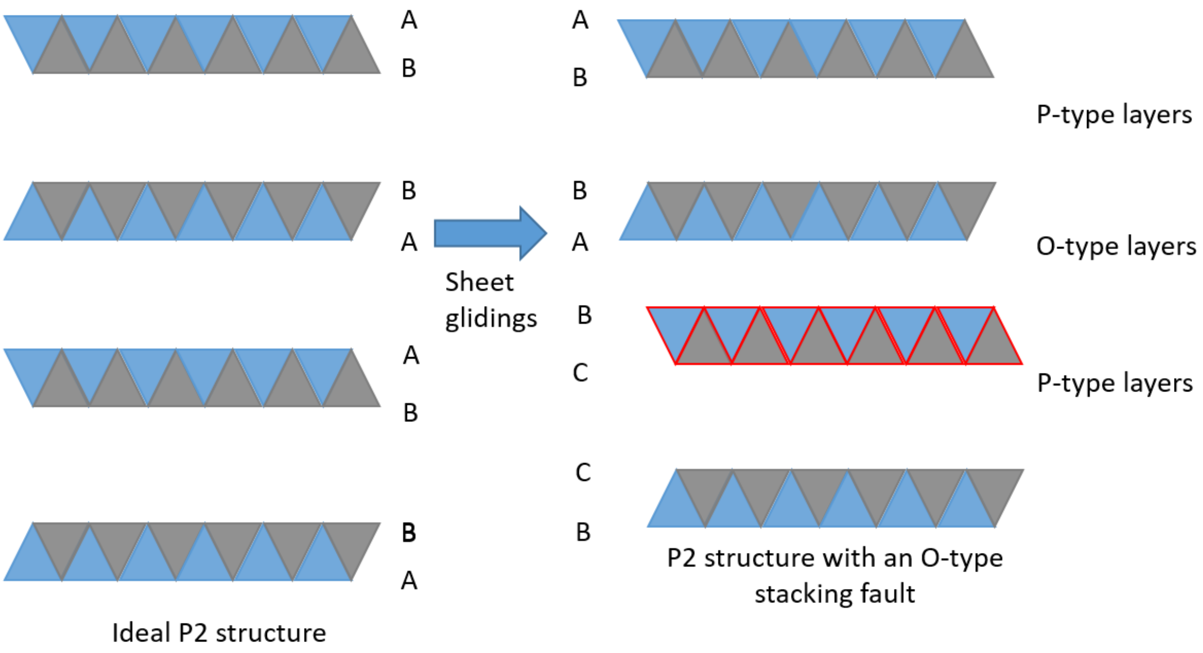

***Figure RE-9**: Représentation de la modification structurale due aux glissement de feuillets*

3.2 Caractérisation de la structure locale et électronique par RMN

La **Figure RE-10** représente l'évolution des spectres RMN du ^{23}Na enregistrés sous un champ magnétique de 7.05 T, à une vitesse de rotation de 30 kHz et une séquence d'impulsion simple. Le temps de relaxation est de 0.5 s. Nous allons discuter dans un premier temps l'évolution de la forme de raie des signaux puis de l'évolution du déplacement chimique en fonction du taux d'ions Na^+ dans la structure. A noter que les échantillons analysés sont, pour chaque phase, les mêmes que ceux analysés en DRX. Le spectre enregistré pour x = 0.7 correspond au spectre enregistré sur la phase initiale. Le spectre enregistré sur la phase « OP » sera discuté à part.

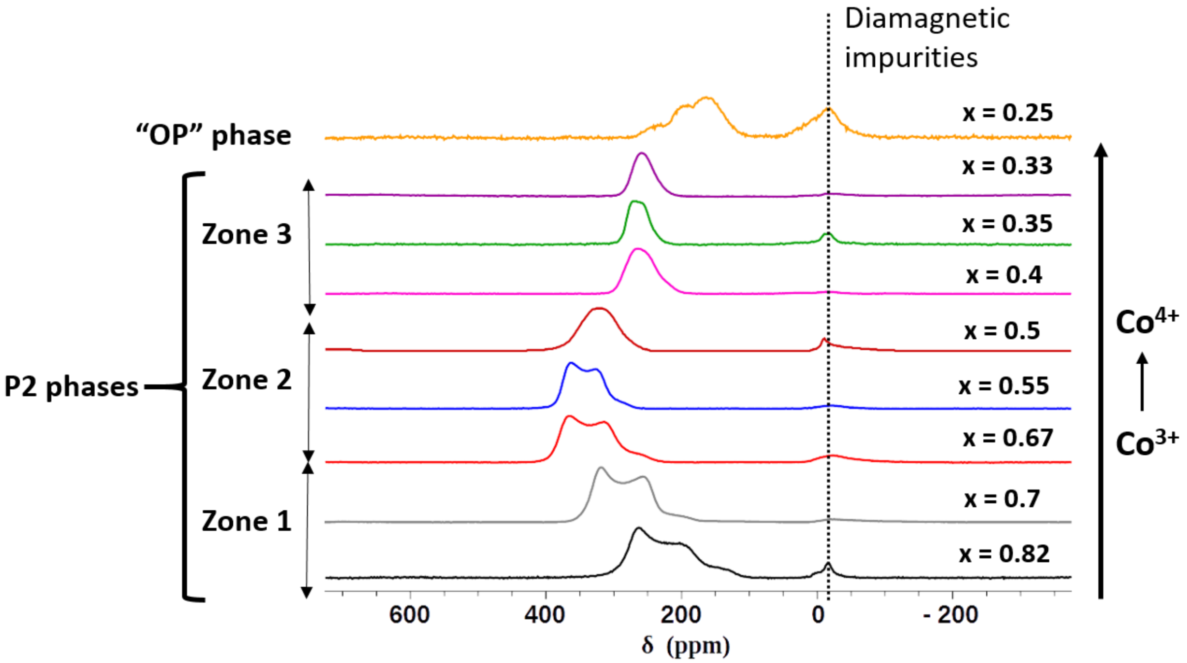

Figure RE-10: *Evolution des spectres RMN enregistrés sur les phases synthétisées par voie électrochimique.*

- ***Evolution de la forme de raie***

La forme de raie des signaux enregistrés sur les phases ayant des valeurs de x entre 0.55 et 0.82 est due aux interactions du second ordre quadripolaire qui ne sont pas entièrement supprimées par la rotation à l'angle magique. Il est important de noter que ce signal correspond à un seul environnement pour les ions Na^+ malgré la présence des deux sites d'intercalation Na_e et Na_f. En effet, la position du signal observé correspond à la position moyenne[39] des signaux pour les deux sites en raison de la mobilité des ions Na^+ dans les espaces interfeuillets[94].

Pour des valeurs de x < 0.55, la forme de raie des signaux RMN est différente et a une forme de type gaussienne-lorentzienne. Ce changement peut s'expliquer grâce à différents points tels que l'augmentation de la mobilité des ions Na^+ lorsque x diminue, l'évolution des occupations des sites Na_e et Na_f, le changement de diffusion, le degré d'oxydation des ions Co ou encore l'évolution des épaisseurs des feuillets lors de la charge et de la décharge de la batterie.

Evolution du déplacement chimique

Comme indiqué précédemment, la valeur du déplacement chimique est gouvernée par les interactions de contact de Fermi et le déplacement de Knight. Par soucis de clarté, l'évolution des spectres en fonction de x a été séparée en trois zones :

- Dans la zone 1 ($0.67 < x < 0.82$), les déplacements chimiques augmentent fortement lorsque x diminue. Les phases sont dans un régime de type « Curie-Weiss métallique ».
- Dans la zone 2, les déplacements chimiques diminuent lorsque x diminue. En raison du changement de régime magnétique pour $x = 0.5$, nous avons décidé limiter la zone 2 entre $x = 0.5$ et $x = 0.67$. Les phases sont dans un régime de type « Curie-Weiss métallique ».
- Dans la zone 3 ($x < 0.5$), les déplacements chimiques sont presque constants. Les phases sont métalliques dans ce domaine.

Ces zones sont représentées sur la **Figure RE-10**. Différents points sont discutés afin de comprendre l'évolution du déplacement chimique dans chaque zone alors que, en première approximation, nous aurions pu imaginer que les déplacements chimiques soient croissants en raison de l'oxydation de l'ion Co^{3+} diamagnétique ($t_{2g}^{6}\ e_{g}^{0}$) en ions Co^{4+} paramagnétique ($t_{2g}^{5}\ e_{g}^{0}$) lorsque x diminue. Les points du vue électronique et géométrique sont alors étudiés et discutés en comparant, respectivement, l'évolution du nombre d'ions Co^{4+} formels et la distance Na-O en fonction de x (**Figure RE-11**). Pour rappel, pour $x > 0.5$ (zones 1 et 2), le régime métallique des phases est de type « Curie-Weiss métallique » avec la contribution des électrons localisés (via le contact de Fermi) et des électrons délocalisés (via le déplacement de Knight) :

$$\delta_{tot} = \delta_{Fermi,a_{1g}}^{Co^{4+}} + \delta_{Knight,e_{g}'}^{Co^{n+}}$$

- Dans la zone 1, l'augmentation des déplacements chimiques lorsque x diminue est en accord avec l'augmentation du nombre d'électrons célibataires sur les ions cobalt en raison de l'oxydation $Co^{3+} \rightarrow Co^{4+}$. Cela augmente alors la quantité de spin transféré de l'ion Co^{4+} vers le noyau de sodium. On peut alors suggérer que la majorité des électrons participant au déplacement chimique sont de type localisés dans la zone 1. Du point de vue géométrique, la distance Na-O augmente entre x = 0.7 et x = 0.67, réduisant alors le recouvrement entre les orbitales Na 3s et O 2p et par conséquent limitant la quantité de spin transféré. Il est donc possible de conclure que, dans cette zone, le facteur électronique est prédominant par rapport au géométrique.

- Dans la zone 2, les déplacements chimiques diminuent lors de la charge de la batterie. Ceci n'est pas cohérent avec l'oxydation du Co^{3+} en Co^{4+} et donc le point de vue électronique ne peut pas prédominer dans cette zone. La distance Na-O, quant à elle, augmente largement entre x = 0.67 et x = 0.5 suggérant une diminution de la quantité de spin transféré et donc de la contribution du contact de Fermi. La modification de la géométrie locale est dans cette zone prédominante.

- Dans la zone 3, les phases sont dans un régime magnétique métallique avec uniquement la participation des électrons délocalisés au déplacement chimique total :

$$\delta_{tot} = \delta_{Knight,e_g'}^{Co^{n+}}$$

Le changement de régime peut expliquer la forte diminution de la valeur du déplacement chimique entre x = 0.5 et x = 0.4 puisqu'il n'y a plus de contribution de type contact de Fermi. Dans cette zone, les déplacements chimiques évoluent peu quel que soit la valeur de x. Nous pouvons alors conclure des résultats obtenus par RMN que la participation de l'orbital Na 3s au déplacement de Knight est presque constante pendant la désintercalation des ions Na^+.

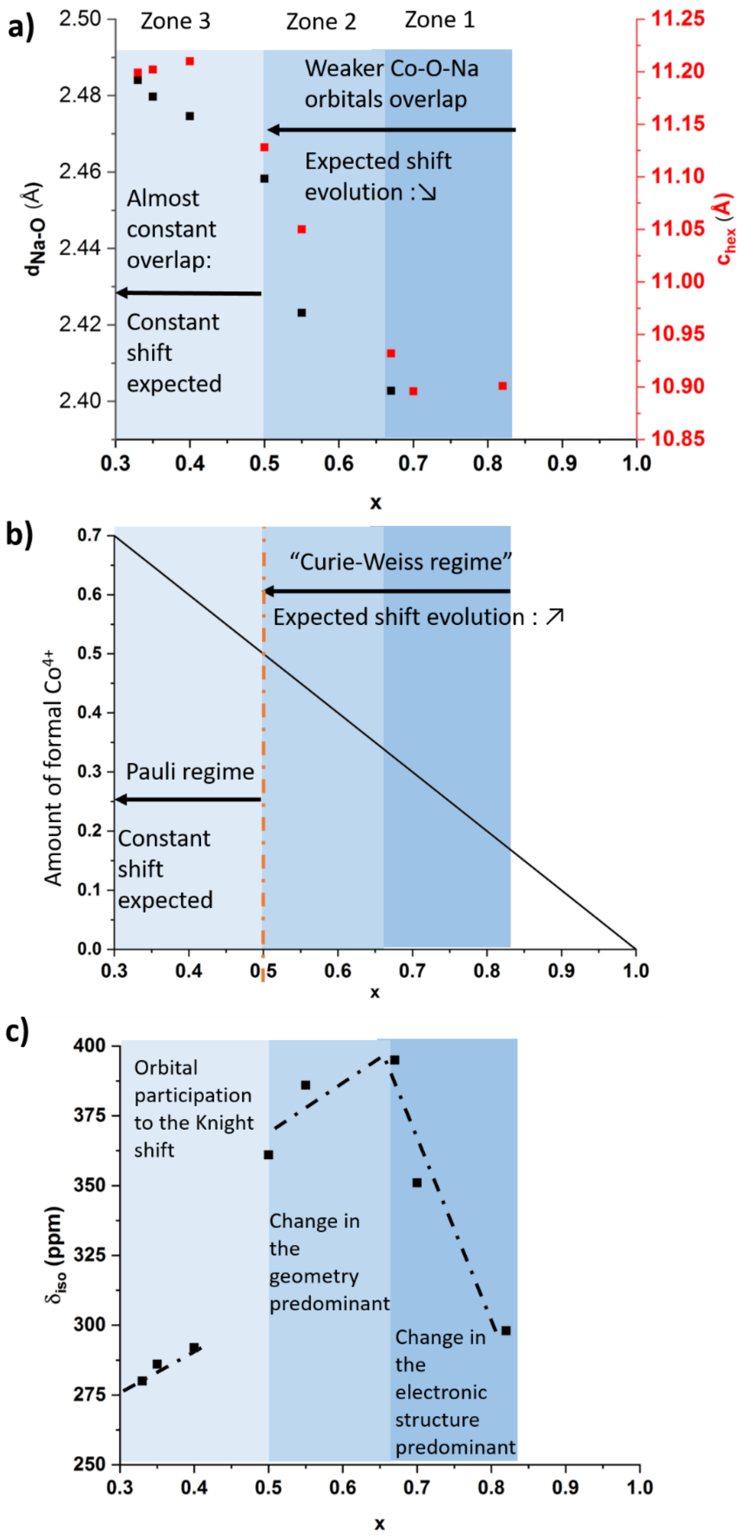

Figure RE-11: *Pour le système* Na_xCoO_2 *(a) Evolution de* c_{hex} *et de la distance Na-O en fonction de x. (b) Evolution du nombre formel d'ion* Co^{4+} *paramagnétique en fonction de x. (c) Evolution du déplacement chimique en fonction de x. La nuance de couleur délimite les zones 1, 2 et 3. La ligne en pointillés orange correspond à la transition entre les deux régimes magnétiques.*

- ***La phase « OP »***

Le spectre RMN enregistré sur la phase « OP » montre un signal largement élargi par rapport aux signaux obtenus sur les phases synthétisées à plus bas potentiel et de structure P2. L'élargissement de ce signal est en accord avec le spectre enregistré à haut potentiel sur le système Na_xMnO_2 et reporté dans la littérature[140]. L'élargissement du signal est la conséquence des glissements de feuillets impliquant la présence de fautes d'empilement et, par conséquent, d'une multitude d'environnements différents pour les ions Na^+. De plus l'élargissement peut aussi s'expliquer par la diminution de la mobilité ionique au sein des feuillets et notamment des feuillets de type O symbolisée par la diminution du paramètre de maille c (**Figure RE- 11a**).

- ***Le système P2-$Na_xCo_{2/3}Mn_{1/3}O_2$***

Il est important de noter que le même protocole (synthèses par voie électrochimique, DRX et RMN ex-situ) a été réalisé sur un autre système, $Na_xCo_{2/3}Mn_{1/3}O_2$. Le paramètre de maille c_{hex} suit la même tendance que pour le système P2-Na_xCoO_2 alors que des glissements de feuillets se produisent également pour $x < 1/3$ (**Figure RE-12a**). Cependant, l'absence de diffractogramme de bonne qualité a empêché la réalisation d'affinements de type Rietveld et donc la détermination de l'évolution des épaisseurs de feuillets. Nous avons alors supposé qu'ils évoluaient de la même manière que pour Na_xCoO_2. L'évolution des positions de signaux en RMN (**Figure RE-12c**) a également suggéré un changement de régime magnétique pour une valeur de x comprise entre 0.4 et 0.45. Tout comme pour Na_xCoO_2, nous avons distingué 3 zones avec la même prédominance dans les zones 1 et 2, respectivement du point de vue électronique et géométrique. Dans la zone 3, la contribution du contact de Fermi due aux électrons localisés sur les ions Co^{4+} est à nouveau nulle, cependant, il est impossible parler d'un régime métallique car nous ne pouvons pas négliger la contribution des électrons localisés sur les ions Mn^{4+} paramagnétiques (t_{2g}^3 e_g^0). A noter que cette contribution est constante dans la zone 3 puisque le paramètre de maille c_{hex} (et on suppose que la distance Na-O aussi) est quasiment constante. Le signal enregistré sur la phase « OP » propose le même « élargissement » que celui observé sur la phase « OP » du système Na_xCoO_2 en raison, à nouveau, de la multiplicité des environnements pour les ions Na^+ et la diminution de la mobilité ionique après glissement de feuillets.

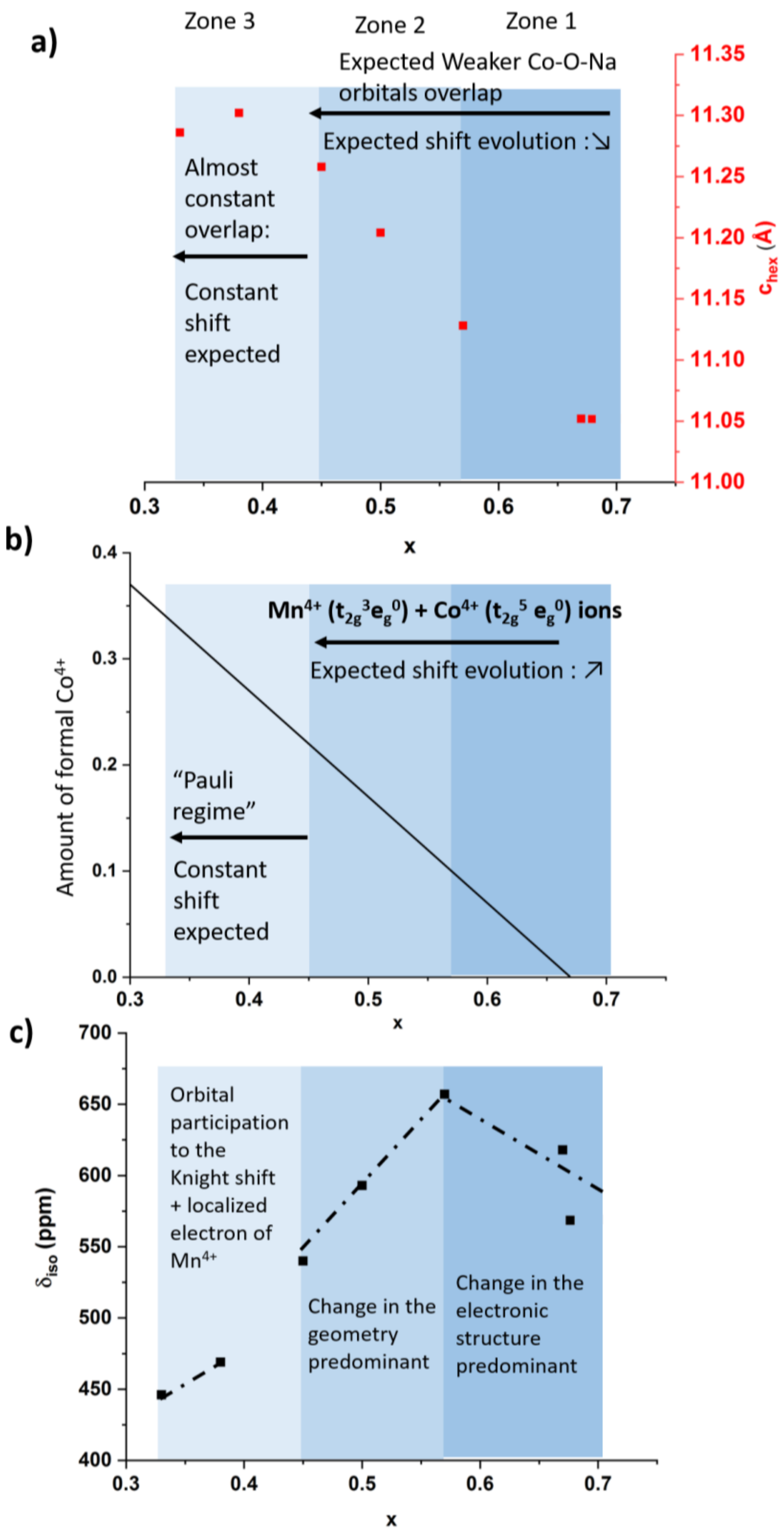

Figure RE-12: *Pour le système* $NaxCo_{2/3}Mn_{1/3}O_2$ *(a) Evolution de* c_{hex} *en fonction de x. (b) Evolution du nombre formel d'ion* Co^{4+} *paramagnétique en fonction de x. (c) Evolution du déplacement chimique en fonction de x. La nuance de couleur délimite les zones 1, 2 et 3. La ligne en pointillés orange correspond à la transition entre les deux régimes magnétiques.*

4. Conclusion générale

Ce travail de thèse a montré que la RMN du solide est une technique de caractérisation puissance et est complémentaire à la DRX. La RMN permet l'étude des structures électronique et locale des matériaux mais également d'étudier les modifications structurales lors de cyclage électrochimique. Les études des phases OP4-(Li,Na)CoO_2 et O4-$LiCoO_2$ (non présentés dans ce résumé étendu) ont également permis de montrer l'intérêt de la RMN pour l'étude de la mobilité ionique au sein des matériaux.

Concernant les systèmes Na_xCoO_2 et $Na_xCo_{2/3}Mn_{1/3}O_2$, la RMN et la DRX ont permis de mettre en évidence la formation d'une phase fautée à haut potentiel en raison de glissement de feuillets pour des matériaux ayant un faible taux de Na^+ dans les espaces interfeuillets. Les différentes phases ont été obtenues par voie électrochimique. Cette étude confirme également la véracité de cette technique pour l'étude de l'influence du taux de N^+ dans les matériaux. La RMN a mis en évidence un comportement complexe du système puisque le déplacement chimique évolue d'une manière inattendue, en effet, il croît d'abord, puis décroît fortement avant de devenir presque constant. Cette évolution dépend si le facteur géométrique (représenté par l'évolution des distances Na-O) ou électronique (représenté par le quantité d'ion Co^{4+} au sein du matériau) est prédominant dans le régime magnétique de type Curie-Weiss métallique. Dans le régime métallique, le déplacement chimique reste quasiment constant signifiant que la participation des orbitales 3s Na est constante.

Pour conclure la RMN nous a permis, de suivre l'évolution de différents paramètres pendant la charge des deux systèmes cités précédemment comme la mobilité ionique, l'asymétrie des sites, les contributions quadripolaires ou encore les déplacements chimiques. Concernant la structure locale des matériaux la RMN informe sur le nombre pour les ions Na^+ ou Li^+, les environnements locaux de ces derniers ou encore les distances et angles des liaisons M-O-A. Concernant la structure électronique, la RMN permet de renseigner sur les régimes magnétiques des phases étudiées et par conséquent sur la présence d'électrons localisés et/ou délocalisés. Enfin, l'étude de la mobilité ionique peut renseigner sur les constantes de vitesse k ou encore les énergies d'activation si les mesures sont réalisées à différentes températures.

References

1. Delmas, C., Fouassier, C., and Hagenmuller, P. “Structural classification and properties of the layered oxides,” *Physica B+ c*, V. 99, Nos. 1–4, 1980, pp. 81–85.
2. Duffiet, M., Blangero, M., Cabelguen, P.-E., et al. “Influence of the Initial Li/Co Ratio in $LiCoO_2$ on the High-Voltage Phase-Transitions Mechanisms,” *The journal of physical chemistry letters*, V. 9, No. 18, 2018, pp. 5334–5338.
3. Shannon, R. D. “Revised effective ionic radii and systematic studies of interatomic distances in halides and chalcogenides,” *Acta crystallographica section A: crystal physics, diffraction, theoretical and general crystallography*, V. 32, No. 5, 1976, pp. 751–767.
4. Bucher, N., Hartung, S., Franklin, J., et al. “P2−$Na_xCo_yMn_{1−y}O_2$ (y = 0, 0.1) as Cathode Materials in Sodium-Ion Batteries-Effects of Doping and Morphology To Enhance Cycling Stability,” *Chemistry of Materials*, V. 28, 2016.
5. Didier, C., Guignard, M., Denage, C., et al. “Electrochemical Na-Deintercalation from $NaVO_2$,” *Electrochemical and Solid-State Letters*, V. 14, No. 5, 2011, pp. A75–A78.
6. Reddy, B. V. R., Ravikumar, R., Nithya, C., et al. “High performance $Na_x CoO_2$ as a cathode material for rechargeable sodium batteries,” *Journal of Materials Chemistry A*, V. 3, No. 35, 2015, pp. 18059–18063.
7. Lei, Y., Li, X., Liu, L., et al. “Synthesis and Stoichiometry of Different Layered Sodium Cobalt Oxides,” *Chemistry of Materials*, V. 26, No. 18, 2014, pp. 5288–96.
8. Eshetu, G. G., Grugeon, S., Kim, H., et al. “Comprehensive Insights into the Reactivity of Electrolytes Based on Sodium Ions,” *ChemSusChem*, V. 9, No. 5, 2016, pp. 462–71.
9. Yabuuchi, N., Kubota, K., Dahbi, M., et al. “Research Development on Sodium-Ion Batteries,” *Chemical Reviews*, V. 114, No. 23, 2014, pp. 11636–82.
10. Terasaki, I., Sasago, Y., and Uchinokura, K. “Large thermoelectric power in $NaCo_2O_4$ single crystals,” *Physical Review B*, V. 56, No. 20, 1997, pp. 685–7.
11. Takada, K., Sakurai, H., Takayama-Muromachi, E., et al. “Superconductivity in two-diemnsional CoO_2 layers,” *Nature*, V. 422, No. 6927, 2003, pp. 53–4.
12. Chou, F. C., Cho, J. H., Lee, P. A., et al. “Thermodynamic and transport measurements of superconducting $Na_{0.3}CoO_2\cdot$ 1.3 H_2O single crystals prepared by electrochemical deintercalation,” *Physical Review Letters*, V. 92, No. 15, 2004.
13. Landron, S., and Lepetit, M.-B. “Ab initio evaluation of the local effective interactions in the superconducting compound $Na_{0.35}CoO_2\cdot 1.3\ H_2O$,” *Physical Review B*, V. 74, No. 18, 2006, p. 184507.
14. Lee, M., Viciu, L., Li, L., et al. “Large enhancement of the thermopower in Na_xCoO_2 at high Na doping,” *Nature Materials*, V. 5, No. 7, 2006, pp. 537–40.
15. Lee, M., Viciu, L., Li, L., et al. “Enhancement of the thermopower in Na_xCoO_2 in the large-x regime (x>0.75),” *Physica B: Condensed Matter*, V. 403, Nos. 5–9, 2008, pp. 1564–8.
16. Huang, Q., Foo, M. L., Lynn, J. W., et al. “Low temperature phase transitions and crystal structure of $Na_{0.5}CoO_2$,” *Journal of physics: Condensed matter*, V. 16, No. 32, 2004, p. 5803.
17. Delmas, C., Fouassier, C., and Hagenmuller, P. “Les bronzes de cobalt K_xCoO_2 (x< 1). L’oxyde $KCoO_2$,” *Journal of Solid State Chemistry*, V. 13, No. 3, 1975, pp. 165–171.
18. Fu, G.-C., Dong, C., Li, M.-X., et al. “Structural, Transport and Magnetic Properties of K_xCoO_2 (x = 0.36),” *Chinese Physics Letters*, V. 22, No. 1478, 2005.
19. Hironaka, Y., Kubota, K., and Komaba, S. “P2-and P3-K_xCoO_2 as an electrochemical potassium intercalation host,” *Chemical Communications*, V. 53, No. 26, 2017, pp. 3693–3696.

20. Wang, X., Xu, X., Niu, C., et al. "Earth Abundant Fe/Mn-Based Layered Oxide Interconnected Nanowires for Advanced K-Ion Full Batteries," *NanoLetters*, V. 17, 2017, pp. 544–50.
21. Vaalma, C., Giffin, G. A., Buchholz, D., et al. "Non-aqueous K-ion battery based on layered $K_{0.3}MnO_2$ and hard carbon/carbon black," *Journal of The Electrochemical Society*, V. 163, No. 7, 2016, pp. A1295–A1299.
22. Liu, C., Luo, S., Huang, H., et al. "Layered potassium-deficient P2-and P3-type cathode materials K_xMnO_2 for K-ion batteries," *Chemical Engineering Journal*, V. 356, 2019, pp. 53–59.
23. Liu, C., Luo, S., Huang, H., et al. "Low-Cost Layered $K_{0.45}Mn_{0.9}Mg_{0.1}O_2$ as a High-Performance Cathode Material for K-Ion Batteries," *ChemElectroChem*, V. 6, No. 8, 2019, pp. 2308–2315.
24. Hwang, J.-Y., Kim, J., Yu, T.-Y., et al. "Development of P3-$K_{0.69}CrO_2$ as an ultra-high-performance cathode material for K-ion batteries," *Energy & Environmental Science*, V. 11, No. 10, 2018, pp. 2821–2827.
25. Hosaka, T., Shimamura, T., Kubota, K., et al. "Polyanionic Compounds for Potassium-Ion Batteries," *The Chemical Record*, V. 19, 2019, pp. 735–45.
26. Nguyen, L. H., Broux, T., Camacho, P. S., et al. "Stability in water and electrochemical properties of the $Na_3V_2(PO_4)_2F_3$–$Na_3(VO)_2(PO_4)_2F$ solid solution," *Energy Storage Materials*, 2019.
27. Castets, A., Carlier, D., Trad, K., et al. "Analysis of the ^7Li NMR signals in the Monoclinic $Li_3Fe_2(PO_4)_3$ and $Li_3V_2(PO_4)_3$ Phases," *The Journal of Physical Chemistry C*, V. 114, No. 44, 2010, pp. 19141–19150.
28. Boivin, E., David, R., Chotard, J.-N., et al. "$LiVPO_4F_{1-y}O_y$ Tavorite-Type Compositions: Influence of the Concentration of Vanadyl-Type Defects on the Structure and Electrochemical Performance," *Chemistry of Materials*, V. 30, No. 16, 2018, pp. 5682–5693.
29. Grey, C. P., and Dupré, N. "NMR Studies of Cathode Materials for Lithium-Ion Rechargeable Batteries," *Chemical Reviews*, V. 104, No. 10, 2004, pp. 4493–512.
30. Pecher, O., Carretero-González, J., Griffith, K. J., et al. "Materials' methods: NMR in battery research," *Chemistry of Materials*, V. 29, No. 1, 2016, pp. 213–242.
31. Dupré, N., Gaubicher, J., Le Mercier, T., et al. "Positive electrode materials for lithium batteries based on $VOPO_4$," *Solid State Ionics*, V. 140, Nos. 3–4, 2001, pp. 209–221.
32. Trease, N. M., Zhou, L., Chang, H. J., et al. "In situ NMR of lithium ion batteries: Bulk susceptibility effects and practical considerations," *Solid state nuclear magnetic resonance*, V. 42, 2012, pp. 62–70.
33. Kitada, K., Pecher, O., Magusin, P. C., et al. "Unraveling the Reaction Mechanisms of SiO Anodes for Li-Ion Batteries by Combining in Situ ^7Li and ex Situ $^7Li/^{29}Si$ Solid-State NMR Spectroscopy," *Journal of the American Chemical Society*, V. 141, No. 17, 2019, pp. 7014–7027.
34. Key, B., Bhattacharyya, R., Morcrette, M., et al. "Real-time NMR investigations of structural changes in silicon electrodes for lithium-ion batteries," *Journal of the American Chemical Society*, V. 131, No. 26, 2009, pp. 9239–9249.
35. Dupré, N., Cuisinier, M., and Guyomard, D. "Electrode/electrolyte interface studies in lithium batteries using NMR," *The Electrochemical Society Interface*, V. 20, No. 3, 2011, pp. 61–67.
36. Dupré, N., Martin, J.-F., Olivieri, J., et al. "Relationship between surface chemistry and electrochemical behavior of $LiNi_{1/2}Mn_{1/2}O_2$ positive electrode in a lithium-ion battery," *Journal of Power Sources*, V. 196, 2011, pp. 4791–800.
37. Marino, C., Darwiche, A., Dupre, N., et al. "Study of the Electrode/Electrolyte Interface on Cycling of a Conversion Type Electrode Material in Li Batteries.," *The Journal of Physical Chemistry C*, V. 117, No. 38, 2013, pp. 19302–19313.
38. Bouayad, H., Wang, Z., Dupre, N., et al. "Improvement of electrode/electrolyte interfaces in high-voltage spinel lithium-ion batteries by using glutaric anhydride as electrolyte additive," *The Journal of Physical Chemistry C*, V. 118, No. 9, 2014, pp. 4634–4648.

39. Clément, R. J., Xu, J., Middlemiss, D. S., et al. "Direct evidence for high Na mobility and high voltage structural processes in P2–$Na_x[Li_yNi_zMn_{1-y-z}]O_2$ (0< x, y, z< 1) cathodes from solid-state NMR and DFT calculations," V. 5, 2017, p. 4129.
40. Clément, R. J., Kitchaev, D., Lee, J., et al. "Short-range order and unusual modes of nickel redox in a fluorine-substituted disordered rocksalt oxide lithium-ion cathode," *Chemistry of Materials*, V. 30, No. 19, 2018, pp. 6945–6956.
41. Balsys, R. J., and Davis, R. L. "The structure of $Li_{0.43}Na_{0.36}CoO_{1.96}$ using neutron powder diffraction," *Solid State Ionics*, V. 69, No. 1, 1994, pp. 69–74.
42. Berthelot, R., Carlier, D., Pollet, M., et al. "Synthesis and Investigations on an O4-$LiCoO_2$ Polytype," *Electrochemical and Solid-State Letters*, V. 12, No. 11, 2009, pp. 207–10.
43. Berthelot, R. "Contribution à l'étude électrochimique du système P2-Na_xCoO_2. Synthèse et caractérisation de nouveaux oxydes lamellaires ordonnés (A/A')CoO_2 (A,A' = Li, Na, Ag)." Bordeaux, 2010.
44. Berthelot, R., Pollet, M., Carlier, D., et al. "Reinvestigation of the OP4-(Li/Na)CoO_2 -Layered System and First Evidence of the (Li/Na/Na)CoO_2 Phase with OPP9 Oxygen Stacking," *Inorganic Chemistry*, V. 50, No. 6, 2011, pp. 2420–30.
45. Carlier, D., Cheng, J. H., Berthelot, R., et al. "The P2-$Na_{2/3}Co_{2/3}Mn_{1/3}O_2$ phase: structure, physical properties and electrochemical behavior as positive electrode in sodium battery," *Dalton Transactions*, V. 40, No. 36, 2011, p. 9306.
46. Mortemard de Boisse, B., Liu, G., Ma, J., et al. "Intermediate honeycomb ordering to trigger oxygen redox chemistry in layered battery electrode," *Nature Communications*, 2016.
47. Berthelot, R., Carlier, D., and Delmas, C. "Electrochemical investigation of the P2–Na_xCoO_2 phase diagram," *Nature Materials*, V. 10, No. 1, 2011, pp. 74–80.
48. Mortemard de Boisse, B., Reynaud, M., Ma, J., et al. "Coulombic self-ordering upon charging a large capacity layered cathode material for rechargeable batteries," *Nature Communications*, 2019.
49. Goldsztaub, S. "Structure cristalline du ferrite de sodium," *Acad. Sci. Paris*, V. 196, 1933, p. 280.
50. Takeda, Y., Nakahara, K., Nishijima, M., et al. "Sodium deintercalation from sodium iron oxide," *Materials research bulletin*, V. 29, No. 6, 1994, pp. 659–666.
51. Tournadre, F., Croguennec, L., Saadoune, I., et al. "The $T^{\#}2$-$Li_{2/3}Co_{2/3}Mn_{1/3}O_2$ System. 1. Its Structural Characterization," *Chemistry of materials*, V. 16, No. 8, 2004, pp. 1411–1417.
52. Shin, Y. J., Doumerc, J. P., Pouchard, M., et al. "Preparation and magnetic properties of some new layer rocksalt-and mixed delafossite-type oxides," *Materials research bulletin*, V. 28, No. 2, 1993, pp. 159–165.
53. Siegel, R., Hirschinger, J., Carlier, D., et al. "^{59}Co, ^{23}Na NMR and electric field gradient calculations in the layered cobalt oxides $NaCoO_2$ and $HCoO_2$," *Solid State Nuclear Magnetic Resonance*, V. 23, No. 4, 2003, pp. 243–62.
54. Singh, D. J. "Electronic structure of $NaCo_2O_4$," *Physical Review B*, V. 61, No. 20, 2000, p. 13397.
55. Baskaran, G. "Electronic Model for CoO_2 Layer Based Systems: Chiral Resonating Valence Bond Metal and Superconductivity," *Physical Review Letters*, V. 91, No. 9, 2003.
56. Yang, H.-B., Pan, Z.-H., Sekharan, A. K. P., et al. "Fermi surface evolution and Luttinger theorem in Na_xCoO_2: a systematic photoemission study," *Physical review letters*, V. 95, No. 14, 2005, p. 146401.
57. Johannes, M. D., Mazin, I. I., Singh, D. J., et al. "Nesting, Spin Fluctuations, and Odd-Gap Superconductivity in $Na_xCoO_2 \cdot y\, H_2O$," *Physical review letters*, V. 93, No. 9, 2004, p. 97005.
58. Landron, S., Soret, J., and Lepetit, M.-B. "An *ab initio* evaluation of the local effective interactions in the Na_xCoO_2 family," *Journal of Physics: Condensed Matter*, V. 22, 2010, pp. 1–8.
59. Rietveld, H. "A profile refinement method for nuclear and magnetic structures," *Journal of applied Crystallography*, V. 2, No. 2, 1969, pp. 65–71.

60. Rodríguez-Carvajal, J. “Recent advances in magnetic structure determination by neutron powder diffraction,” *Physica B: Condensed Matter*, V. 192, Nos. 1–2, 1993, pp. 55–69.
61. Duer, M. J., ed. “Solid-state NMR spectroscopy: principles and applications,” Malden, MA, Blackwell Science, 2002, 567 pp.
62. Bertini, I., Luchinat, C., and Parigi, G. “Magnetic susceptibility in paramagnetic NMR,” *Progress in Nuclear Magnetic Resonance Spectroscopy*, V. 40, No. 3, 2002, p. 249.
63. Mustarelli, P., Massarotti, V., Bini, M., et al. “Transferred hyperfine interaction and structure in $LiMn_2O_4$ and Li_2MnO_3 coexisting phases: A XRD and ^{7}Li NMR-MAS study,” *Physical Review B*, V. 55, No. 18, 1997, p. 12018.
64. Lee, Y. J., Wang, F., and Grey, C. P. “^{6}Li and ^{7}Li MAS NMR Studies of Lithium Manganate Cathode Materials,” *Journal Of the Amercian Chemical Society*, V. 120, 1998, pp. 12601–13.
65. Massiot, D., Fayon, F., Capron, M., et al. “Modelling one-and two-dimensional solid-state NMR spectra,” *Magnetic resonance in chemistry*, V. 40, No. 1, 2002, pp. 70–76.
66. Ashbrook, S., E. “Recent advances in solid-state NMR spectroscopy of quadrupolar nuclei,” *Physical Chemistry Chemical Physics*, V. 11, 2009, pp. 6892–905.
67. Smiley, D. L., Davis, L. J., and Goward, G. R. “An Improved Understanding of Li^+ Hopping Pathways and Rates in $Li_3Fe_2(PO_4)_3$ Using Selective Inversion ^{6}Li NMR Spectroscopy,” *The Journal of Physical Chemistry C*, V. 117, No. 46, 2013, pp. 24181–24188.
68. Kresse, G., and Furthmüller, J. “Efficiency of ab-initio total energy calculations for metals and semiconductors using a plane-wave basis set,” *Computational materials science*, V. 6, No. 1, 1996, pp. 15–50.
69. Bamine, T., Boivin, E., Boucher, F., et al. “Understanding Local Defects in Li-Ion Battery Electrodes through Combined DFT/NMR Studies: Application to $LiVPO_4F$,” *The Journal of Physical Chemistry C*, V. 121, No. 6, 2017, pp. 3219–27.
70. Carlier, D., Ménétrier, M., Grey, C. P., et al. “Understanding the NMR shifts in paramagnetic transition metal oxides using density functional theory calculations,” *Physical Review B*, V. 67, No. 17, 2003.
71. Aykol, M., Kim, S., and Wolverton, C. “van der Waals Interactions in Layered Lithium Cobalt Oxides,” *The Journal of Physical Chemistry C*, V. 119, No. 33, 2015, pp. 19053–8.
72. Hinuma, Y., Meng, Y. S., and Ceder, G. “Temperature-concentration phase diagram of P2 Na_xCoO_2 from first-principles calculations,” *Physical Review B*, V. 77, No. 22, 2008.
73. Van der Ven, A., Aydinol, M. K., Ceder, G., et al. “First-principles investigation of phase stability in Li_xCoO_2,” *Physical Review B*, V. 58, No. 6, 1998, pp. 2975–87.
74. Levasseur, S., Menetrier, M., Suard, E., et al. “Evidence for structural defects in non-stoichiometric HT-$LiCoO_2$: electrochemical, electronic properties and ^{7}Li NMR studies,” *Solid State Ionics*, V. 128, Nos. 1–4, 2000, pp. 11–24.
75. Igarashi, D., Miyazaki, Y., Yubuta, K., et al. “Precise Control of Na Content in the Layered Cobaltate γ-Na_xCoO_2,” *Journal of Electronic Materials*, V. 39, No. 9, 2010, pp. 1669–73.
76. Delmas, C., Braconnier, J.-J., Fouassier, C., et al. “Electrochemical intercalation of sodium in Na_xCoO_2 bronzes,” *Solid State Ionics*, V. 3, No. 4, 1981, pp. 165–9.
77. Huang, Q., Foo, M. L., Pascal, R. A., et al. “Coupling between electronic and structural degrees of freedom in the triangular lattice conductor Na_xCoO_2,” *Physical Review B*, V. 70, No. 18, 2004.
78. Ren, Z., Shen, J., Jiang, S., et al. “Enhanced thermopower in an intergrowth cobalt oxide $Li_{0.48}Na_{0.35}CoO_2$,” *Journal of Physics: Condensed Matter*, V. 18, No. 29, 2006, pp. L379–84.
79. Bos, J. W. G., Hertz, J. T., Morosan, E., et al. “Magnetic and thermoelectric properties of layered $Li_xNa_yCoO_2$,” *Journal of Solid State Chemistry*, V. 180, No. 11, 2007, pp. 3211–7.
80. Semenova, A., Kellerman, D., Baklanova, I., et al. “Raman spectroscopy study of sodium–lithium cobaltite,” *Chemical Physics Letters*, V. 491, Nos. 4–6, 2010, pp. 169–71.

81. Kellerman, D. G., Zhuravlev, N. A., Semenova, A. S., et al. "^{23}Na NMR in binary lithium-sodium cobaltite," *Bulletin of the Russian Academy of Sciences: Physics*, V. 75, No. 8, 2011, pp. 1157–9.
82. Mesilov, V. V., Galakhov, V. R., Semenova, A. S., et al. "X-ray spectra and specific features of the structure of lithium-sodium cobaltite $Li_xNa_yCoO_2$," *Physics of the Solid State*, V. 53, No. 2, 2011, pp. 271–5.
83. Yabuuchi, N., Kawamoto, Y., Hara, R., et al. "A comparative study of $LiCoO_2$ polymorphs: structural and electrochemical characterization of O2-, O3-, and O4-type phases," *Inorganic chemistry*, V. 52, No. 15, 2013, pp. 9131–9142.
84. Cahill, L. S., Chapman, R. P., Kirby, C. W., et al. "The challenge of paramagnetism in two-dimensional ^{6,7}Li exchange NMR," *Applied Magnetic Resonance*, V. 32, No. 4, 2007, pp. 565–581.
85. Davis, L. J. M., Heinmaa, I., and Goward, G. R. "Study of lithium dynamics in monoclinic $Li_3Fe_2(PO_4)_3$ using ^{6}Li VT and 2D exchange MAS NMR spectroscopy," *Chemistry of Materials*, V. 22, No. 3, 2009, pp. 769–775.
86. Cahill, L. S., Chapman, R. P., Britten, J. F., et al. "^{7}Li NMR and two-dimensional exchange study of lithium dynamics in monoclinic $Li_3V_2(PO_4)_3$," *The Journal of Physical Chemistry B*, V. 110, No. 14, 2006, pp. 7171–7177.
87. Cahill, L. S., Kirby, C. W., and Goward, G. R. "^{6}Li{^{31}P} Rotational-Echo, Double-Resonance Studies of Lithium Ion Site Dynamics in $Li_3V_2(PO_4)_3$," *The Journal of Physical Chemistry C*, V. 112, No. 6, 2008, pp. 2215–2221.
88. Takahata, K., Iguchi, Y., Tanaka, D., et al. "Low thermal conductivity of the layered oxide $(Na,Ca)Co_2O_4$: Another example of a phonon glass and an electron crystal," *Physical Review B*, V. 61, No. 19, 2000, p. 12551.
89. Motohashi, T., Naujalis, E., Ueda, R., et al. "Simultaneously enhanced thermoelectric power and reduced resistivity of $Na_xCo_2O_4$ by controlling Na nonstoichiometry," *Applied Physics Letters*, V. 79, No. 10, 2001, pp. 1480–1482.
90. Menetrier, M., Rougier, A., and Delmas, C. "Cobalt segregation in the $LiNi_{1-y}Co_yO_2$ solid solution: a preliminary ^{7}Li NMR study," *Solid state communications*, V. 90, No. 7, 1994, pp. 439–442.
91. Ménétrier, M., Saadoune, I., Levasseur, S., et al. "The insulator-metal transition upon lithium deintercalation from $LiCoO_2$: electronic properties and ^{7}Li NMR study," *Journal of Materials Chemistry*, V. 9, No. 5, 1999, pp. 1135–1140.
92. Platova, T. A., Mukhamedshin, I. R., Alloul, H., et al. "Nuclear quadrupole resonance and X-ray investigation of the structure of $Na_{2/3}CoO_2$," *Physical Review B*, V. 80, No. 22, 2009.
93. Pan, C., Lee, Y. J., Ammundsen, B., et al. "^{6}Li MAS NMR studies of the local structure and electrochemical properties of Cr-doped lithium manganese and lithium cobalt oxide cathode materials for lithium-ion batteries," *Chemistry of materials*, V. 14, No. 5, 2002, pp. 2289–2299.
94. Carlier, D., Blangero, M., Ménétrier, M., et al. "Sodium Ion Mobility in Na_xCoO_2 ($0.6 < x < 0.75$) Cobaltites Studied by ^{23}Na MAS NMR," *Inorganic Chemistry*, V. 48, No. 15, 2009, pp. 7018–25.
95. Mizushima, K., Jones, P. C., Wiseman, P. J., et al. "Li_xCoO_2 ($0< x<1$): A new cathode material for batteries of high energy density," *Materials Research Bulletin*, V. 15, No. 6, 1980, pp. 783–789.
96. Delmas, C., Braconnier, J.-J., and Hagenmuller, P. "A new variety of $LiCoO_2$ with an unsual oxygen packing obtained by exchange reaction," *Materials Research Bulletin*, V. 17, 1982, pp. 117–23.
97. Tournadre, F., Croguennec, L., Saadoune, I., et al. "On the mechanism of the P2–$Na_{0.70}CoO_2 \rightarrow$ O2–$LiCoO_2$ exchange reaction—Part I: proposition of a model to describe the P2–O2 transition," *Journal of Solid State Chemistry*, V. 177, No. 8, 2004, pp. 2790–2802.
98. Tournadre, F., Croguennec, L., Willmann, P., et al. "On the mechanism of the P2–$Na_{0.70}CoO_2 \rightarrow$ O2–$LiCoO_2$ exchange reactionPart II: an in situ X-ray diffraction study," *Journal of Solid State Chemistry*, V. 177, 2004, pp. 2803–9.

99. Carlier, D., Saadoune, I., Croguennec, L., et al. "On the metastable O2-type $LiCoO_2$," *Solid State Ionics*, V. 144, Nos. 3–4, 2001, pp. 263–276.
100. Komaba, S., Yabuuchi, N., and Kawamoto, Y. "A New Polymorph of Layered $LiCoO_2$," *Chemistry letters*, V. 38, No. 10, 2009, pp. 954–955.
101. Paulsen, J. M., Mueller-Neuhaus, J. R., and Dahn, J. R. "Layered $LiCoO_2$ with a different oxygen stacking (O2 structure) as a cathode material for rechargeable lithium batteries," *Journal of The Electrochemical Society*, V. 147, No. 2, 2000, pp. 508–516.
102. Amatucci, G. G., Tarascon, J. M., and Klein, L. C. "CoO_2, the end member of the Li_xCoO_2 solid solution," *Journal of The Electrochemical Society*, V. 143, No. 3, 1996, pp. 1114–1123.
103. Mendiboure, A., Delmas, C., and Hagenmuller, P. "New layered structure obtained by electrochemical deintercalation of the metastable $LiCoO_2$ (O2) variety," *Materials research bulletin*, V. 19, No. 10, 1984, pp. 1383–1392.
104. Carlier, D., Saadoune, I., Ménétrier, M., et al. "Lithium Electrochemical Deintercalation from O2-$LiCoO_2$," *Journal of The Electrochemical Society*, V. 149, No. 10, 2002, p. A1310.
105. Carlier, D., Croguennec, L., Ceder, G., et al. "Structural Study of the $T^{\#}2$-Li_xCoO_2 ($0.52 < x \leq 0.72$) Phase," *Inorganic Chemistry*, V. 43, No. 3, 2004, pp. 914–22.
106. Fouassier, C., Matejka, G., Reau, J.-M., et al. "Sur de nouveaux bronzes oxygénés de formule NaχCoO2 (χ1). Le systeme cobalt-oxygene-sodium," *Journal of Solid State Chemistry*, V. 6, No. 4, 1973, pp. 532–537.
107. Zandbergen, H. W., Foo, M., Xu, Q., et al. "Sodium ion ordering in Na_xCoO_2 : Electron diffraction study," *Physical Review B*, V. 70, No. 2, 2004.
108. Foo, M. L., Wang, Y., Watauchi, S., et al. "Charge Ordering, Commensurability, and Metallicity in the Phase Diagram of the Layered Na_xCoO_2," *Physical Review Letters*, V. 92, No. 24, 2004.
109. Igarashi, D., Miyazaki, Y., Kajitani, T., et al. "Disorder-order transitions in Na_xCoO_2 ($x = 0.58$)," *Physical Review B*, V. 78, No. 18, 2008, p. 184112.
110. Williams, A. J., Attfield, J. P., Foo, M. L., et al. "High-resolution neutron diffraction study of possible charge ordering in $Na_{0.5}CoO_2$," *Physical Review B*, V. 73, No. 13, 2006.
111. Meng, Y. S., Hinuma, Y., and Ceder, G. "An investigation of the sodium patterning in Na_xCoO_2 ($0.5 \leqslant x \leqslant 1$) by density functional theory methods," *The Journal of chemical physics*, V. 128, No. 10, 2008, p. 104708.
112. Alloul, H., Mukhamedshin, I. R., Collin, G., et al. "Na atomic order, Co charge disproportionation and magnetism in Na_xCoO_2 for large Na contents," *EPL (Europhysics Letters)*, V. 82, No. 1, 2008, p. 17002.
113. Zhang, P., Capaz, R. B., Cohen, M. L., et al. "Theory of sodium ordering in Na_xCoO_2," *Physical Review B*, V. 71, No. 15, 2005, p. 153102.
114. Wang, Y., and Ni, J. "Effect of electronic correlation on the Na ordering of Na_xCoO_2," *Journal of physics: Condensed matter*, V. 19, 2007.
115. Wang, Y., and Ni, J. "Ground state structure of sodium ions in Na_xCoO_2: A combined Monte Carlo and first-principles approach," *Physical Review B*, V. 76, No. 9, 2007, p. 94101.
116. Zhou, S., and Wang, Z. "Charge and Spin Order on the Triangular Lattice: Na_xCoO_2 at $x = 0.5$," *Physical Review Letters*, V. 98, No. 22, 2007.
117. Paulsen, J. M., and Dahn, J. R. "Studies of the layered manganese bronzes, $Na_{2/3}[Mn_{1-x}M_x]O_2$ with M= Co, Ni, Li, and $Li_{2/3}[Mn_{1-x}M_x]O_2$ prepared by ion-exchange," *Solid State Ionics*, V. 126, No. 1, 1999, pp. 3–24.
118. Cheng, J.-H., Pan, C.-J., Lee, J.-F., et al. "Simultaneous Reduction of Co^{3+} and Mn^{4+} in P2-$Na_{2/3}Co_{2/3}Mn_{1/3}O_2$ As Evidenced by X-ray Absorption Spectroscopy during Electrochemical Sodium Intercalation," *Chemistry of Materials*, V. 26, No. 2, 2014, pp. 1219–25.

119. Bucher, N., Hartung, S., Gocheva, I., et al. “Combustion-synthesized sodium manganese (cobalt) oxides as cathodes for sodium ion batteries,” *Journal of Solid State Electrochemistry*, V. 17, 2013.

120. Wang, X., Tamaru, M., Okubo, M., et al. “Electrode Properties of P2–$Na_{2/3}Mn_yCo_{1-y}O_2$ as Cathode Materials for Sodium-Ion Batteries,” *The Journal of Physical Chemistry C*, V. 117, No. 30, 2013, pp. 15545–15551.

121. Beck, F. R., Cheng, Y. Q., Bi, Z., et al. “Neutron diffraction and electrochemical studies of $Na_{0.79}CoO_2$ and $Na_{0.79}Co_{0.7}Mn_{0.3}O_2$ cathodes for sodium-ion batteries,” *Journal of The Electrochemical Society*, V. 161, No. 6, 2014, pp. A961–A967.

122. Hemalatha, K., Jayakumar, M., and Prakash, A. S. “Influence of the manganese and cobalt content on the electrochemical performance of P2-$Na_{0.67}Mn_xCo_{1-x}O_2$ cathodes for sodium-ion batteries,” *Dalton Transactions*, V. 47, No. 4, 2018, pp. 1223–1232.

123. Baster, D., Zając, W., Kondracki, \Lukasz., et al. “Improvement of electrochemical performance of $Na_{0.7}Co_{1-y}Mn_yO_2$—cathode material for rechargeable sodium-ion batteries,” *Solid State Ionics*, V. 288, 2016, pp. 213–218.

124. Pai, W. W., Huang, S. H., Meng, Y. S., et al. “Sodium Trimer Ordering on a Na_xCoO_2 Surface,” *Physical review letters*, V. 100, No. 20, 2008, p. 206404.

125. Caballero, Hernan, Morales, et al. “Synthesis and characterization of high-temperature hexagonal P2-$Na_{0.6}MnO_2$ and its electrochemical behaviour as cathode in sodium cells,” *Journal of Materials Chemistry*, V. 12, 2002.

126. Buchholz, D., Moretti, A., Kloepsch, R., et al. “Toward Na-ion Batteries⍰ Synthesis and Characterization of a Novel High Capacity Na Ion Intercalation Material,” *Chemistry of Materials*, V. 25, No. 2, 2013, pp. 142–148.

127. Singh, V. K., Singh, S. K., Gupta, H., et al. “Electrochemical investigations of $Na_{0.7}CoO_2$ cathode with PEO-NaTFSI-BMIMTFSI electrolyte as promising material for Na-rechargeable battery,” *Journal of Solid State Electrochemistry*, V. 22, No. 6, 2018, pp. 1909–1919.

128. Yabuuchi, N., Kajiyama, M., Iwatate, J., et al. “P2-type $Na_x[Fe_{1/2}Mn_{1/2}]O_2$ made from earth-abundant elements for rechargeable Na batteries,” *Nature materials*, V. 11, No. 6, 2012, p. 512.

129. Fauth, F., Peral, I., Popescu, C., et al. “The new material science powder diffraction beamline at ALBA synchrotron,” *Powder Diffraction*, V. 28, No. S2, 2013, pp. S360–S370.

130. Billaud, J., Singh, G., Armstrong, A. R., et al. “$Na_{0.67}Mn_{1-x}Mg_xO_2$ ($0 < x < 0.2$): a high capacity cathode for sodium-ion batteries,” *Energy & Environmental Science*, V. 7, 2014, p. 1387.

131. Liu, Z., Hu, Y.-Y., Dunstan, M. T., et al. “Local structure and dynamics in the Na ion battery positive electrode material $Na_3V_2(PO_4)_2F_3$,” *Chemistry of Materials*, V. 26, No. 8, 2014, pp. 2513–2521.

132. Broux, T., Bamine, T., Fauth, F., et al. “Strong Impact of the Oxygen Content in $Na_3V_2(PO_4)_2F_{3-y}O_y$ ($0 \leq y \leq 0.5$) on Its Structural and Electrochemical Properties,” *Chemistry of Materials*, V. 28, 2016, p. 7683−7692.

133. Hu, J. Z., Jaegers, N. R., Hu, M. Y., et al. “In situ and ex situ NMR for battery research,” *Journal of Physics: Condensed Matter*, V. 30, No. 46, 2018, p. 463001.

134. Märker, K., Reeves, P. J., Xu, C., et al. “Evolution of structure and lithium dynamics in $LiNi_{0.8}Mn_{0.1}Co_{0.1}O_2$ (NMC811) cathodes during electrochemical cycling,” *Chemistry of Materials*, V. 31, No. 7, 2019, pp. 2545–2554.

135. Pigliapochi, R., O’Brien, L., Pell, A. J., et al. “When Do Anisotropic Magnetic Susceptibilities Lead to Large NMR Shifts? Exploring Particle Shape Effects in the Battery Electrode Material $LiFePO_4$,” *Journal of the American Chemical Society*, V. 141, No. 33, 2019, pp. 13089–13100.

136. Reeves, P. J., Seymour, I. D., Griffith, K. J., et al. “Characterizing the Structure and Phase Transition of Li_2RuO_3 Using Variable-Temperature ^{17}O and ^{7}Li NMR Spectroscopy,” *Chemistry of Materials*, V. 31, No. 8, 2019, pp. 2814–2821.

137. Carlier, D., Ménétrier, M., and Delmas, C. “^{7}Li MAS NMR study of electrochemically deintercalated $Li_xLi_{0.30}Co_{0.70}O_2$ phases: evidence of electronic and ionic mobility, and redox processes,” *Journal of Materials Chemistry*, V. 11, 2001, pp. 594–603.
138. Billaud, J., Clément, R. J., Armstrong, A. R., et al. “β-$NaMnO_2$: a high-performance cathode for sodium-ion batteries,” *Journal of the American Chemical Society*, V. 136, No. 49, 2014, pp. 17243–17248.
139. Xu, J., Lee, D. H., Clément, R. J., et al. “Identifying the critical role of Li substitution in P2–$Na_x[Li_yNi_zMn_{1-y-z}]O_2$ (0< x, y, z< 1) intercalation cathode materials for high-energy Na-ion batteries,” *Chemistry of Materials*, V. 26, No. 2, 2014, pp. 1260–1269.
140. Clément, R. J., Billaud, J., Armstrong, A. R., et al. “Structurally stable Mg-doped P2-$Na_{2/3}Mn_{1-y}Mg_yO_2$ sodium-ion battery cathodes with high rate performance: insights from electrochemical, NMR and diffraction studies,” *Energy & Environmental Science*, V. 9, No. 10, 2016, pp. 3240–3251.
141. Clément, R. J., Middlemiss, D. S., Seymour, I. D., et al. “Insights into the Nature and Evolution upon Electrochemical Cycling of Planar Defects in the β-$NaMnO_2$ Na-Ion Battery Cathode: An NMR and First-Principles Density Functional Theory Approach,” *Chemistry of Materials*, V. 28, 2016, pp. 8228–39.
142. Yoshizumi, D., Muraoka, Y., Okamoto, Y., et al. “Precise Control of Band Filling in NaxCoO2,” *Journal of the Physical Society of Japan*, V. 76, No. 6, 2007.
143. Mogare, K. M., Friese, K., Klein, W., et al. “Syntheses and crystal structures of two sodium ruthenates: Na_2RuO_4 and Na_2RuO_3,” *Zeitschrift für anorganische und allgemeine Chemie*, V. 630, No. 4, 2004, pp. 547–552.
144. Rozier, P., Sathiya, M., Paulraj, A.-R., et al. “Anionic redox chemistry in Na-rich $Na_2Ru_{1-y}Sn_yO_3$ positive electrode material for Na-ion batteries,” *Electrochemistry Communications*, V. 53, 2015, pp. 29–32.
145. Lu, Z., Beaulieu, L. Y., Donaberger, R. A., et al. “Synthesis, Structure, and Electrochemical Behavior of $Li[Ni_xLi_{1/3-2x/3}Mn_{2/3-x/3}]O_2$,” *Journal of The Electrochemical Society*, V. 149, No. 6, 2002, pp. A778–A791.
146. Koga, H., Croguennec, L., Mannessiez, P., et al. “$Li_{1.20}Mn_{0.54}Co_{0.13}Ni_{0.13}O_2$ with different particle sizes as attractive positive electrode materials for lithium-ion batteries: insights into their structure,” *The Journal of Physical Chemistry C*, V. 116, No. 25, 2012, pp. 13497–13506.
147. Sathiya, M., Rousse, G., Ramesha, K., et al. “Reversible anionic redox chemistry in high-capacity layered-oxide electrodes,” *Nature Materials*, V. 12, No. 9, 2013, pp. 827–35.
148. Koga, H., Croguennec, L., Ménétrier, M., et al. “Reversible oxygen participation to the redox processes revealed for $Li_{1.20}Mn_{0.54}Co_{0.13}Ni_{0.13}O_2$,” *Journal of The Electrochemical Society*, V. 160, No. 6, 2013, pp. A786–A792.
149. Lee, Y. J., and Grey, C. P. “Determining the Lithium Local Environments in the Lithium Manganates $LiZn_{0.5}Mn_{1.5}O_4$ and Li_2MnO_3 by Analysis of the ^{6}Li MAS NMR Spinning Sideband Manifolds,” *Journal of Physical Chemistry B*, V. 106, 2002.
150. Kobayashi, H., Kanno, R., Kawamoto, Y., et al. “Physical properties of the de-lithiated $Li_{2-x}RuO_3$ with the layered structure,” *Solid State Ionics*, V. 86, 1996, pp. 859–863.
151. Maitra, U., House, R. A., Somerville, J. W., et al. “Oxygen redox chemistry without excess alkali-metal ions in $Na_{2/3}[Mg_{0.28}Mn_{0.72}]O_2$,” *Nature Chemistry*, V. 10, No. 3, 2018, pp. 288–95.
152. Mortemard de Boisse, B., Nishimura, S., Watanabe, E., et al. “Highly Reversible Oxygen-Redox Chemistry at 4.1 V in $Na_{4/7-x}[\square_{1/7}Mn_{6/7}]O_2$ (□: Mn Vacancy),” *Advanced Energy Materials*, 2018, p. 1800409.
153. Perez, A. J., Batuk, D., Saubanère, M., et al. “Strong oxygen participation in the redox governing the structural and electrochemical properties of Na-rich layered oxide Na_2IrO_3,” *Chemistry of Materials*, V. 28, No. 22, 2016, pp. 8278–8288.

154. Vallée, C., Saubanère, M., Sanz-Camacho, P., et al. “Alkali-Glass Behavior in Honeycomb-Type Layered $Li_{3-x}Na_xNi_2SbO_6$ Solid Solution,” *Inorganic chemistry*, V. 58, No. 17, 2019, pp. 11546–11552.
155. Yang, L., Li, X., Liu, J., et al. “Lithium-Doping Stabilized High-Performance P2–$Na_{0.66}Li_{0.18}Fe_{0.12}Mn_{0.7}O_2$ Cathode for Sodium Ion Batteries,” *Journal of the American Chemical Society*, V. 141, No. 16, 2019, pp. 6680–6689.

List of Figures

List of Tables

Titre : Étude de la structure, structure électronique et de la dynamique dans des oxydes lamellaires pour batteries Na-ion

Résumé : Les oxydes lamellaires de type A_xMO_2 (A = alcalin, M = métal de transition) sont largement étudiés comme matériaux d'électrode positive dans des batteries Li-ion ou Na-ion. Par ailleurs, ils peuvent présenter également de propriétés physiques originales. Une première partie de ce travail de thèse vise à étudier par RMN du ^{23}Na et ^{7}Li, la structure moyenne, locale et électronique ainsi que la mobilité des ions Li^+ dans les espaces interfeuillets de deux oxydes lamellaires originaux : OP4-(Li,Na)CoO_2 et O4-Li_xCoO_2. Des mesures en température ont mis en évidence la présence à la fois d'électrons localisés et délocalisés au sein de la structure. De plus, La RMN 2D du ^{7}Li a montré l'absence de mobilité des ions Li^+ dans la phase OP4 à cause d'interfeuillets partiellement remplis d'ions Na^+. Concernant la phase O4, une mobilité des ions Li^+ au sein de la structure est mise en évidence. P2-Na_xCoO_2 est un matériau modèle comme matériau d'électrode positive pour batteries Na-ion. Lors de cette thèse, les diagrammes de phase de P2-Na_xCoO_2 ainsi que de trois autres systèmes P2-$Na_xCo_yMn_{1-y}O_2$ (y = 1/3, 1/2 et 2/3) ont été étudiés par DRX in-situ, avec une attention particulière sur les phénomènes se déroulant à hauts potentiels (> 4.3 V vs Na^+/Na). De nombreux changements structuraux sont reportés et des sur-structures inédites ont été observées. Par la suite, des glissements de feuillets ont été mis en évidence pour des compositions en Na^+ inférieures à 1/3 à la fois par DRX in-situ et ex-situ. Enfin, des phases des systèmes Na_xCoO_2, $Na_xCo_{2/3}Mn_{1/3}O_2$ et O3-Na_xRuO_3 avec différentes teneurs en ions Na^+ ont été stabilisées et analysées ex-situ par DRX et RMN du ^{23}Na afin de comprendre les mécanismes se produisant lors de la charge et la décharge de ces matériaux d'électrode. La RMN a permis de suivre les processus redox et les modifications parfois complexe, des liaisons chimiques.

Mots clés : RMN, batteries Na-ion, structure, dynamique, structure électronique

Title: Structure, electronic structure and dynamics in layered transition metal oxides for Na-ion batteries

Abstract: The lamellar oxides A_xMO_2 (A = alkali ions, M = transition metal) are largely studied as positive electrode materials for Li-ion or Na-ion batteries. They can also propose interesting and none-common physical properties. The first part of this work concerns the study of the average, local and electronic structure besides the Li^+ ions mobility in the interslab spaces of two unusual phases: OP4-(Li,Na)CoO_2 et O4-Li_xCoO_2 by ^{7}Li and ^{23}Na MAS NMR. Concerning the OP4 phase, variable temperature measurements highlight the presence of localized and delocalized electrons in the structure. Moreover, ^{7}Li 2D NMR suggests that the Li^+ ions are not mobile in the structure because of a partial filling of interslabs by Na^+ ions while in the O4 phase, a mobility of Li^+ ions can be observed. P2-Na_xCoO_2 is a model material as positive electrode material for Na-ion batteries. In this work, the phase diagrams of this system and of three others systems P2-$Na_xCo_yMn_{1-y}O_2$ (y = 1/3, 1/2 and 2/3) were studied by in-situ XRD with a specific attention to the phenomena occurring at high voltages (> 4.3 V vs Na^+/Na). Many structural changes are reported and new super-structures are shown. Layers' glidings were also highlighted for compositions in Na^+ ions below 1/3 by in-situ and ex-situ XRD. Finally, phases of Na_xCoO_2, $Na_xCo_{2/3}Mn_{1/3}O_2$ and O3-Na_xRuO_3 with various x values were stabilized and analyzed ex-situ by XRD and ^{23}Na NMR in order to understand the mechanisms occurring during the charge and the discharge of these electrode materials. NMR shows a complex behavior of the different systems et especially a modification in the chemical bonds nature.

Keywords : NMR, Na-ion batteries, structure, dynamics, electronic structure

Unité de recherche ICMCB, UMR 5026, 87 Avenue du Dr Albert Schweitzer, 33600 Pessac